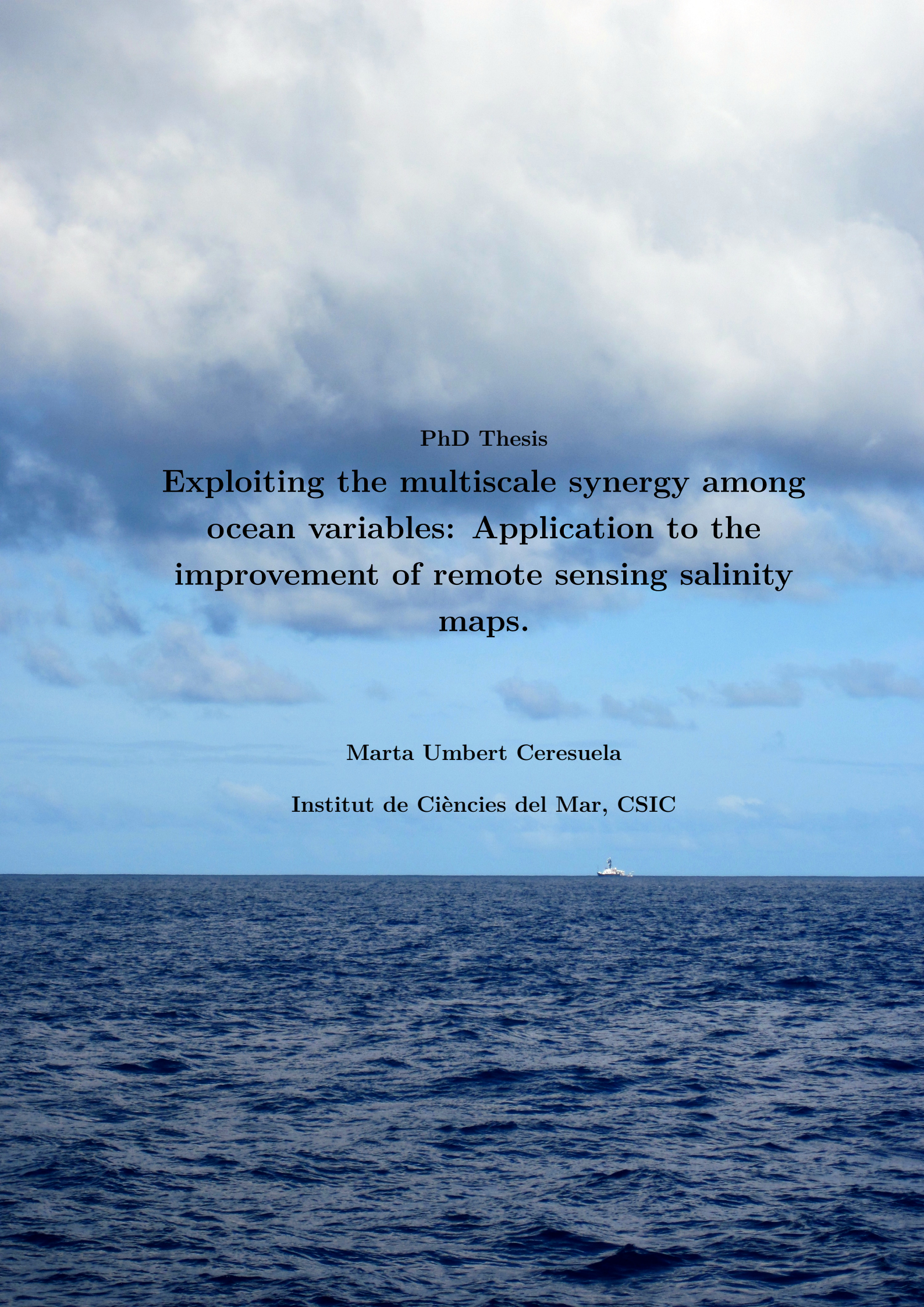

PhD Thesis

Exploiting the multiscale synergy among ocean variables: Application to the improvement of remote sensing salinity maps.

Marta Umbert Ceresuela

Institut de Ciències del Mar, CSIC

Exploiting the multiscale synergy among ocean variables: Application to the improvement of remote sensing salinity maps.

Marta Umbert Ceresuela

Institut de Ciències del Mar, CSIC

Dissertation submitted to the Universitat Politècnica de Catalunya as a requirement for the Doctoral degree with international mention. Speciality: Marine Sciences

Advisor - Dr. Antonio Turiel Martínez (ICM-CSIC)
Co-advisor - Dr. Joaquim Ballabrera Poy (ICM-CSIC)
Tutor - Dr. Adriano Camps Carmona (UPC)

Tribunal - Dr. Emilio García Ladona (ICM-CSIC)
Tribunal - Dra. Mercè Vall-Llossera Ferran (UPC)
Tribunal - Dra. Jaqueline Boutin (LOCEAN-France)

External reviewer - Dr. Bruno Buongiorno Nardelli (CNR-Italy)
External reviewer - Dr. Nicolas Reul (IFREMER-France)

Cover: SPURS-MIDAS Campaign, North Atlantic Subtropical Gyre. April 2013

Barcelona September 30, 2015

Abstract

Remote sensing imagery of the ocean surface provides a synoptic view of the complex geometry of ocean circulation, which is dominated by mesoscale variability. The signature of filaments and vortices is present in different ocean scalars advected by the oceanic flow. The most probable origin of the observed structures is the turbulent character of ocean currents, and those signatures are persistent over time scales compatible with ocean mesoscale dynamics. At spatial scales of kilometers or more, turbulence is mainly 2D, and a complex geometry, full of filaments and eddies of different sizes, emerges in remote sensing images of surface chlorophyll-a concentration and surface salinity, as well as in other scalars acquired with higher quality such as surface temperature and absolute dynamic topography.

The aim of this thesis is to explore and apply mapping methodologies to improve the quality of remote sensing maps in general, but focusing in the case of remotely sensed sea surface salinity (SSS) data. The different methodologies studied in this thesis have been applied with the specific goal of improving surface salinity maps generated from data acquired by the European Space Agency's mission SMOS, the first satellite able to measure soil moisture and ocean salinity from space at a global scale.

The first part of this thesis will introduce the characteristics of the operational SMOS Level 2 (L2) SSS products and the classical approaches to produce the best possible SSS maps at Level 3 (L3), namely data filtering, weighted average and Optimal Interpolation. In the course of our research we will obtain a set of recommendations about how to process SMOS data starting from L2 data.

A fusion technique designed to exploit the common turbulent signatures between different ocean variables is also explored in this thesis, in what represents a step forward from L3 to Level 4 (L4). This fusion technique is theoretically based on the geometrical properties of advected tracers (Turiel et al., 2005a). Due to the effect of the strong shear in turbulent flows, the spatial structure of tracers inherit some properties of the underlying flow and, in particular, its geometrical arrangement. As a consequence, different ocean variables exhibit scaling properties, similar to the turbulent energy cascade (Seuront and Schmitt, 2005; Nieves et al., 2007; Nieves and Turiel, 2009; Isern-Fontanet et al., 2007).

The fusion method takes a signal affected by noise, data gaps and/or low resolution, and improves it in a geophysically meaningful way. This signal improvement is achieved by using an appropriate data, which is another ocean variable acquired with higher quality, greater spatial coverage and/or finer resolution. A key point in this approach is the assumption of the existence of a multifractal structure in ocean images (Lovejoy et al., 2001b), and that singularity lines of the different ocean variables coincide. Under these assumptions, the horizontal gradients of both variables, signal and template, can be related by a smooth matrix. The first, simplest approach to exploit such an hypothesis assumes that the relating matrix is proportional to the identity, leading to a local regression scheme. As shown in the thesis, this simple approach allows reducing the error and improving the coverage of the resulting Level 4 product; More-

over, information about the statistical relationship between the two fields is obtained since the functional dependence between signal and template is determined at each point.

Resum

Les imatges de teledetecció de la superfície oceànica proporcionen una vista sinòptica de la complexa geometria de la circulació oceànica, dominada per la variabilitat de mesoescala. Estructures com filaments i vòrtex són presents en els diferents escalars advectats pel flux oceànic. L'origen més probable d'aquestes estructures és el caràcter turbulent dels corrents, aquestes estructures són persistents amb el temps i compatibles amb la dinàmica mesoscalar oceànica. A escales espacials de quilòmetres o més, la turbulència és principalment 2D, i una complexa geometria, plena de filaments i remolins de mides diferents, emergeix en les imatges superficials de teledetecció de concentració de clorofil · la-a, salinitat superficial, així com en altres escalars més coneguts com són la temperatura superficial i la topografia dinàmica.

L'objectiu d'aquesta tesi és explorar i aplicar metodologies de mapatge que permeten millorar la qualitat de mapes de teledetecció oceànica en general, i en particular de la salinitat superficial del mar (SSS). Les diferents metodologies emprades en aquesta tesi han estat aplicades amb l'objectiu específic de millorar els mapes de teledetecció de salinitat superficial del mar proveïts per la missió SMOS de l'Agència Espaial Europea. SMOS és el primer satèl · lit capaç de mesurar la humitat del sol i salinitat oceànica des de l'espai a escala global.

La primera part d'aquesta tesi se centra a analitzar les característiques dels productes de nivell 2 (L2) de salinitat de SMOS i produir mapes de nivell 3 (L3) de salinitat utilitzant aproximacions clàssiques: millora del filtratge, mitjana ponderada i Interpolació Òptima. En el curs de la nostra recerca obtenim un conjunt de recomanacions de com processar les dades de SMOS començant des del nivell L2.

Aquesta tesi també presenta una nova tècnica de fusió de dades que permet explotar les estructures turbulentes comunes entre diferents variables oceàniques, representant un pas endavant en la cadena de processat per generar mapes de nivell 4 (L4). Aquesta tècnica de fusió es basa teòricament en les propietats geomètriques dels traçadors advectats per la dinàmica oceànica (Turiel et al., 2005a). Degut a l'efecte de forta cissalla als fluits turbulents, l'estructura espacial d'un traçador oceànic hereta algunes propietats del flux subjacent, i en particular el seu arranjament geomètric. Com a conseqüència, les diferents variables oceàniques mostren propietats d'escala similars a la cascada d'energia turbulenta (Seuront and Schmitt, 2005; Nieves et al., 2007; Nieves and Turiel, 2009; Isern-Fontanet et al., 2007).

El mètode de fusió agafa un senyal de menor qualitat (afectat per soroll, forats de dades i/o de resolució més baixa) i en millora la seva qualitat. A més d'això, el mètode de fusió és capaç d'extrapolar les dades de forma geofísicament coherent. Aquesta millora del senyal s'aconsegueix utilitzant una altra variable oceànica adquirida amb major qualitat, cobertura espacial més gran i/o millor resolució. Un punt clau d'aquesta aproximació és la suposició de l'existència d'una estructura multifractal de les imatges de teledetecció oceànica (Lovejoy et al., 2001b), i que les línies de singularitat de les diferents variables de l'oceà coincideixen. Sota aquestes premises, els gradients de les dues variables a fusionar estan relacionats per una matriu suau. Com a primera i simple aproximació, s'assumeix que aquesta matriu és proporcional a la identitat;

això porta a un esquema de regressió lineal local. Aquesta tesi mostra que aquesta aproximació senzilla permet reduir l'error i millorar la cobertura del producte de nivell 4 resultant. D'altra banda, s'obté informació sobre la relació estadística entre les dues variables fusionades, ja que la dependència funcional entre elles es determina per cada punt de la imatge.

"A todas las mujeres que me han precedido y me han hecho el camino un poco más claro y más fácil."

-Clarissa Pinkola Estés. *Women Who Run With the Wolves.*

Contents

Acronyms List

AMSR-E : Advanced Microwave Scanning Radiometer - Earth Observing System

ACC : Antarctic Circumpolar Current

ADT : Absolute Dynamic Topography

ATBD : Algorithm Theoretical Basis Document

AVHRR : Advanced Very High Resolution Radiometer

BWR : Barcelona World Race

CESBIO : Centre d'Etudes Spatiales de la Biosphere

CHL : Chlorophyll

CSIC : Consejo Superior de Investigaciones Científicas

CTD : Conductivity, Temperature, Depth (in situ ocean measurements)

CONAE : Comisión Nacional de Actividades Espaciales

DAP : Data Analysis Product

ECMWF : European Centre for Medium Range Weather Forecasts

ECV : Essential Climate Variable

ENSO : El Niño Southern Oscillation

ENVISAT : Environmental Satellite

ESA : European Space Agency

FMC : Forum Marítim Català

FOV : Field Of View

GCOS : Global Climate Observing System

GDAC : Global Data Assembly Center

GHRSST : Group for High Resolution SST

GOC : Global Overturning Circulation

GODAE : Global Data Assimilation Experiment

GOES : Geostationary Operational Environmental Satellite

GS : Gulf Stream

ICM : Institut de Ciències del Mar

IFREMER : Institut Français de Recherche pour l'exploitation de la Mer

IQR : Inter-Quartile range

IR : Infrared

ITCZ : Intertropical Convergence Zone

ISO : International Organization for Standardization

JAMSTEC : Japan Agency for Marine-Earth Science and Technology

L2 : Level 2 Product: Directly retrieved (derived) geophysical variables in given locations

L3 : Level 3 Product: Composite of L2 Product for a period of time, mapped on uniform space-time grid scales, usually with some completeness and consistency method applied

L4 : Level 4 Product: Model output or results from analyses of combination of lower level data of at least two different variables

MIRAS : Microwave Imaging Radiometer with Aperture Synthesis

MLD : Mixed Layer Depth

MMF : Microcanonical Multifractal Formalism

MOC : Meridional Overturning Circulation

MODIS : Moderate Resolution Imaging Spectroradiometer

MW : Microwave

MYO : MyOcean

NASA : National Aeronautics and Space Administration

NCDC : National Climatic Data Center

netCDF : Network Common Data Format

NOAA : National Oceanic and Atmospheric Administration

NODC : National Oceanographic Data Center

OFES : Ocean general circulation model For the Earth Simulator

OGCM : Ocean General Circulation Models

OI : Optimal Interpolation

OpenDAP: Open-Source Project for a Network Data Access Protocol Protocol to download subset of data from n-dimensional gridded dataset

OSCAR : Ocean Surface Current Analyses

OSTIA : Operational Sea Surface Temperature and Sea Ice Analysis

OTT : Ocean Target Transformation

PIRATA : Prediction and Research Moored Array in the Atlantic

PMEL : Pacific Marine Environmental Laboratory (NOAA)

PO.DAAC : Physical Oceanography Distributed Active Archive Centre (US)

RMS : Root Mean Square

RFI : Radio Frequency Interference

ROV : Remote Operated Vehicle

SLA : Sea Level Anomalies

SMOS : Soil Moisture and Ocean Salinity

SPCZ : South Pacific Convergence Zone

SSM/I : Special sensor microwave imager

SSS : Sea Surface Salinity

SST : Sea Surface Temperature

Sv : Sverdrup (10^6 m^3 s^{-1})

TAO : Tropical Atmosphere Ocean

THREDDS : Thematic Realtime Environmental Distributed Data Services

TRITON : Triangle Trans-Ocean Buoy Network

TSG : Thermosalinograph

UDP : User Data Product

Introduction

To enhance our understanding and our ability to predict the Earth's climate system and their changes. A key area of uncertainty is the role of the ocean processes interacting with land, atmosphere and ice systems (Clayson and Bogdanoff, 2013). The ocean has a major role in regulating the global climate and the hydrological cycle, as it stores and releases a large amount of heat, water and carbon. To reduce the current uncertainties in the complex and intimately linked ocean processes, hydrological cycle and climate system, the scientific community needs more and improved observations.

Historical observations of the ocean essentially come from single water samples, followed by thermosalinograph measurements on board research vessels and ships of opportunity, and from moored buoys. More recently, autonomous profiling floats (Argo program) and ROVs had greatly improved the spatio-temporal coverage of in situ measurements. Starting in the 70s, remote sensing sensors on-board satellite platforms offered an original, synoptic view of the ocean surface. Nowadays, maps of several ocean variables are systematically produced by processing the data acquired with remote sensing platforms. Passive sensors carried by satellites measure the natural electromagnetic emissions by the Earth. Active sensors transmit a signal and measure its modified echo signal. Among the ocean variables that are operationally sensed or derived from observations, we can include: ocean color, water quality, solar radiation flux, sea ice, sea surface temperature, wind speed, water vapor, surface topography, wind speed modulus and direction, sea level, significant wave height and currents.

Global maps of remote sensing products usually suffer of data gaps, and also require the application of noise-reduction techniques. This is especially true for high-spatial (few kilometers), high-temporal (daily-weekly) resolution maps, as orbital gaps or data loss due to natural (clouds, aerosols or sun glint) or instrumental limitations reduce the amount of available information. In remote sensing products, gap-filling, in addition to noise-reduction techniques, are crucial to provide uniform products suitable for applications such as real-time or near real-time, environmental monitoring or initialization of physical and ecosystem models.

This thesis studies and applies methodologies to generate spatio-temporal averaged gridded maps of ocean variables derived from remote sensing measurements. The studied methodologies aim at improving the quality of the final products in terms of noise reduction and enhancement of their geophysical consistency. In the first part of this thesis, two widely used methodologies for improving remote sensing mapping are studied. The first method to be applied is the weighted average. The weighted average rests a well-known, simple, robust method, which only considers data acquired by the satellite. The second method is optimal interpolation (OI), introduced by Bretherton et al. (1976) in oceanography. OI it is a statistical method in which information coming from satellites is combined with other prior sources of data.

The second part of this manuscript, presents a novel technique based on previous studies; this method improves the signal-to-noise ratio and allows filling data gaps by enhancing the geophysical information of the remote sensed variable. The mesoscale activity in form of fronts,

eddies and filaments has a clear signature in different ocean variables, even in the raw radiance recorded by the satellites (Crocker et al., 2007; Isern-Fontanet et al., 2007). This coincidence led to the following question: can the information from different structures observed in a given ocean variable be used to improve our knowledge about another variable? In the last years a recent scheme for extracting the structural information from ocean scalar variables has arisen, that of singularity analysis in the microcanonical multifractal formalism (MMF) (Turiel et al., 2008b). In this thesis the correspondence of singularity exponents among different variables is explored and used to define a functional relation that is exploited to produce enhanced gridded maps.

All the methodologies explored in this thesis are applied to sea surface salinity (SSS) products from remote sensing measurements. SSS is a recognized essential climatic variable (ECV) (Global Climate Observing System) that is linked to the mass and heat balances between the atmosphere and the ocean through evaporation, precipitation and river runoff. Besides, SSS, together with temperature, determine the seawater density and acts as a tracer of oceanic flow dynamics. Thus, the synoptic spatio-temporal characterization of surface salinity achieved by satellites will serve to improve understanding the hydrological cycle, the global ocean dynamics and climate variability.

Launched in 2009, the ESA Soil Moisture and Ocean Salinity (SMOS) mission is the first Earth observing satellite designed for the remote sensing of sea surface salinity over the oceans. SMOS single playload is the radiometer MIRAS (Microwave Imaging Radiometer with Aperture Synthesis). This passive instrument measures the emissions of the ocean at the microwave L-band (Kerr et al., 2001). It is possible to estimate SSS from passive microwave measurements because the emisivity of the ocean is a function of the dielectric constant of sea water, which depends on temperature, salinity and the electromagnetic frequency.

The amplitude of the radiometric signal associated with SSS variability is small as compared to the sensitivity of SMOS radiometer; therefore, to obtain quality measurements, careful calibration, sophisticated correction, processing algorithms and spatio-temporal averaging to increase the signal-to-noise ratio are required (Font et al., 2010). However, several open issues are still present in SMOS mission as it is innovative both in its measurement and in its technology; the mapping techniques explored in this work are a required step in order to allow the scientific community to incorporate remotely sensed SSS in ocean and climate models.

The outline of this thesis is as follows. The first chapter, reviews the state of the art necessary for this work. Then, a second chapter describes the data to be used in the experiences of this study. In the third chapter, the first two methodologies used to create sea surface salinity maps, weighted average and optimal interpolation, are described, tested and compared. The resulting SSS maps and their errors are characterized using several validation SSS datasets: measurements from opportunity vessels, oceanographic campaign data, drifting buoys, and long term average of in situ data or climatologies. The fourth chapter presents the theory on which the third approach to improve the quality of SSS maps is based. An extensive discussion about the performance of our fusion algorithm, and the effect of choosing different template variables, is discussed in the fifth chapter. The sixth chapter presents an oceanographic application of the methodologies

introduced along the thesis: we study the SSS signature of mesoscale rings in western boundary currents. The study of this oceanographic process allows to explore the ability of the data fusion technique on resolving mesoscale features from remote sensing SSS products and evaluate their realism. As an outlook of this work, we also explore in the seventh chapter the potential of the novel technique introduced in this thesis when it is applied to a different variable, i.e., surface chlorophyll concentration. Finally, a general conclusion and future perspectives are presented.

Chapter 1

State of the Art

1.1 Remote sensing of ocean system

Oceans represent the 70 percent of the Earth's total surface. They play a primary role to regulate the world climate and weather, and also on their changes, by means of the continuous exchange of heat, moisture, momentum and gases across the ocean-atmosphere interface. However, the huge dimension of the ocean and its great structural complexity (consequence of its turbulent character) have historically limited the acquisition of in situ data. As a long-term global observation system, remote sensing of the oceans is essential to understand and predict the evolution of the climate system.

Remote sensing of the ocean (Le Traon, 2002) is based on the derivation of geophysical quantities from electromagnetic signals captured by specific sensors. There are passive and active sensors. Passive sensors measure the natural electromagnetic field which radiates from land and ocean surfaces. On the other hand, active sensors send a signal and measures the modified echo signal. The frequency/energy spectrum used for ocean observation ranges from high frequencies or low wavelengths of tenths of microns (visible range) to low frequencies or large wavelengths of tens of meters (microwave). Higher the used frequency is, higher is the resolution; however, higher frequencies are affected by cloud cover. Lower frequencies (wavelengths of tens of meters) are used by radars. Radars can observe during day and night and through almost any whether conditions (affected only by intense rain).

The visible band (0.4-0.8μm), sensitive to cloud coverage, is used to derive ocean color products, water quality, solar radiation flux and sea ice coverage. The infrared band (0.8-1000 μm), which is also sensitive to cloud coverage, is used to derive sea surface temperature, and some fluxes. The microwave band (0.1 cm to 100 cm) is used to derive sea surface temperature, salinity, wind speed, water vapor and thin sea ice thickness. The microwave band is not affected by clouds, although retrieved products have coarser resolution and limited accuracy as compared to infrared products.

Active microwave sensors or radars (altimeters, scatterometes and Synthetic Aperture Radars) are used to derive surface topography, wind speed modulus, sea level, significant wave height, currents and sea ice thickness by measuring the specular reflection scattering. Microwave scatterometers measure the electromagnetic reflection or "backscatter" of microwaves that are returned by small sea surface waves. Microwaves reflection depends on wind speed and direction, being really sensitive to rain conditions (Weissman et al., 2012).

Ships sample the ocean in a relatively small area, often with a great deal of difficulty. Data from ships, buoys and drifters are too scarce to characterize the conditions of the spatially and temporally diverse ocean. In contrast, satellite measurements have an unprecedented repetitive capability and provide synoptic surface views over large areas. The main disadvantage of ocean

remote sensing is that it just provides information about the surface layer of the sea surface in contact with the atmosphere (with a penetration depth depending on the used wavelength, from one micron for thermal infrared to several meters for optical passing through some centimeters for microwave). Despite of this limitation the scientific picture of the oceans available from remote sensing has a spatial and time resolution not available by other observing systems.

The collection and analysis of long-term ocean data using remote sensing is a relatively modern field of exploration. Satellite remote sensing allows acquiring key global information of the state of the ocean and constant efforts are made to increase the quality, quantity, duration and integration of their ocean observations of ocean-related satellite missions. The first oceanographic satellite, SEASAT, was launched by NASA in June 1978. It carried five sensors to monitor the ocean from space: i) A radar altimeter to measure wave heights at surface ocean, ii) a microwave scatterometer to measure wind speed and direction, iii) a microwave radiometer to measure sea surface temperature (SST), iv) a visible and infrared radiometer to identify clouds and v) a synthetic aperture high resolution radar to measure surface wave fields and ice concentrations.

Today, satellite altimetry has become a key component of ocean observing system and its benefits in the open ocean have been thoroughly demonstrated during the last two decades (Morrow and Le Traon, 2012). Satellite altimetry and SAR (synthetic aperture radar) platforms allows deriving surface wave data (significant wave height and direction wave spectra), mean geostrophic ocean currents, circulation patterns and eddy kinetic energy (Johannessen et al., 2000). Another key component of ocean state is SST, operationally measured by, among others NOAA satellites (AVHRR). It is also measured by geostationary satellites (GOES and METEOSAT), that have superior temporal sampling, but lower resolution and accuracy. SST is vital for understanding and predicting heat and moist fluxes among the ocean and the atmosphere, to assess ocean currents and to understand the mechanisms of heat transport in the ocean which are critical to assess some processes (some global as the thermal hiatus or ENSO triggering, other more local such as the warm blob close to California) associated with climate change. Ocean color measurements (SEAWIFS, MODIS) allow deriving suspended sediments and phytoplankton (Chl-a) concentration, therefore the biological or living part of the remote sensing ocean variables. Phytoplankton is the primary step of the food chain of ocean biological activity and play a major role regulating the global $C0_2$ concentration.

1.2 Ocean circulation and turbulence

The ocean is in constant motion. The processes injecting energy to the ocean dynamics at planetary scales (mainly through wind forcing at ocean surface and tidal forces) create large scale mean flows that are constantly breaking down into small-scale features. Winds are the main forcing, and they are primarily created by the differential heating at the bottom of the atmosphere, that induce atmospheric convection; due to the differential solar heating in latitude, warmer at the equator and colder in the poles, planetary atmospheric cells (Hadley, medium latitudes and polar) organize the general circulation of the atmosphere and grant a systematic

forcing on the oceans that is utterly the real engine of ocean motion. Due to bathymetry, basin boundaries and the conservation of potential vorticity, the ocean circulation at medium to large scales is that of a quasi-2D turbulent flow, dominated by the presence of eddies and filaments generated by flow instabilities. Eddies are the main responsible of long-range transport of properties across the ocean (Chelton et al., 2007; Chelton and Xie, 2010); mass, heat, nutrients, salt, organisms and chemical particles in the ocean can be displaced over distances of thousands of kilometers, regulating the planet weather, climate and marine ecosystems.

At surface, temperature and salinity of sea water are modified through processes at surface level and in the mixed layer, including heating, cooling, rain, evaporation, wind, waves and currents. Once they sink below the mixed layer, temperature and salinity may be altered only by mixing processes with adjacent water bodies. Seen from this perspective, the temperature and salinity are not independent variables, and their knowledge allows us to recognize water masses. Oxygen can also be used as a tracer, although it is a non-conservative property; is acquired at surface and is slowly reduced over time due to oxidation of organic matter and respiration of organisms.

Currents are coherent streams of water moving through the ocean. Currents are primarily forced by winds and by differences in temperature, density and pressure of water. Currents are also governed by the Earth rotation and constrained by the location of the continents. To study the movements of a volume of water in the ocean, Newton's second law (the acceleration to which is subjected a water volume is proportional to the sum of forces acting on it) is used. The main forces acting on any volume of water in the ocean are: i) gravity force, ii) pressure gradient force, iii) Coriolis force and iv) friction force. The resulting expression is called Navier-Stokes equation, which is the basis for the physical description of the oceanic motion. These forces generate different ocean dynamics that shape the currents and waves at different temporal and spatial scales.

The two main components of large-scale ocean circulation are:

i) Thermohaline vertical circulation: evaporation, cooling and freezing produce increases in density causing the sinking of water masses. Below the surface, ocean circulation is primarily driven by variations in seawater density, which is determined by salinity and temperature. The thermohaline vertical circulation allows the exchange of heat between the equatorial and high latitude regions. The time scales of the thermohaline circulation (conveyor belt representation) are typically of one to several hundred years. Density-controlled circulation is key for transporting heat in the ocean and maintaining Earth's climate.

ii) Wind driven generated circulation: Surface winds drive currents in the upper ocean (up to 1000 meters depth). These currents coincide with the main superficial currents of the oceans. Permanent subtropical high-pressure systems centered at 30 degrees north and south in latitude (the higher latitude boundary of Hadley cell) create steady wind patterns known as westerlies and trade winds. Friction between the air and the water starts the water movement at the sea surface. The wind driven movement of oceanic water creates five permanent subtropical gyres in the ocean basins, two in the Atlantic Ocean, two in the Pacific Ocean and one in the Indic Ocean. These gyres turn clockwise in the northern hemisphere and anticlockwise in

the Southern hemisphere. These large scale gyres have slow, diffuse equatorward currents at the eastern boundary, and fast, intense, poleward flows at the western boundary (the so-called western boundary currents). The placement of land masses and the Earth rotation cause the boundary currents to be narrower and deeper in the western part of the subtropical gyres. Western boundary currents are the fastest ocean currents on Earth, reaching speeds of more than 2.5 m/s. These currents include the Gulf Stream in the North Atlantic, the Kuroshio in the North Pacific and the Agulhas in the Indian Ocean. The currents on the Eastern part of the subtropical gyres are slower and more diffuse until they reach the equator and speed up driven by trade winds and heat from tropical latitudes.

Smaller gyres can be found around 60 degrees North created by the winds around subarctic low pressure systems called subpolar gyres. Another subpolar gyre circle around the Antarctica, in the zonally unbounded Southern Ocean, is driven by the westerly winds that blow over the southern ocean without any land impediment creating the Antarctic Circumpolar Current (ACC). It flows continuously around the globe and provides a major link for water property exchanges between the Atlantic, Indian and Pacific Oceans. Time scales of this large scale horizontal circulation are typically of a few years.

This characterization of the ocean circulation, which results from theories of large scale wind driven and thermohaline ocean circulation (Pedlosky, 1998), is a first order approximation to real ocean. The ocean is indeed a turbulent system and the ocean circulation is not a large scale and temporally stable phenomenon; it varies over an almost continuous frequency/wavenumber spectrum with space and time scales ranging from tens to thousands of kilometers and from days to years (Le Traon Pierre-Yves, 1999). Any instantaneous view of the ocean circulation would thus reveal areas with intense and small scale ocean currents almost everywhere and would be dominated by mesoscale variability. In particular, Western boundary currents and the ACC are areas of intense mesoscale variability. Open ocean currents, which are part of the large scale gyre circulation, are also often intense and narrow currents embedded with mesoscale eddies. At the eastern boundaries, superimposed on the broad equatorward flow, we can find energetic currents and coastal upwelling currents, which can be highly variable in space and time.

The mesoscale variability is the dominant signal in the ocean circulation at the scales resolved by remote sensing. There is not a precise definition of mesoscale variability, but it usually refers to a subclass of energetic motions with typical space and time scales of 50 to 500 km and 10 to 100 days. Phenomenological representations of this variability include eddies, vortices, fronts, narrow jets, meanders, rings, filaments and planetary waves (Rossby and Kelvin waves) (Fu and Cazenave, 2000).

Regional salinity and temperature variations are also affected by ocean circulation (advection and mixing). When surface salinity increases due to evaporation, the increased surface density contributes to a destabilization of upper-ocean stratification. Though the total buoyancy flux also depends on the sign and magnitude of the heat flux, surface salinification will generally contribute to deeper convective mixing of surface waters. Conversely, freshwater inputs due to rainfall or river runoff will decrease surface salinity, make a positive contribution to the stratification, and generally inhibit mixing (Schmitt, 2008).

Turbulence is the underlying dominant influence of ocean variables distributions. A turbulent flow is characterized by chaotic property variations. This includes low momentum diffusion, high momentum convection, and rapid variation of pressure and flow velocity in space and time. Variables of primary physical origin, such as temperature, have the spectral signature expected for a passive tracer in a turbulent system (Lovejoy et al., 2001a). A first approach to the study of turbulence is to establish analogies between molecular and turbulent properties transfer mechanisms. In this case the eddies that make up the turbulent flow would be analogous to the molecules in the molecular processes. Also by similarity is defined a turbulent viscosity coefficient, with the difference that its value is orders of magnitude greater than the coefficient of molecular viscosity. The problem presented by this analogy is that the effects of the turbulent transfer depend on the size of the eddies, but typically a single value from the turbulent viscosity coefficient is used.

Turbulent flows are system with an infinite number of degrees of freedom, and are also characterized by a lack of definite scale, since the possible substructures are repeated across the flow with many different sizes, looking the same at any possible scale of observation. Fractality is a concept used to describe self-similar systems. The study of turbulence favored the introduction of multifractals: coordinated ensemble of fractals, organized in a hierarchical way. A multifractal is a scale invariant system; this means that the statistical properties of small-scale regions are the same as those of the whole system: they are self-similar (Pont et al., 2009). Many oceanic fields that have (or are distributed by) turbulent characteristics are expected to follow scaling and possibly multifractal properties (Turiel et al., 2008b). These include the velocity field, passive tracers (potential temperature, potential salinity, sea surface temperature (SST), sea surface salinity (SSS), chlorophyll concentration, and its surrogates such as fluorescence), and fields related by integrations or derivations to the velocity field (vorticity, absolute dynamic topography (ADT)) (Verrier et al., 2014).

1.3 Sea Surface Salinity: Interest of the measure and principles

Sea Surface Salinity (SSS) is the salinity in the very top ocean layer. Seawater is composed from 96.5% of pure water and 3.5% of other components being salt, dissolved gases, organic substances and non-dissolved particles. The main difference between pure water and seawater is the existence of a small amount of dissolved salts in seawater, which will cause major deviations in its thermodynamic behavior. The presence of dissolved salts in seawater is due to the large capacity of dissolution of the pure water that through the centuries has been gradually dissolving salts from rocks of the Earth's crust by rains and rivers which transported and accumulated their mineral washings into the sea.

Salinity is a dimensionless quantity as it is theoretically defined as the solid weight of salts in grams contained in one kilogram of seawater (g/kg) or parts per million (ppm), when all carbonates have been transformed into oxides, bromine and iodine replaced by chlorine and organic matter oxidized (Sverdrup et al., 1942). Seawater has a mean salinity of 35,000 ppm, equivalent to 35 grams of salt per one liter (or kilogram) of water. As it can be seen in Table

1.1, the 99.99% of the salt content is due to eleven ions called major constituents. The rest of the elements present in the seawater receive the name of trace constituents, have concentrations of less than one part per million and include all the natural elements of the periodic table. A significant feature of the seawater is that while the total concentration of dissolved salts varies from one place to another, the proportions between them it remain constant up to the second decimal. This is known as the rule of constant composition (Dittmar, 1884).

Table 1.1: Major constituents of seawater

Constituents	Concentration g/Kg	Percentage
Chlorine Cl-	18.98	55.07
Sodium Na+	10.556	30.62
Sulfate So42-	2.649	7.72
Magnesium Mg2+	1.272	3.68
Calcium Ca2+	0.40	1.17
Potassium K+	0.38	1.10
Bicarbonate HCO3-	0.14	0.40
Bromine Br-	0.067	0.19
Strontium Sr2+	0.008	0.02
Boron B-	0.004	0.01
Fluoride F-	0.001	0.01
Total	**34.457**	**99.99**

In the last thirty years, in situ salinity determination is carried out by measurements of electrical conductivity and it is expressed in the practical salinity scale (pss) (Lewis, 1980; UNESCO, 1981). The presence of disassociated ions makes seawater a conductor of electricity and therefore susceptible to quantify the amount of salts dissolved from the electrical conductivity. In the practical salinity scale, practical salinity is defined as the conductivity ratio to a standard potassium chloride (KCl) solution.

Ocean salinity is a key geophysical variable for understanding the global water cycle. 97% of the Earth's free water reside in the oceans (Schmitt, 1995) and the global water cycle main components are precipitation and evaporation (Yu, 2011; Vinogradova and Ponte, 2013). Precipitation over the oceans account for 78% of the global precipitation (12 Sverdrups; 1 Sv = 1 million $m^3 s^-1$), and an additional Sv of fresh water flow into the oceans from terrestrial runoff. Evaporation over the ocean is equal to 86% of the global evaporation (13 Sv). In contrast, precipitation and evaporation over land account only for 3 Sv and 2 Sv respectively (Schmitt, 2008). The mean global salinity distribution is dominated by processes that increase or decrease the fresh water amount on the ocean surface, mainly in the form of precipitation and evaporation, but also in a smaller proportion as input of fresh water from river discharge and ice melting.

Sea surface salinity can therefore be used to measure the difference between these two processes, with excess precipitation resulting in lower salinities and excess evaporation giving higher sea surface salinity. The spatial distribution of surface salinity in the ocean over large portions of the ocean is a mirror image of the distribution of the difference between evaporation - precipitation (E-P), as it can be seen in Figure 1.1 extracted from published work of Schmitt (2008). Taking the difference between evaporation (E) and precipitation (P) tells us the net gain or loss of water by the ocean. The map of E-P shows where, in net balance, water evaporates (warm

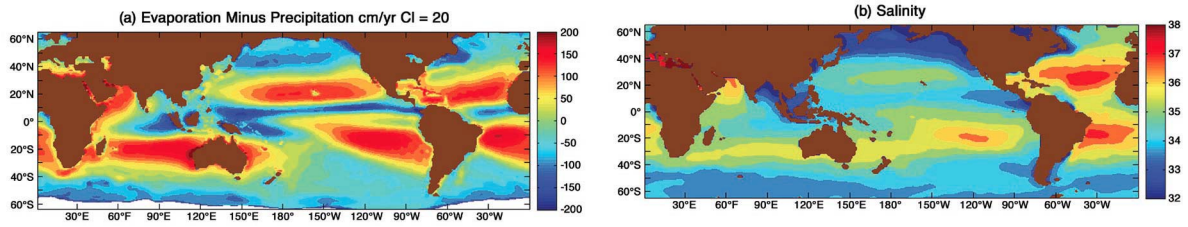

Figure 1.1: A new estimate of annual average evaporation minus precipitation, based on the evaporation climatology of Yu (2007) and satellite-based precipitation estimates from the Global Precipitation Climatology Program (GPCP). (b) Average surface salinity of the world ocean, contoured from the World Ocean Database of NODC.

colors) and precipitates (cool colors).

The general patterns of surface salinity reflect the behavior of the global water cycle and generally hold throughout the year (Johnson et al., 2012; Reul et al., 2014b,c). The mid-latitude evaporation leads to salinity maxima in all the subtropical gyres (Schanze et al., 2010). There is a fresh belt in the Equator displaced toward the northern hemisphere that coincides with the thermal Equator and results from the high precipitation in the Intertropical Convergence Zone (ITCZ) that compensates the large evaporation. The fresh region in the western tropical South Pacific is related to the South Pacific Convergence Zone (SPCZ) (Delcroix et al., 1996). Precipitation zones at high latitudes also induce low salinity. Melting and freezing of the poles is more significant in the Northern Hemisphere, and this generates a lower salinity at high latitudes of this hemisphere. In general the North hemisphere is less salty having into account that the majority of the river discharges take place there.

The high latitude North Pacific is fresher than the North Atlantic as evaporation dominates over precipitation in the Atlantic, whereas the terms come closer to balancing in the Pacific. In general the Pacific is fresher than the Atlantic, as westerly winds are blocked by the Andes and easterly are blocked by the Himalayas, what holds precipitations in the Pacific Ocean. Also, there is a transport of water vapor from the Atlantic to the Pacific across Central America, the surface mixed layer just west of Columbia and additionally the Gulf of Panama is remarkably fresh owing to the strong precipitation in the region.

The flow of salty water from the North Atlantic into the Arctic is evident along the West coast of Northern Europe, as it reflects the fresh influence of the flow of Pacific waters into the Arctic through the Bering Strait (Coachman and Aagaard, 1988). There is a strong contrast between the salty Arabian Sea, where the monsoon winds carry moisture from the oceans to the Indian subcontinent, and the relatively fresh Bay of Bengal, where precipitation and riverine freshwater sources have a strong effect on the mixed layer salinity (Han and McCreary, 2001). The Mediterranean and Red seas are remarkably salty owing to the strong dominance of evaporation over precipitation there, as can even be inferred from the two-layer reverse estuarine exchanges between these arid marginal seas and the open ocean (Bryden et al., 1994; Johns et al., 2003).

Salinity is also intimately tied to the general ocean circulation. Salinity, together with temperature, determines seawater density. A SSS increase of 0.2 pss or a decrease of 1°C in SST would each increase seawater density by approximately the same amount. Density differences,

and the energy input from surface winds, modify the pressure field in the whole ocean, even at great depths, and changes the geostrophic adjustment of which drives the ocean currents. Modifications in surface salinity are transferred to the deep ocean and spread to other regions by advection and diffusion mechanisms. For example, in the North Atlantic there are salty surface waters that flow north, become cooled by the atmosphere and become dense water which sinks to depth and flows southward. It is one of the main sinking sites of the meridional overturning circulation (MOC).

There exist a high potential to assimilate surface salinity in ocean models (Hackert et al., 2014; Zhu et al., 2014) to improve the description and forecast of the upper ocean ocean dynamics. Understanding how sea surface salinity varies will allow the scientific community to improve forecasting of oceanic and climatic events such as ENSO (El Niño Southern Oscillation), an irregularly periodical climate oscillation caused by variations in sea surface temperatures over the central and eastern tropical Pacific Ocean that can bring devastating weather in many parts of the world. The study of ocean surface salinity will also enhance our understanding of phenomena like the formation of dense water masses at Atlantic high latitudes through interaction with the atmosphere, the evaporation minus precipitation balance in many ocean regions, the sea ice freezing and melting, and many other processes; with the use of the new satellites for monitoring salinity from space we will improve our present knowledge of global hydrologic budgets, ocean circulation and its role in climate.

1.4 Methodologies for data mapping

In remote sensing field there exist different processing levels. Specifically for remotely sensed SSS, we distinguish the following: Level 0 (L0) consists of the raw data received from the satellite at the ground stations; these are raw binary data, unprocessed and uncalibrated. Level 1 (L1) is built from data collected at L0, which are processed and calibrated to retrieve the actual brightness temperature emitted by the ocean surface. Level 2 (L2) is formed by SSS retrievals, obtained by inverting a Geophisical Model Function applied to L1 brightness temperatures; the data points are georeferenced but the data are arranged according to the satellite track, as L1 data. Level 3 (L3) data are obtained using data mapping methodologies, where L2 data are averaged, interpolated or otherwise extrapolated using information on SSS only to create regular maps on a defined projection, with a given space and time resolution, which is lower than that of L2 but with greater data coverage. Finally, Level 4 (L4) data are, by definition, the regular maps with the highest attainable quality; they are obtained by combining SSS with any other source of data of different geophysical variables to improve the final product.

The first data mapping procedure, from which a set of punctual observations is converted to a data map, was the subjective analysis. Opposed to objective analysis methodologies, the subjective analysis relies on expert human knowledge to draw by hand the field based on existing observations. During the last decades, increasing computer power has contributed to advances in methods for data mapping objective analysis.

When mapping remote sensing data to generate more uniform products, data interpolation

and noise reduction are required. Both data interpolation and noise reduction are commonly performed by using univariate data mapping methods (Smith and Reynolds, 2004) or multivariate methods. Multivariate methods combine information from different sources; examples of multivariate approaches include optimal interpolation (Buongiorno, 2012), empirical orthogonal functions (Alvera-Azcarate et al., 2007; Sirjacobs et al., 2011) and classification methods (Jouini et al., 2013). Taking into account the present and increasing volume of satellite data, improved methodologies to explore and exploit synergies among the ocean satellite missions is absolutely required. The different satellite sensors can be combined to provide higher spatio-temporal sampling required for many oceanographic studies by using physically or statistically based merging approaches (Tandeo et al., 2014).

Synergistic approaches for the generation of high-level remote sensing maps are based on the combination of the information given by maps of different oceanic variables which are dynamically linked. This link is typically an underlying evolution equation based on the same driving factor (ocean circulation), in addition to other specific, variable-dependent terms. This information from the diverse observations can be integrated by assimilating them in a numerical model. The results from the assimilation step will provide analysis fields that incorporate all the available knowledge and are of better quality than the original observations. Data assimilation is a commonly used method to dynamically interpolate the observed variables available at a given subdomain to the rest of the domain, combining different observations of variables by using a numerical model (Hoareau et al., 2014). Data assimilation of remote sensed images and in situ data is also critical to achieve three dimensional ocean information and forecasts (Johannessen et al., 2000).

A less computationally expensive synergistic approach is the use of multivariate statistical methods such as optimal interpolation or data interpolating empirical orthogonal functions (on their multivariate formulation). Those statistical methods, however, rely on having a relatively large data record, and also require the knowledge of a priori estimates of some key statistical quantities (such as correlation matrices or orthogonal bases). Multi-satellite measurements of altimeter-derived absolute dynamic topography (ADT) and multisensor measurements of sea surface temperature (SST) have provided a wealth of information as regards ocean circulation and atmosphere–ocean interactions. Furthermore, several studies (Klein et al., 2009; Isern-Fontanet et al., 2008; Hausmann and Czaja, 2012; LaCasce and Mahadevan, 2006; Lapeyre and Klein, 2006) provide the theoretical rationale and demonstrate that fields of SST can become an active tracer coupled to the dynamics, leading to strong correlations with ADT fields.

In this thesis, a new multifractal-based fusion method is introduced (Chapter 4 and Chapter 5). The multifractal fusion is based on the correspondence of singularity exponents for different oceanic variables, a recurrently observed property. Relying on the correspondence of singularity exponents and making certain appropriate assumptions, a simple fusion algorithm is presented and applied to the specific case of denoising one sea surface salinity maps using a better known variable as a template (Umbert et al., 2014). The performance of this algorithm under different levels of noise (Turiel et al., 2014) has been tested in Chapter 4, showing a consistent noise decrease under realistic conditions. The method has also been tested for specific oceanographic

applications (Chapter 6), as for instance to improve the spatial resolution and coverage of salinity maps in order to detect and track the evolution of cold-core rings in the Gulf Stream area (Umbert et al., 2015). This method is currently being used at the CP34 SMOS Barcelona Expert Centre for the operational generation of Level 4 Sea Surface Salinity maps.

Chapter 2

Observations

The second chapter aims at giving a detailed presentation of the sets of data (remote sensing, in situ data and numerical model outputs) used in this thesis.

2.1 Sea surface salinity data

2.1.1 Remote sensing of sea surface salinity

The first two missions specifically designed to measure the ocean surface salinity are the SMOS mission (Soil Moisture and Ocean Salinity) by the European Space Agency (ESA) (Kerr et al., 2001) and the Aquarius mission of the National Aeronautics and Space Administration (NASA) (Lagerloef, 2012).

The ability to estimate SSS from space relies on the fact that thermal emissions of the ocean at the L-band are proportional to its physical temperature. The proportionality coefficient, the emissivity, is a function of the dielectric constant, a parameter which depends on temperature and conductivity, i.e. salinity.

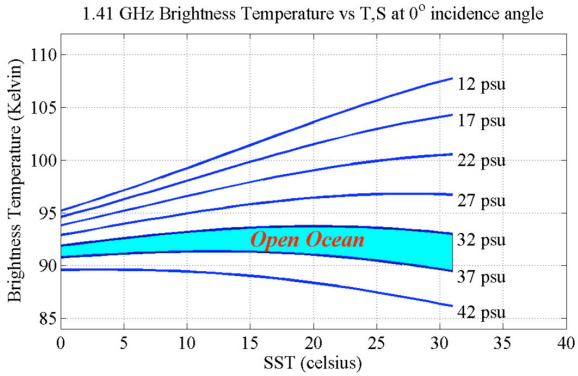

Figure 2.1: Brightness temperature vs temperature and salinity. Nasa Aquarius Mission webpage.

The thermal emission of the ocean is measured by radiometer, which are instruments capable of measuring the natural electromagnetic emissions of the bodies as brightness temperatures (Tb). To retrieve salinity, the microwave L-band (from 1.4 GHz to 1.43 GHz) is used, because the sensitivity of brightness temperature to salinity is maximum at this frequency band. Another advantage of the L-band is that the atmosphere is transparent at these frequencies, therefore L-band allow the acquisitions not to be affected by clouds. Moreover, this frequency band is reserved and protected from emissions by international radio regulations. Such protection is of extreme importance as the radiometers can misinterpret any man-made signal as a variation in the geophysical parameter measured.

Despite these advantages, the sensitivity of brightness temperature to salinity is weak and depends on sea surface temperature (Figure 2.1). The latter reaches a maximum in warm waters (0.7 K for a variation of 1 pss in SSS at SST=30°C) and strongly decreases in cold ones (0.2 K for a variation of 1 pss in SSS at SST=0°C) (Klein and Swift, 1977).

SMOS sea surface salinity data

The SMOS satellite was launched on November 2, 2009, on a sun-synchronous circular orbit at an altitude of 758 km with a local equator crossing time at 6 AM on ascending phase and at 6 PM. in descending phase (Mecklenburg et al., 2012). The satellite platform carries a fully polarimetric radiometer called MIRAS (Microwave Imaging Radiometer using Aperture Synthesis) (Berger et al., 2002). This new instrument allows the reconstruction of a bi-dimensional multiangular field of view (FOV) of Tb measurements (L1), out of which the inversion scheme retrieves SSS at 15 km sampling in a single satellite overpass (L2). Coverage of the global ocean is achieved every 3 days with a repeat cycle of 149 days and a mean spatial resolution of 43 km over the FOV (Figure 2.2).

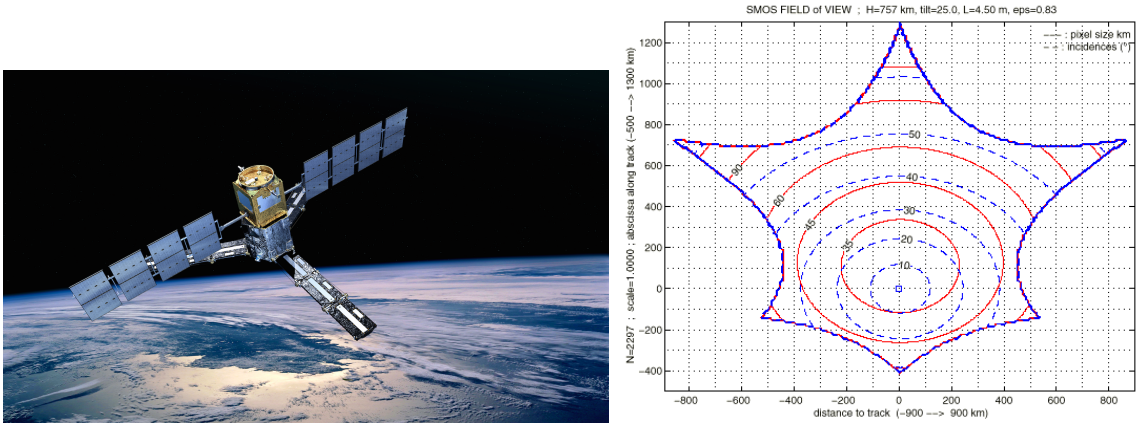

Figure 2.2: SMOS Satellite and SMOS Field of View. Centre d'Etudes Spatiales de la Biosphere (CESBIO).

The retrieval scheme implemented by the ESA (European Space Agency) processing services retrieve SSS, wind speed, sea surface temperature (SST), total electron content, and their theoretical errors, from the multiangular and polarized SMOS Tbs collected at an earth pixel during the satellite pass, using the Levenberg-Marquard (L.M.) minimization method as described in Zine et al. (2008). Prior values for wind speed and SST are taken from European Centre for Medium Range Weather Forecasts (ECMWF). The theoretical errors are retrieved from the Jacobian of Tb with respect to the geophysical parameters and from the a posteriori covariance matrix of errors in Tb and geophysical parameters. At first order, the theoretical error of SSS depends on the number of Tb data used in the retrieval and on SST as a consequence of the strong dependency of $dTb/dSSS$ with SST (Boutin et al., 2014).

The SMOS mission was designed to provide global, synoptic estimates of the SSS with an accuracy of approximately 0.1 pss (practical salinity scale) every 30 days and a spatial resolution of 100 km. To meet the mission accuracy a Level 3 product is obtained through an adequate

spatiotemporal averaging of the retrieved L2 values. Relative accuracy of SMOS data has been estimated as 0.3 - 0.4 in tropical and subtropical regions and 0.5 in cold regions, when compared against in situ salinity observations for SSS averaged over 100 x 100 km2 and 10 days (Banks et al., 2012; Boutin et al., 2013).

In this thesis, the SMOS ESA L2 SSS (ESA version 5.50) is used. In this reprocessing version, an Ocean Target Transformation (OTT) correction is applied every two weeks. The OTT correction aims to correct SMOS brightness temperatures (Tb) from systematic differences with respect to modelled Tb in the FOV (Yin et al., 2012). It is computed from Tb observations between 45°S and 5°S in the eastern Pacific, a region far from land and any Radio Frequency Interference contamination (Yin et al., 2013). However, seasonal and latitudinal biases are still present. Attempts to reduce such biases (including improved SMOS raw data calibration as well as the use of a time-varying OTT) remains under study (Martin-Neira et al., 2013).

Challenges of remote sensed SSS

The pioneer nature of these missions, both from the technological and data processing points of view, poses several challenges that are still being addressed by the SMOS and the Aquarius international teams: **(i)** The weak sensitivity of brightness temperatures to salinity (Sabia et al., 2014), **(ii)** Improvement in TB systematic errors estimation/removal (Gourrion et al., 2013), **(iii)** Refinement of L-band geophysical model function to retrieve salinity from radiometric measurements Guimbard et al. (2012). **(iv)** The geophysical model needs to correct the effect of the atmospheric radiative transfer (Liebe et al., 1993), ionospheric Faraday rotation (Reul et al., 2012a), the occurrence of galactic glints (Reul et al., 2008; Tenerelli et al., 2008), the Sun (Yin et al., 2013) and the Moon glints and the impact of sea surface roughness in ocean L-band emission (Font et al., 2010).

Another relevant aspect of the SMOS and Aquarius L-band measurements is the presence of radio-frequency interferences (RFI) that degrade the quality of the retrieved SSS maps. Although this frequency band is allocated to the Earth Exploration Satellite Service, the first data acquisitions made by SMOS in the western North Atlantic Ocean evidenced high RFI occurrence. Due to military radar arrays installed over North America, SMOS data in the North Atlantic has been contaminated by RFI until the end of 2011. Since then, the switch-off of unauthorized emissions (Daganzo-Eusebio et al., 2013) (e.g., predominantly radio devices) within the protected L-band has led to a noticeable improvement of the data quality in this area (Oliva et al., 2012).

Near the coast, salinity retrievals are less accurate due to signal contamination associated with the abrupt brightness temperature transition between the sea (∼100 K) and the land (∼220 K). This land-sea contamination effect is most noticeable in the SMOS data due to image reconstruction issues associated with the interferometric design of the instrument. In SMOS SSS maps, that contamination can extend up to several hundreds of kilometers offshore (Zine et al., 2007).

The Aquarius measurements are contaminated by instrument noise and contain large-scale satellite biases and spatially correlated errors (Melnichenko et al., 2014). Despite the relatively

large noise still present in the SMOS-derived SSS fields (salinity errors of around 0.3 - 0.4 in tropical and subtropical regions and 0.5 in cold regions, when compared against in situ salinity observations), their unprecedented spatial and temporal resolution capability has already given interesting results such as the study of salinity variation in marginal seas (Gierach et al., 2013), ocean response to tropical cyclones (Grodsky et al., 2012; Reul et al., 2012b) and the study of rain-induced surface salinity variability (Boutin et al., 2012a).

SMOS Level 3 products

Three European Expert Centers on Ocean Salinity produce Level 3 products from the official SMOS ESA Level 2 SSS: (i) CEC-OS LOCEAN (Laboratoire d'Océanographie et du Climat, Paris), (ii) CATDS-IFREMER (Centre Aval de Traitement des Données, Institut Français de Recherche pour l'Exploitation de la Mer, Brest) and (iii) BEC-ICM (Institut de Ciències del Mar, Barcelona) (see Table 2.1 adapted from Hernandez et al. (2014)).

The Level 3 product named CEC-LOCEAN, is generated using ESA Level 2 v5, using roughness-model 1, using only retrievals performed under moderate wind speed (3-12 m/s) and according to the flags described in Boutin et al. (2013). Level 3 SSS is flagged and averaged over one month, 100 x 100 km2 and oversampled every 0.25°. When averaging Level 2 SSS, each retrieved SSS is weighted by its spatial resolution and its theoretical uncertainty as derived by the L.M. algorithm (Yin et al., 2012).

The CATDS-IFREMER expert center has developed an alternative processing chain starting from Level 1B products, in which SSS is retrieved from the first Stokes parameter (wind speed is not retrieved). RFI filtering is more efficient as only one OTT is applied over the whole period and a large scale bias correction is applied. Their Level 3 SSS maps are averaged over 50 x 50 km^2 and oversampled every 0.25° with a daily 5°x 5° adjustment with respect to World Ocean Atlas 2001 climatology (Reul and CATDS -CECOS Team, 2012).

The BEC-ICM Level 3 product has been generated from ESA Level 2 v5.50 reprocessed products, using wind-model 3 (Guimbard et al., 2012) using retrievals performed under low and moderate wind speed (<12 m/s), and according to the flags described in SMOS-BEC Ocean and Land Products Description documentation. No galactic noise flag or land mask is used. Level 2 SSS are flagged and averaged over 0.25° and periods of 3 days, 9 days, monthly, seasonal and annual.

Aquarius Salinity data

The Aquarius/SAC-D satellite was launched in June 2011 and positioned on a polar sun-synchronous orbit at 657 km, crossing the equator at 18 pm (local time) in ascending orbits and at 6 am (local time) in descending orbits (Le Vine et al., 2007; Lagerloef et al., 2008). Aquarius/SAC-D is a collaboration mission between National Aeronautics and Space Administration (NASA) and Argentina's space agency Comisión Nacional de Actividades Espaciales (CONAE). Ascending orbits cross the equator at 6 PM and descending orbits at 6 AM local time. The Aquarius instrument consisted on three microwave (MW) radiometers at 1.413 GHz

Table 2.1: Summary of characteristics of SMOS SSS Level 3 products. Table adapted from Hernandez et al. 2014

	SMOS LOCEAN	SMOS IFREMER	**SMOS BEC**
SSS method retrieval	SSS retrieved from polarized Tbs along dwell lines using an iterative retrieval (see ESA L2OS ATBD)	SSS retrieved from first Stokes parameter (Reul and Tenerelli, 2011)	SSS retrieved from polarized Tbs along dwell lines using an iterative retrieval (see ESA L2OS ATBD)
Region of the instrument field of view (FOV) considered for SSS	Alias Free Field of View (AFFOV) and extended AFFOV along dwell lines with at least 130 Tb in AFFOV (± 300 km from swath center)	AFFOV only	AFFOV and extended AFFOV along dwell lines with at least 30 Tb in AFFOV (being >0.5 of total Tb) (± 360 km from swath center)
Tb sortings	Determined from consistency along dwell lines as reported in ESA Level 2 products	Determined from interorbit consistency in incidence angles classes and thresholding	Determined from consistency along dwell lines as reported in ESA Level 2 products
Galactic model	Kirchoff Approx. scattering at 3m/s	Geometrical optics model	Kirchoff Approx. scattering at 3m/s
Wind model	Model 1 (Empirical adjustment of parameters in roughness model and foam coverage models (Yin et al., 2012))	Model 2 (Empirical adjustment of Tb dependencies to wind speed by using bin average)	Model 3 (Empirical adjustment using a neural network of Tb dependencies to wind speed and incidence angle (Guimbard et al., 2012)
Calibration	Variable OTT (every 2 weeks synchronised with Noise Injection Radiometer as defined by ESA reprocessing	Single OTT + daily 5°x5° adjustment wrt World Ocean 2001 SSS climatology	Variable OTT (every 2 weeks synchronised with Noise Injection Radiometer as defined by ESA reprocessing
Grid resolution	Averaged over 100 x 100 km^2 and oversampled every 0.25°	Averaged over 50 x 50 km^2	Averaged over 0.25°
Averaging method	Average weighted by theoretical error on retrieved SSS and spatial resolution (footprint)	Simple average	Average weighted by theoretical error on retrieved SSS and spatial resolution (footprint)

along with a scatterometer at 1.26 GHz for surface roughness correction. The three MW radiometers generate three beams that form three elliptical footprints at sea surface (76 x 94 km, 84 x 120 km, and 96 x 156 km), aligned across a 390 km-wide swath. The nominal resolution of Aquarius satellite is roughly 100 km with a 7 days global coverage.

Significant sources of error as sensor drift, ascending/descending biases and interbeam biases as large as 0.2 (Melnichenko et al., 2014) are still present and mitigation strategies under ongoing research (Lagerloef and Coauthors, 2013). The official Aquarius level 3 (L3) products have a resolution of one degree, the latest L3 version is the Aquarius version 3.0 (Meissner et al., 2014). In the Aquarius V3 version, SSS is retrieved with the Combined Active Passive (CAP) algorithm which utilizes simultaneously data from the on board radiometer and scatterometer to retrieve SSS, wind speed and direction by minimizing the sum of squared differences between model and observations (Yueh et al., 2013, 2014).

2.1.2 In situ data

Historical SSS knowledge essentially comes from the analysis of single water samples and thermosalinograph (TSG) measurements on board research vessels and ships of opportunity. Since 2000, moored buoy arrays have been deployed for long term monitor of climatic events and pro-

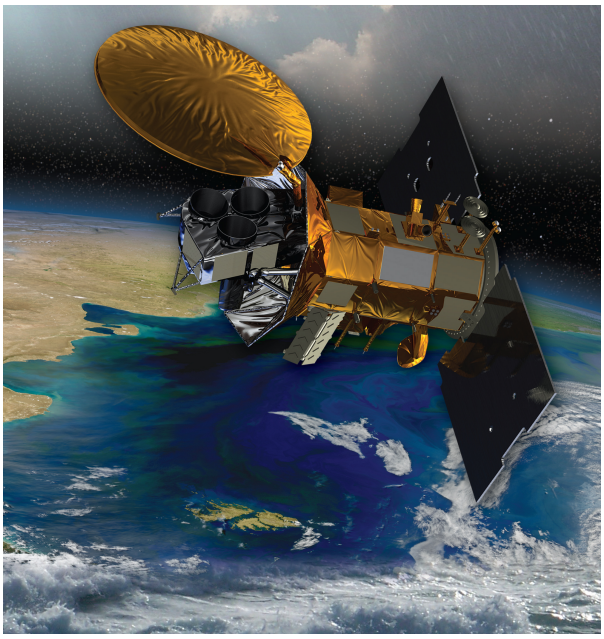

Figure 2.3: Aquarius Satellite

vide a reference data for remote sensing validation. This global network of offshore moorings is composed of NOAA/TAO(Tropical Atmosphere Ocean) array, JAMSTEC/TRITON (Triangle Trans-Ocean Buoy Network) array in the Tropical Pacific, PIRATA (Prediction and Research Moored Array in the Atlantic) array in the Atlantic, and RAMA (Research Moored Array for African-Asian-Australian Monsoon Analysis and Prediction) in the Indic Ocean. Additionally, the deployment of Argo automated devices for long term monitoring of the physical and biochemical properties of the ocean are increasing the coverage of in situ data. The Argo program has allowed the first global maps of in situ salinity maps (Figure 2.5).

Argo is an international collaboration with more of 30 countries contributing to maintain a global array of more than 3500 free drifting profiling floats that measure temperature and salinity from the upper 2000 meters of the sea-ice free global ocean. The floats drift neutrally buoyant at a 1000 meters 'parking depth'. At 10-day intervals, the float sinks to 2000 m and then rises to the surface over 6 hours while measuring the vertical profile of T and S. The GPS determines the position and the float transmits the data via satellite. Then, the float sinks to their parking depth until the cycle is repeated. There are several float models: PROVOR and ARVOR are built by NKE-INSTRUMENTATION in France in collaboration with IFREMER, the APEX float are produced by Teledyne Webb Research, the SOLO float designed and built by Scripps Institution of Oceanography (USA).

The Argo salinity measurements are not taken, in most cases, not shallower than 3-5 m from the surface. Under most conditions (moderate to high winds) the surface ocean mixed layer extends much deeper, and the buoy provides an accurate measurement of the 1-2 cm of the surface layer that emits the microwave signal seen by the satellite. Therefore Argo floats provide a global quasi-SSS dataset considering the difference in the 1 cm and 5 m depths of the satellite and Argo measurements, respectively, is most of the time smaller than the expected

accuracy of Aquarius and SMOS SSS measurements. However, under tropical rain conditions, stratification leads to gradients between the surface and the buoy measurement depth higher of 0.1 pss (Drucker and Riser, 2014).

The Argo array of profiling floats has a repeat cycle of one profile every 10 days and the current array extent provides a coverage of one profiler for an area of 300 km. Vinogradova and Ponte (2013) estimated the daily SSS mean differences between modeled and in situ SSS in boxes of 1 degree to be about 0.1, but greater than 0.2 in higher dynamical regions as near strong currents, outflows of major rivers and in coastal regions. When comparing in situ and satellite data it is also necessary to take into account that the horizontal SSS variability within the footprint of SSS remote sensing missions is typically larger than the vertical variations between the Argo and satellite estimate (Drucker and Riser, 2014). SSS variability with spatial scales smaller than the nominal 150 km footprint (in the case of SMOS), will contribute to differences between the satellite and in situ measurements. Therefore Argo is not only valuable to assess the quality of SMOS retrievals but also to highlight the differences between the two observation types.

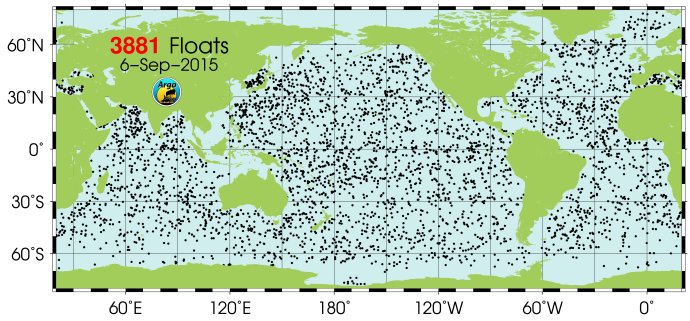

Figure 2.4: Argo floats distribution for the September 6th 2015, 3881 active floats. Image source: Argo Program webpage

To validate the satellite products presented in this thesis we use global in situ data for the year 2012, both coming from TSG and Argo floats. The in situ salinity data used were collected and made freely available by the Coriolis project and programs that contribute to it (Coriolis project webpage). The Argo data used have been compiled, quality controlled and distributed to users through the French Global Data Assembly Center (GDAC) of Coriolis Project. Then, the profiles are selected following these criteria: **(i)** Only Delayed Mode data are being used. **(ii)** Only primary CTD measurements (N-PROF=1) from each profile are used. **(iii)** Only data with the highest Quality Control value (QC=1) are used. **(iv)** The Quality Control of geographical position and date position is accepted if it has been set to 1 (good), 2 (probably good), 5 (Value changed) or 8 (Interpolated value). **(v)** Uppermost valid salinity measurement, without accepting any salinity value closer than 0.5 m to the surface, because some authors have observed erroneous measurements likely due to inaccuracies in the pressure measurement (Boutin et al., 2012b). **(vi)** Salinity data from PROVOR, SOLO instruments are not considered at depths shallower than 5 m, as these profilers types did not pump water at a depth shallower than 5 m (Wong et al., 2014).

A set of in situ data coming from the SPURS-MIDAS cruise (Las Palmas de Gran Canaria

16 March 2013 – Ponta Delgada, Açores 12 April) on board the Spanish R/V Sarmiento de Gamboa is also used. The SPURS experiment (Salinity Processes in the Upper ocean Regional Study) aimed at understanding the processes that drive the upper ocean dynamics and the role that salinity plays on them in the area of maximum salinity in the center of the North Atlantic subtropical gyre. The experiment was coordinated by WHOI (R. Schmitt) and sponsored by NASA (E. Lindstrom), and includes intensive field work with a large variety of state-of-the-art instrumentation, the use of satellite remotely sensed salinity information (Aquarius and SMOS), as well as dedicated numerical modeling.

The Sarmiento de Gamboa was at the SPURS site together with the US R/V Endeavor in a coordinated program to continue the SPURS field work initiated by the French R/V Thalassa (STRASSE cruise, August-September 2012) and US R/V Knorr (September-October 2012). The main role of the Sarmiento de Gamboa cruise was to first run a general survey for mesoscale mapping of the area by means of thermosalinograph (TSG), Acoustic Doppler Current Profilers (ADCP) and Seasoar ondulating CTD (conductivity temperature depth sensor) while the Endeavor arrived at the site and serviced the moorings and gliders deployed in the September cruise. At the same time a total of 48 surface salinity drifters were deployed.

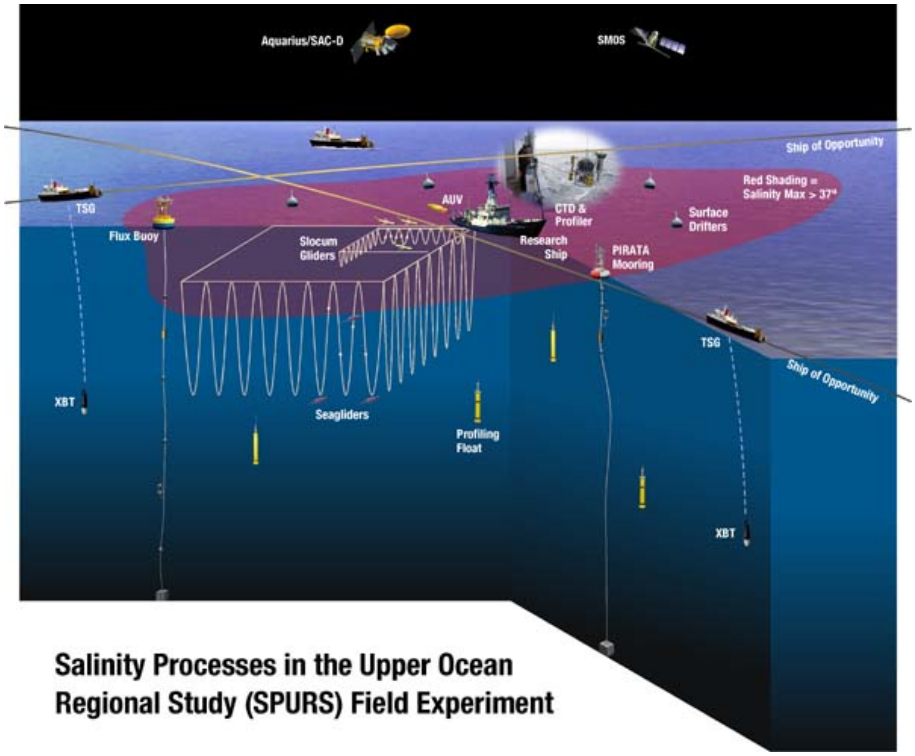

Figure 2.5: Schematics of SPURS field campaign measurements Spurs experiment

2.2 Sea surface temperature estimates

The knowledge of the SST is of major importance in meteorology, oceanography and climate sciences as it provides the boundary condition for estimating air-sea heat fluxes. Having this information on a global scale offers insights about the heat balance of the climate system, general

circulation patterns, and thermal anomalies. At smaller scales, it provides information about the presence of fronts between different water masses and the intensity of coastal and equatorial upwellings. Satellite estimates of SST rely on thermal emissions from the surface through the atmosphere. The use of infrared (3.7 μm and/or 10 μm) radiometers dates back to the end of the 1960s. The main drawback of infrared observations is that they are obscured by clouds. More recently, passive microwave (4–10 GHz) measurements have solved this problem, although their precision is lower than infrared estimates since microwave emission is not as strongly tied to the temperature of an object as infrared. Since the two methods have different strengths and weaknesses, their combination provides the most accurate remote sensing SST data.

We will use in this thesis two products of SST. The first product is OSTIA SST maps (Donlon et al., 2012). The OSTIA system is part of the GHRSST project for obtaining high-resolution operational SST maps, and is presently integrated at the MyOcean web portal. OSTIA SST maps are produced by combining satellite data and in situ observations with the help of an adapted version of the OI algorithm. OSTIA maps are produced daily at a resolution of 1/20°. To be used in this study, SST maps are reinterpolated to the 0.25° × 0.25° by block averaging and with the same pixel boundaries as SMOS SSS maps. Additionally, we average the daily data to 10-day averages, so they have the same temporal sampling as SMOS.

The second SST data set used correspond to the Advanced Very High Resolution Radiometer (AVHRR) and AMSR-E (Advanced Microwave Scanning Radiometer) daily quarter-degree resolution, optimally-interpolated (OI) product of Reynolds et al. (2007), which is available at NOAA-NCDC. This product results from the application of OI to data from the 4-km AVHRR Pathfinder Version 5 time series (when available, otherwise operational NOAA AVHRR data are used), AMSR-E SST and in situ ship and buoy observations. The OI analysis is a daily average SST that is bias-adjusted using a spatially smoothed 7-day in situ SST average. Both day and night satellite fields are independently bias-adjusted.

2.3 Altimetry data

Delayed time merged Global Ocean Gridded Sea Level Anomalies (SLA) and the Absolute Dynamic Topography SSALTO/DUACS L4 products are used in this thesis. All relevant information concerning these products can be found at AVISO web portal. Optimal interpolation (OI) is used to generate combined daily quarter-degree resolution maps that merge sea level observations from Cryosat-2, Jason-1 and Jason-2 satellites. In this study, SLA maps are used for eddy-tracking, while absolute dynamic topography maps are used as a template field for data fusion.

2.4 Ocean Chlorophyll

The Moderate-resolution Imaging Spectroradiometer (MODIS) is a scientific instrument (radiometer) launched by NASA in 2002 on board the Aqua satellite platform (a second series is on the Terra platform) to study global dynamics of the Earth's atmosphere, land and oceans. MODIS captures data in 36 spectral bands ranging in wavelengths from 0.4 μm to 14.4 μm

and at varying spatial resolutions (2 bands at 250 m, 5 bands at 500 m and 29 bands at 1 km). The Aqua platform is in a Sun-synchronous, near-polar orbit at 705 km altitude and the MODIS instrument images the entire Earth every 1 to 2 days. The Level 3 standard mapped image (SMI) chlorophyll-a dataset has a daily temporal resolution and 4.6 km (at the equator) spatial resolution. The SMI dataset is an image representation of binned MODIS data (more detailed information on the SMI format can be found at Ocean Color webpage). The MODIS Aqua instrument provides quantitative data on global ocean bio-optical properties to examine oceanic factors that affect global change and to assess the oceans' role in the global carbon cycle, as well as other biogeochemical cycles. Subtle variations in chlorophyll-a concentration correspond to various types and quantities of marine phytoplankton, the knowledge of which has both scientific and practical applications. This is a remote dataset from the NASA Ocean Biology Processing Group (OBPG). The OBPG is the official NASA data center that archives and distributes ocean color data (Ocean Color webpage).

2.5 Earth Simulator numerical simulation

Ocean General Circulation Models (OGCM) are used to solve the numerical equations of motion (momentum equation, conservation of mass and tracer concentrations) over a three dimension spatial grid. Usually the equations are simplified with certain hypothesis. Ocean numerical models are of great use for the understanding and forecasting both ocean and climatic systems.

The output of a global circulation model is used to validate the hypothesis of the correspondence between singularity exponents of SST and SSS and to test the sensitivity of the data fusion approach to the presence of noise. Our dataset consists of an output from the *Ocean general circulation model For the Earth Simulator* (OFES) (Masumoto et al., 2004; Masumoto, 2010). This is a near-global ocean model that has been spun up for 50 years under climatological forcing taken from monthly mean NCEP (National Centers for Environmental Prediction) atmospheric data. After that period the OFES is forced by the daily mean NCEP reanalysis for 48 years from 1950 to 1998. See Masumoto et al. (2004) for additional details on the forcings.

The output of the model corresponds to daily data for the last 8 years. Horizontal angular resolution is the same in both the zonal, ϕ, and meridional, θ, directions, with values of $\Delta\theta = \Delta\phi = 1/10°$. The calculations are restricted to the surface-layer temperature and salinity to emulate remote sensing data. The results shown in this thesis refer to January 1st, 1990, although results are similar for any other day.

2.6 Additional data sets

The daily 1/3° resolution surface current product from the Ocean Surface Current Realtime Analysis (OSCAR), described in Bonjean and Lagerloef (2002) and available at OSCAR webpage, is also used. This global, surface (0-30 m) velocity field is estimated from TOPEX/Poseidon altimeter data, Special Sensor Microwave Imager (SSM/I) wind data, and the gridded SST product of Reynolds et al. (2007) merged by the means of a steady, quasi-linear

model of the ocean mixed layer. In this work, surface velocity fields are only used to highlight the position of mesoscale rings and their rotation direction.

World Ocean Atlas (WOA) is a set of objectively analyzed climatological fields of in situ temperature, salinity, dissolved oxigen, phosphate, silicate, nitrate, and other variables at different depth levels for annual, seasonal and monthly periods produced by National Oceanographic Data Center - Ocean Climate Laboratory and available at NOAA webpage. In this study we use monthly products of World Ocean Atlas version 2009 (WOA09) interpolated linearly to 0.25^o degree (Antonov et al., 2010), and World Ocean Atlas version 2013 (WOA13) (Zweng et al., 2013) which is produced in a 0.25^o grid.

Finally, we use the monthly fields of salinity ISAS-13 (Gaillard, 2012), available for the period 2002-2012. They are produced using ISAS (In Situ Analysis System) (Gaillard et al., 2009), an optimally interpolation tool applied mainly to Argo floats measurements and complemented by data from the Tropical Moored Buoy Array program (TAO/TRITON, PIRATA and RAMA). ISAS fields are produced at Ifremer and can be downloaded in Copernicus Marine environment monitoring service. We use the first level of the ISAS analysis that essentially corresponds to the shallowest valid Argo measurement between the surface and 5 meters depth. ISAS-13 monthly fields are computed at 0.5^o; here we have linearly interpolated this products to 0.25^o.

Chapter 3

Weighted average and Optimal Interpolation

This chapter presents two classic methods of objective analysis, which are applied here to produce sea surface salinity maps from data provided by the SMOS mission. The first method is a weighted average and the second is an optimal interpolation (OI). In the case of the weighted average, Level 2 (L2) SSS values along satellite track are averaged together with an appropriate weight to produce Level 3 (L3) maps of surface salinity. The OI method incorporates available statistical information concerning the signal, its uncertainties and spatial correlations to generate an interpolated, higher quality SSS OI maps.

In this work, the two mapping methods are applied to generate SSS global maps with a spatial resolution of 0.25°, and 9-day and monthly averages. Validation of the resulting L3 and OI products for the year 2012 is addressed using in situ salinity measurements from Argo and TSG in addition to climatological values.

3.1 Objective Analysis

The aim of objective analysis is to determine the value of a field x_i^a at a given grid position i by combining an arbitrary set of observations. The majority of the objective analysis methods express the analysis value as a linear combination of a background value x_i^b and a data innovation vector d_j, where the components data innovation are the difference of the observed values y_j^o minus the background field at that location x_j^b:

$$x_i^a = x_i^b + \sum_{j=1}^{N} w_{ij}(y_j^o - x_j^b) \tag{3.1}$$

The background field x_i^b (also known as reference or first guess) is determined *a priori*, and the innovation values d_j are calculated with respect to their background value. Different definitions of the weighting function w_{ij} result in different objective analysis techniques.

Equation 3.1 can be expressed in matricial form by defining the concept of state or analysis vector $\mathbf{x}^a$ as a column vector containing the unknown values of the field to be estimated at each grid location (x_i^a):

SMOS SSS maps using the approaches summarized in this chapter were presented in the paper: ***Salat, J., Umbert, M., Ballabrera-Poy, J., Fernandez, P., Salvador, J. and Martinez, J., 2014. The contribution of the Barcelona World Race to improve the ocean surface information. IEEE Contributions to Science, in press.***

Partially developed during first PhD stage in Laboratoire en Géophysique et Océanographie Spatieles (LEGOS) in Toulouse (France), under the supervision of Prof. Véronique Garçon.

$$\mathbf{x}^a = \mathbf{x}^b + \mathbf{K}\left(\mathbf{y}^o - \mathbf{H}\mathbf{x}^b\right) \tag{3.2}$$

The observation vector $\mathbf{y}^o$ contains the observations. The interpolation of the background field $\mathbf{x}^b$ to the location of observations is done by means of the matrix $\mathbf{H}$ (usually, a bilinear interpolation operator). The matrix $\mathbf{H}$ applied to the vector $\mathbf{x}^b$ returns the background field interpolated at the location of the observations ($\mathbf{H}\mathbf{x}^b$).

With the help of Eq. 3.2, the innovation values $\mathbf{y}^o - \mathbf{H}\mathbf{x}^b$, are linearly combined with the background field, $\mathbf{x}^b$, by means of the gain matrix $\mathbf{K}$. This matrix represents the gridding operation and contains the weighting function w_{ij} in Eq. 3.1). As stated before, the form of the gain matrix $\mathbf{K}$ determines the objective analysis technique.

The specific problem addressed here is how to interpolate horizontally SMOS Level 2 salinity retrievals in order to construct synoptic maps of sea surface salinity. As detailed in section 2.1, the sensitivity of brightness temperature (T_b) to SSS is low and depends on SST (0.5°K / 1pss at 20°C and 0.3°K / 1pss at 5°C). That low sensitivity implies that the errors at the acquisition on T_b have a strong impact on the retrieval of SSS. In contrast, the SMOS satellite has a quite large spatio-temporal resolution (around 40 km and 3-days revisiting time). In the present work the large amount of low-quality data is synthesized using objective analysis methodologies in order to reduce the error of individual SSS observations.

3.2 Weighted Average

The first objective analysis approach that we are going to use to produce SMOS L3 maps is weighted average. The formulation of the weighted average can be derived from Eq. 3.1 by assuming a zero background field and a weight factor which is independent of the analysis point:

$$x_i^a = \sum_{j=1}^{N} w_j y_j^o \tag{3.3}$$

where y_j^o represents each of the L2 SSS retrievals. Following Boutin et al. (2012b) each retrieved SSS is weighted by its theoretical uncertainty provided by the Levenberg-Marquardt retrieval algorithm (Yin et al., 2012), and by its spatial footprint. That is,

$$w_j = \frac{1}{R_j^2 \sigma_j^2}\left(\sum_{l=1}^{N} \frac{1}{R_l^2 \sigma_l^2}\right)^{-1} \tag{3.4}$$

where σ_j is the theoretical uncertainty computed for SSS at a grid point j, R_j is the footprint size centered on the grid point j associated with each L2 SSS observation and N is the number of retrievals contained in the cell i.

3.2.1 Application to SMOS Sea Surface Salinity

Before applying the weighted average, and the subsequent mapping techniques applied in this manuscript, a data selection is performed to L2 SSS retrievals to discard data suspect of having

low quality. To do so, the official ESA L2 v5.50 reprocessed products are flagged according to the criteria used in Barcelona Expert Center (BEC) Ocean Products (BEC, 2014). At Level 1 (L1), T_b images are reconstructed, and errors related to radiometric sensitivity and accuracy are added to the signal. T_b images are transformed into SSS at Level 2 (L2) by using an inversion algorithm that requires auxiliary information on climatological SSS, SST and winds. At this stage new errors are introduced related to the auxiliary data, the semiempirical model used and geophysical factors as the sea roughness, rain or wind that have great impact on SSS errors.

The flags and descriptors of the quality of the salinity retrievals are generated by ESA and contained in L2 Ocean Salinity User Data Product (UDP) and Ocean Salinity Data Analysis Product (DAP). The UDP and DAP files contain information, along the satellite orbit, about the geophysical conditions present in the area at the time of the measurements, theoretical accuracy of SSS estimates and descriptors for the retrieval process of SSS (section 2.1).

The current filtering process applied at BEC uses the criteria described as follows. Retrievals flagged as valid (that is, the retrieval algorithm succeeded and the resulting salinity pass the adequate fit criteria defined in the ESA L2OS ATBD) are initially kept. However, they may be discarded if: more than 50 % of brightness temperature measurements are suspicious of ice presence; rain rate larger than 0.01 mm/h; a high number of outliers (more than 20% of measures) are detected; more than 10% of measures are flagged for sunlight or moonlight; salinity is retrieved using less than 30 brightness temperature valid measures; wind speed larger than 12 m/s; the grid point is suspected of being contaminated by RFI, the retrieved value is outside the valid range (SSS have to be positive and <42 pss); the theoretical uncertainty computed for SSS is larger than 5; the normalized cost function at the last iteration is greater than 5% 0.05, more than 20 iterations of the Levenberg-Marquardt minimization algorithm or if measurements are farther than 360 km from the satellite track.

Once all the flags are applied and the data are filtered accordingly for both ascending and descending orbits, we obtain an spatial coverage about 28% of the global ocean surface per day. An example of daily global coverage of SSS filtered measures along the SMOS track is illustrated in Figure 3.1 for 1-6 of June 2012.

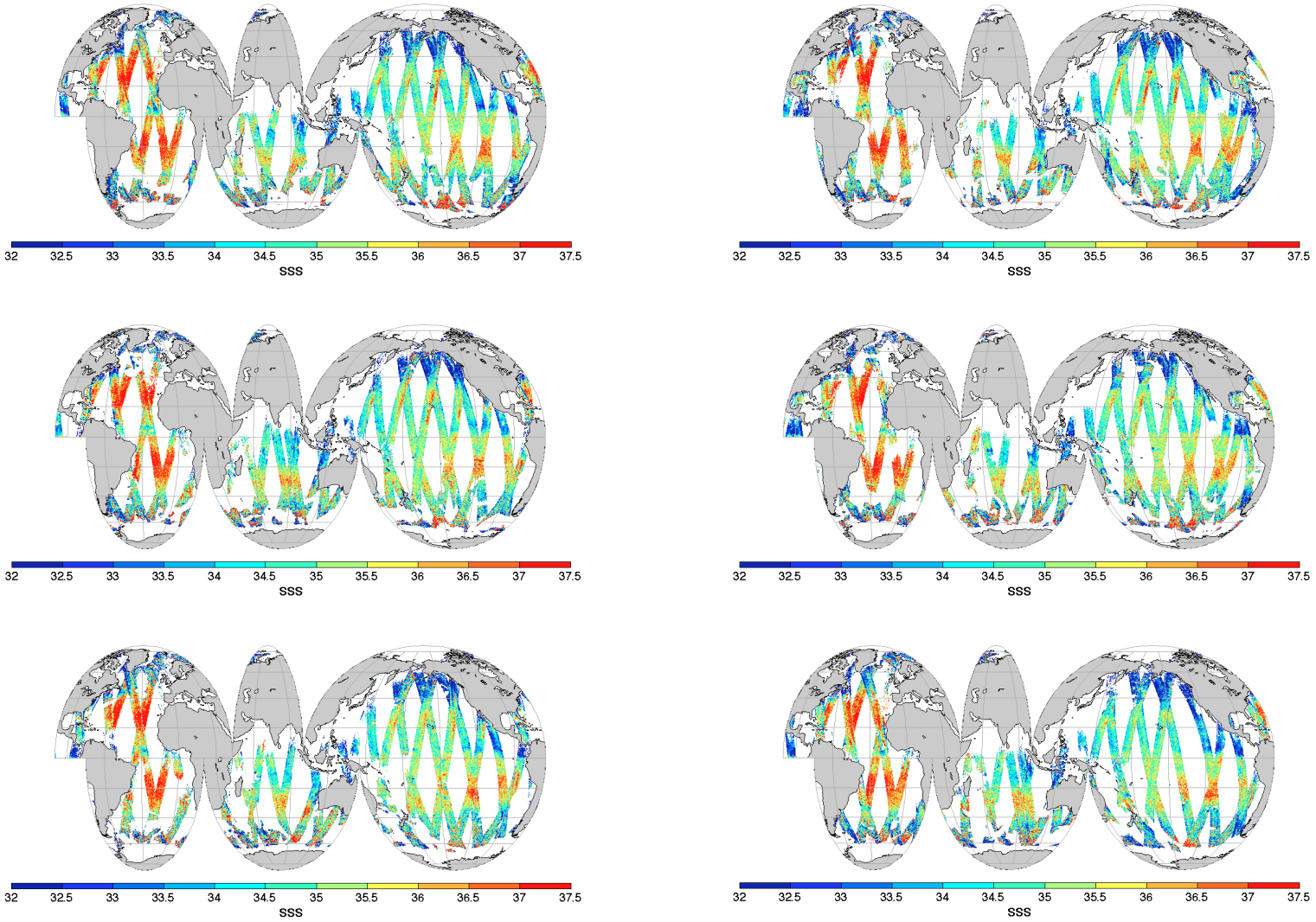

Figure 3.1: a-f) Sea Surface Salinity level 2 daily measurements for 1st to 6th of June 2012.

The results obtained by applying the weighted average algorithm to the input data in Figure 3.1 are shown in Figure 3.2, for the 9-day and for the one month average. As expected, the weighted average synthesizes the information from the different semi-orbits and, in addition, reduces the error of the resulting SSS maps compared with the error of individual L2 SSS retrievals. The global SSS structure is coherently represented by SMOS measurements, although errors are still present in the measurements, especially in areas with associated known issues for SMOS measurements as explained in section 2.1. The largest errors can be attributed to: i) potential errors in the satellite product due to land-sea contamination (Zine et al., 2007), ii) potential errors when the measurements are contaminated by RFI, iii) potential errors associated with the retrieval of SSS in cold waters. A dedicated validation of this products accuracy and quality is found section 3.4.

The maps of the number of grid points per cell (N) used to create the weighted averages of Figure 3.2 are shown in Figure 3.3. The number of used L2 measurements increases as the temporal window increases. This fact should, in theory, decrease the dispersion of the average at each grid point, and therefore increase the accuracy of the product. If the errors inside each cell were Gaussian distributed, the fractional error at each cell would be $1/\sqrt{2n-2}$ of the error for individual measurements. For cells with 9 measurements the error is thus estimated to have 25% of the original standard deviation, with 50 measurements the error dispersion is 10 %. In our case, we use the mean of 12 L2 measurements to produce each grid point of the 9-day SSS maps, so an error of 21% is expected. In the case of monthly analysis, the mean of 35 L2 measurements is used to produce each monthly-averaged grid point, for which an error of 12% is expected.

To measure the spread of the L2 measures ($\mathbf{y}^o$) at each cell i we use the standard deviation error. Figure 3.4 represents the standard deviation of L2 measurements inside each cell of $0.25°\times0.25°$, both for the 9-day product (top) and to the monthly analysis (bottom). We clearly identify a large spread between measurements inside cells close to the coastal areas affected by land-sea contamination, likewise at high latitudes, where the cold waters push the Tb measures to the limit of their sensitivity to SSS. It is worth noticing that intra-cell standard deviation increases when increasing the temporal averaging. This is an indication of the large dispersion of L2 data, and maybe a warning of the necessity to find an alternative way to decrease the L2 measurements dispersion other than temporal averaging.

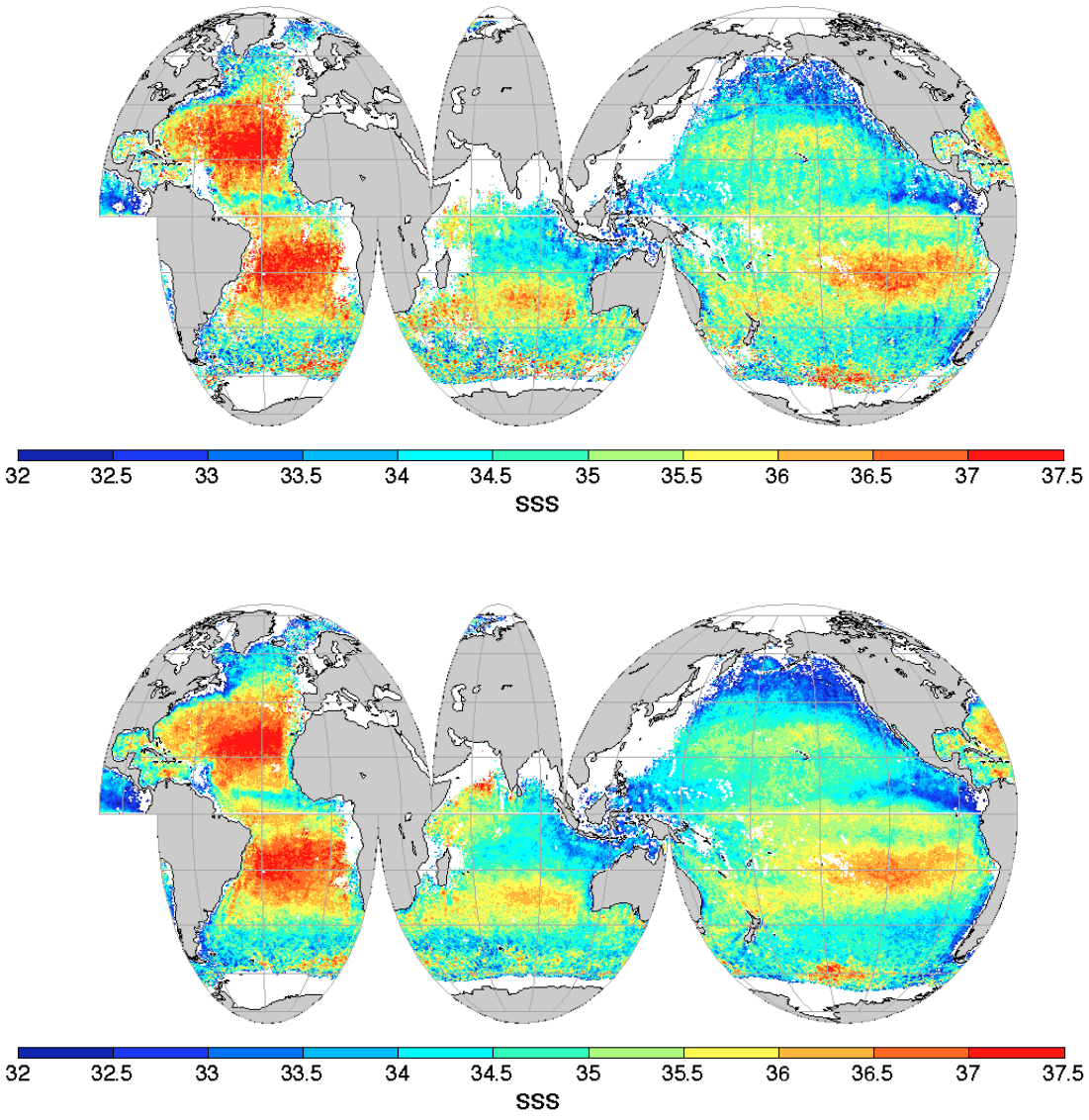

Figure 3.2: Map of surface salinity obtained by applying a weighted average on SMOS data for first nine days of June 2012 (top) and the entire month of June (bootom).

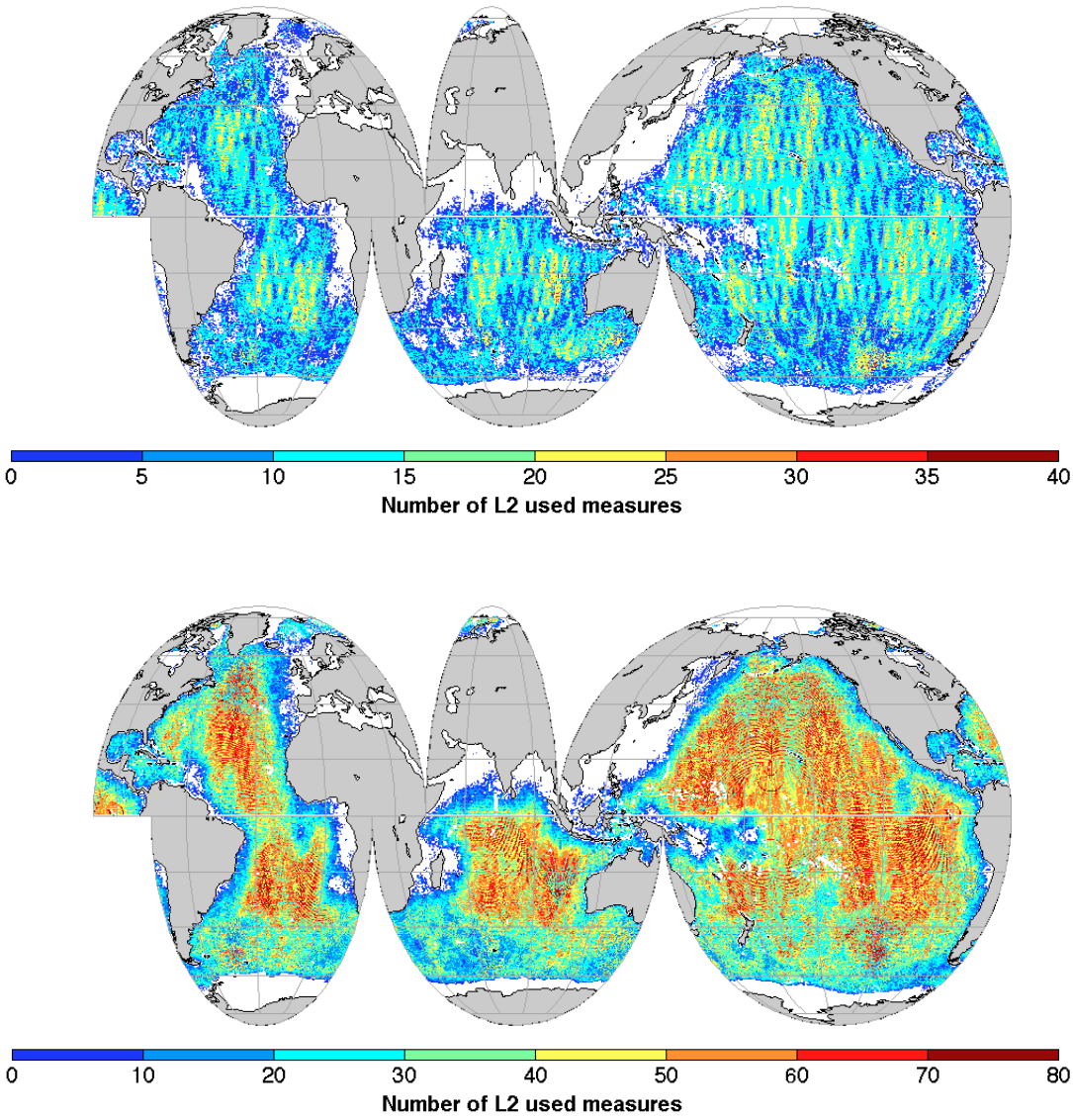

Figure 3.3: Number of L2 measurements used inside each cell of $0.25° \times 0.25°$ for first nine days of June 2012 (top) and the entire month of June (bootom).

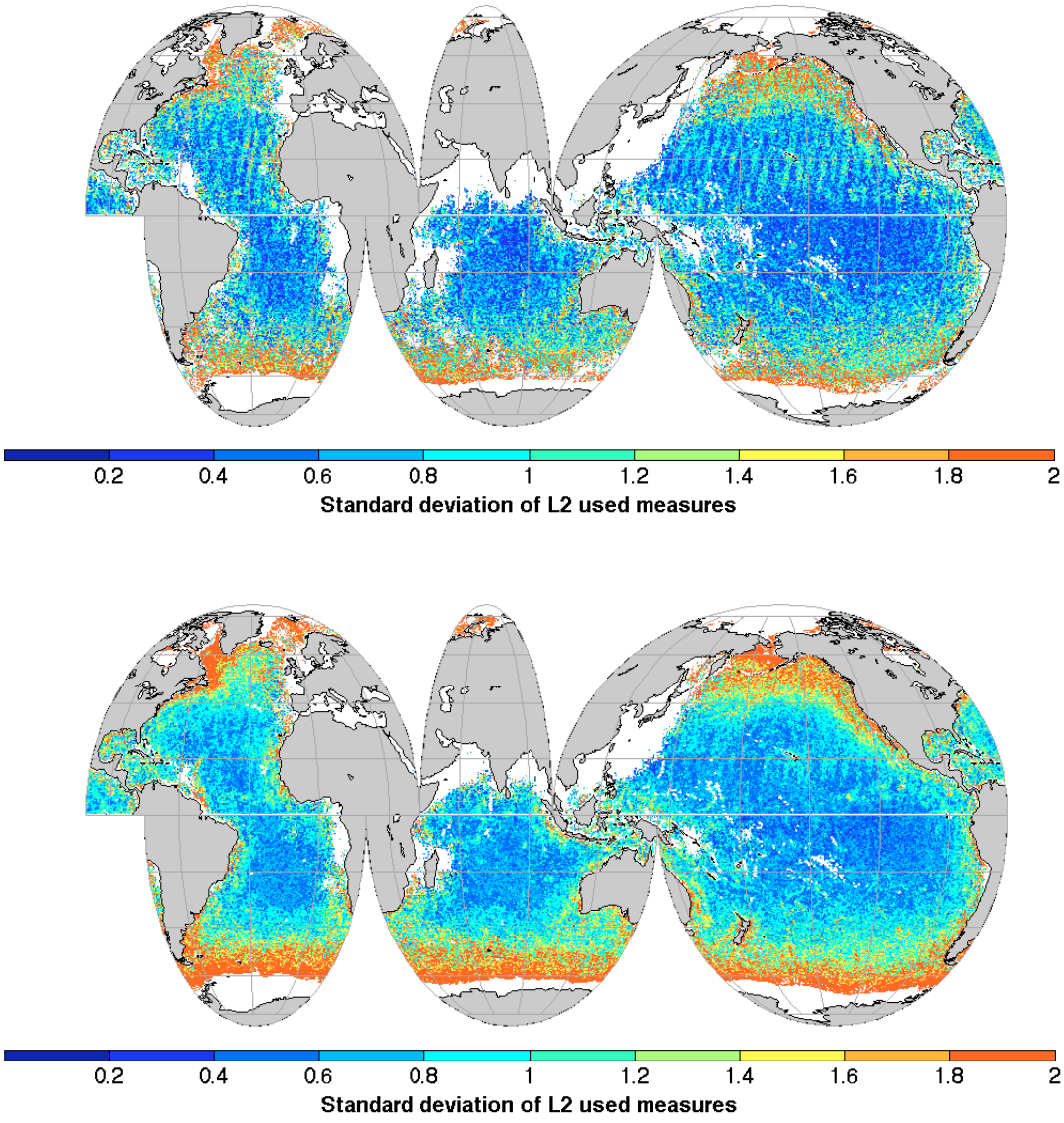

Figure 3.4: Standard deviation of L2 measurements inside each cell of $0.25° \times 0.25°$ for first nine days of June 2012 (top) and the entire month of June (bootom).

3.3 Optimal Interpolation

Optimal interpolation (OI) is a robust method of objective analysis extensively used in oceanography. The technique is based on the Gauss-Markov theorem, and determines the estimate of the interpolated physical variable with the least mean-square error, given the information about the variances and correlation functions of both the physical variable and the data (Gandin and Hardin, 1965; Bretherton et al., 1976; McIntosh, 1990). In other words, it is based on the minimization of the errors between the analyzed field and a true field. The OI methodology has been successfully applied to ocean remote sensing variables as SST (Reynolds and Smith, 1994; Reynolds et al., 2007; Thiébaux et al., 2003), SSS (Melnichenko et al., 2014) and sea level anomaly (LeTraon et al., 1998; Ducet et al., 2000).

The analysis at each point $\mathbf{x}^a$ will be influenced by all observations $\mathbf{y}^o$ that lie within a predefined region of influence. In contrast with the weighted average, OI uses a previous estimate of the analysis or background field $\mathbf{x}^b$ and the weight $\mathbf{K}$ in Eq. 3.2 depends on the distance between the observation and the point of analysis. In other words, the estimate or analysis is equal to the first guess plus little increments consisting on an interpolation of the first guess of the observation points and an interpolation of the differences between the observed and first guess values back to the analysis point. The gain matrix $\mathbf{K}$ is built from matrices that encode the covariances of the field, from the grid point to the observation point and from any observation point to another observation point.

The covariance between variables x and y describe how close are they related in average:

$$cov(x, y) = E[(x - E[x])(y - E[y])] \tag{3.5}$$

where $E[\cdot]$ is the expectation value. The covariance is larger in absolute value if variables have a close-to-linear mutual dependence, so that equal increases of the value of one variable lead to almost equal increases or decreases of the other. The sign of the covariance tells us if the slope of variations in value of both values are of the same or opposite signs.

When working with vector variables a covariance matrix $\mathbf{C}$ needs to be calculated. The element (i, j) of the covariance matrix associated with the random vector $\mathbf{x}$ is the covariance between the elements x_i and x_j.

$$\mathbf{C} = E\left[(\mathbf{x} - E[\mathbf{x}])(\mathbf{x} - E[\mathbf{x}])^T\right] \tag{3.6}$$

When applying objective analysis we always want to estimate an analysis state $\mathbf{x}^a$, which is as close as possible to the true state vector $\mathbf{x}^t$, given a reference field $\mathbf{x}^b$ and the observations $\mathbf{y}^o$. It is assumed that both the reference field and the observation have errors:

$$\mathbf{x}^b = \mathbf{x}^t + \boldsymbol{\eta}^b \tag{3.7}$$

$$\mathbf{y}^o = \mathbf{H}\mathbf{x}^t + \varepsilon \tag{3.8}$$

where η^b represents the error in the first guess and ε the error of the observations. We also assume that the first guess and the observations are unbiased, what means that the average of

the error is zero:

$$E[\eta^b] = 0 \tag{3.9}$$

$$E[\varepsilon] = 0 \tag{3.10}$$

However it is necessary to have an *a priori* knowledge about the magnitude of the observation and the first guess errors, expressed as the error covariances matrices:

$$E\left[\boldsymbol{\eta}^b(\boldsymbol{\eta}^b)^T\right] = \mathbf{B} \tag{3.11}$$

$$E\left[\varepsilon\varepsilon^T\right] = \mathbf{R} \tag{3.12}$$

$$E\left[\boldsymbol{\eta}^b\varepsilon^T\right] = 0 \tag{3.13}$$

where $\mathbf{B}$ is the covariance matrix of the background error, $\mathbf{R}$ the covariance matrix of the observation error, and we also assume that the error of the background is independent of the observations error (Eq. 3.13).

The weights that form the gain matrix $\mathbf{K}$ (Eq. 3.2) can be thus derived by imposing that departures between the analyzed and reference field are minimized. The solution of this minimization problem is:

$$\mathbf{K} = \mathbf{S}^T\mathbf{D}^{-1} \tag{3.14}$$

where $\mathbf{D}$ is the observation covariance matrix, and $\mathbf{S}$ is a matrix equal to the covariance between each observation point with the reference field:

$$\mathbf{S} = \mathbf{HB} \tag{3.15}$$

The covariance matrix $\mathbf{D}$ is divided in two parts, assuming that observational errors are not correlated with the reference field:

$$\mathbf{D} = \mathbf{HBH}^T + \mathbf{R} \tag{3.16}$$

where $\mathbf{B}$ describes the covariance between pairs of the reference field values at the observation points, and $\mathbf{R}$ describes the observational error covariances. In matrix $\mathbf{R}$, the diagonal terms represent the observational error variances and the non-diagonal terms represent the observational error covariances.

A proof that $\mathbf{K}$ minimizes the differences between reference and analyzed field follows: in OI method we chose that the matrix $\mathbf{K}$ is the one that minimizes the variance of the analysis $\mathbf{P}^a$. If the total variance is at its minimum, then a slight increment of the gain $\delta\mathbf{K}$ does not modify the value of the total variance in the first order of $\delta\mathbf{K}$.

$$
\begin{aligned}
tr(\mathbf{P}^a(\mathbf{K}+\delta\mathbf{K})) - tr(\mathbf{P}^a(\mathbf{K})) &= 0 \\
&= 2tr(\mathbf{KHBH}^T\delta\mathbf{K}^T) - 2tr(\mathbf{BH}^T\delta\mathbf{K}^T) + 2tr(\mathbf{KR}\delta\mathbf{K}^T) \\
&= 2tr([\mathbf{K}(\mathbf{HBH}^T+\mathbf{R}) - \mathbf{BH}^T]\delta\mathbf{K}^T)
\end{aligned}
\tag{3.17}
$$

Since the perturbation of the gain matrix $\delta\mathbf{K}$ is arbitrary, the expression in the brackets have to be zero. The optimal gain, or the gain matrix $\mathbf{K}$ is thus:

$$
\mathbf{K} = \mathbf{BH}^T(\mathbf{HBH}^T+\mathbf{R})^{-1} \tag{3.18}
$$

(analog to Eq. 3.16). One relevant feature of OI is that it also provides an estimate of the analysis error:

$$
\begin{aligned}
\mathbf{P}^a &= \mathbf{B} - \mathbf{KHB} \\
&= \mathbf{B} - (\mathbf{HBH}^T+\mathbf{R})^{-1}\mathbf{HB}
\end{aligned}
\tag{3.19}
$$

Thus, granted the above stated assumptions, Eq. 3.2 yields at every point i an analysis or estimate $\mathbf{x}_i^a$ which is optimal in the sense that from all estimates that depend linearly on the data supplied, this one has the least error variance. An important element of the method is that adequate estimates of the statistics of the fields should be known considering that the accuracy of the analysis depends on how accurately these statistics are known, on the density of sampling points, and on the variable to be mapped.

3.3.1 Application to SMOS Sea Surface Salinity

To apply optimal interpolation method to generate SMOS SSS OI products it is necessary to first address the following: i) the definition of a suitable correlation model; ii) the characterization of the observational error statistics; and iii) the prescription of a reference or background field.

The first key point of the algorithm is the definition of the spatio-temporal covariance B. In the case of unbiased errors, the spatial structure of the covariance functions is usually expressed in terms of their normalized expression, i.e. the correlation matrix. The covariance matrix B are usually modeled by using analytical functions of the correlation function with certain basic characteristics: i) the correlation is essentially a function of distance, ii) the correlation is one for zero distance and iii) the correlation decreases as distance increases.

The correlation function is often a Gaussian function or a Gaussian function multiplied by a polynomial. The characteristic length scale of the function determines the typical distance over which a data point can be extrapolated. This scale length is the typical scale of the oceanographic processes acting on the field.

The correlation functions used in SMOS-BEC to generate OI maps were originally computed using the results of a numerical model developed by Jorda et al. (2011) as there did not exist,

at that time, any satellite SSS data for computing the spatio-temporal correlations necessary to properly describe the required correlation matrix **B**. Today, with both SMOS and Aquarius satellites on orbit since 2009 and 2011 respectively, new attempts to estimate realistic correlation scales for satellite SSS are being addressed. Taking advantage of this new knowledge, we use correlation functions as the ones calculated by Melnichenko et al. (2014) to produce Aquarius OI products in the generation of the SMOS OI products.

Melnichenko et al. (2014) estimated the correlation functions of SSS from Aquarius data as follows. The L2 SSS data are low-pass filtered and divided into latitudinal regions. A first guess of the reference field (monthly mean SSS from Argo buoys) is subtracted, and mean autocorrelation functions are estimated for repeated swaths over the North Atlantic at each latitudinal region. Figure 3.5a displays the mean autocorrelation of SSS; besides autocorrelation functions for ancillary Aquarius data (coming from a HYCOM model solution) are displayed and shown to be in great correspondence (dashed lines). Fig. 3.5b shows the corresponding wavenumber spectra: in the wavelength corresponding to 60 to 300 km, the spectrum follows a power law of the form of k^{-2}, where k is the wavenumber, what is consistent with the expected shape for the power spectrum.

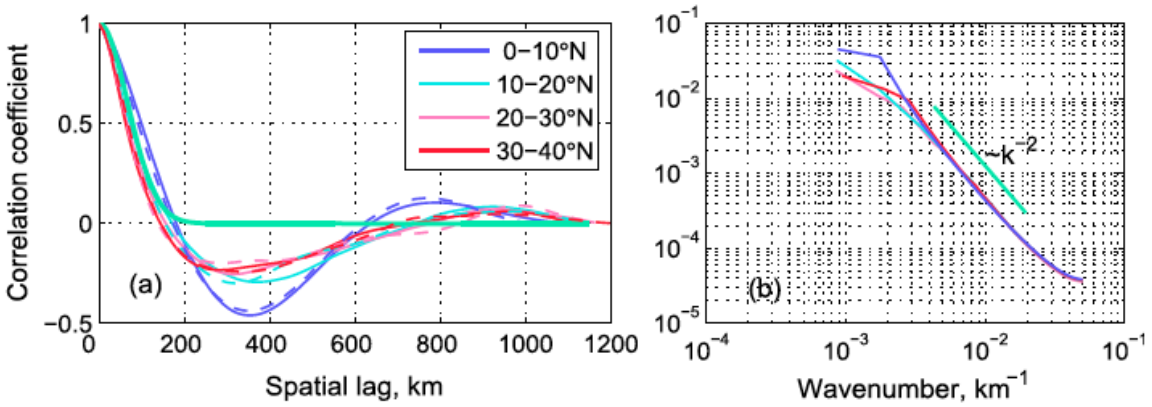

Figure 3.5: (a) Autocorrelation functions for SSS from Aquarius (solid lines) and from HYCOM SSS (dashed lines) over the SPURS region. The ensemble mean approximations by a Gaussian function with e-folding of 90 km is shown in heavy green line. (b) Corresponding normalized wavenumber spectra. Extracted from published work of Melnichenko et al. (2014).

The spatial meridional scales of mesoscale SSS variability (defined in their study as the scale associated with the first zero crossing of the corresponding correlation function) are displayed in Figure 3.6. They found the structure of the correlation functions to be similar to a high degree in all latitude bands (see also Figure 3.6) and approximate the observed correlation functions using a simple Gaussian curve, given by:

$$b(r) = e^{-r^2/R^2} \tag{3.20}$$

where r is the spatial lag and $R = 90$km is the decay scale. The Gaussian function with such decay scale (green curve in Figure 3.5) represents well the observed results. The Gaussian model assumes that the correlations are isotropic, which it is non true for tropical latitudes where salinity structures are strongly anisotropic, and zonal scales are larger than meridional

scales. Then, the Gaussian model is modified to account for two scales of decorrelation:

$$b(r_x, r_y) = e^{-r_x^2/R_x^2 - r_y^2/R_y^2} \tag{3.21}$$

where r_x and r_y are the spatial lags in the zonal and meridional directions and R_x and R_y are the associated zonal and meridional decorrelation scales. The meridional scale is set to $R_y = 90$ km while the zonal scales varies from 180 km in the equator and 90 km as follows:

$$R_x(y) = 180e^{-y^2/324.6}, 0^o \leq y \leq 15^o N \tag{3.22}$$

Latitude band (°N)	Variance (psu^2)	Length scale (km)
0–10	0.249	150
10–20	0.046	160
20–30	0.023	135
30–40	0.079	140

Figure 3.6: The variance and correlation length scales (the lag of the first zero crossing of the spatial correlation function) of mesoscale SSS variability as seen by Aquarius in the North Atlantic. Extracted from published work of Melnichenko et al. (2014).

The influence radius determining the number of observations that will influence the analysis at each grid point is set to 192 km to allow sufficient observations to be weighted using correlation matrix **B** as defined above. The error of the observations are here assumed to be uncorrelated to each other, so the observation error covariance **R** becomes a diagonal matrix. This hypothesis is not guaranteed for satellite SSS data, since the errors in satellite retrievals are of different types and are spatially correlated (Lagerloef and Coauthors, 2013; Melnichenko et al., 2014). A procedure to reduce the noise and the noise correlation is spatio-temporal averaging of observations instead of working with all observations.

With this in mind, we chose to apply the optimal interpolation method to the L3 SSS fields produced as explained in section 3.2. The downside of this procedure is that the spatial resolution of the data is also reduced and that small-scale structures visible in the original data are not present in the binned observations (Barth et al., 2008). The dispersion in terms of standard deviation of the L2 measures computed at each bin (Figure 3.4) is used as an approximation of the observational error **R**.

Finally, we use a climatological field as a background field, obtained from the time average of historical data. Climatological fields constitute proper first guesses from the statistical point of view (the residuals have a zero statistical mean by definition) and they ensure that there will be no discontinuities in the background field used for the analysis of the neighboring points.

The first background or reference field used to apply the OI methodology is the WOA09 climatology (Antonov et al., 2010). This climatology is linearly interpolated into 0.25 spatial grid and daily time resolution. The error variance of this first guess is supposed to be 0.09 (ε in Eq. 3.8). An example of this climatological SSS field for the month of June is shown in Figure 3.23. It must be noted, however, that using WOA09 as a background field is not theoretically

correct, as this climatology is being used as ancillary data to retrieve SMOS SSS, and in OI approach it is a requirement that the reference field is an independent source of information. The impact on using different background fields is assessed in section 3.5.

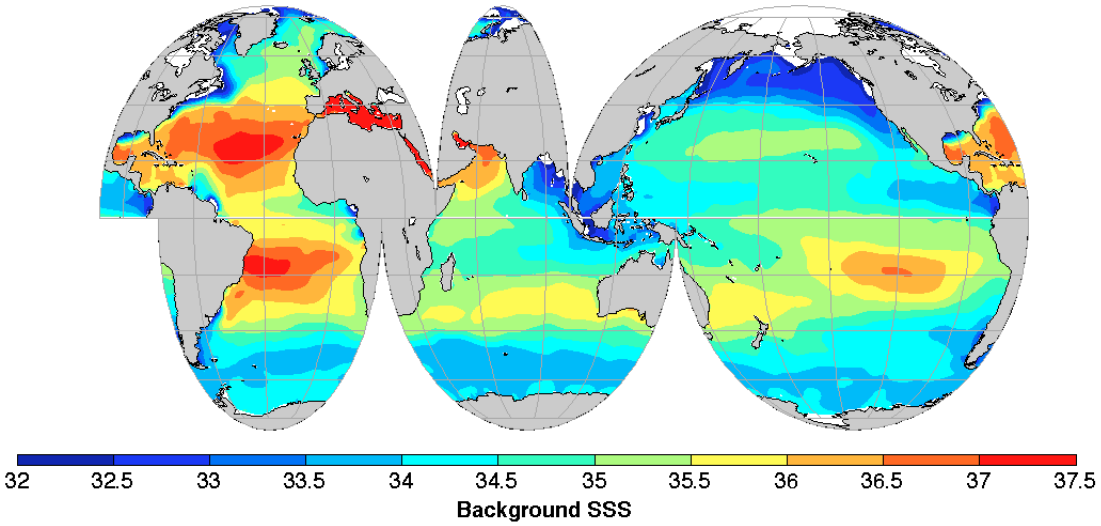

Figure 3.7: Background surface salinity World Ocean Atlas for month of June.

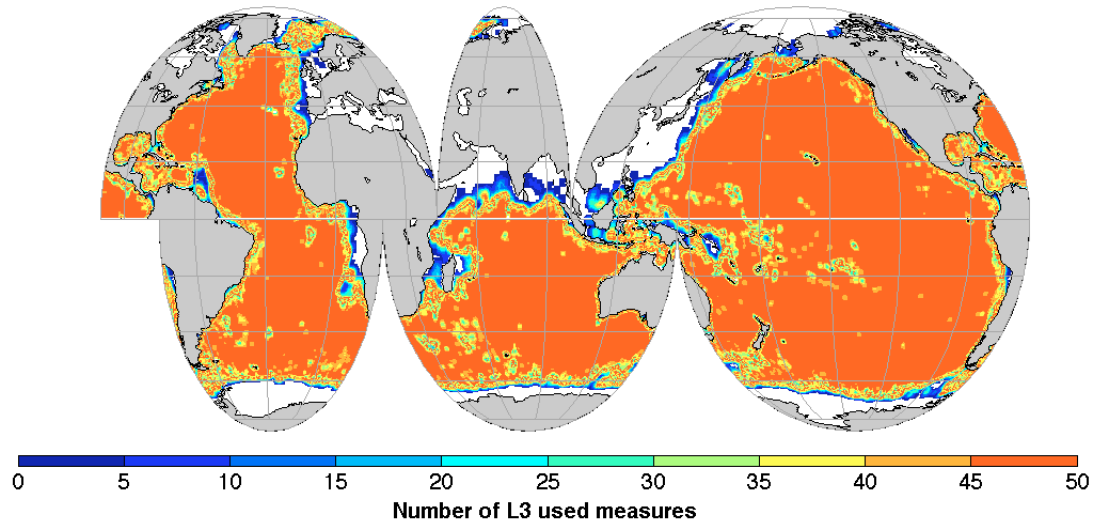

Figure 3.8: Number of L3 measures of 0.25°×0.25° used in each analysis point for the first 9 days of June 2012.

The map with the number of L3 measurements used to create the optimal analysis at each grid point for an example of 9-day map for June 2012 is shown in Figure 3.8. On average, 50 observations are used to interpolate the field at each analysis point for a 9-day map.

The application of the OI scheme to interpolate the weighted averaged SMOS SSS data for 1st-9th of June 2012 and for the entire month of June 2012 are shown in Figure 3.9. These maps

have better spatial coherence compared to the used observations (Figures 3.2). Moreover, the resulting field contains signal coming from observations that was not in the background field (Figure 3.23). Comparing the results with the monthly climatology, the SSS is fresher in the equatorial zone, and saltier in the subtropical gyres.

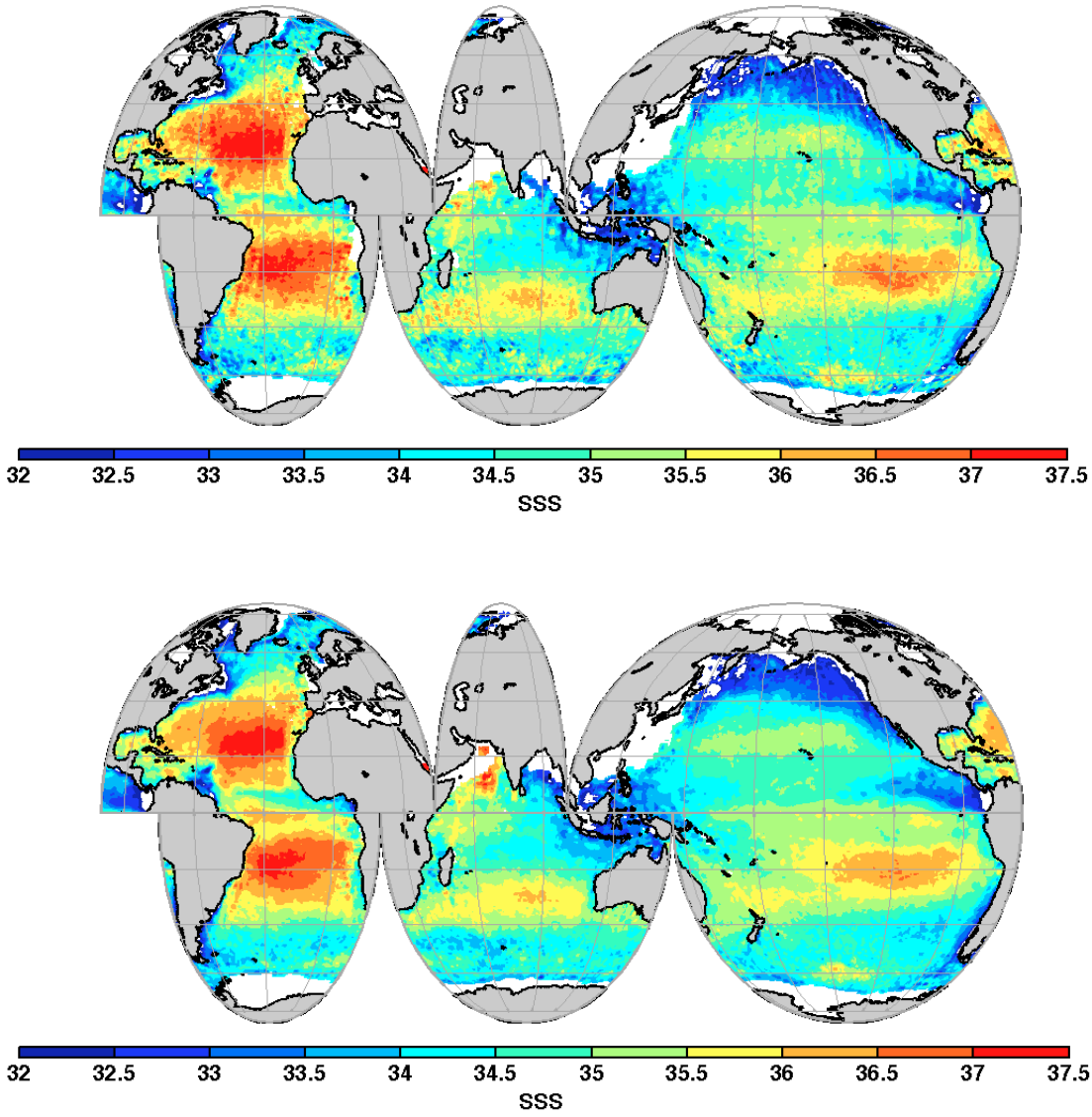

Figure 3.9: Map of surface salinity applying optimal interpolation on SMOS data for first nine days (top) and the entire month of June 2012 (bottom).

3.4 Validation

In order to determine the quality of satellite data S, a conventional validation method is to compare the satellite data with a set of in situ data I. Often the in situ data are placed at the same regular grid that the satellite measurement to be validated. With this aim, the in situ

data coincident in time and localized at the same pixel of the grid under study are averaged. As a result, every satellite data are compared to the in situ data coincident in space and time, if it existed, this operation is called *matchup*.

The validation set (ground truth) is formed by an ensemble of measurements (normally, in situ data) that we assume to have an smaller error than that of the products being validated. The quality of our satellite products will be measured by specific parameters that describe their accuracy and their precision with respect to the ground truth. The accuracy is described by the mean difference between the satellite data and the in situ data. If this value is (almost) zero data are accurate or unbiased. When the mean difference is not zero, our data is said to be biased and this value is called bias. The bias is defined as the average of the deviations of satellite data from the in situ measures:

$$bias = \frac{1}{N}\sum_{n=1}^{N}(S_n - I_n) \tag{3.23}$$

To study the precision of a measure, the amount of variation or dispersion from the average of a data distribution is taken. This quantity is provided by the variance:

$$var(\Delta S) = E\left[(\Delta S - E[\Delta S])^2\right] \tag{3.24}$$

where $\Delta S = S - I$. The variance is always positive and measure how far a set of values are spread out around the expected value. An equivalent measure is the square root of the variance called standard deviation ($\sigma(x)$). The standard deviation has the same dimensions as the variable and thus is comparable to deviations from the expectation value:

$$\sigma(\Delta S) = \sqrt{\sigma^2(\Delta S)} \tag{3.25}$$

A low standard deviation indicate that data points tend to be close to the mean difference value.

Another statistical measure that will be used to measure the dispersion of the error in data, comprising both accuracy and precision, is the root mean square error (RMSE):

$$RMSE = \sqrt{\frac{1}{N}\sum_{n=1}^{N}(S_n - I_n)^2} \tag{3.26}$$

From the covariance and standard deviation one can compute the correlation coefficient, which is always bounded between -1 and 1, and measures the degree of linear dependence between two variables: 1 means positive linear dependence, 0 means that variables cannot be linearly related, and -1 means negative linear dependence.

$$corr_{(S,I)} = \frac{cov_{(S,I)}}{\sigma_{(S)}\sigma_{(I)}} \tag{3.27}$$

When validating satellite measures using in situ data, it is important to notice than satellite estimates and in situ data have different sampling characteristics leading to different spatio-temporal resolutions. In our specific application, SMOS satellite estimates SSS within a footprint

of 50-100 km, and temporal averages of 9 days, whereas an in situ instrument measures SSS at a precise time and point location. These differential sampling characteristics of remote sensing platforms and in situ measurements can lead to substantial discrepancies between both sources of data, associated with the internal variability of SSS in the range of size and times characteristic to SMOS SSS data.

9-day SSS products

The validation of the 9-day L3 and OI SSS products calculated every three days is made using close-to-surface data from Argo profilers. Figure 3.10 shows the SMOS L3 and SMOS OI differences with Argo in situ data (as described in section 2.1.2) at the buoy matchup for the year 2012. The Argo value used to match up SMOS SSS is taken as the uppermost valid salinity value.

The largest differences between L3 SSS and in situ are found close to land, at high latitudes and in areas of higher spatio-temporal variability associated with the main currents as in the western boundary currents of Kuroshio (along the East coast of Japan), the Gulf Stream (along the East coast of US), and Agulhas Current (coast of South Africa). A uniform global reduction of the difference with Argo SSS can be seen when the optimal interpolation is applied to L3 SSS, although salinity differences as large as 1 are still present, associated with the areas of larger expected error as detailed for L3 SSS products.

To better understand the origin of inaccuracy of these areas, Figure 3.11 presents the values of uppermost SST value of Argo profiles, and rain and wind values provided by the ECMWF at the pixels where SMOS SSS was retrieved for the year 2012. It should be remembered that the sensitivity of the brightness temperature to conductivity is reduced for cold waters (section 2.1), therefore in higher latitudes where SST is lower, higher inaccuracy in SSS is expected despite of the larger number of retrievals at those latitudes. One of the auxiliary fields required for the retrieval of the SSS is the wind speed. The SMOS retrieval algorithm for SSS disregards any pixel at which wind speed is larger than 12 m/s: as shown in Figure 3.11, also in high latitudes, winds are higher and this factor will also contribute to decrease the quality of SSS.

The SMOS retrieval algorithm does not depend on precipitation. However rain-induced surface salinity variability has been identified to be an important process to be taken into account (Boutin et al., 2012a). This process should be taken into account as SMOS satellite senses the first cm of the ocean, which would be more influenced by rain than Argo measurements, specially in cases of strong vertical stratification. Strong stratification is associated with low winds, consequently it is most expected in tropical areas where rain events are larger.

Figure 3.12 shows the differences of ECMWF SST with respect to Argo in situ temperature data at the buoy matchup for the year 2012. When comparing Figures 3.10 and 3.12 we can clearly find defined coincidences between locations of large SSS differences and locations of large SST differences. The origin of these differences is probably related to the different spatio-temporal resolution of both SST values (ECMWF versus punctual Argo profilers) and/or to erroneous ECMWF SST or in situ temperature values. Anyhow, if there is a mismatch between the temperature of Argo and ECMWF (independently of the origin), salinity values provided by

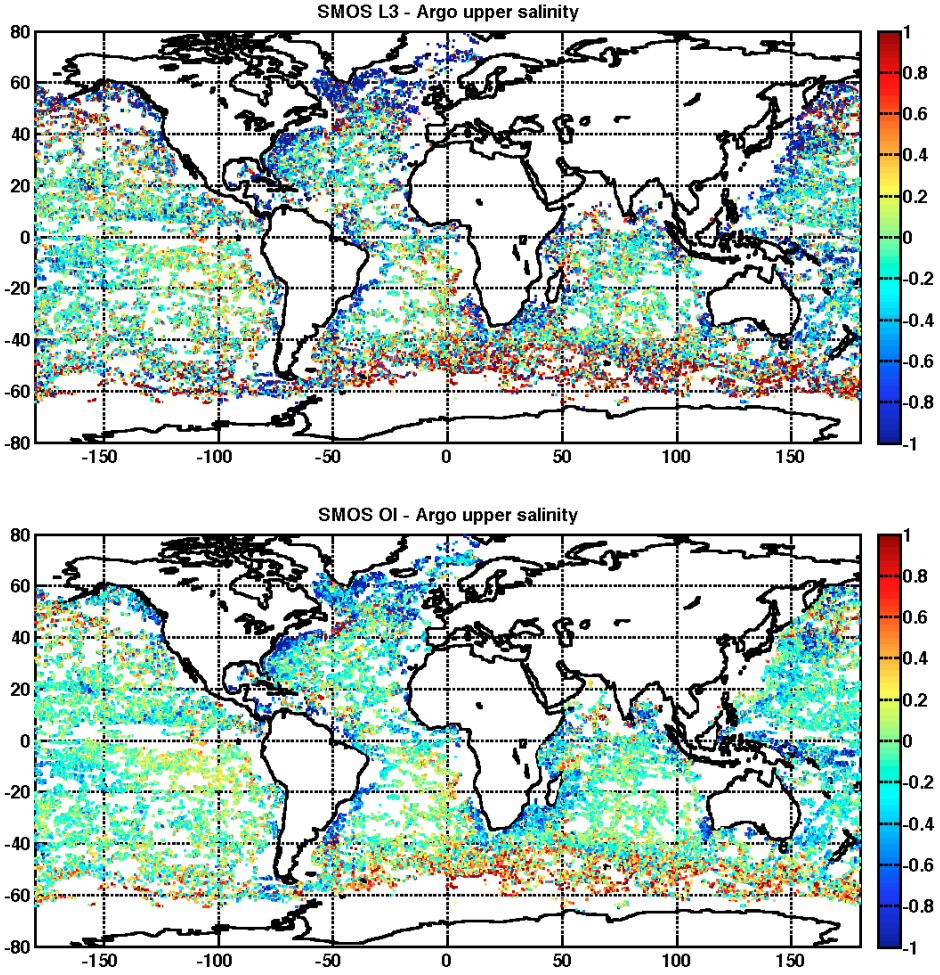

Figure 3.10: Global maps of SSS differences as defined by L3 SSS (top) and data OI SSS (bottom) minus the collocated Argo data.

that buoy should not be used to validate SMOS as the ECMWF SST is used to retrieve SMOS SSS, and therefore differences will likely be found between SMOS SSS and Argo SSS.

The tables below compile the results of the differences between SMOS maps and collocated buoys, arranged by latitude bands, distance to coast, depth of the Argo uppermost measurement and SST differences between Argo and ECMWF, to quantitatively assess the SSS maps errors. Both L3 and OI maps used in this comparison are defined on 9-day windows and computed every 3 days; the matchups are accumulated during the year 2012 and the average and standard deviation of the SMOS products minus Argo value are calculated (Tables 3.1 and 3.2).

Latitude		**Global**	**60S-60N**				**30S-30N**				**Zone 122**			
Maximum depth				**>10 m**				**>10 m**				**>10 m**		
Coast distance					**1000 km**				**1000 km**				**1000 km**	
ECMWF-Argo SST						**<0.3 ºC**				**<0.3 ºC**				**<0.3 ºC**
L3	n	213734	210619	204610	128614	85614	114581	112248	74139	56900	7658	7534	6324	5151
	$\langle \Delta S \rangle$	-0.10	-0.09	-0.08	-0.00	-0.01	-0.12	-0.12	-0.06	-0.06	-0.04	-0.04	-0.01	-0.01
	$\sigma_{<\Delta S>}$	0.75	0.72	0.72	0.61	0.52	0.50	0.50	0.41	0.40	0.32	0.32	0.31	0.30

Table 3.1: Statistics between 9-day L3 vs Argo SSS measurements for the year 2012.

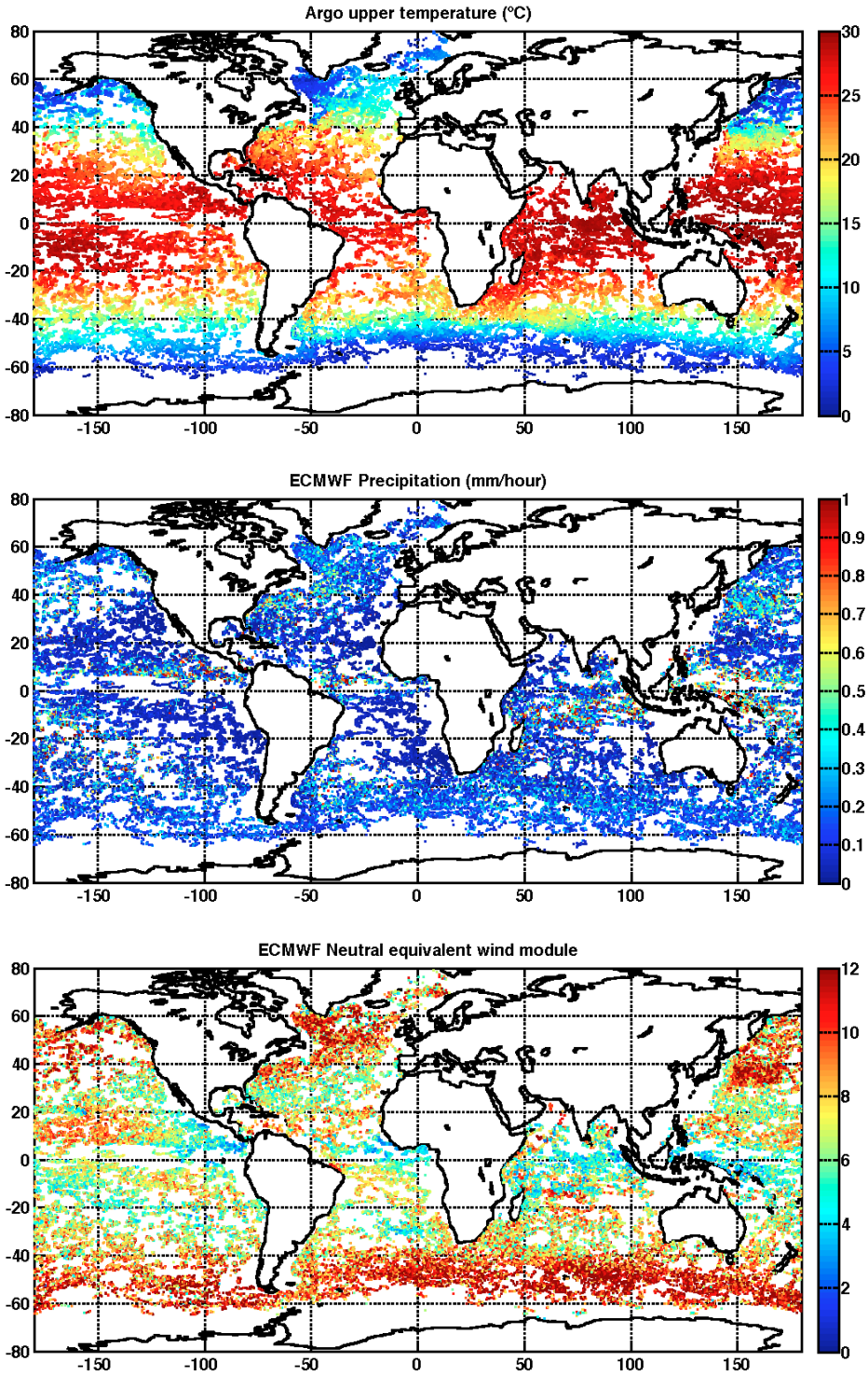

Figure 3.11: Argo upper most temperature value for the year 2012 (top). Global maps of rain (middle) and wind (bottom) as defined by ECMWF at the buoy matchup.

The number of total matchups are of the order of two-hundred thousand. The number of points in OI maps is larger than in the binned maps due to the extrapolation properties of the optimal interpolation algorithm. At global scale (first column) the standard deviation of the

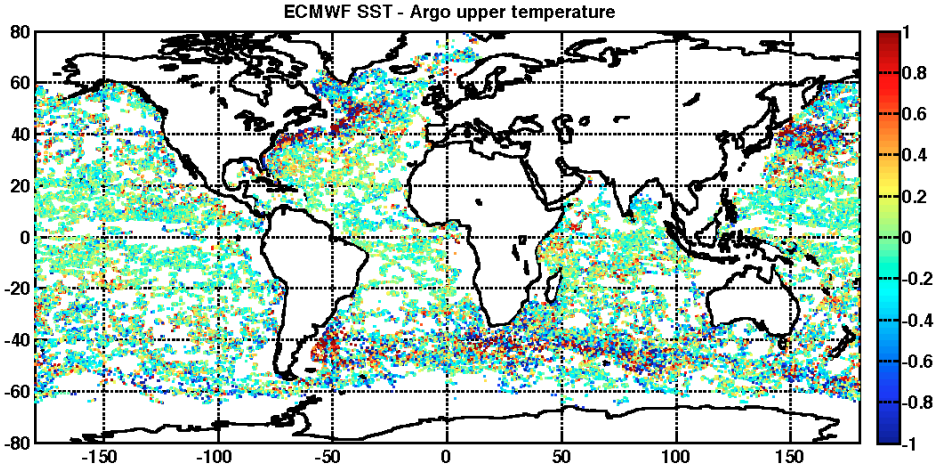

Figure 3.12: Global maps of SST differences as defined by ECMWF data minus the collocated Argo data.

Latitude		Global	60S-60N				30S-30N				Zone 122			
Maximum depth				>10 m				>10 m				>10 m		
Coast distance					1000 km				1000 km				1000 km	
ECMWF-Argo SST						<0.3 ºC				<0.3 ºC				<0.3 ºC
OI	n	239125	234637	226413	132191	87639	127624	124805	75826	58029	7693	7576	6281	5123
	$\langle \Delta S \rangle$	-0.10	-0.09	-0.08	-0.01	-0.02	-0.11	-0.11	-0.06	-0.06	-0.03	-0.03	-0.01	-0.01
	$\sigma_{<\Delta S>}$	0.48	0.47	0.47	0.42	0.32	0.35	0.35	0.27	0.26	0.20	0.20	0.19	0.19

Table 3.2: Statistics between 9-day OI vs Argo SSS measurements for the year 2012.

SMOS minus Argo differences is reduced for OI SSS products. At global scale, the binned product has larger dispersion (0.75) than the OI product (0.48). The bias is systematically negative. That means that in all cases, SMOS SSS retrievals are fresher than the in situ uppermost Argo value. This can be due to a bias in the processing or to the fact that Argo data are measures several meters below the surface.

The statistics of the global differences reflect the effectiveness of measuring space-based SSS, but also reflect the various algorithmic limitations near land areas or at high latitudes as the sensitivity of the brightness temperature to conductivity is reduced at cold temperatures, in addition to areas that could be affected by RFI emissions.

In order to isolate the different contributions to error, data are selected by latitudinal band and distance to coast. Besides, a region of the Pacific defined as Zone 122 [0-30S, 120-150S], which is far from RFI emissions and land contamination and which is used to compute the Ocean Target Transformation (OTT; see Chapter 2) is analyzed. As soon as the data are restricted in latitude, the random error is reduced. In the case of L3, the global error reduces from 0.75 (global), to 0.72 (bounded by latitude 60), to 0.50 (bounded to latitude 30) and to 0.32 (in Zone 122). In the case of OI, the global error reduces from 0.48 (global), to 0.47 (bounded by latitude 60), to 0.35 (bounded to latitude 30) and to 0.20 (in Zone 122). The large effect of restricting the comparison to the tropical band is to remove data points in cold waters and data points under the influence of large winds, also known to reduce the accuracy of the salinity retrievals.

The impact of limiting the comparison of SMOS and Argo to those profiles whose uppermost

valid salinity value is in the first ten meters below the surface has also been investigated. The impact of removing the profiles with the uppermost salinity value too deep is small. The reason for that is that only four thousand math-up pairs are removed (around 16% of the profiles).

To remove the effect of land sea contamination, statistics are also computed for matchups located farther than 1000 km from the largest shorelines. In the case of L3, the standard deviation is reduced from 0.72 (60° latitude limit) to 0.61 and the bias is also reduced from -0.09 to 0.00. At the tropical band, the standard deviation error reduced from 0.50 to 0.41 and the bias is also reduced from -0.12 to -0.06. The larger negative bias in the tropical band is related to the increase of the frequency of rain events.

In the case of OI, the standard deviation is reduced from 0.47 (60° latitude limit) to 0.42. At this latitude band, the systematic error is also reduced from -0.09 to -0.01. At the tropical band, the impact of considering matchups far from the coast is even larger, as the standard deviation error is reduced from 0.35 to 0.27.

When we restrict our analysis to the data more than 1000 km from the coast, upper Argo measurement in the first 10 m below the ocean surface and points with differences between reference and in situ SST lower than 0.3°C, the number of available floats is reduced to 85614 (60° latitude band) and 56900 (30° latitude band). According to this set of matchups, it seems reasonable to say that current L3 SSS produces a salinity estimate with a slight negative bias of -0.01, -0.06 and -0.01 at the 60°, 30° latitude bands and Zone 122 respectively, and standard deviation error of 0.52, 0.40 and 0.30 at the 60°, 30° latitude bands and Zone 122 respectively. For the case of OI SSS, the salinity estimate has also a slight negative bias of -0.02, -0.06 and -0.01 at the 60°, 30° latitude bands and Zone 122 respectively, and standard deviation error of 0.32, 0.26 and 0.19 at the 60°, 30° latitude bands and Zone 122 respectively.

Histograms and scatter plots of the matchup salinity differences are shown in Figure 3.13 for 9-day SMOS L3 and in Figure 3.14 for 9-day SMOS OI when the matchup is verified at 60° latitude band against the uppermost valid salinity value, provided that the Argo value has been measured in the first 10 meters of the water column. The matchup has also to be located more than 1000 km from the coast and the differences between the reference SST used for the retrieval of the salinity should differ from the Argo uppermost temperature value by less than 0.3°C.

The OI estimate is in better agreement with buoy data than L3 SSS product, as the histogram of the differences with the ground truth is narrower. The difference with Argo are contained in the interval [-0.2, 0.2] for the 55% of the points for the 9-day OI map and for the 38% of the points for the 9-day L3 map. As shown in Figure 3.14 the scatterplots of SMOS SSS vs Argo buoy data evidence where the closer agreement between SMOS maps and in situ data is achieved, the scatter of points is significantly reduced for OI SSS specially where SSS is higher than ∼34. The RMSE decreases from 60% to 41% for the L3 and OI estimate respectively, and the correlation coefficient increases from 0.81 to 0.89 for the L3 and OI estimate respectively.

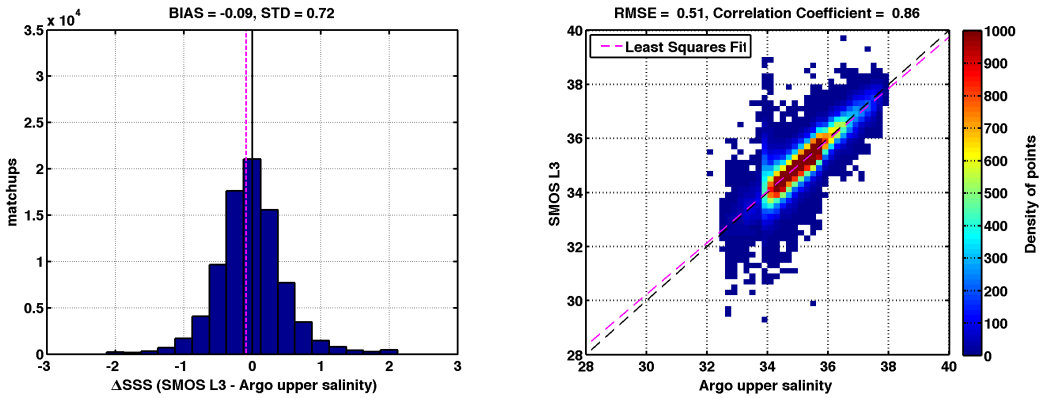

Figure 3.13: Histograms for SMOS-buoy differences 9-day L3 SSS (left). Scatter plot for SMOS (abscissa) and collocated buoy data (ordinate) for 9-day L3 SSS (right)

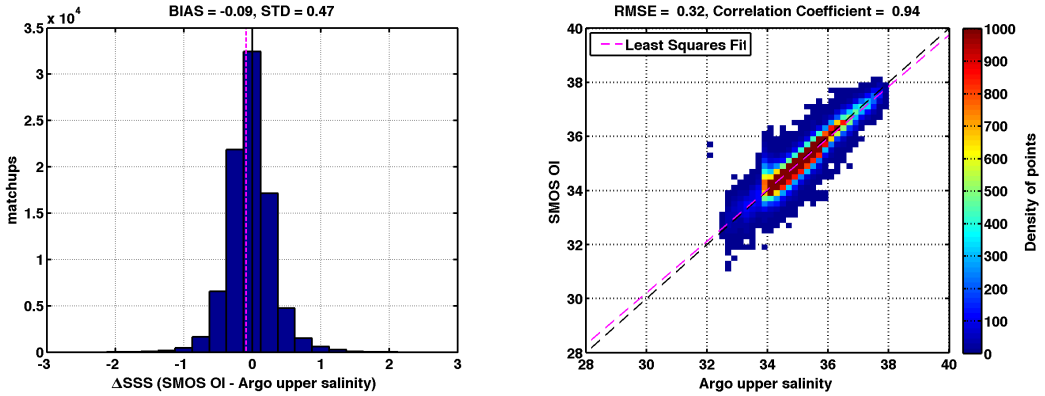

Figure 3.14: Histograms for SMOS-buoy differences 9-day OI SSS (left). Scatter plot for SMOS (abscissa) and collocated buoy data (ordinate) for 9-day OI SSS (right)

Monthly SSS products

According to SMOS mission requirements, SMOS should provide an estimate of SSS within an accuracy of 0.1-0.2 on 100 x 100 km^2 over one month (GODAE[1] scale (Smith, 2000)). To assess the mission requirements, monthly quality assessments of L3 and OI SSS monthly products with respect to both climatological fields and in situ data have been evaluated although using products defined on a 0.25° spatial grid.

First, a comparison with Argo SSS applied to the monthly products of SSS (both weighted average and optimal interpolation) has been carried out following the same validation analysis as for 9-day products. Figure 3.15 shows the monthly SSS L3 and monthly SSS OI differences with Argo data for the year 2012. A general reduction of the difference between SMOS products and in situ measurements is found when analyzing monthly maps, although discrepancies as large as 1 are found in areas with known issues of the SSS retrieval process. Tables 3.3 and 3.4 summarize the results of buoy collocation differences by latitude bands (global, 60S-60N, 30S-30N, and Zone 122), distance to coastal areas, depth of the Argo uppermost measurement and SST differences between Argo and ECMWF to quantitatively assess SSS error maps.

[1]Global Ocean Data Assimilation Experiment

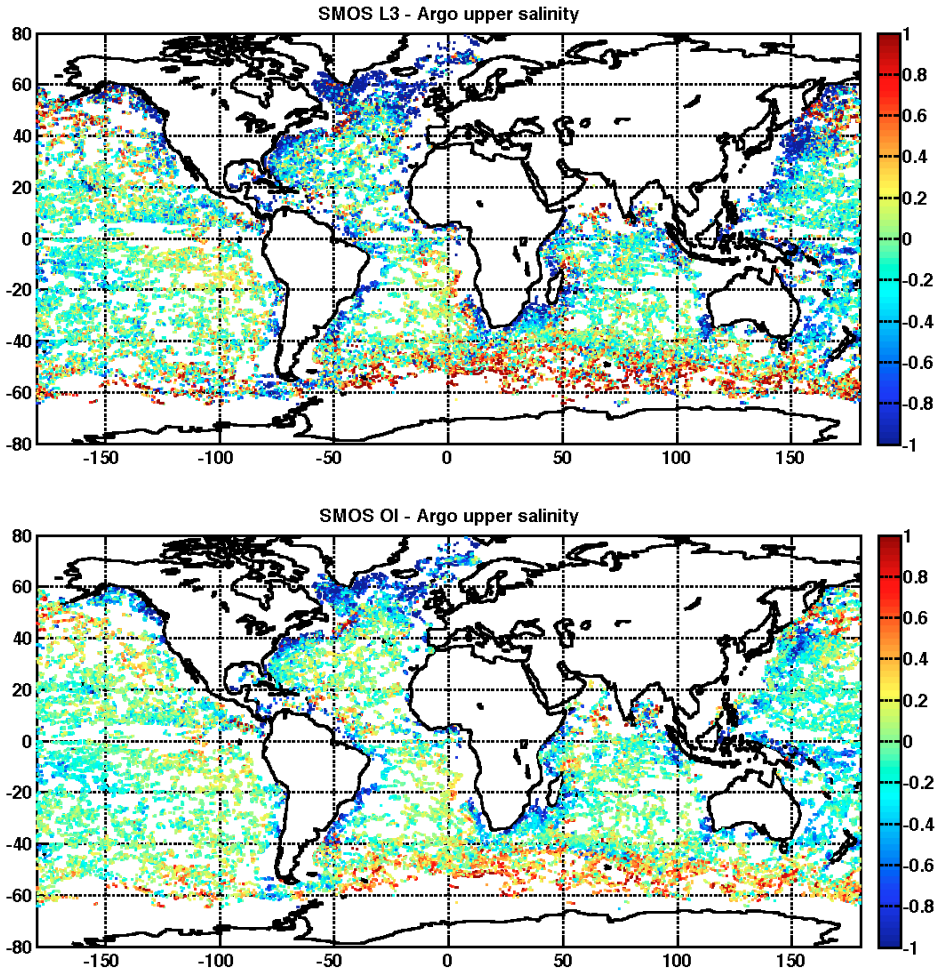

Figure 3.15: Global maps of SSS differences as defined by monthly L3 SSS (top) and data monthly OI SSS (bottom) minus the collocated Argo data for the entire year 2012.

Latitude		**Global**	**60S-60N**				**30S-30N**				**Zone 122**			
Maximum depth				**>10 m**				**>10 m**				**>10 m**		
Coast distance					**1000 km**				**1000 km**				**1000 km**	
ECMWF-Argo SST						**<0.3 ºC**				**<0.3 ºC**				**<0.3 ºC**
L3	n	72239	70970	68675	41422	27383	38195	37381	23575	18011	2384	2344	1965	1600
	$\langle \Delta S \rangle$	-0.14	-0.13	-0.12	-0.02	-0.03	-0.14	-0.14	-0.07	-0.07	-0.04	-0.04	-0.02	-0.02
	$\sigma_{<\Delta S>}$	0.66	0.62	0.61	0.47	0.38	0.43	0.43	0.30	0.30	0.21	0.21	0.20	0.19

Table 3.3: Statistics of the comparison of monthly L3 vs Argo SSS measurements for year 2012.

In the case of monthly products, the number of total matchups is reduced to the order of seventy thousand (two-hundred thousand for 9-day SSS maps). The reason for the higher number of matchups in the 9-day products is that the same Argo measurement will matchup with various 9-day maps. As the 9-day maps are produced every 3 days, consecutive maps have overlapping days. At global scale the standard deviation of SMOS minus Argo differences is reduced when monthly temporal averages are taken. Again, the largest random error (0.66) corresponds to the binned product and the smallest random error corresponds to the product generated by OI (0.45): in both cases the bias is consistently negative (-0.14 and -0.11).

Latitude		Global	60S-60N				30S-30N				Zone 122			
Maximum depth				>10 m				>10 m				>10 m		
Coast distance					1000 km				1000 km				1000 km	
ECMWF-Argo SST						<0.3 ºC				<0.3 ºC				<0.3 ºC
OI	n	58019	56761	54672	31222	20614	30887	30155	17901	13645	1822	1796	1503	1244
	$\langle \Delta S \rangle$	-0.11	-0.10	-0.09	-0.00	-0.02	-0.11	-0.11	-0.05	-0.06	-0.04	-0.04	-0.02	-0.02
	$\sigma_{<\Delta S>}$	0.45	0.44	0.43	0.39	0.26	0.32	0.31	0.23	0.22	0.15	0.15	0.15	0.14

Table 3.4: Statistics of the comparison of monthly OI vs Argo SSS measurements for year 2012.

Restricting the matchups by latitudinal bands results in reduced standard deviation errors. In the case of L3, the global error reduces from 0.66 (global), to 0.62 (bounded by latitude 60), to 0.43 (bounded to latitude 30) and to 0.21 (in Zone 122). In the case of OI, the global error reduces from 0.45 (global), to 0.44 (bounded by latitude 60), to 0.32 (bounded to latitude 30) and to 0.15 (in Zone 122).

matchups located farther than 1000 km from major coastlines results in the case of L3, in a reduction in standard deviation from 0.62 (60° latitude limit) to 0.47, and the bias is also reduced from -0.13 to -0.02. At the tropical band, the standard deviation error is reduced from 0.43 to 0.30 and the bias is also reduced from -0.14 to -0.07. Again, the larger negative bias in the tropical band is expected to be related to the increase of the frequency of rain events. In the case of OI, the standard deviation is reduced from 0.44 (60° latitude limit) to 0.39. At this latitude band, the systematic error is also reduced from -0.11 to 0.00. At the tropical band, the impact of considering matchups far from the coast is even larger, as the standard deviation error reduced from 0.32 to 0.23.

If matchups in regions affected by well-known issues (land-sea contamination, low surface water temperature, high surface wind) are not used, the number of available floats is reduced to 27383 (60° latitude band) and 18011 (30° latitude band). Using these matchups, monthly L3 SSS maps have a slight negative bias of -0.03, -0.07 and -0.02 at the 60°, 30° latitude bands and Zone 122 respectively and standard deviations of 0.38, 0.30 and 0.19 at the 60°, 30° latitudinal bands and Zone 122 respectively. In the case of monthly OI SSS maps, the salinity estimate has also a slight negative bias of -0.02, -0.06 and -0.02 at the 60°, 30° latitude bands and Zone 122 respectively, and standard deviations of 0.26, 0.22 and 0.14 at the 60°, 30° latitudinal bands and Zone 122 respectively.

Histograms of the differences of SMOS maps with matchup salinity differences and scatter-plots of SMOS vs in situ are shown in Figure 3.16 for monthly SMOS L3 and in Figure 3.17 for monthly SMOS OI, restricting the matchups to 60° latitudinal band and uppermost valid Argo salinity value in the first 10 meters of the water column. The matchup is also required to be located more than 1000 km from the coast and the differences between the Reference SST used for the retrieval of the salinity should differ from the Argo uppermost value by less than 0.3°C.

The OI estimate is in better agreement with buoy data than the L3 SSS product, as evidenced by a narrower histogram of differences: the percentage of points associated with differences in the range [-0.2, 0.2] is 50% for the 9-day L3 map and 64% for the 9-day OI map. The scatter of differences between SMOS SSS and Argo buoy data is reduced with respect to 9-day maps when monthly maps are used, especially for OI SSS estimates. The RMSE decreases from 37%

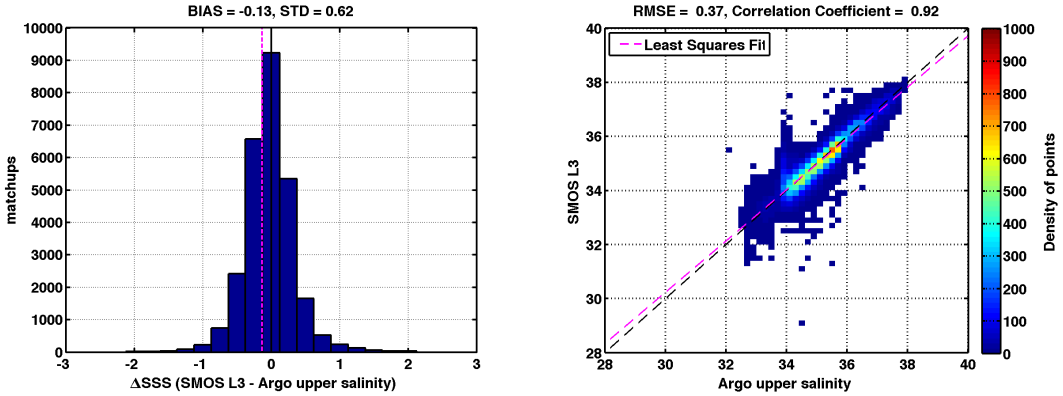

Figure 3.16: Histograms for SMOS-buoy differences monthly L3 SSS (left). Scatter plot for SMOS (abscissa) and collocated buoy data (ordinate) for monthly L3 SSS (right)

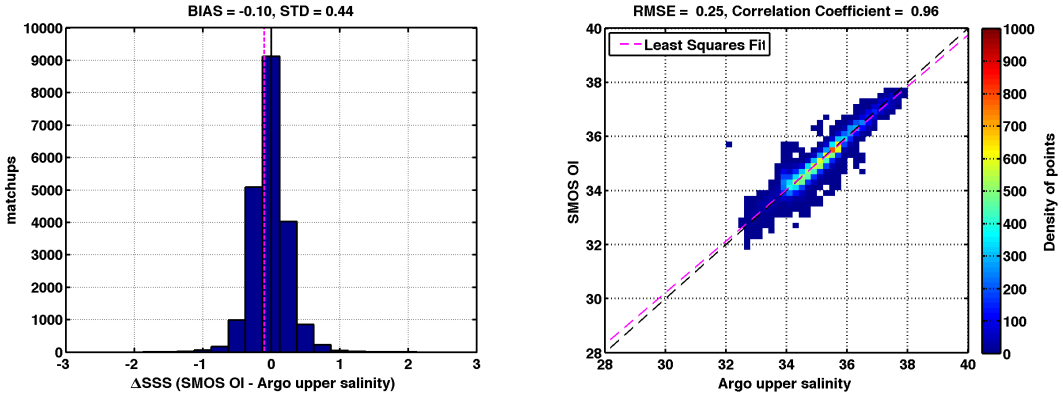

Figure 3.17: Histograms for SMOS-buoy differences monthly OI SSS (left). Scatter plot for SMOS (abscissa) and collocated buoy data (ordinate) for monthly OI SSS (right)

to 25 % for the L3 and OI estimates respectively, and the correlation coefficient increases from 0.92 to 0.96 for the L3 and OI estimate respectively.

Monthly L3 and OI SSS products can also be validated by comparing them with climatological values, as they are defined on the same time frame. We have thus studied the difference of SMOS monthly maps with respect to climatological values of SSS. The difference between the monthly weighted average and OI with respect to WOA09 climatology for the month of June is shown in Figure 3.18. Also in this case, as the used observations contain errors, certain parts of the anomalies highlights those deficiencies in the lower levels of the processor chain, as zones affected by RFI, high-latitudes biases or land-sea contamination.

Latitude		**Global**			**60S-60N**			**30S-30N**			**Zone 122**		
Climatology		WOA09	WOA13	ISAS	WOA09	WOA13	ISAS	WOA09	WOA13	ISAS	WOA09	WOA13	ISAS
L3	$\langle \Delta S \rangle$	-0.16	-0.17	-0.16	-0.10	-0.10	-0.10	-0.16	-0.17	-0.17	-0.02	-0.02	-0.02
	$\sigma_{<\Delta S>}$	1.04	1.03	1.02	0.72	0.72	0.70	0.60	0.59	0.55	0.26	0.25	0.21

Table 3.5: Statistics of the comparison between monthly L3 vs climatological SSS for the year 2012.

Notice that the OI map uses this specific climatology as background field, and is then not an independent source of validation of this product. To overcome this issue, ISAS monthly

Latitude		Global			60S-60N			30S-30N			Zone 122		
Climatology		WOA09	WOA13	ISAS	WOA09	WOA13	ISAS	WOA09	WOA13	ISAS	WOA09	WOA13	ISAS
OI	$\langle \Delta S \rangle$	-0.09	-0.10	-0.08	-0.08	-0.09	-0.09	-0.14	-0.14	-0.14	-0.02	-0.03	-0.03
	$\sigma_{<\Delta S>}$	0.43	0.55	0.53	0.41	0.44	0.42	0.40	0.43	0.40	0.19	0.18	0.15

Table 3.6: Statistics of the comparison between monthly OI vs climatological SSS for the year 2012.

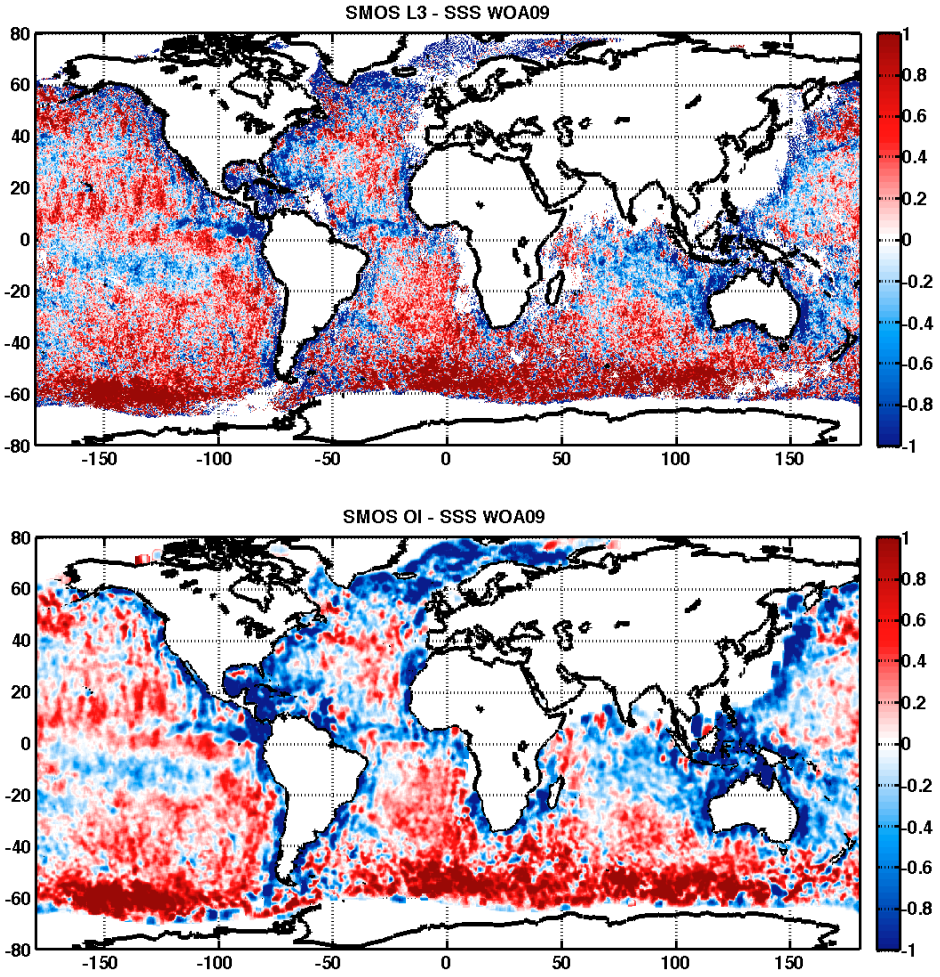

Figure 3.18: Weighted average minus WOA09 climatology for June 2012 (top) and OI minus WOA09 for June 2012 (bottom).

analysis for June 2012 (optimal interpolation from Argo global data set) and the latest version of World Ocean Atlas 2013 (WOA13) have also been used to test the accuracy of SMOS monthly products. The difference between the monthly weighted average and OI with respect to ISAS SSS for the month of June 2012 is shown in Figure 3.19. The difference is reduced when SMOS data is compared to ISAS SSS, especially in the Pacific. This probably reflect the same temporal sampling time of SSS by SMOS satellite and Argo buoys (year 2012 in this case) and therefore capturing the same interannual variability, whereas WOA climatologies could be affected by long term SSS patterns not present today leading to the observed greatest discrepancies.

Tables 3.5 and 3.6 summarize the validation results of monthly L3 and OI respectively against

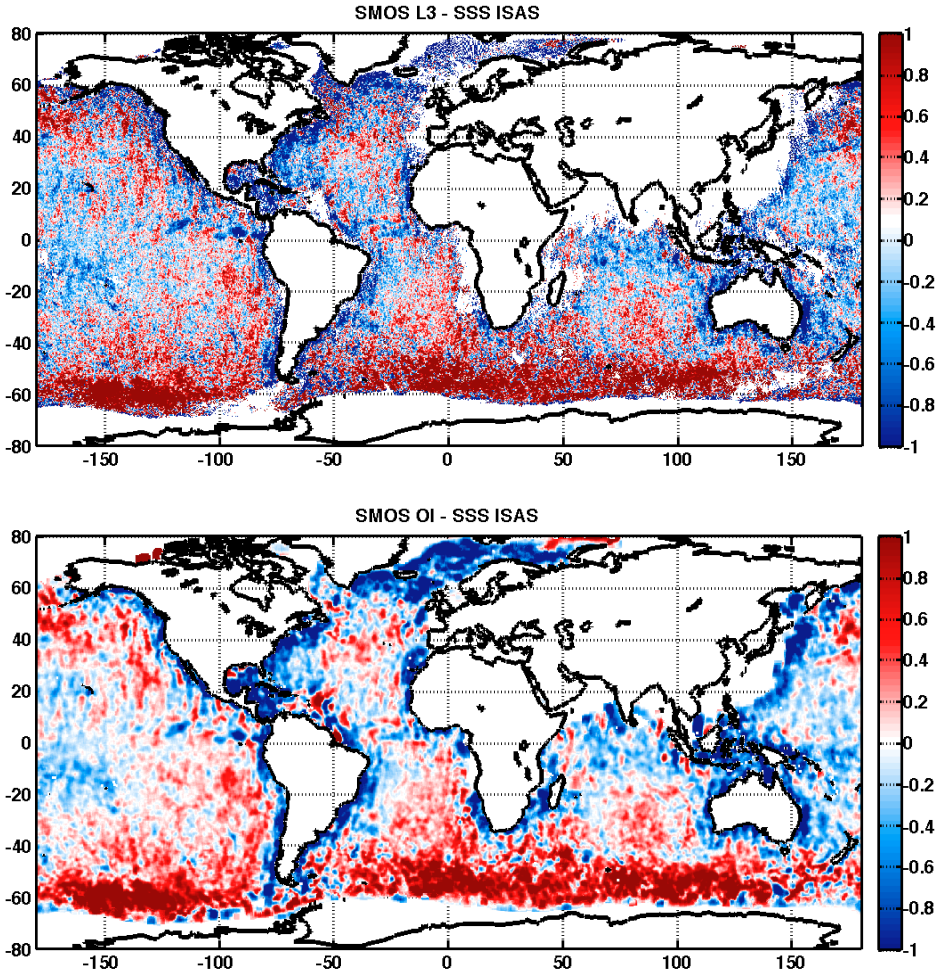

Figure 3.19: Weighted average minus ISAS analysis for June 2012 (top) and OI minus ISAS for June 2012 (bottom).

the different climatological products used at different latitudinal bands for the entire year 2012. In the case of ISAS, the global standard deviation is 1.02 for L3 and 0.53 for the OI, and a bias is consistently negative once more (-0.16 for L3 and -0.08 for OI). This means than the satellite estimates are fresher than the climatological SSS although, as seen in Figures 3.18 and 3.19, the satellite estimate becomes saltier depending on the region, specially in the South Ocean. When restricting the latitude the standard deviation is also reduced, from 1.02 (global) to 0.70 (bounded by latitude 60), 0.55 (bounded by latitude 30) and 0.21 (Zone 122) for the case of L3 and from 0.53 (global) to 0.42 (bounded by latitude 60), 0.40 (bounded by latitude 30) and 0.15 (Zone 122) in the case of OI. The bias is also reduced, from -0.16 (global) to -0.10 (bounded by latitude 60), -0.17 (bounded by latitude 30) and -0.02 (Zone 122) for the case of L3 and from -0.08 (global) to -0.09 (bounded by latitude 60), -0.14 (bounded by latitude 30) and -0.03 (Zone 122) in the case of OI.

3.5 Sensitivity tests

3.5.1 L2 filtering

One of the steps in the algorithm used to derive SSS from the brightness temperatures acquired by SMOS that has a considerable impact on the quality of the retrieved salinities is the application of quality filters. Quality filters are used to discard those retrievals that do not meet certain prefixed standard of quality because: the brightness temperatures are contaminated by a specific or inferred perturbation; the existence of a problem during the retrieval algorithm; or the detection of any kind of inconsistency with the geophysical model. In this section we study the question of the impact of the filtering strategy on the quality of the resulting SMOS SSS maps.

In this section a filtering strategy alternative to that of the standard Level 2 processor is going to be applied and compared with the original set of filters producing the official SMOS-BEC SSS products. The filtering procedure tested here is analogous to the one used to produce SMOS-BEC SSS products as described in section 3.2.1, but using a more restrictive swath of 300 km to get rid of lower quality retrievals far from the center of the track of the satellite swath. In addition, when L2 SSS measurements are close to coastal areas (distance closer than 500 km) we use a reduced swath of 100 km to diminish the impact of land-sea contamination. In addition, retrievals too far from the climatological values are discarded. This alternative filtering aims at improving the accuracy and reducing the bias present in SMOS L2 measurements, although at the cost of reducing the amount of L2 SSS values used to generate our L3 and OI maps. There is thus a trade-off between having a statistical set large enough and having values of enough quality to provide an accurate estimate of SSS. To filter outliers, all L2 SSS differing more than 2 with respect to WOA09 SSS are discarded.

The results of applying the weighted average algorithm to this filtered L2 SSS are shown in Figure 3.20 for 9-day and for monthly L3 maps. Compared with the results presented in section 3.2.1, the new 9-day and monthly L3 maps loose global coverage specially close to land, although the global SSS structure is correctly represented, and the results are consistent with the previous filtering procedure. The number of grid points per cell used to create the weighted averaged maps of 9 days and one month has also been reduced, as shown in Figure 3.21. In both cases the reduction of number of L2 measurements is most noticeable close to the coast.

As commented above, we face a trade-off between the coverage of SSS maps and the quality of the L2 SSS used to generate the maps. If a more restrictive filtering is applied to L2 SSS, the resulting coverage would be dramatically decreased, which would not be justified if the error on the resulting SSS maps does not greatly decrease accompanying. With the tested filtering procedure here, 8 L2 measurements are used on average to produce each grid point of the L3 SSS 9-day maps, so a relative error of 27% of L2 error is expected; an average of 22 L2 measurements is used to produce each grid point of the L3 SSS monthly maps, so a relative error of 16% is expected.

To study the error reduction associated with this new filtering, the standard deviation of L2 measurements inside each cell of $0.25^\circ \times 0.25^\circ$, is presented in Figure 3.22 for 9-day and monthly

maps. In this case, as compared with results presented in section 3.2.1, the spread between measurements inside each cell close to the coast areas and in high latitudes is being reduced.

To quantitatively validate the proposed filtering procedure, we compare a year of data against Argo floats measurements, as presented in section 3.4. Tables 3.7 and 3.8 synthesize the results of differences between 9-day L3 and OI SSS vs collocated measurements from Argo buoys by latitudinal bands (global, 60S-60N, 30S-30N, and Zone 122), distance to coast, depth of the Argo uppermost measurement and SST differences between Argo and ECMWF to quantitatively assess SSS error maps.

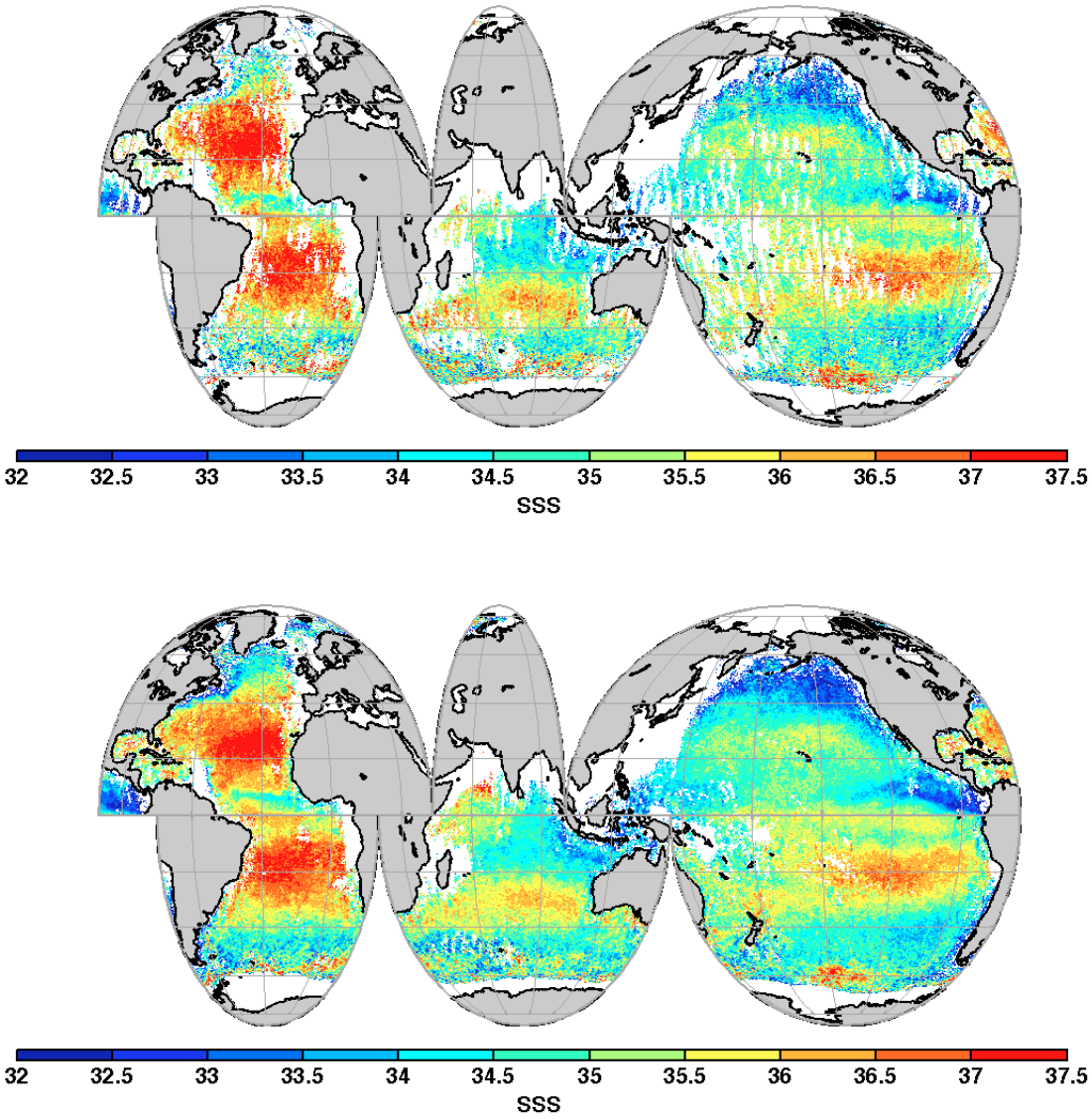

Figure 3.20: Map of surface salinity obtained with the alternative strategy applying a weighted average on SMOS data for first nine days (top) and month of June 2012 (bottom).

In the case of 9-day products using the alternative filtering scheme on L2, that includes a bias correction with respect to climatology, the number of total matchups is reduced to seventy

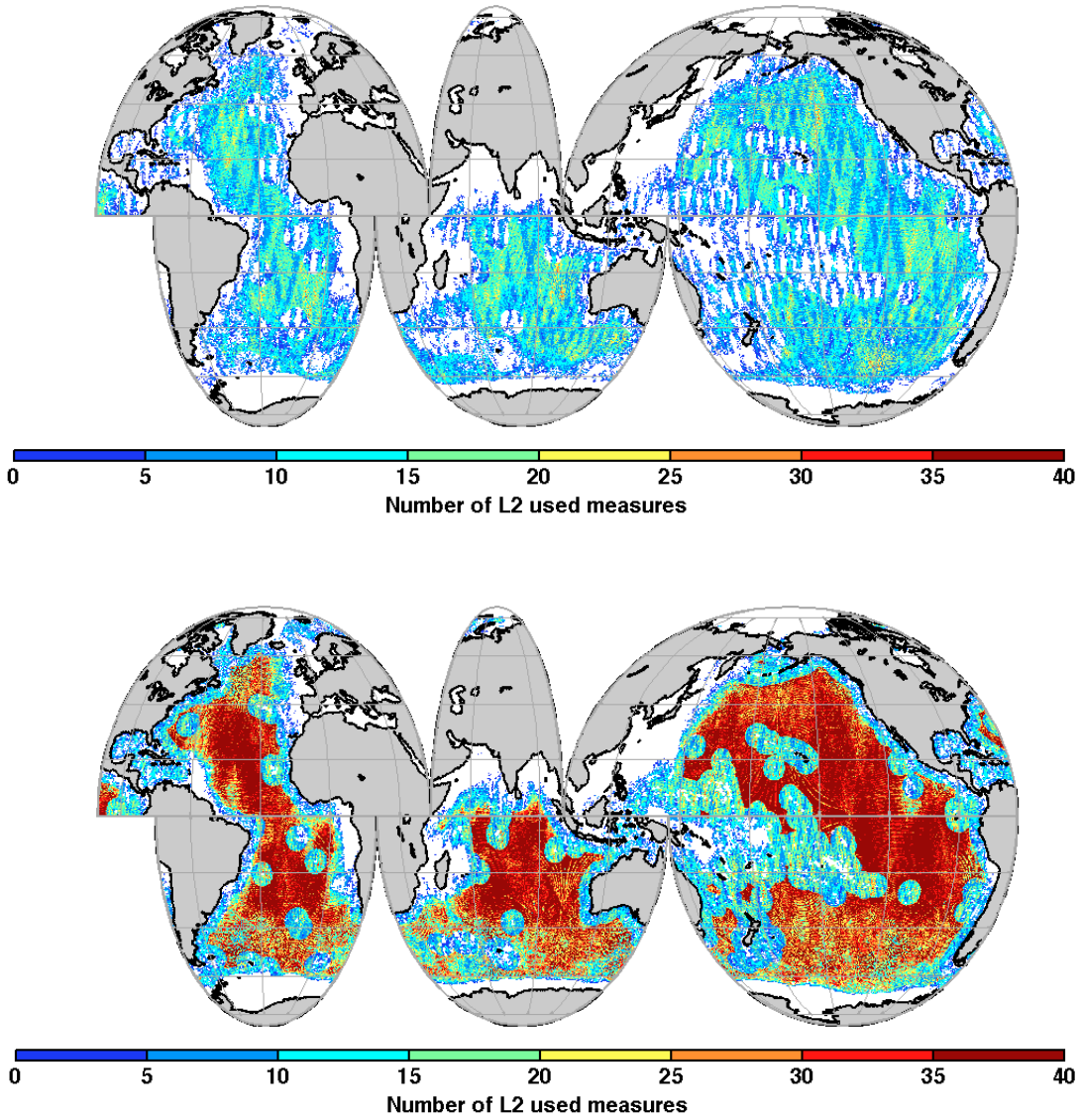

Figure 3.21: Number of L2 measurements used for 9-day (top) and monthly products (bottom).

Latitude		**Global**	**60S-60N**				**30S-30N**				**Zone 122**			
Maximum depth				**>10 m**				**>10 m**				**>10 m**		
Coast distance					**1000 km**				**1000 km**				**1000 km**	
ECMWF-Argo SST						**<0.3 ºC**				**<0.3 ºC**				**<0.3 ºC**
L3	n	176033	174008	169094	116147	76711	92565	90742	64966	49705	6473	6355	5515	4575
	$\langle \Delta S \rangle$	-0.01	-0.01	-0.01	0.03	0.02	-0.05	-0.05	-0.02	-0.03	0.00	0.00	0.02	0.01
	$\sigma_{<\Delta S>}$	0.71	0.70	0.70	0.64	0.54	0.49	0.49	0.44	0.43	0.38	0.39	0.37	0.36

Table 3.7: Statistics of the comparison of 9-day L3 (alternative filtering of L2) vs Argo SSS measurements for the year 2012.

thousand (two-hundred thousand for original 9-day SSS maps). As shown in the tables, at global scale the standard deviation of SMOS minus Argo differences is reduced when using the alternative filtering. The standard deviation is 0.71 for L3 and 0.48 for the OI (originally they

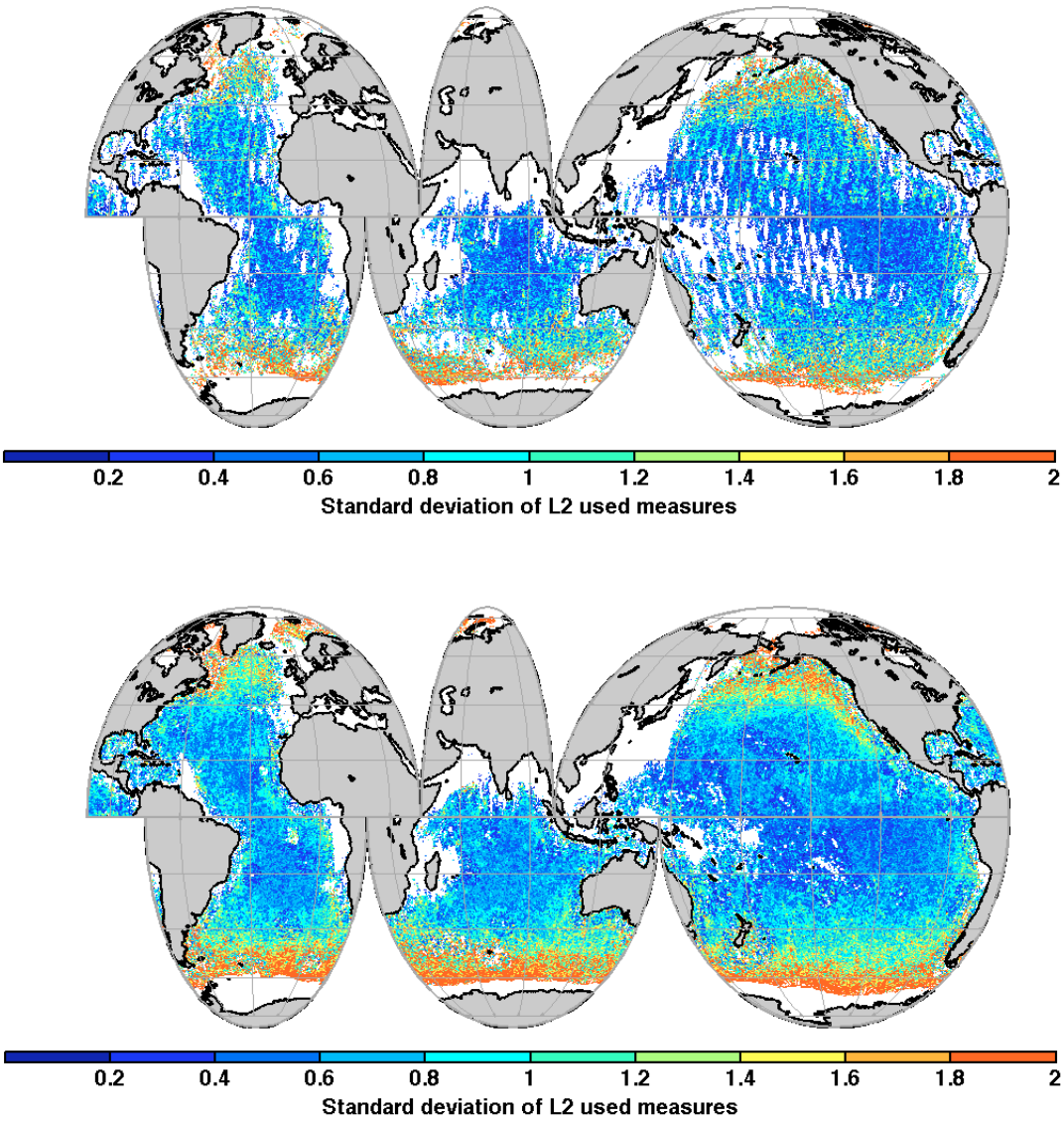

Figure 3.22: Standard deviation of L2 measurements inside each cell of 0.25°×0.25° for 9-day (top) and monthly products (bottom).

Latitude		**Global**	**60S-60N**				**30S-30N**				**Zone 122**			
Maximum depth				**>10 m**				**>10 m**				**>10 m**		
Coast distance					**1000 km**				**1000 km**				**1000 km**	
ECMWF-Argo SST						**<0.3 ºC**				**<0.3 ºC**				**<0.3 ºC**
OI	n	235446	231658	223773	133312	88382	125347	122672	76151	58360	7802	7683	6370	5196
	$\langle \Delta S \rangle$	-0.04	-0.04	-0.04	0.01	-0.00	-0.07	-0.07	-0.04	-0.04	-0.01	-0.01	0.01	0.01
	$\sigma_{<\Delta S>}$	0.48	0.47	0.47	0.44	0.34	0.36	0.36	0.30	0.29	0.25	0.25	0.24	0.23

Table 3.8: Statistics of the comparison of 9-day OI (alternative filtering of L2) vs Argo SSS measurements for the year 2012.

were 0.75 and 0.48), with biases of -0.01 for L3 and -0.04 for OI (originally they where -0.10 and -0.10).

As with the original validation, the comparison with matchups restricted by latitude, located farther than 1000 km from major coasts and restricted to verify the Argo consistency criteria on SST as above, leads to reduced standard deviations and bias. Using these matchups, the 9-day L3 SSS produces a salinity estimate with bias of 0.02, -0.03 and 0.01 at the 60°, 30° latitudinal bands and Zone 122 respectively, and standard deviations of 0.54, 0.43 and 0.36 at the 60°, 30° latitudinal bands and Zone 122 respectively. In the case of 9-day OI SSS, the salinity estimate has also a slight negative bias of 0.00, -0.04 and -0.01 at the 60°, 30° latitudinal bands and Zone 122 respectively, and standard deviations of 0.34, 0.29 and 0.23 at the 60°, 30° latitudinal bands and Zone 122 respectively. These results represent an improvement with respect to original filtering criteria, based on the decrease of bias error, although similar standard deviation are found.

Tables 3.9 and 3.10 synthesize the results of the differences with collocated buoys for monthly L3 and OI SSS, classified by latitudinal bands (global, 60S-60N, 30S-30N, and Zone 122), distance to coast, depth of the Argo uppermost measurement and SST differences between Argo and ECMWF to quantitatively assess the SSS error maps.

Latitude		**Global**	**60S-60N**				**30S-30N**				**Zone 122**			
Maximum depth				**>10 m**				**>10 m**				**>10 m**		
Coast distance					**1000 km**				**1000 km**				**1000 km**	
ECMWF-Argo SST						**<0.3 ºC**				**<0.3 ºC**				**<0.3 ºC**
L3	n	67573	66577	64470	40368	26628	35357	34615	22773	17397	2354	2316	1945	1588
	$\langle \Delta S \rangle$	-0.06	-0.06	-0.05	0.00	-0.01	-0.08	-0.08	-0.05	-0.05	-0.03	-0.03	-0.01	-0.01
	$\sigma_{<\Delta S>}$	0.60	0.59	0.58	0.48	0.39	0.41	0.41	0.32	0.32	0.26	0.27	0.25	0.24

Table 3.9: Statistics of the comparison of monthly L3 (alternative filtering of L2) vs Argo SSS measurements for the year 2012.

Latitude		**Global**	**60S-60N**				**30S-30N**				**Zone 122**			
Maximum depth				**>10 m**				**>10 m**				**>10 m**		
Coast distance					**1000 km**				**1000 km**				**1000 km**	
ECMWF-Argo SST						**<0.3 ºC**				**<0.3 ºC**				**<0.3 ºC**
OI	n	75602	74121	71468	41684	27546	40124	39236	23845	18201	2423	2385	1973	1609
	$\langle \Delta S \rangle$	-0.08	-0.07	-0.06	-0.01	-0.02	-0.08	-0.08	-0.05	-0.05	-0.03	-0.03	-0.00	-0.00
	$\sigma_{<\Delta S>}$	0.43	0.42	0.41	0.37	0.26	0.32	0.31	0.24	0.23	0.18	0.18	0.17	0.16

Table 3.10: Statistics of the comparison of monthly OI (alternative filtering of L2) vs Argo SSS measurements for the year 2012.

In the case of monthly products using alternative filtering of L2, the number of total matchups reduce to the order of seventy thousand (seventy-five thousand for original monthly SSS maps). At global scale the standard deviation of the SMOS minus Argo differences is reduced when using the alternative filtering. The standard deviation are 0.60 for L3 and 0.43 for the OI (originally they were 0.66 and 0.45), and the biases are -0.06 for L3 and -0.08 for OI (originally they were -0.14 and -0.11).

When the matchups are restricted by latitude, located farther than 1000 km from major coasts and restricted to verify the consistency Argo SST criteria as above, reduced standard deviations and bias are obtained. With such a selection of matchups, monthly L3 SSS products yields a slightly negative biases of -0.01, -0.05 and -0.01 at the 60°, 30° latitudinal bands and

Zone 122 respectively and standard deviations of 0.39, 0.32 and 0.24 at the 60°, 30° latitudinal bands and Zone 122 respectively. For the case of monthly OI SSS, the salinity estimate has also slight negative biases of -0.02, -0.05 and -0.00 at the 60°, 30° latitudinal bands and Zone 122 respectively, and standard deviations of 0.26, 0.23 and 0.15 at the 60°, 30° latitudinal bands and Zone 122 respectively. Also for monthly products, the alternative filtering results in an improvement of the mean bias compared to the results from filtering criteria originally used in L3 and OI SSS maps.

When comparing with monthly SSS maps not coming from remote sensing (Table 3.11), as done in previous section, the results are also improved (compare to Table 3.5). For the case of OI (not shown), this comparison is not much affected by the filtering procedure.

Latitude		**Global**			**60S-60N**			**30S-30N**			**Zone 122**		
Climatology		WOA09	WOA13	ISAS	WOA09	WOA13	ISAS	WOA09	WOA13	ISAS	WOA09	WOA13	ISAS
L3	$\langle \Delta S \rangle$	-0.01	-0.02	-0.01	0.00	-0.01	-0.01	-0.06	-0.07	-0.08	-0.00	-0.01	-0.01
	$\sigma_{<\Delta S>}$	0.85	0.83	0.85	0.65	0.65	0.64	0.50	0.48	0.47	0.31	0.30	0.27

Table 3.11: Statistics of the comparison between monthly L3 (alternative filtering of L2) vs climatological SSS for the year 2012.

3.5.2 OI reference field

The second sensitivity test addressed in this chapter consists of using an alternative reference field in the optimal interpolation mapping procedure. The choice here is to use as a first guess an optimally interpolated field from monthly mean SSS of Argo buoy measurements according to the ISAS analysis for the year 2012 implemented at Coriolis data center (Gaillard et al., 2009).

The advantage of using Argo-derived SSS field is that it is an independent source of data, different from satellite data. Since Argo program started in 2009 ISAS field provides unbiased estimates compared to climatological values, that could be affected by large-scale biases due to the presence of climatic trends, or the inconsistency between different types of instruments and sources of in situ data.

The validation results of 9-day OI products using ISAS-12 as a background field and the alternative filtering of L2 measurements as explained in section 3.5.1, comparing with the data coming from Argo buoys for year 2012, are summarized in Table 3.12.

Latitude		**Global**	**60S-60N**				**30S-30N**				**Zone 122**			
Maximum depth				**>10 m**				**>10 m**				**>10 m**		
Coast distance					**1000 km**				**1000 km**				**1000 km**	
ECMWF-Argo SST						**<0.3 ºC**				**<0.3 ºC**				**<0.3 ºC**
Isas-based OI	n	233234	229468	221650	132157	87612	124064	121413	75489	57852	7733	7616	6317	5151
	$\langle \Delta S \rangle$	-0.03	-0.03	-0.03	0.01	0.00	-0.06	-0.06	-0.03	-0.03	-0.01	-0.00	0.01	0.01
	$\sigma_{<\Delta S>}$	0.47	0.46	0.46	0.44	0.34	0.34	0.34	0.29	0.29	0.25	0.25	0.24	0.23

Table 3.12: Statistics of the comparison of 9-day OI (alternative filtering of L2 and ISAS as a reference field) vs Argo SSS measurements for the year 2012.

Recall that our alternative filtering scheme of L2 data, includes a bias correction with respect to WOA09 climatology, and that OI uses ISAS as a reference field. The standard deviation of the

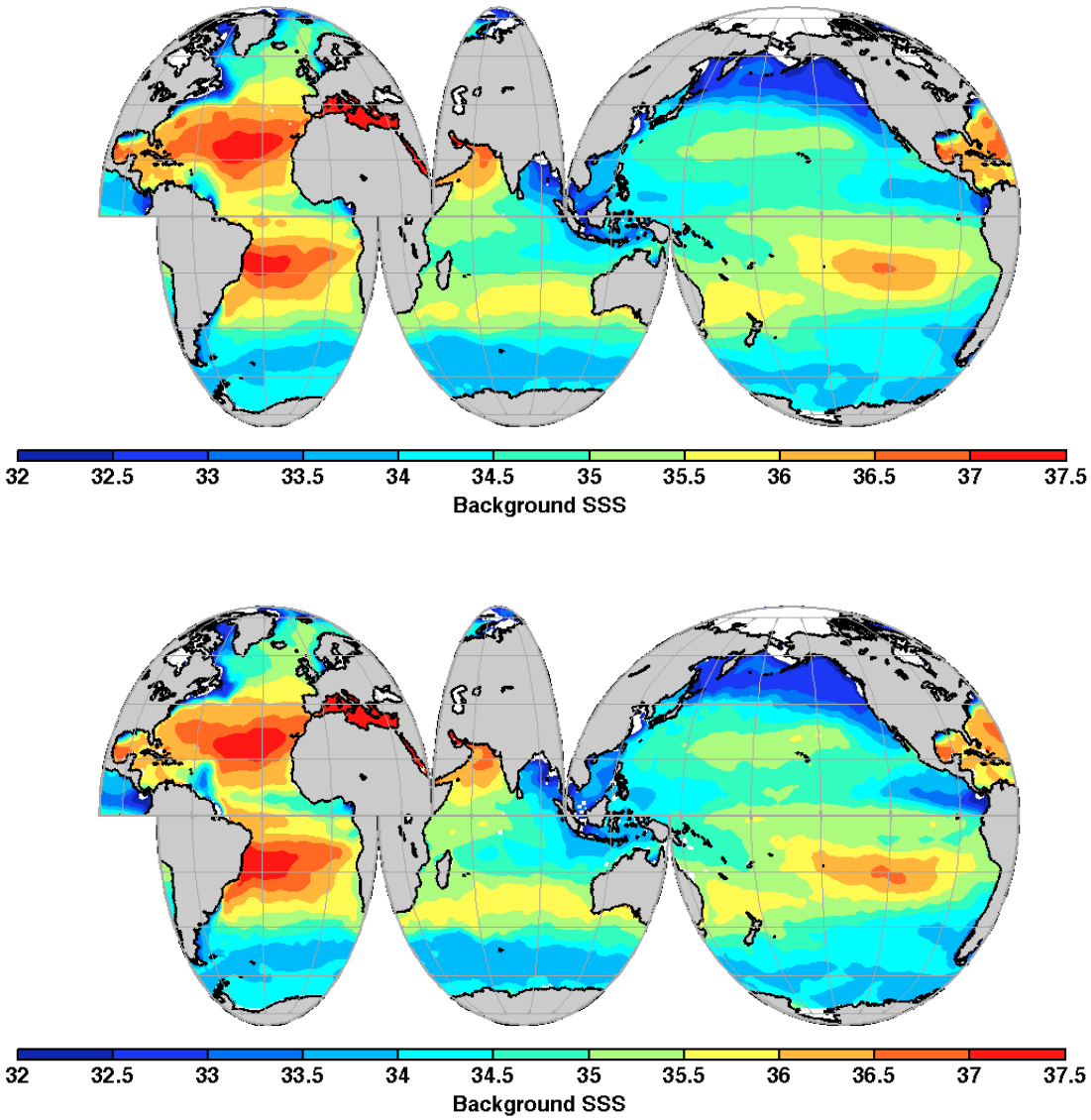

Figure 3.23: Reference field of surface salinity from World Ocean Atlas (top) and from ISAS SSS (bottom) for June 2012.

SMOS minus Argo differences in the new product is slightly reduced as compared to the results obtained when using WOA09 as a reference field. The standard deviation is 0.47 (originally was 0.48), the bias is -0.03 (originally was -0.04). If we take, as before, a set of matchups restricted in latitude, located farther than 1000 km from major coasts and restricted to the Argo verifying the SST consistency criteria, the standard deviation and bias are again slightly better than when using WOA09 climatology as a reference field (compare Tables 3.8 and 3.12). Therefore, in order to find the best possible OI SSS field, we recommend the use of ISAS as a ground truth, and it will be used in subsequent sensitivity tests.

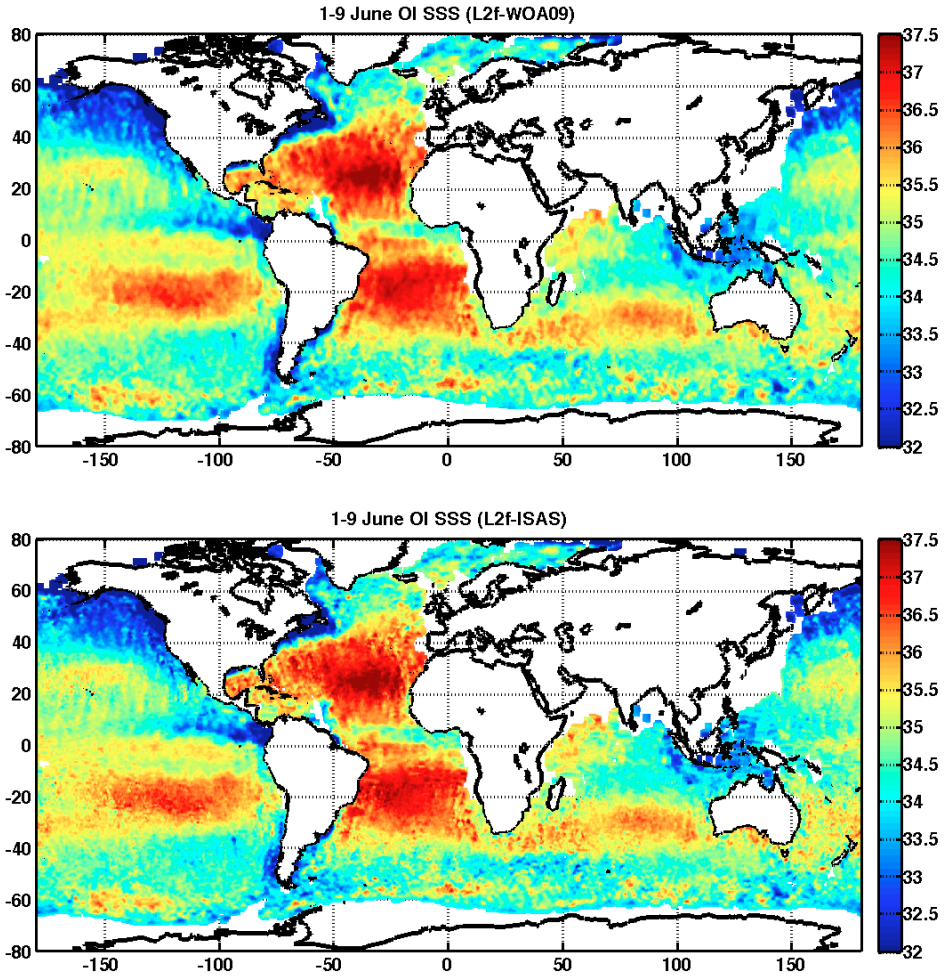

Figure 3.24: Map of surface salinity obtained by applying a weighted average on SMOS data for first nine days (top) and month of June 2012 (bottom).

3.5.3 Observation error covariance matrix

To apply the OI algorithm, the observation error covariance matrix **R** needs to be specified and it plays an important role on the accuracy of the output. In Melnichenko et al. (2014) the authors compute an error covariance model for Aquarius data which takes into account correlated long-wavelength errors (inter-beam biases) along the satellite tracks (non-diagonal elements of the matrix **R**), as well as uncorrelated noise (diagonal elements of matrix **R**). The uncorrelated noise is assumed to be 10% of the signal variance, independent of the geographical location. To infer the correlated part, they compare interbeam differences as recorded by HYCOM and Aquarius SSS. The mean covariances of the interbeam differences are computed as a function of along-track separation (Figure 3.25). Using an analytic model they find a long-wavelength error of 0.085.

Here, we follow the results of this study for Aquarius SSS, and apply them for the case of SMOS. The instrument differences between SMOS and Aquarius make not viable to apply the correlated errors as no inter-beam biases are present in SMOS data, although other correlated

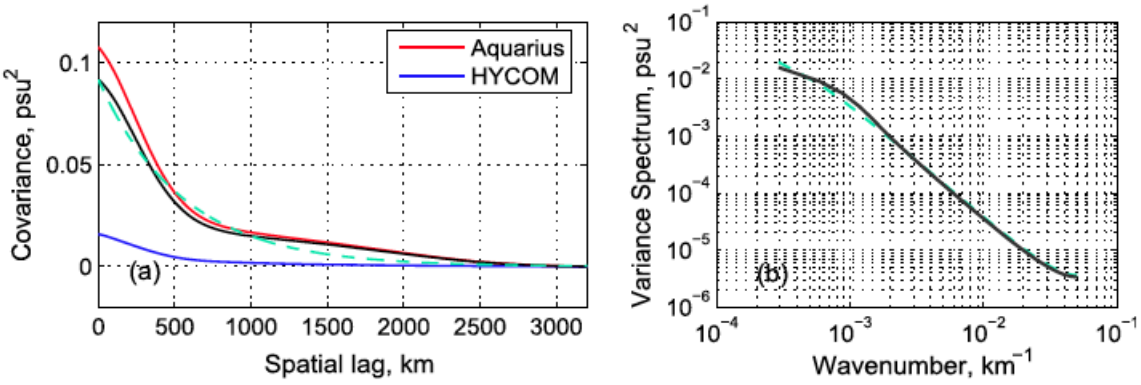

Figure 3.25: (a) Autocovariances of Aquarius interbeam differences computed for the North Atlantic. Red and blue lines represent Aquarius and HYCOM SSS respectively, black curve is the difference between the two. Its approximation by the exponential function is shown as a green dashed curve. (b) Associated spectra. Extracted from published work of Melnichenko et al. (2014).

errors are present and need to be properly modeled using SMOS measurements, as a possible work beyond this thesis.

The sensitivity test addressed here applies only the same non-correlated error used for Aquarius; we thus assume again the matrix **R** to be a diagonal matrix. Compared with the original configuration, in which uncorrelated errors were supposed to be defined by the standard deviation of the L2 SSS measurements used in the weighted average at each grid point, we study here the effect of setting the diagonal terms of **R** to be 10% of the same variance, as done for Aquarius OI products. This allows studying the effect of lowering the observational error supposed for SMOS data.

An example of the resulting OI SSS products for the period 1st-9th of June 2012 is shown in Figure 3.26 bottom (the best option according to Jorda et al. (2011) is shown on Figure 3.26 top). A too large estimate of the observational error implies that the observations are less reliable than the background, so the modulation of the reference field has a too low amplitude and the resulting product is excessively close to climatology.

On the other hand, when the value of the observational error is estimated following Melnichenko et al. (2014) for Aquarius data as a 10% of the variance, the values of **R** are smaller that the actual errors in SMOS data, so the analysis tries to fit spurious anomalies associated with noise and in consequence degrading the quality of the resulting OI SSS (Figure 3.26 bottom).

We have once again performed an extensive validation of 9-day OI products generated using the alternative **R**, also using the alternative filtering selection defined in section 3.5.1 and the background field presented in section 3.5.2. Data are once more validated by its direct comparison with measurements from Argo buoys for year 2012, as summarized in Table 3.13.

When using alternative filtering of L2, ISAS as a reference field, and the alternative **R** definition, the standard deviation of the SMOS minus Argo differences are worse than when using the value of the standard deviation of L2 SSS used at each grid point. Globally, the standard deviation is 0.66 (originally it was 0.47), and the bias is -0.05 (originally it was -0.03). We conclude that the OI rejects overfitting SMOS data, and that the spatial regularity of noise

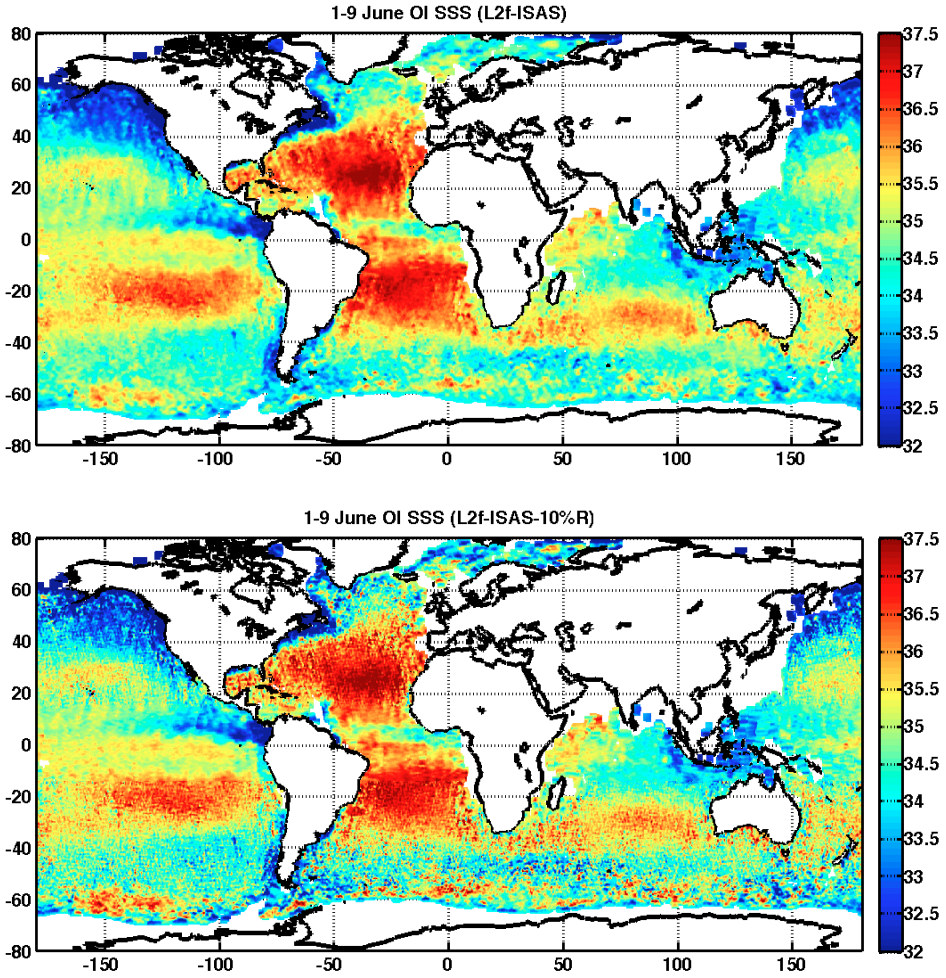

Figure 3.26: OI SSS maps obtained when using the original $\boldsymbol{R}$ *(equal to the standard deviation of L2 SSS used at each gridpoint) (top) and when using alternative* $\boldsymbol{R}$ *(equal to the 10% of the variance of L2 SSS used at each gridpoint) (bottom): both maps are referred to the first 9 days of June 2012.*

Latitude		**Global**	**60S-60N**				**30S-30N**				**Zone 122**			
Maximum depth				**>10 m**				**>10 m**				**>10 m**		
Coast distance					**1000 km**				**1000 km**				**1000 km**	
ECMWF-Argo SST						**<0.3 ºC**				**<0.3 ºC**				**<0.3 ºC**
Modified R OI	n	235237	231453	223573	133308	88378	125163	122491	76147	58356	7802	7683	6370	5196
	$\langle \Delta S \rangle$	-0.05	-0.04	-0.04	0.01	-0.00	-0.06	-0.06	-0.03	-0.03	-0.00	-0.00	0.02	0.01
	$\sigma_{<\Delta S>}$	0.66	0.65	0.65	0.58	0.48	0.44	0.44	0.36	0.35	0.33	0.33	0.32	0.31

Table 3.13: Statistics of the comparison of 9-day OI (alternative filtering of L2, ISAS as a reference field and observational error equal to 10 percent of the variance of L2 used at each grid point) vs Argo SSS measurements for the year 2012.

data.

3.6 Regional case study

To study the accuracy of the best SMOS SSS product at smaller spatial scales, in this section we briefly asses the quality of our SSS analysis (L3 weighted average as in section 3.5.1, and OI as in section 3.5.2) in a region at the North Atlantic salinity maximum region [25°N, 38°W]. This choice is motivated by the field experiments carried out during SPURS-MIDAS oceanographic campaign that took place from 16 March to 13 April 2013 (Las Palmas de Gran Canaria-Ponta Delgada). This campaign was part of the Salinity Process in the Upper Ocean Regional Study (SPURS) field experiment that aimed at studying the physical processes responsible for the maintenance and amplitude of the subtropical Atlantic salinity maximum.

Most of the water at the North Atlantic salinity maximum comes from the northwestern part of the subtropical gyre as a result of the large excess of evaporation over precipitation. This water gradually sees its salinity to increase on the route until it reaches the central subtropical gyre. From there on, the salinity maximum water is subducted and flows back to the western boundary in the depth range of the thermocline. With its high-salinity nature, a major portion of this water penetrates into the subpolar region and directly contributes to the deep thermohaline circulation (Qu et al., 2011, 2013).

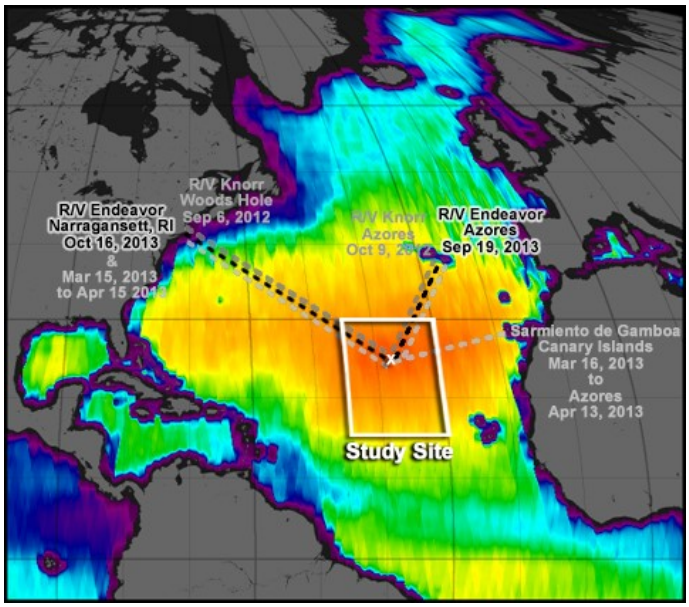

Figure 3.27: Salinity Processes in the Upper Ocean Regional Study (SPURS) field program exploring the salinity maximum region in the North Atlantic Ocean.

The SPURS experiment area (Figure 3.27) provided an exceptional opportunity for the validation of satellite sensed SSS measurements (Bingham et al., 2014; Hernandez et al., 2014). During our field campaign on board the Spanish R/V Sarmiento de Gamboa, measures of salinity from drifters, TSG, and SeaSoar undulating CTD were taken; this set of in situ data is used in this chapter to assess the quality of our L3 and OI products at regional scale. Analysis of SPURS campaign data already revealed several relatively fresh anomalies, which deviate strongly from climatological conditions. The observed scales and evolution of the salinity features

strongly suggests a connection to mesoscale dynamics in the area (Busecke et al., 2014), a hypothesis reinforced by the presence of eddies with distinct salinity/temperature signatures of up to 0.2/1°C, with horizontal scales of up to 200 km (Gordon and Giulivi, 2014).

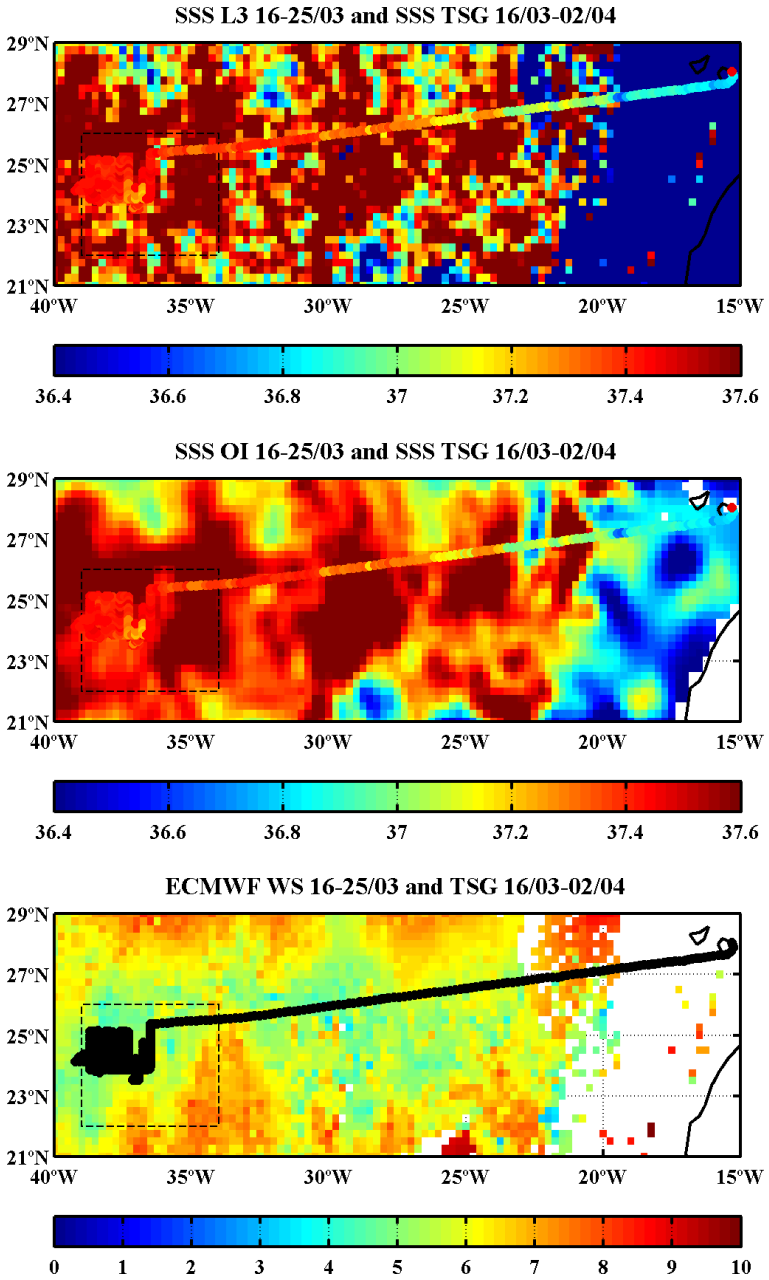

Figure 3.28: L3 SSS using filtering as in section 3.5.1 (top). OI SSS using background as in sections 3.5.2 (middle). ECMWF wind (m/s) used as ancillary data for SMOS SSS retrieval (bottom) for 16-25 of March 2013

Figure 3.28 shows both L3 and OI SSS maps for the 16-25 march of 2013 and the SSS registered by the thermosalinograph (TSG) along all the cruise transect during 16-29 march over-imposed (top and middle). SMOS maps are still deeply affected by bias errors as compared to TSG data. Bias removal is an issue still being under improvement for SMOS mission, with several origins, some of them geophysical. For instance, if we compare the wind speed as provided by ECMWF (bottom) we can see a close spatial correlation between low ECMWF winds (< 5

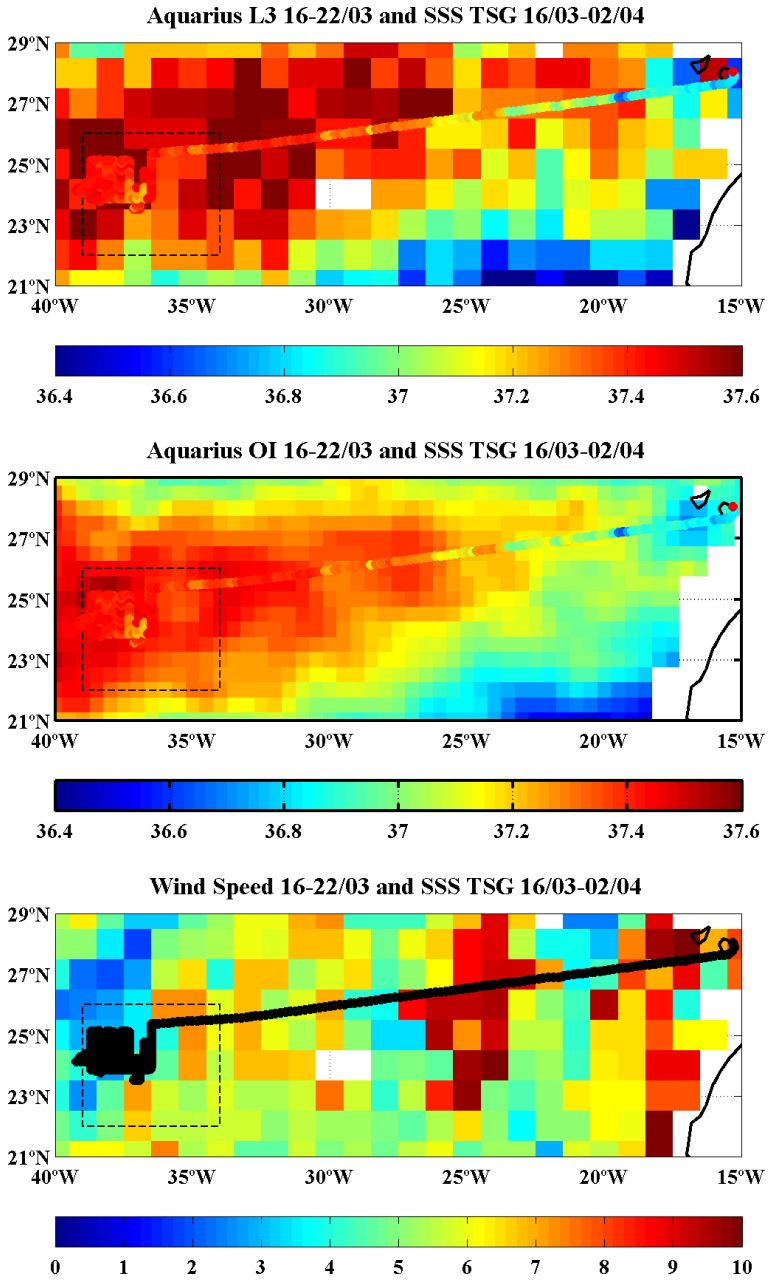

Figure 3.29: Aquarius L3 SSS v03 (top). Aquarius OI developed as explained in Melnichenko et al. (2014) (middle). Wind speed (m/s) sensed by Aquarius scatterometer (bottom) for 16-22 of March 2013

m/s) and anomalous salty values in SMOS maps (positive biased with respect to TSG SSS).

ECMWF winds are used as ancillary data in the retrieval process of SMOS SSS, and for winds lower than 5 m/s and higher than 12 m/s errors in ECMWF exponentially increase. For the specific case of low-winds scenarios, the ocean is known to be less mixed and to develop intermittent patchiness, filaments and small scale variability of ocean variables. This variability is completely absent in ECMWF products, but can be observed in brightness temperatures produced by SMOS, what probably leads to a poor correction for this specific case. The same issue affects other remote sensing variables as for instance scatterometer data (Shankaranarayanan and Donelan, 2001).

Aquarius SSS OI is less biased as compared to in situ data (Figure 3.29). The OI developed by Melnichenko et al. (2014) from Aquarius L3 SSS (top) leads to an OI SSS (middle) in good agreement with the TSG data, although TSG show a higher spatio-temporal variability not captured by the satellite. The different instrumental characteristics of both SMOS and Aquarius missions (interferometry versus direct radiometer measurement) leads to a less biased but lower resolution data of Aquarius maps compared to SMOS maps. Another crucial improvement of Aquarius mission is the possibility of directly measuring collocated surface wind speeds as it has onboard a scatterometer, what enables the possibility of using these measurements as ancillary data for SSS retrieval (Figure 3.29 bottom). As a consequence, the spatial structure of wind speed and Aquarius SSS is less correlated (or even non correlated) than in the case of SMOS data.

It is also important to notice how the OI on Aquarius data is able to get rid of inter-beam biases affecting L3 SSS (as detailed in section 3.5.3). This is mainly due to the error covariance matrix used, that takes into account spatially correlated errors in Aquarius measurements. It is therefore crucial to improve SMOS OI products to take into account the spatially correlated errors in brightness temperature measurements, probably related to wind estimates and probably to correlated antenna errors.

We have compared the L3 and OI maps from 3-12 April to different in situ salinity data sets collected during SPURS-MIDAS at SPURS location [22-26°N - 41-35°W]. The period was chosen near to the end of the cruise to include a complete deployment of surface salinity drifters. Figures 3.30 and 3.30 (right) show near-surface salinity in the SPURS area as measured by SMOS L3 and OI (∼1 cm) respectively, S drifters (∼50 cm), onboard along track TSG (∼4 m) and SeaSoar undulating CTD (∼15 m). All in situ datasets show a higher spatio temporal variability not captured by satellite measurements and a clear salty bias is present in SMOS OI specifically at low winds areas.

A statistical comparison between L3 and in situ data sets is explored using the histograms in Figure 3.30 (left). The biases are always positive: 0.03 (drifters), 0.15 (TSG) and 0.12 (SeaSoar-CTD). The standard deviation with respect to in situ data are equal to 0.24 (buoys), 0.28 (TSG) and 0.25 (SeaSoar-CTD) evidencing that the error in the measurement is about double that of the natural variability of SSS in the area.

The histograms in Figure 3.31 (right) summarize the statistics of the point comparison between OI SSS and the three in situ data sets. The mean biases are again always positive: 0.08 (drifters), 0.14 (TSG) and 0.10 (SeaSoar-CTD), lower than when comparing with L3 maps. Regarding the different measurement depths within the first 15 meters of the water column, SMOS salinity estimations have a lower bias with respect to buoys (measuring at 50 cm depth) than with respect to TSG and SeaSoar-CTD, which measurements of salinity refer to deeper layers (5-15 meters). The same is true regarding the standard deviation with respect to in situ data, equal to 0.08 (buoys), 0.12 (TSG) and 0.09 (SeaSoar-CTD). Notice than the standard deviation is greatly reduced when applying the OI methodology; in this region mean errors are in line with mission requirements, although spatially they reflect the natural variability of the spatio-temporal scales (0.25° degrees and 9 days) of SSS estimates for this area.

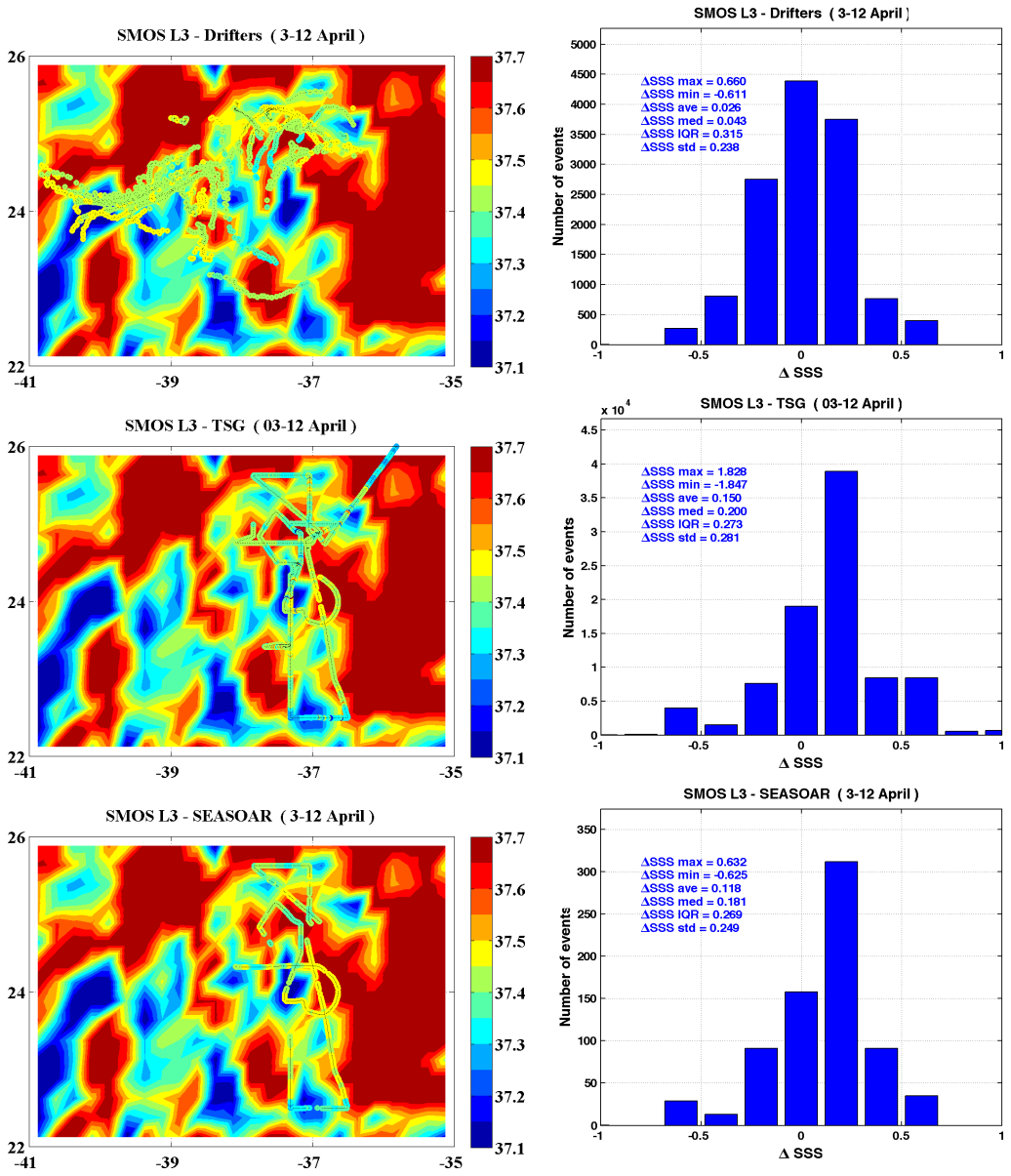

Figure 3.30: ***Left column****: Background image: Near surface salinity in the SPURS area as measured by SMOS L3 at 1-2 cm depth. From top to bottom, overimposed: drifters at 50 cm depth, onboard alongtrack TSG at 4 m depth and SeaSoar undulating CTD at 15 m depth; all data are adquired in the period running since 3 to 12 of April 2012.* ***Right column****: Histograms of the difference: SMOS L3 vs drifters (top), TSG (middle) and SeaSoar undulating CTD (bottom) for the same period 3-12 of April 2012.*

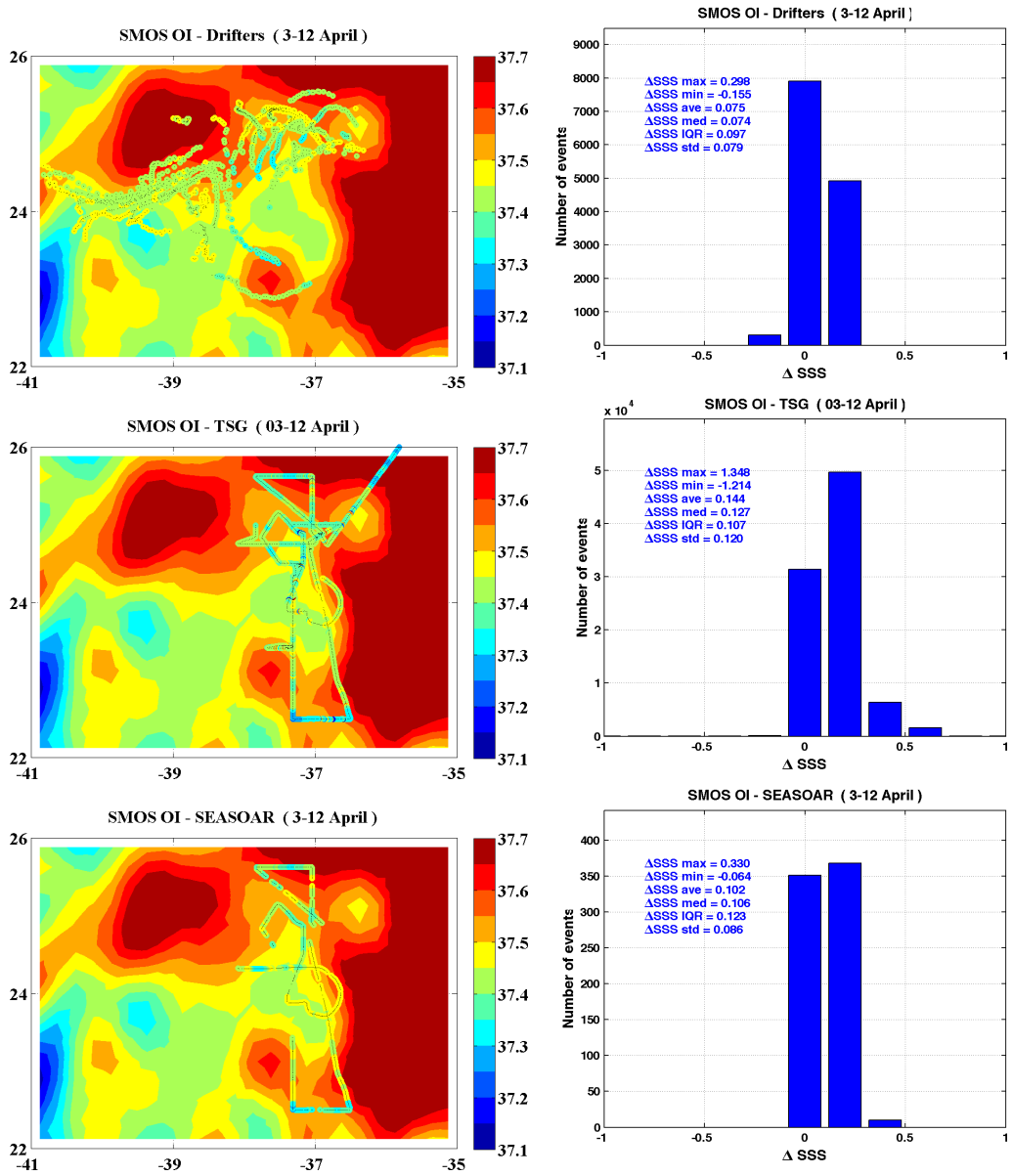

Figure 3.31: ***Left column****: Background image: Near surface salinity in the SPURS area as measured by SMOS OI at 1-2 cm depth. From top to bottom, overimposed: drifters at 50 cm depth, onboard alongtrack TSG at 4 m depth and SeaSoar undulating CTD at 15 m depth; all data are adquired in the period running since 3 to 12 of April 2012.* ***Right column****: Histograms of the difference: SMOS OI vs drifters (top), TSG (middle) and SeaSoar undulating CTD (bottom) for the same period 3-12 of April 2012.*

Chapter 4

Multifractal synergy between different variables

In this chapter we present a new approach for combining two ocean variables to create Level 4 (L4) remote sensing maps. The method introduced here exploits the theoretical correspondence between the singularity exponents associated with the variables to be merged. A singularity exponent is a dimensionless variable that characterizes the sharpness or regularity of the spatial variation of the scalar around a given point.

As it will be shown, the multifractal fusion allows to reduce the noise level on the signal to be restored. On the other hand, this method can also be used for gap filling of an incomplete field, efficiently exploiting the correlation between ocean variables. The method introduced here has several important advantages: it is not parametric (no need of parameter tuning), is instantaneous (so no learning of a time series is implied), requires no underlying numerical model and is not time nor data demanding. In this chapter, we will present the method, discussing its features and capabilities. At the end of the chapter we address the response of the method to the noise of the input variable.

4.1 Ocean turbulence and advected tracers

Chaos Theory deals with nonlinear phenomena that are extremely difficult to predict or control due to the large number of involved degrees of freedom. Examples of chaotic systems include ocean turbulence, the weather, stock market, brain activity, and so on. These phenomena are often described using fractal or multifractal geometries, which capture an essential ingredient of the infinite complexity of Nature. Fractals are sets of points (Figure 4.1) originated by chaotic equations and which typically contain self-similar patterns of complexity, which can be found (either in an affine way or statistically) at any observation scale. Thus, if you divide a fractal set into parts you get a nearly identical, reduced-size copy of the whole. Multifractal is a scale-free or scale-invariant system, this means that the statistical properties of of small-regions are self similar to those of the whole system. In other words, a system is multifractal if it can be split into different fractal components, each one characterized by having a specific scale-invariant physical structure. To see how a fractal variable behaves under changes of scale, a single exponent (the fractal dimension) is needed, while as a multifractal is formed by a hierarchy of multiple fractals,

Part of the results presented in this chapter are included in the following papers: ***Turiel, A., Isern-Fontanet, J., Umbert, M., 2014. Sensibility to noise of new multifractal fusion methods for ocean variables. Nonlinear Processes in Geophysics, in press.***

Olmedo, E., Martinez, J., Umbert, M., Hoareau, N., Portabella, M., Ballabrera-Poy, J. and Turiel, A., 2015. Improving time and space resolution of SMOS saliniy maps using multifractal fusion. Special Issue on SMOS in Remote Sensing of Environment, under revision.

all their dimensions (singularity spectrum) are needed to characterize how the system evolves under changes of scale (Pont et al., 2009).

Fractal organization is fully compatible with the behavior observed in turbulent fluids as they react to external energy inputs (differential Sun heating, wind pulses, pressure gradients) by forming structures that self-repeat at different scales forming a cascade of energy that ends with dissipation and degradation as heat at molecular scales. The study of physical oceanography phenomena is however mainly based on the traditional movement equations based on Newton's second law, witch characterize turbulent behavior as an analogy to molecular diffusion, with empirical parameters that define the turbulent fluid. This strategy allows to characterize the general ocean circulation, but it is not enough to be fully characterize and understand turbulent flows.

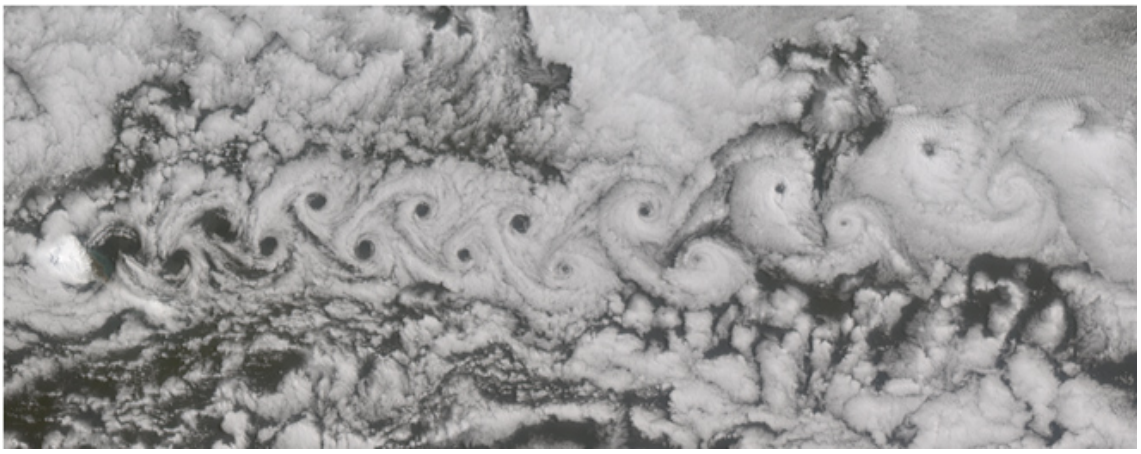

Figure 4.1: Marine stratus clouds seen by the Aqua/MODIS satellite over the South Atlantic Ocean off the west coast of Africa. Jeff Schmaltz, NASA Earth Observatory.

Remote sensing imagery of the ocean surface provides a synoptic view of the complex geometry of filaments and vortices spawning and being advected by the turbulent oceanic flow. The repeated observation of such structures show that ocean circulation is dominated by mesoscale variability (space scales of 50-500 km, time scales of 10-100 days, and currents of a few km/h). Ocean structures can be associated with many different processes (frontogenesis and eddy generation (Hallberg and Gnanadesikan, 2006), eddy propagation (Isern-Fontanet et al., 2003; Chelton et al., 2007), variations in sea roughness, upwelling (Mason et al., 2011), etc.), and have been repeatedly shown to leave a recognizable footprint in many different variables. This common footprint is the result of the nonlinear advection terms in the evolution equations within the equations defining the evolution of ocean scalars (such as sea surface temperature (SST), sea surface salinity (SSS), chlorophyll concentration (CC), absolute dynamic topography (ADT), etc.), even if those non-linear terms are not the dominant contribution (in terms of relative amplitude) to the dynamics of the particular scalars. This common signature in ocean scalars indicates that a part of the information conveyed by the different ocean variables is in fact redundant.

4.2 Multifractal formalism and singularity exponents

New techniques for analyzing the structure of remote sensing maps of ocean variables have been developed during recent years. These techniques have been designed in the framework of the Multifractal Microcanonical Formalism (MMF) (Turiel and Parga, 2000; Turiel et al., 2008b), and are appropriate for dealing with scalars submitted to the action of a chaotic turbulent flow. They represent a new approach to turbulence analysis, based on the geometrical organization of the flow, that intend to characterize local scaling properties at each point of the turbulent flow.

The spatial structure of any tracer advected by the oceanic flow inherits certain properties of the underlying flow dynamics. In turbulent flows , the chaotic almost scale-free organization of the velocity field leads to sharp transitions and singular fronts (Frisch, 1995). This is due to the interaction between coherent vortices that continuously stretch and fold small-scale filaments ejected from vortex cores, generating small-scale gradients between eddies. This leads to the keystone of the MMF: the singularity analysis; in this framework, the fluid can be understood as a hierarchical arrangement of different fractal sets, each one with its own fractal dimension and characterized by a particular value of the singularity exponent $h(\vec{x})$. The existence of scaling properties of scalars submitted to specific types of turbulent flow can be traced back to Kolmogorov's seminal works (Kolmogorov, 1941b,a), lately generalized to different scalars and non-linear scaling laws (She and Leveque, 1994; She and Waymire, 1995).

Singularity analysis allows to characterize each point of an ocean field according to its singularity exponent $h(\vec{x})$. The singularity exponent is a dimensionless variable which characterizes the sharpness or regularity of the variation of the scalar around that given point. In a multifractal signal, s, the behavior around any point $\vec{x}$ is described by a local power law:

$$\frac{1}{r}|s(\vec{x}+r) - s(\vec{x})| \sim r^{h(\vec{x})} \tag{4.1}$$

The local singularity exponent $h(\vec{x})$ of a given signal $s(\vec{x})$ can be estimated for any scale or resolution r. The singularity exponents can be classified from the most singular (negative values), associated with the sharpest transitions, to the least singular (postive values), associated with smooth transitions. The values of the $h(\vec{x})$ typically fall in the range (-1,2) (no units).

Equation 4.1 is easy to compute and relate intuitively to the properties of the flow. However, long-range correlations can mask the largest singularity exponents; thus the signal $s(\vec{x})$ needs to be previously filtered using wavelet projections. Moreover, working with the modulus of the gradient of the signal has been found to improve the spatial resolution of the determination of the singularity exponents $h(\vec{x})$ (Turiel and Pérez-Vicente, 2005; Turiel et al., 2006).

Therefore, given a signal s, its singularity exponents can be estimated from the wavelet projections of the gradient of the signal. Given a wavelet ψ, we define the wavelet projection of s at a given point $\vec{x}$ and for a given scale r, denoted by $T_\psi|\nabla s|(\vec{x},r)$, as:

$$T_\psi|\nabla s|(\vec{x},r) = \int d\vec{y}\,|\nabla s|(\vec{y})\,\frac{1}{r^2}\,\psi\left(\frac{\vec{x}-\vec{y}}{r}\right). \tag{4.2}$$

The wavelet projection is the convolution of the wavelet with the gradient of the signal s. The wavelet projection (Eq. 4.1) averages the gradient content around the point $\vec{x}$ at a distance

modulated by r. The dispersion of the wavelet can be increased or reduced by increasing or reducing the scale r. The signal s is multifractal, has a singularity exponent $h(\vec{x})$ at a given point $\vec{x}$ if the following relation holds:

$$T_\psi|\nabla s|(\vec{x},r) = \alpha(\vec{x})r^{h(\vec{x})} + o\left(r^{h(\vec{x})}\right), \tag{4.3}$$

where $\alpha(\vec{x})$ is the amplitude factor, and the term $o\left(r^{h(\vec{x})}\right)$ is negligible in comparison with $r^{h(\vec{x})}$ when the scale r goes to zero. Thus, the dependency on the scale parameter, r, is a power law of exponent $h(\vec{x})$, meaning that the system is scale invariant. The multiplicative term $\alpha(\vec{x})$ depends on the particular functional $T_\psi|\nabla s|(\vec{x},r)$ chosen, but $h(\vec{x})$ is independent of it (Turiel et al., 2008b). For that reason, the singularity exponents are the most informative part of the decomposition above. The singularity exponent $h(\vec{x})$ at the point $\vec{x}$ can be computed by performing a linear regression between $\ln(T_\psi|\nabla s|(\vec{x},r))$ and $\ln(r)$. It has been found that the most efficient wavelets to obtain good discrimination and resolution are the Lorentzian family: $\Psi_{\gamma(\vec{x})} = 1/(1+|\vec{x}|^2)^\gamma$ (Pont et al., 2013a). We use the numerical implementation of $\Psi_{\gamma=1}$ for the results presented in this manuscript.

The existence of a multifractal structure in synoptic maps of ocean scalars has been searched for several years now. There exist extensive evidences that singularity fronts can be extracted from SST maps of different types and resolutions (Turiel et al., 2005b, 2008a). It has been also observed that other scalars, such as chlorophyll concentration (Lovejoy et al., 2001b; Nieves et al., 2007; Montera et al., 2011) and brightness temperature (Isern-Fontanet et al., 2007) present the same multifractal structure, which can be put into correspondence among the different scalars. In fact, the multifractality of several oceanic fields (temperature, chlorophyll concentration) has been established by various studies based on in situ measurements (Seuront et al., 1996a,b, 1999). The emergence of such a singular structure is the result of the advective forces acting on a quasi-2D turbulence regime, and can be thus observed for scales ranging from kilometers to the planetary scale.

Singularity exponents arise due to differential shear in the flow, and thus they are characteristic to the velocity field, and not specific to the advected scalar. A correspondence between multifractal patterns of SST and the flow structures is found by Isern-Fontanet et al. (2007); it is reportedly a consequence of the establishment of a multiplicative cascade of the scalar analogous to the energy cascade of the flow due to the fully developed turbulent regime (Parisi and Frisch, 1985). Experiments with data from numerical simulations and from remote sensing sensors show that singularity exponents are almost independent of the scalar and related to the flow structure, even more, singularity lines align with the streamlines of the flow (Turiel et al., 2009). For that reason the singularity exponents of different scalars are expected to be the same. This is the basis of the proposed fusion method.

4.3 Correlation between ocean variables

4.3.1 Relationship between Salinity and Temperature: Density of seawater

Establishment the temperature-salinity relation in the ocean water masses is of major importance for understanding ocean circulation. Temperature and salinity determine density of sea water, and changes in density is, together with winds, a driver of the ocean circulation. Density is defined as the mass per unit of volume. In oceanography, nevertheless, it is more common to use the specific density (ratio of the density of a sample of water compared to the density of the distilled water at a temperature 4°C, which by definition has a density of 1 g/cm^3).

Seawater density depends on temperature, salinity and, due to the slightly compressibility of water, also to pressure. The density of seawater is higher than that of pure water due to the presence of dissolved salts. At the sea surface, the average density of the seawater is equal to 1.025 g/cm^3 (notice that we are neglecting the changes in pressure associated with the atmosphere, taking a standard atmospheric pressure of 1 atmosphere or 10^5 pascals). The density of the sea surface is modified at the surface by two distinct processes: heat fluxes (heating and cooling, which changes the temperature), and the precipitation/evaporation balance (which changes the salinity). In many oceanic regions these two density modifying processes work contrarily to one another (Stommel, 1961).

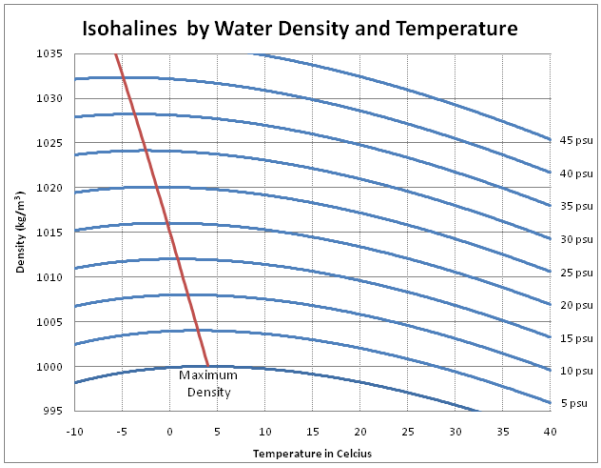

Figure 4.2: Isohalines by Water Density and Temperature.

The dependency of density to temperature changes is complex (Figure 4.2). The effect of increasing salinity on the density of seawater is always to increase it. This increase in density is due to two factors: i) a saline contraction (the ions of salt electrostatically coordinate with the polar molecules of water, creating ionic bonds) and ii) an increase of the average molecular weight, as the molecular weights of salt ions are greater than that of the water molecule.

Studies of temperature and salinity relationship have focused in the asymmetry in the molecular diffusion of heat and salt (Schmitt, 1994). However, double diffusion is unlikely to be important in the mixed layer where mechanical mixing is really strong. A measure of the relative effect of temperature and salinity changes on density is the density ratio:

$$R = \frac{\alpha \Delta \theta}{\beta \Delta S}, \tag{4.4}$$

defined as the ratio between the effect of a temperature change on density divided by the effect of a salinity change. For example, when a front separates cold and fresh waters from warm and salty waters, $\Delta\theta$ and ΔS have opposite effects on density. The horizontal front is said to be compensated if it has a density ratio of 1. A front where the effect of temperature on density doubles that of salinity will also be a density front and will have a density ratio of 2.

Density compensation is a situation where temperature (T) and salinity (S) gradients tend to cancel each other so that their effect on density is as much compensated as possible. Scientific literature suggests that horizontal gradients at ocean surface tend to be density compensated over a range of spatial scales. Density compensation has been observed on large scales for decades (Rodex, 1975; Niller and Reynolds, 1984).

More recently, high resolution observations have revealed compensation down to scales of tens of meters (Rudnick and Ferrari, 1999; Schmitt, 1999; Ferrari and Rudnick, 2000; Rudnick and Martin, 2002; Johnson, 2006). As $\Delta\theta$ and ΔS tend to have a compensated effect on density, both variables may vary along a surface of constant density. This variability, called spiciness, is a result of air-sea fluxes, turbulent mixing and advection and produces a horizontal mixing in the mixed layer that depends on density gradient. The mixed layer is a layer at the ocean surface that is relatively vertically uniform in properties such as temperature and salinity. The turbulence that mixes this layer mainly results from wind stirring and surface cooling.

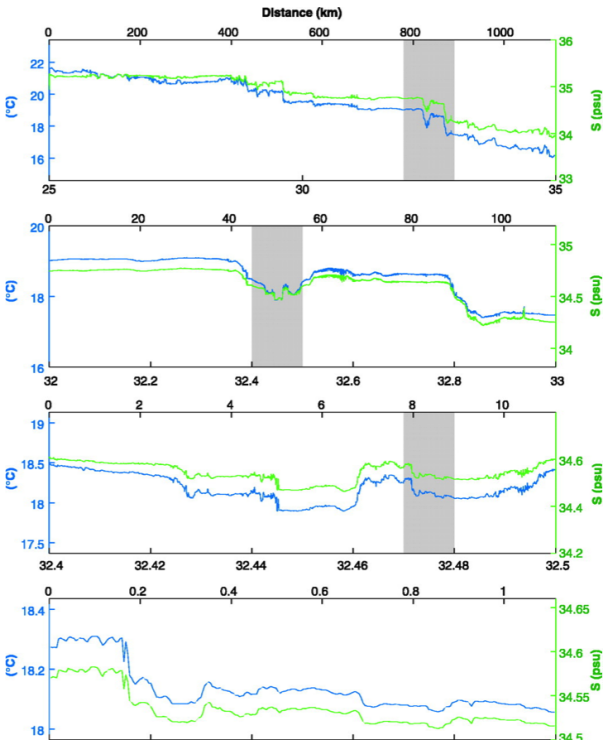

Figure 4.3: Potential temperature θ and salinity S at 50 dbar. D L Rudnick, and R Ferrari Science 1999;283:526-529

Figure 4.3 shows potential temperature θ and salinity S at 50 dbar measured by SeaSoar in the subtropical gyre of North Pacific (as shown in Rudnick and Ferrari (1999)). Each successive panel is a magnification by a factor of 10 of the shaded region of the panel above. The vertical axes are scaled by the thermal and haline expansion coefficients so that a variation of the same apparent amplitude in temperature and in salinity imply identical effects on density. Temperature and salinity structures are compensated at all scales.

A regulating mechanism for temperature and salinity in the mixed layer was suggested by Stommel (1993). The horizontal diffusivity in the mixed layer is proportional to the density gradient squared. Young (1994) and Ferrari and Young (1997) suggest that compensation is the result of the selective diffusion of horizontal density gradients. This happens because the combined action of unbalanced motions and vertical mixing rapidly removes density gradients but leaves behind compensated temperature and salinity gradients. Density fronts are diffused whereas compensated fronts persist. The mixing driven by density gradients is symmetric with respect to temperature and salinity, and it is responsible for the tight correlation between fronts in the two tracers.

4.3.2 Correspondence between singularity exponents of SST and SSS

Singularity analysis provides a scheme to characterize the presence of ocean structures in different oceanic variables. Moreover, as singularity exponents are dimensionless variables, they allow a direct comparison among the structures detected in different ocean variables. As we have discussed in the previous sections, the isolines associated with the singularity exponents of SSS and SST should be coincident. This can be verified by direct comparison of the singularity exponents obtained from any remote sensing source of SST data and those obtained from SMOS SSS maps. However, satellite SSS data are still affected by many processing issues that greatly increase the error in the signal; henceforth, the singularity exponents retrieved from satellite SSS maps have low quality. We have then used an alternative strategy to assess if the assumed correspondence between SSS and SST singularity exponents actually holds.

We have used model data to check if the hypothesis of correspondence between singularity exponents holds. We have thus analyzed the outputs of Ocean general circulation model For the Earth Simulator (OFES) (Masumoto et al., 2004), which is a high-quality simulation with appropriate grid spacing (1/10 degree) for our purposes. In Figure 4.4 we present one selection of SST and SSS maps taken from OFES outputs, and their associated singularity exponents.

The maps of the singularity exponents associated with SST and SSS delineate the same structures; structures that, as in (Turiel et al., 2008a), correspond quite accurately with the streamlines of the velocity field, shown in the bottom of Figure 4.4. This implies that on a levelset of singularity exponents for SST (where the value of the singularity exponent is constant) the value of singularity exponents of SSS is also constant, although not necessarily the same: this value could even be different on the different connected parts of the levelset (the isolines).

We define the histogram of singularities of SSS conditioned by a value h_0 of the singularity of SST, denoted by $\rho(h_{SSS}|h_{SST} = h_0)$ namely:

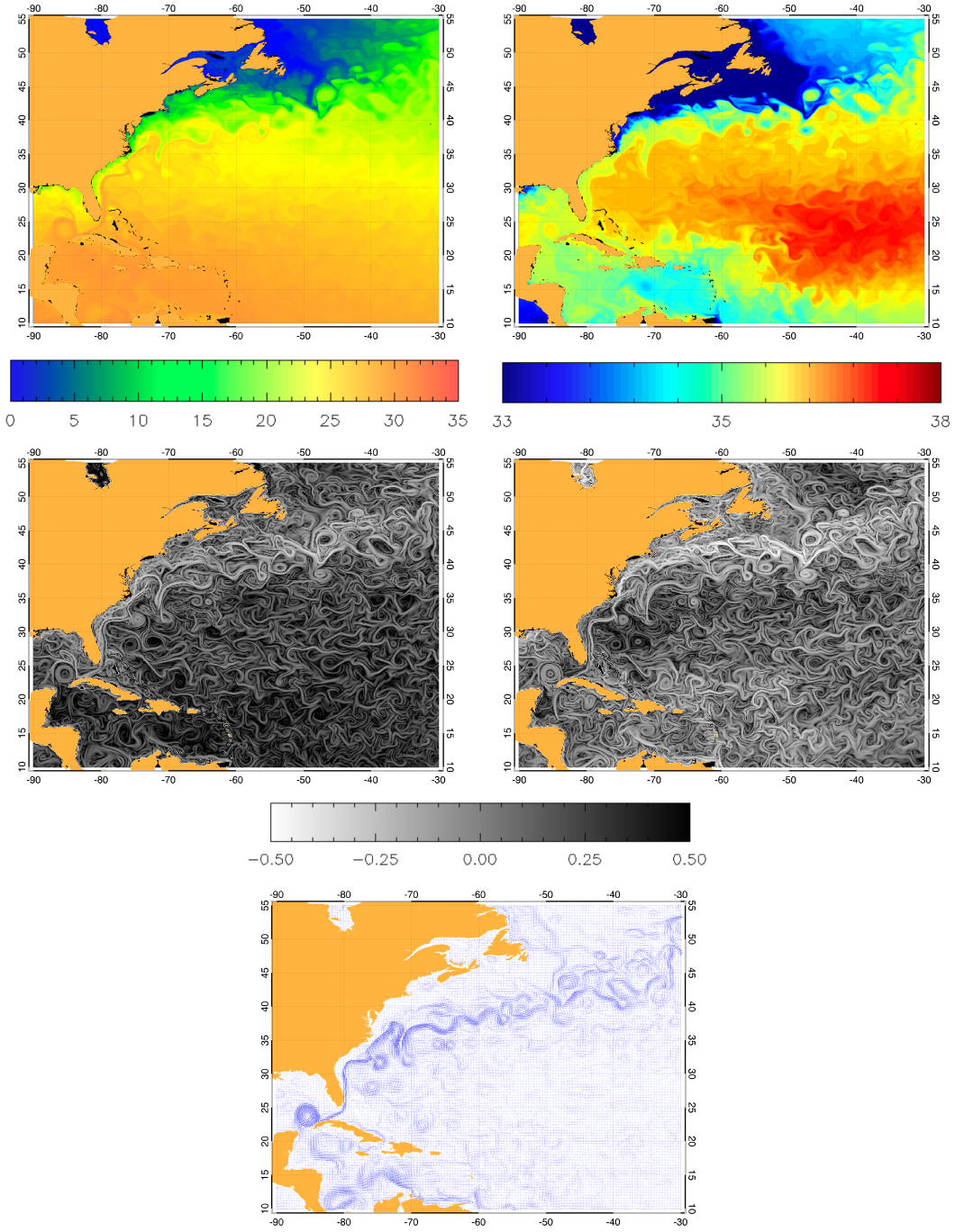

Figure 4.4: **Top:** *OFES output SST (left) and SSS (right) maps for January 1st, 1990.* **Middle:** *Associated singularity exponents.* **Bottom:** *Horizontal velocity field at surface layer*

$$\rho(h_{SSS}|h_{SST} = h_0) \;=\; \frac{\rho(h_{SST} = h_0, h_{SSS})}{\rho(h_{SST} = h_0)} \tag{4.5}$$

where $\rho(h_{SST}, h_{SSS})$ is the joint histogram of both variables and $\rho(h_{SST})$ is the histogram for the values of singularity exponents of SST only. For each value h_0 we have a different histogram, so at the end we have a 2D array, shown in Figure 4.5, middle. For comparison, the histogram of SSS conditioned by SST is shown in the top panel of the same figure. The results correspond

to a single day of OFES but similar results are obtained for any other day.

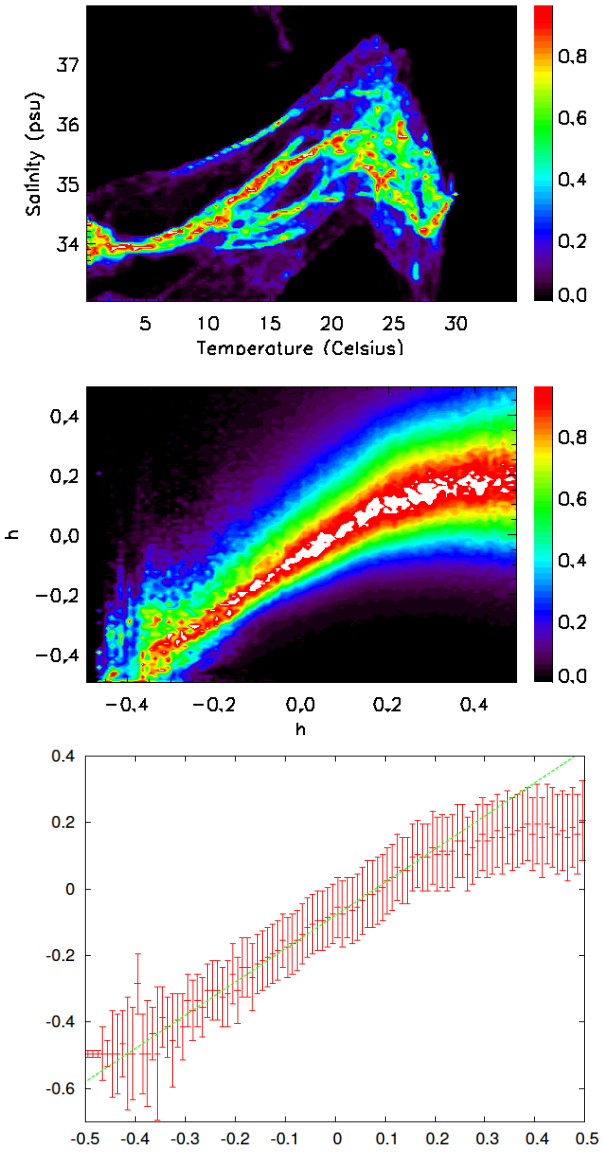

Figure 4.5: Histograms of a variable related to SSS conditioned by the value of the associated variable related to SST from the OFES simulation for the whole globe on January 1st, 1990. For each column of the histogram the value of the SST-related variable is fixed, so the values in that column represent the distribution of probability of values of the SSS-related variable for that fixed value of the SST-related variable. To enhance visualization, in this figure the histogram is normalized by its maximum probability at each row (so the maximum is always 1 for each row). ***Top:*** *SSS conditioned by SST.* ***Middle:*** *h_{SSS} conditioned by h_{SST} (middle).* ***Bottom:*** *Modal line (line joining the maximum probability) for the histogram of h_{SSS} conditioned by h_{SST}; the error bars are given by the standard deviation of h_{SSS} conditioned by h_{SST}, with a typical value of 0.15, similar to the numerical accuracy of our method for singularity analysis, 0.10 (Turiel et al., 2006). The green line is given as a visual reference, approximately following the modal line in the center of the range; it is given by the expression $h_{SSS} = h_{SST} - 0.08$.*

The histogram of SSS conditioned by SST shows that there is not a general function relating SSS with SST valid for all the ocean. The histogram looks like a superposition of different, narrow straight lines indicating that, regionally, there exist strong functional dependencies between

SSS and SST, but those relations change from one region to another. On the contrary, the histogram of SSS singularity exponents conditioned by the SST singularity exponents shows that the functional dependency is highly consistent and the same all over the ocean. In fact, the maximum probability line (modal line) is a straight line of slope 1 for the majority of the range of h_{SST}, deviating slightly by the end of the described range, where the errors in the determination of the singularity exponent are expected to be larger (Turiel et al., 2006). Deviations seem also important at the beginning of the range, but this is just an effect associated with the lack of statistics for a single snapshot and gets improved when multiple snapshot statistics is considered.

From the conditioned histogram we can obtain the conditioned average and the conditioned standard deviation, what translates to the following relation: $h_{SSS} = h_{SST} - 0.08 \pm 0.15$. The range of uncertainty (0.15) is comparable with the accuracy of our method for singularity analysis, about 0.10 (Turiel et al., 2006). Regarding the slight observed bias of about 0.08, it may be related to particularities of the diffusive scheme used in OFES that may render SST smoother than SSS. Specific additional research is required to clarify this issue.

These results show that, in a good extent, the singularities of SST and SSS correspond. In the following sections we are going to assume that $h_{SSS} = h_{SST}$ and try to extract all the theoretical consequences of this hypothesis.

4.4 Theoretical basis of the fusion algorithm

As we have already seen, the values of the singularity exponents of SSS and SST maps from a numerical model are shown to correspond over large areas. This correspondence implies that both variables can be linked by a functional relation.

Let us suppose that we have two different ocean variables measured by remote sensing, s being the *signal* and θ being the *template* (which is considerably a less noisy and a more reliable source of information), such that both are multifractal in the microcanonical sense, as discussed in Section 4.2. It is also assumed that both scalars have the same singularity exponents at all the points as previously discussed. According to Eq. 4.3, we can write:

$$\begin{aligned} T_\Psi|\nabla s|(\vec{x},r) &= \alpha_s(\vec{x})\, r^{h(\vec{x})} + o\left(r^{h(\vec{x})}\right) \\ T_\Psi|\nabla \theta|(\vec{x},r) &= \alpha_\theta(\vec{x})\, r^{h(\vec{x})} + o\left(r^{h(\vec{x})}\right) \end{aligned} \tag{4.6}$$

The expression above is valid for any wavelet Ψ, and even scaling functions (functions with non-zero integral, contrarily to what is required to standard wavelets Mallat (1999)) can be used if we are just interested in analyzing the signal, not in representing it. There is a particular case of interest, consisting in taking $\Psi = \chi_{B_1}$, that is, the set function of the ball of radius 1 - such a function simply equals 1 on that ball and 0 outside. Then,

$$\int_{B_r(\vec{x})} d\vec{x}'\, |\nabla s|(\vec{x}') = \beta_s(\vec{x})\, r^{h(\vec{x})} + o\left(r^{h(\vec{x})}\right) \tag{4.7}$$

and analogously for θ. That is, when the gradient modulus of s is integrated in the ball of radius

r centered on $\vec{x}$ we observe the same type of scaling property. If we define the multifractal measures associated with s and θ (Turiel et al., 2008b) as:

$$\begin{aligned} d\mu_{|\nabla s|}(\vec{x}) &= dx|\nabla s|(\vec{x}) \\ d\mu_{|\nabla \theta|}(\vec{x}) &= dx|\nabla \theta|(\vec{x}) \end{aligned} \tag{4.8}$$

then Eq. (4.7) states that the measure $\mu_{|\nabla s|}$ of balls of radius r centered around $\vec{x}$ scales as $r^{2+h(\vec{x})}$:

$$\mu_{|\nabla s|}(B_r(\vec{x})) \;=\; \beta_s(\vec{x})\, r^{2+h(\vec{x})} \;+\; o\left(r^{2+h(\vec{x})}\right) \tag{4.9}$$

and analogously for $\mu_{|\nabla \theta|}$. If the singularity exponents of both measures coincide at every point, then the measure $\mu_{|\nabla s|}$ is absolutely continuous (Rudin, 1987) with respect to $\mu_{|\nabla \theta|}$ and conversely. That is, any collection of sets (A_n) with decreasing measure according to $\mu_{|\nabla s|}$ are also decreasing according to $\mu_{|\nabla \theta|}$ and conversely, i.e.,

$$\mu_{|\nabla s|}(A_n) \to 0 \;\Leftrightarrow\; \mu_{|\nabla \theta|}(A_n) \to 0 \tag{4.10}$$

The formulas above say that when a set has a very small measure according to $\mu_{|\nabla s|}$, then it has also a very small (although not coincident) measure according to $\mu_{|\nabla \theta|}$, and conversely. This means that, with an adequate approximation (which is better as the set is smaller), one measure is proportional to the other. Absolute continuity means that, in essence, both measures can be locally related by a linear relation, but this relation depends on the point under consideration.

This can be expressed in a more rigorous, mathematical way, by making use of the Riesz's representation theorem (Rudin, 1987). We express that proportionality relation in the limit of set size going to zero, therefore:

$$d\mu_{|\nabla s|}(\vec{x}) \;=\; \Phi(\vec{x})\, d\mu_{|\nabla \theta|}(\vec{x}) \tag{4.11}$$

where $\Phi(\vec{x})$ is the so-called Radon-Nikodym derivative (Rudin, 1987) of the measure $\mu_{|\nabla s|}$ with respect to $\mu_{|\nabla \theta|}$. By construction, the Radon-Nikodym derivative must be a Borelian function. This fact implies that it is continuous almost everywhere. $\Phi(\vec{x})$ is not an arbitrary function but one that varies smoothly enough in space. It follows that:

$$|\nabla s|(\vec{x}) \;=\; \Phi(\vec{x})\, |\nabla \theta|(\vec{x}) \tag{4.12}$$

So that, the modulus of the gradients of both functions are not equal, but can be related by the function $\Phi(\vec{x})$ which is smooth, in the sense that has not sharp transitions: those transitions are coded in the gradients of s and θ and are responsible of the singularity exponents $h(\vec{x})$; as both scalars have the same singularity exponents, $\Phi(\vec{x})$ cannot introduce new transitions and must be a smooth, slowly varying function. If that was not the case, $\Phi(\vec{x})$ would be a source of singularity, and the singularity lines of s and θ would differ.

Equation 4.12 is appealing but hard to use in practice. It would be more convenient if we could relate the gradients instead of the modulus of the gradients. In fact, we could have defined vector-valued measures $\mu_{\nabla s}$ and $\mu_{\nabla \theta}$ in the following way:

$$\begin{aligned} d\mu_{\nabla s}(\vec{x}) &= dx \nabla s(\vec{x}) \\ d\mu_{\nabla \theta}(\vec{x}) &= dx \nabla \theta(\vec{x}) \end{aligned} \tag{4.13}$$

It follows that their scalar, positive counterparts are the absolute variations of these measures, namely

$$\begin{aligned} \| \mu_{\nabla s} \| &= \mu_{|\nabla s|} \\ \| \mu_{\nabla \theta} \| &= \mu_{|\nabla \theta|} \end{aligned} \tag{4.14}$$

Notice that the absolute variation of a measure is not obtained by just taking the modulus of its value over Borelian sets but rather a positive measure that strictly bounds that modulus. We have once again that $\mu_{\nabla s}$ and $\mu_{\nabla \theta}$ are absolutely continuous the one with respect to the other (what is a consequence of having the same property of absolute continuity for its absolute variations). The vectorial version of Riesz's representation theorem is now:

$$\nabla s(\vec{x}) \;=\; \Phi(\vec{x})\, \nabla \theta(\vec{x}), \tag{4.15}$$

where Φ is now a 2×2 smooth matrix. Let us recall it once more: this strong functional relation between the gradients of s and θ is a direct, unavoidable consequence of the correspondence of singularity exponents of s and θ. Also recall that the matrix $\Phi(\vec{x})$ must be slowly varying (that is, has small gradient).

4.4.1 Matrix approach

Let us now analyze the matrix $\Phi(\vec{x})$. Remember that $\Phi(\vec{x})$ must have a more regular behavior than both multifractal measures, as its inclusion should not generate any additional singularity exponents (since the singularities of both measures coincide).

From Eq. 4.15 we express the matrix relation $\Phi(\vec{x})$ between the gradients of signal s and template θ in a given coordinate system (x,y), which naturally correspond to longitude and latitude:

$$\begin{aligned} \partial_x s &= \phi_{xx} \partial_x \theta + \phi_{xy} \partial_y \theta + \epsilon_x \\ \partial_y s &= \phi_{yx} \partial_x \theta + \phi_{yy} \partial_y \theta + \epsilon_y \end{aligned} \tag{4.16}$$

where $\nabla \theta = (\partial_x \theta, \partial_y \theta)$ and $\nabla s = (\partial_x s, \partial_y s)$, with:

$$\Phi(\vec{x}) = \begin{pmatrix} \phi_{xx} & \phi_{xy} \\ \phi_{yx} & \phi_{yy} \end{pmatrix} \tag{4.17}$$

To invert the matrix $\Phi(\vec{x})$, we want to minimize the norm of the error vector $\vec{\epsilon} = (\epsilon_x, \epsilon_y)$, so we define a cost function $E[\mathbf{\Phi}]$ as:

$$E[\mathbf{\Phi}] \;=\; \langle(\partial_x s - \phi_{xx}\partial_x\theta - \phi_{xy}\partial_y\theta)^2\rangle \;+\; \langle(\partial_y s - \phi_{yx}\partial_x\theta - \phi_{yy}\partial_y\theta)^2\rangle \tag{4.18}$$

where the average $\langle\cdot\rangle$ is taken over a local neighborhood of the point of interest with a giving weighting function, typically decaying with the distance to that point (the weighting function used is presented in next section 4.4.3). In order to minimize $E[\mathbf{\Phi}]$ the derivatives with respect to all the elements of $\mathbf{\Phi}$ must cancel so we have:

$$\left\{\begin{array}{rcrcrcrcr}
0 &=& \partial_{\phi_{xx}}E &=& -2\langle\partial_x s\partial_x\theta\rangle &+& 2\phi_{xx}\langle\partial_x\theta^2\rangle &+& 2\phi_{xy}\langle\partial_x\theta\partial_y\theta\rangle \\
0 &=& \partial_{\phi_{xy}}E &=& -2\langle\partial_x s\partial_y\theta\rangle &+& 2\phi_{xx}\langle\partial_x\theta\partial_y\theta\rangle &+& 2\phi_{xy}\langle\partial_y\theta^2\rangle \\
0 &=& \partial_{\phi_{yx}}E &=& -2\langle\partial_y s\partial_x\theta\rangle &+& 2\phi_{yx}\langle\partial_x\theta^2\rangle &+& 2\phi_{yy}\langle\partial_x\theta\partial_y\theta\rangle \\
0 &=& \partial_{\phi_{yy}}E &=& -2\langle\partial_y s\partial_y\theta\rangle &+& 2\phi_{yx}\langle\partial_x\theta\partial_y\theta\rangle &+& 2\phi_{yy}\langle\partial_y\theta^2\rangle
\end{array}\right. \tag{4.19}$$

from where we obtain:

$$\begin{pmatrix} \langle\partial_x s\partial_x\theta\rangle \\ \langle\partial_x s\partial_y\theta\rangle \\ \langle\partial_y s\partial_x\theta\rangle \\ \langle\partial_y s\partial_y\theta\rangle \end{pmatrix} = \begin{pmatrix} \langle\partial_x\theta^2\rangle & \langle\partial_x\theta\partial_y\theta\rangle & 0 & 0 \\ \langle\partial_x\theta\partial_y\theta\rangle & \langle\partial_y\theta^2\rangle & 0 & 0 \\ 0 & 0 & \langle\partial_x\theta^2\rangle & \langle\partial_x\theta\partial_y\theta\rangle \\ 0 & 0 & \langle\partial_x\theta\partial_y\theta\rangle & \langle\partial_y\theta^2\rangle \end{pmatrix} \begin{pmatrix} \phi_{xx} \\ \phi_{xy} \\ \phi_{yx} \\ \phi_{yy} \end{pmatrix} \tag{4.20}$$

Let $\mathbf{T}$ be the 2×2 matrix defined by the averages of cross derivatives of θ as:

$$\mathbf{T} \;=\; \begin{pmatrix} \langle\partial_x\theta^2\rangle & \langle\partial_x\theta\partial_y\theta\rangle \\ \langle\partial_x\theta\partial_y\theta\rangle & \langle\partial_y\theta^2\rangle \end{pmatrix} \tag{4.21}$$

If we denote $\mathbf{0}_{2\times2}$ a 2×2 matrix with all zero matrix elements, we have

$$\begin{pmatrix} \phi_{xx} \\ \phi_{xy} \\ \phi_{yx} \\ \phi_{yy} \end{pmatrix} = \begin{pmatrix} \mathbf{T}^{-1} & \mathbf{0}_{2\times2} \\ \mathbf{0}_{2\times2} & \mathbf{T}^{-1} \end{pmatrix} \begin{pmatrix} \langle\partial_x s\partial_x\theta\rangle \\ \langle\partial_x s\partial_y\theta\rangle \\ \langle\partial_y s\partial_x\theta\rangle \\ \langle\partial_y s\partial_y\theta\rangle \end{pmatrix} \tag{4.22}$$

where

$$\mathbf{T}^{-1} \;=\; \frac{1}{\det\mathbf{T}} \begin{pmatrix} \langle\partial_y\theta^2\rangle & -\langle\partial_x\theta\partial_y\theta\rangle \\ -\langle\partial_x\theta\partial_y\theta\rangle & \langle\partial_x\theta^2\rangle \end{pmatrix} \tag{4.23}$$

and $\det\mathbf{T} = \langle\partial_x\theta^2\rangle\langle\partial_y\theta^2\rangle - \langle\partial_x\theta\partial_y\theta\rangle^2$. The estimate of the matrix $\mathbf{\Phi}$ which minimizes the error of reconstructing the gradient of the signal s using the gradient of the template t in the multifractal approximation is thus given by:

$$
\begin{aligned}
\phi_{xx} &= \frac{+\langle\partial_y\theta^2\rangle\langle\partial_x s\partial_x\theta\rangle - \langle\partial_x\theta\partial_y\theta\rangle\langle\partial_x s\partial_y\theta\rangle}{\langle\partial_x\theta^2\rangle\langle\partial_y\theta^2\rangle - \langle\partial_x\theta\partial_y\theta\rangle^2} \\
\phi_{xy} &= \frac{-\langle\partial_x\theta\partial_y\theta\rangle\langle\partial_x s\partial_x\theta\rangle + \langle\partial_x\theta^2\rangle\langle\partial_x s\partial_y\theta\rangle}{\langle\partial_x\theta^2\rangle\langle\partial_y\theta^2\rangle - \langle\partial_x\theta\partial_y\theta\rangle^2} \\
\phi_{yx} &= \frac{+\langle\partial_y\theta^2\rangle\langle\partial_y s\partial_x\theta\rangle - \langle\partial_x\theta\partial_y\theta\rangle\langle\partial_y s\partial_y\theta\rangle}{\langle\partial_x\theta^2\rangle\langle\partial_y\theta^2\rangle - \langle\partial_x\theta\partial_y\theta\rangle^2} \\
\phi_{yy} &= \frac{-\langle\partial_x\theta\partial_y\theta\rangle\langle\partial_y s\partial_x\theta\rangle + \langle\partial_x\theta^2\rangle\langle\partial_y s\partial_y\theta\rangle}{\langle\partial_x\theta^2\rangle\langle\partial_y\theta^2\rangle - \langle\partial_x\theta\partial_y\theta\rangle^2}
\end{aligned}
\tag{4.24}
$$

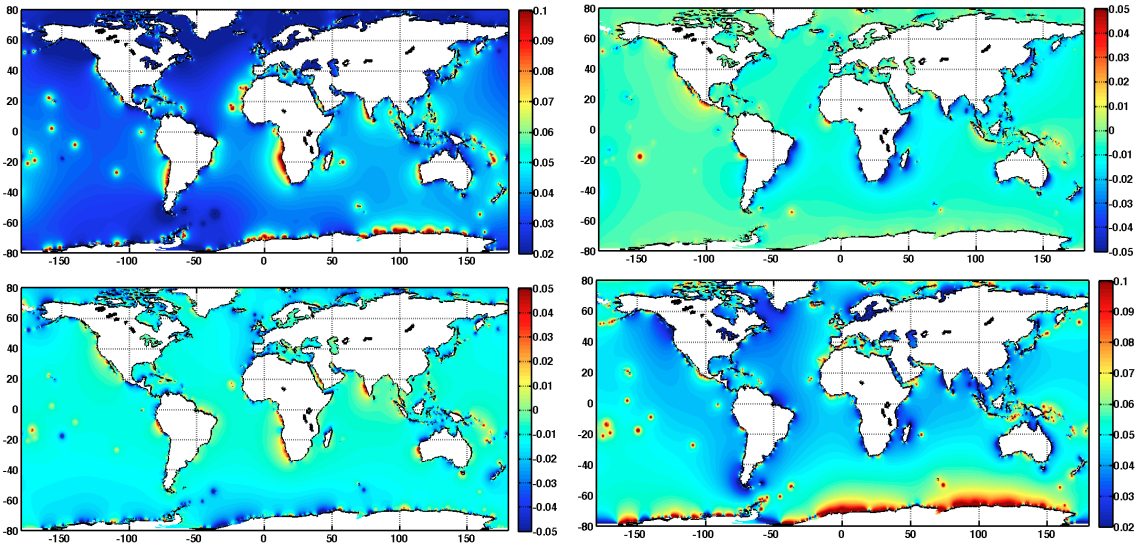

Figure 4.6: Matrix Φ (pss/°C) when SMOS L3 SSS is used as signal and OSTIA SST is used as template; data for day 12 of June of year 2014. ϕ_{xx} (top left), ϕ_{xy} (top right), ϕ_{yx} (bottom left) and ϕ_{yy} (bottom right).

We show in Figure 4.6 the estimates of the matrix $\mathbf{\Phi}$ obtained when Eq. 4.24 is applied by taking SMOS SSS L3 as signal and OSTIA SST as template for a 9-day sample map starting the 12 of June of year 2014. Those estimates are a multifractal regularization of the raw gradients between SST and SSS, and can be used to calculate the gradient of a denoised enhanced version of s, by applying Eq. 4.15: $\nabla\tilde{s} = \mathbf{\Phi}\nabla\theta$. If we apply the matrix approach, Eq. 4.24, to the the gradient of SST template (Figure 4.7 middle), we obtain a new gradient for SSS ($\nabla\tilde{s}$) with a great amount of spatially decorrelated noise removed (Figure 4.7bottom). Compare the amount of noise present in the initial SSS gradient map (compare Figures 4.7top).

The direct reconstruction of the corrected signal $\tilde{s}$ from the estimate of its gradient yields poor results due to problems at the boundaries (i.e. coastlines), as Eq. 4.24 is not valid on such sharp transitions and leads to large values tht corrupt vast areas of the image. In order to express the Eq. 4.15, using the approximation given by Eq. 4.24 in an integral form to avoid these boundary problems, a series of additional simplifications are investigated below.

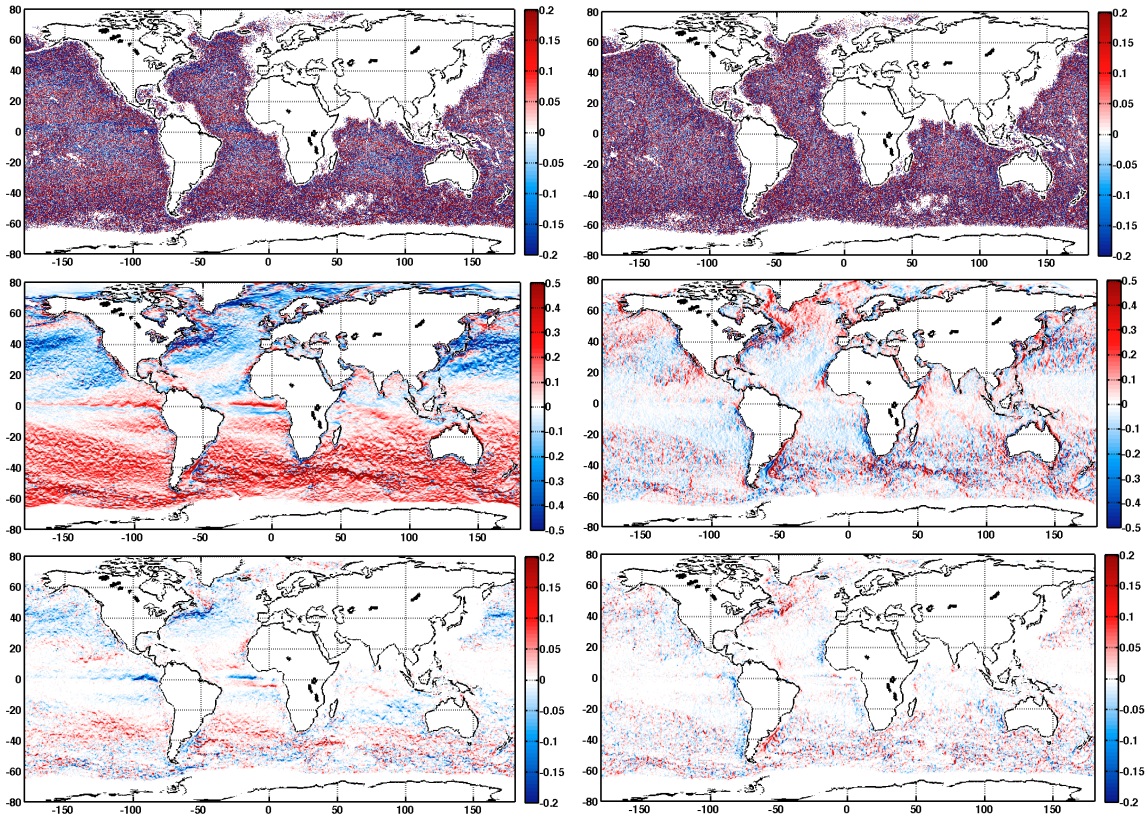

Figure 4.7: Latitudinal (left column) and longitudinal (right column) gradients. ***Top:*** *SMOS L3 SSS.* ***Middle:*** *OSTIA SST (°C) and* ***Bottom:*** *reconstructed SSS gradient from matrix approach.*

4.4.2 Vector approach

We can simplify the matrix relating the template and signal gradients, Eq. 4.15, assuming that the matrix $\mathbf{\Phi}$ corresponds a rotation plus a scaling factor. Then the matrix $\mathbf{\Phi}$ can be represented as a complex number and its action on a vector is just the standard complex multiplication. By representing this complex number by the vector $\vec{\rho}$, Eq. 4.16 becomes:

$$\nabla s(\vec{x}) \;=\; \vec{\rho}\,\nabla\theta(\vec{x}) \;+\; \vec{\epsilon} \tag{4.25}$$

It follows:

$$\begin{aligned} \partial_x s \;&=\; \rho_x\,\partial_x\theta \;-\; \rho_y\,\partial_y\theta \;+\; \epsilon_x \\ \partial_y s \;&=\; \rho_x\,\partial_y\theta \;+\; \rho_y\,\partial_x\theta \;+\; \epsilon_y \end{aligned} \tag{4.26}$$

As before, we want to minimize the error vector $\vec{\epsilon}$, so we define a new cost function $E[\vec{\rho}]$ as:

$$E[\vec{\rho}] \;=\; \langle(\partial_x s - \rho_x\partial_x\theta + \rho_y\partial_y\theta)^2\rangle \;+\; \langle(\partial_y s - \rho_x\partial_y\theta - \rho_y\partial_x\theta)^2\rangle \tag{4.27}$$

In order to minimize $E[\vec{\rho}]$ the derivatives with respect the elements of $\vec{\rho}$ must cancel:

$$\begin{cases} 0 \;=\; \partial_{\rho_x}E \;=\; -\langle\partial_x s\partial_x\theta\rangle \;+\; \rho_x(\langle\partial_x\theta\rangle^2 + \langle\partial_y\theta\rangle^2) \;-\; \langle\partial_y s\partial_y\theta\rangle \\ 0 \;=\; \partial_{\rho_y}E \;=\; -\langle\partial_y s\partial_x\theta\rangle \;+\; \rho_y(\langle\partial_x\theta\rangle^2 + \langle\partial_y\theta\rangle^2) \;-\; \langle\partial_x s\partial_y\theta\rangle \end{cases} \tag{4.28}$$

from where:

$$\begin{aligned}\rho_x &= \frac{+\langle \partial_x s \partial_x \theta \rangle + \langle \partial_y s \partial_y \theta \rangle}{\langle \partial_x \theta \rangle^2 + \langle \partial_y \theta \rangle^2} \\ \rho_y &= \frac{+\langle \partial_y s \partial_x \theta \rangle - \langle \partial_y s \partial_y \theta \rangle}{\langle \partial_x \theta \rangle^2 + \langle \partial_y \theta \rangle^2}\end{aligned} \tag{4.29}$$

This equation is easier to work with Eq. 4.24. In Figure 4.8 we show the components of the vector $\vec{\rho}$ obtained when SMOS SSS L3 is used as signal and SST from OSTIA is used as a template, for the same day as for the matrix approach (14th of June 2014).

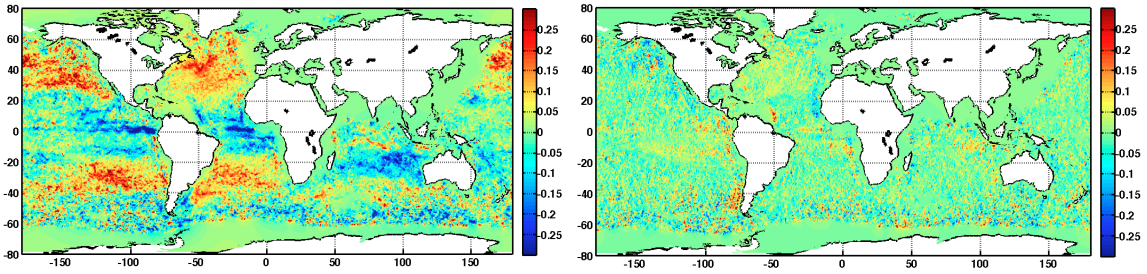

Figure 4.8: Vector relation function between signal and template (psu/°C). ρ_x (left) and ρ_y (right).

The reconstructed gradient (Figure 4.9) from the vector approach displays very similar to the matrix case. The SSS gradient is clearly improving (much less noisy than the gradient of original L3 SSS). However the artifacts induced by the domain boundaries still make unfeasible the direct usage of this expression for denoising purposes of the signal s.

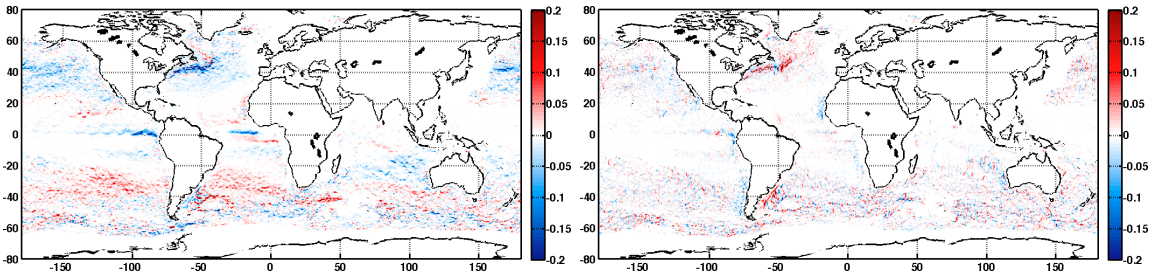

Figure 4.9: Latitudinal (left) and longitudinal (right) SSS gradients from vector approach.

The most interesting result from vector approximation is that ρ_x component is significantly greater than the ρ_y (global mean of 0.01, maximum absolute value of 0.80, and standard deviation of 0.03 for the case of ρ_x; and global mean of 0.00, maximum absolute value of 0.57, and standard deviation of 0.02 for the case of ρ_y), what naturally leads to the approach discussed in next section.

4.4.3 Scalar approximation

A further simplification can be obtained if we assume than the correspondence matrix between the gradients of both scalars $\mathbf{\Phi}$ in Eq. 4.15 is assumed to be proportional to the identity

matrix. This approach does not impose a global alignment of the gradients of s and θ, but suppose that locally they should be almost aligned. The work of Ferrari and Paparella (2003) reveals that SSS and SST horizontal gradients at intermediate scales tend to align in the ocean, justifying the scalar approximation over wide regions, while large deviations from parallelism may occur at the frontiers of those areas.

Thus, in this case, $\mathbf{\Phi}$ simplifies to a scalar function:

$$\nabla s(\vec{x}) \;=\; a(\vec{x})\,\nabla\theta(\vec{x}), \tag{4.30}$$

The expression 4.30 can be integrated assuming that the gradient of a is negligible as compared to the gradients of s and θ, we obtain:

$$s(\vec{x}) \;\approx\; a(\vec{x})\,\theta(\vec{x}) \;+\; b(\vec{x}) \tag{4.31}$$

where $a(\vec{x})$ and $b(\vec{x})$ are smooth functions over large regions. Here, smooth means that their gradients are much smaller than those of s and θ; if we take gradients on the expression above we obtain:

$$\nabla s \;\approx\; a\nabla\theta \;+\; \theta\nabla a \;+\; \nabla b \;\approx\; a\nabla\theta \tag{4.32}$$

where the second approximation is justified precisely when $|\nabla a|\ ,\ |\nabla b| \ll |\nabla s|\ ,\ |\nabla\theta|$. Notice also that, even within the regions of validity of this approximation, the gradients of s and θ, although close to parallel are not exactly aligned in light of the small deviation term $\theta\nabla a + \nabla b$, making the result more realistic.

The integral expression above has an advantage compared with the differential expression, Eq. 4.30: now, the boundaries are precisely localized and not disturb the whole image.

We construct a corrected variable $\tilde{s}$, applying Eq. (4.31), namely:

$$\tilde{s}(\vec{x}) \;=\; \hat{a}(\vec{x})\,\theta(\vec{x}) \;+\; \hat{b}(\vec{x}) \tag{4.33}$$

where $\hat{a}(\vec{x})$ and $\hat{b}(\vec{x})$ are estimates of the actual parameters $a(\vec{x})$ and $b(\vec{x})$ in Eq. (4.31). These estimates are obtained from the values of original s and θ by performing linear regressions weighted around each point as in Nieves et al. (2007), in the following way.

Let us define the total weight of a point $\vec{x}$, $N(\vec{x})$, as follows:

$$N(\vec{x}) = \sum_{\vec{x}\neq\vec{x}'\in\text{sea}} \frac{1}{|\vec{x}'-\vec{x}|^2} \tag{4.34}$$

For any function f we define its local average around the point $\vec{x}$, $\langle f\rangle_{\vec{x}}$, as:

$$\langle f\rangle_{\vec{x}} = \frac{1}{N(\vec{x})} \sum_{\vec{x}\neq\vec{x}'\in\text{sea}} \frac{f(\vec{x}')}{|\vec{x}'-\vec{x}|^2} \tag{4.35}$$

so obviously $\langle 1\rangle_{\vec{x}} = 1$. By construction $\langle f\rangle_{\vec{x}}$ is an averaging function which gives more weight to the points closer to $\vec{x}$. This weighting function is chosen because it is scale invariant; otherwise it might introduce a scale in the analysis and so perturbing singularity analysis. The fact that

the weighting function gives zero weight to the central point (required; otherwise a scale length will be introduced) is not crucial considering that $a(\vec{x})$ and $b(\vec{x})$ are smooth, so they change slowly in space and the inference from points nearby will equally be rather satisfactory.

As $a(\vec{x})$ and $b(\vec{x})$ should not have sharp variations over large regions, we evaluate $\hat{a}(\vec{x})$ and $\hat{b}(\vec{x})$ as the linear regression coefficients using this local averaging. We first compute the order-2 moments with this local averaging function:

$$\sigma_s^2(\vec{x}) \ = \langle s^2 \rangle_{\vec{x}} - \langle s \rangle_{\vec{x}}^2 \tag{4.36}$$

$$\sigma_\theta^2(\vec{x}) \ = \langle \theta^2 \rangle_{\vec{x}} - \langle \theta \rangle_{\vec{x}}^2 \tag{4.37}$$

$$\sigma_{s\theta}(\vec{x}) \ = \langle s\theta \rangle_{\vec{x}} - \langle s \rangle_{\vec{x}} \langle \theta \rangle_{\vec{x}} \tag{4.38}$$

We obtain the local slope $\hat{a}(\vec{x})$:

$$\hat{a}(\vec{x}) = \frac{\sigma_{s\theta(\vec{x})}}{\sigma_s^2(\vec{x})} \tag{4.39}$$

and the local intercept $\hat{b}(\vec{x})$

$$\hat{b}(\vec{x}) = \langle s \rangle_{\vec{x}} \ - \ \hat{a}(\vec{x}) \langle \theta \rangle_{\vec{x}} \tag{4.40}$$

An additional benefit of the use of local regressions to estimate $a(\vec{x})$ and $b(\vec{x})$ is that it diminishes the impact of noise on the variable s, leading to a filtered variable $\tilde{s}$. Besides, as we are performing local linear regressions we can retrieve the local regression coefficient:

$$r(\vec{x}) \ = \ \frac{\sigma_{s\theta(\vec{x})}}{\sigma_s(\vec{x}) \sigma_\theta(\vec{x})} \tag{4.41}$$

This local regression coefficient informs us about quality of the local regression, which is affected by the local level of noise being filtered and the fitness of the local regression scheme to describe the data. We will discuss about its oceanographic interpretation in the next chapter.

Figure 4.10 shows the gradient of the resulting $\tilde{s}$. As in the case of the the two previous approaches, a large amount of noise has been removed. Additionally, the spatial structure is more coherent that that of the original SSS map. Besides, despite of its simplicity, the scalar approach provides a remarkably rich gradient structure. While in Figures 4.7 bottom and 4.9 there are certain areas of negligible gradient, Figure 4.10 shows gradients all over the map in an apparent coherent way. This may be due to the fact that the scalar approach is integral and therefore is defined in terms of the same ocean variables, while the matrix and vector approaches are differential and as such they are defined by the gradients of these variables. Using gradients leads to reduced signal to noise ratio and as a consequence the results are more affected by noise. Matrix and vector approaches, although accounting for more general transformations of the gradient, are globally less accurate from the numerical point of view and more affected by problems at the boundaries.

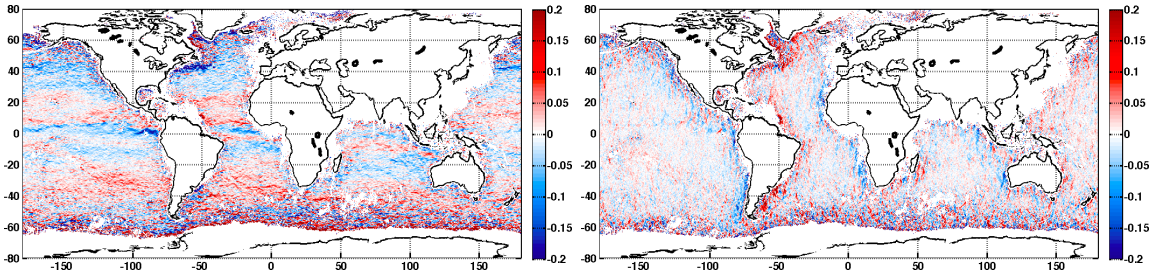

Figure 4.10: Latitudinal (left) and longitudinal (right) SSS gradients from scalar approach.

4.5 Sensitivity to noise

In this section we discuss the sensitivity of the data fusion method to the presence of noise of different types and amplitudes. To that goal, we have started from a controlled situation, in which the amplitude and characteristics of noise are known and a ground truth is available by using the output of global circulation model OFES as described in Chapter 2.

The noise sources $\eta_\beta(\vec{x})$ studied here are Gaussian with zero mean and marginal standard deviation σ_n which is the same at all the points. The spatial correlation of the noise is given by the exponent β of its power spectrum, namely:

$$|\hat{n}_\beta|^2(k) \propto \| \, k \, \|^{-\beta} \tag{4.42}$$

The value of the exponent can be taken between $\beta = 0$ (purely decorrelated noised) and $\beta = 2$ (strongly correlated noise). In this study we will consider the cases $\beta = 0, 1$ and 2.

4.5.1 No noise

In the absence of noise, the fusion algorithm creates a map with slight deviates from the original one, as can be observed in Figure 4.11.

The map of singularity exponents, Figure 4.12, shows that some particular structures have become a bit blurred. This is probably a consequence of the approximation implied by Eq. (4.33). The error map on bottom of Figure 4.11 has a standard deviation of 0.3. This is an indication that the error correction by our multifractal fused method cannot go below this threshold within the present formulation, at least under the parametrizations defining OFES model.

4.5.2 Decorrelated noise ($\beta = 0$)

In Figure 4.13 we show an example of white noise added to the original SSS map and of the result of applying the fusion algorithm on it, as well as the difference map.

Decorrelated noise is the easiest to filter away by our fusion algorithm. Significantly, the average error is negligible (0.02) and the standard deviation of the error map (obtained by averaging over all spatial locations) is 0.33 for an input noise with a standard deviation of 1.0, a considerable reduction in the error, to very nearly the same level occurring when no noise is introduced. Nevertheless, the restoration of singularity exponents, Figure 4.14, is very

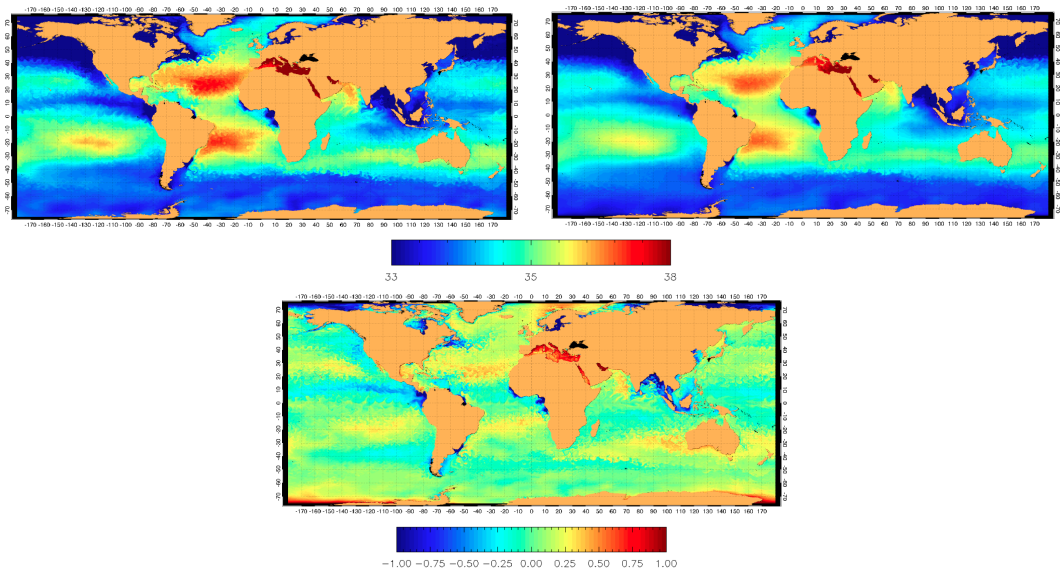

Figure 4.11: Top left: Original SSS; Top right: SSS map after filtering using SST map as a template; Bottom: Map of differences.

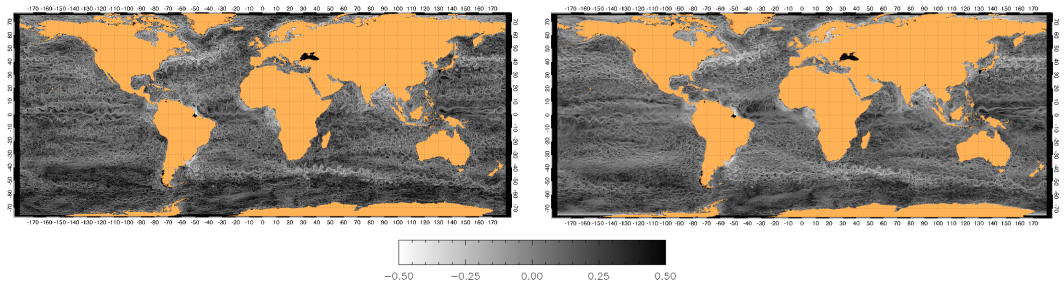

Figure 4.12: Left: Singularity exponents associated with SSS; Right: Singularity exponents derived from fused SSS map.

incomplete: just the singularity exponents associated with the main currents can be recognized. Notice however that the level of input noise is rather high.

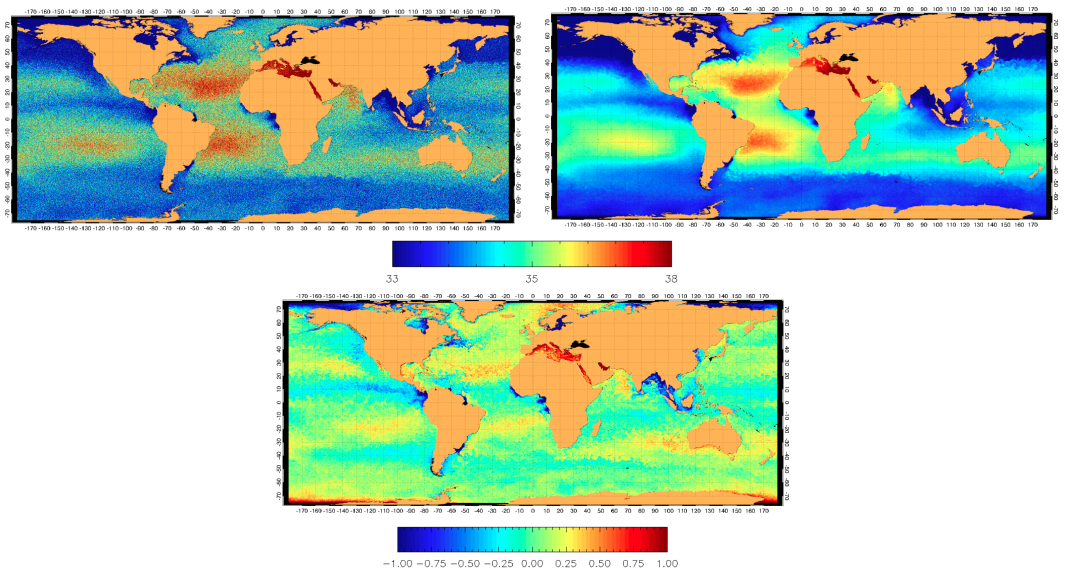

Figure 4.13: Top left: SSS after the introduction of decorrelated noise with input noise of standard deviation $\sigma_i = 1$ pss. Top right: SSS map after filtering the map on top using SST map as a template. Bottom: Differences between the original (no noise) SSS map and the fused SSS map.

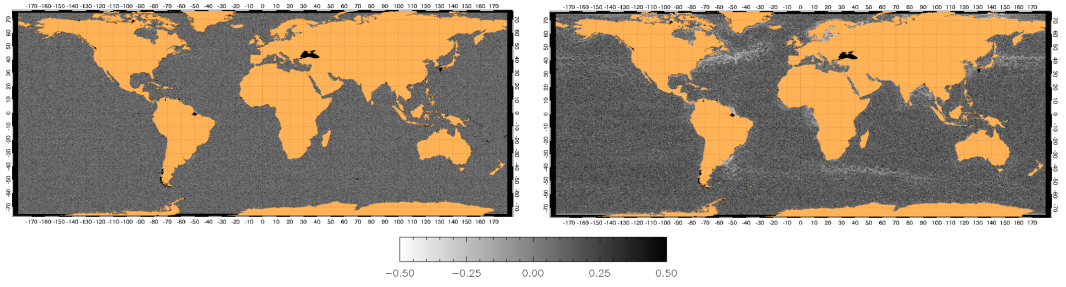

Figure 4.14: Left: Singularity exponents associated with SSS after applying noise of unity amplitude and $\beta = 0$. Right: Singularity exponents derived from the fused SSS map.

4.5.3 Correlated noise ($\beta = 1$)

In Figure 4.15 we show an example of noise added to the original SSS map with the spatial correlation of the noise proportional to k^{-1} and of the result of applying the fusion algorithm to it, as well as the difference map.

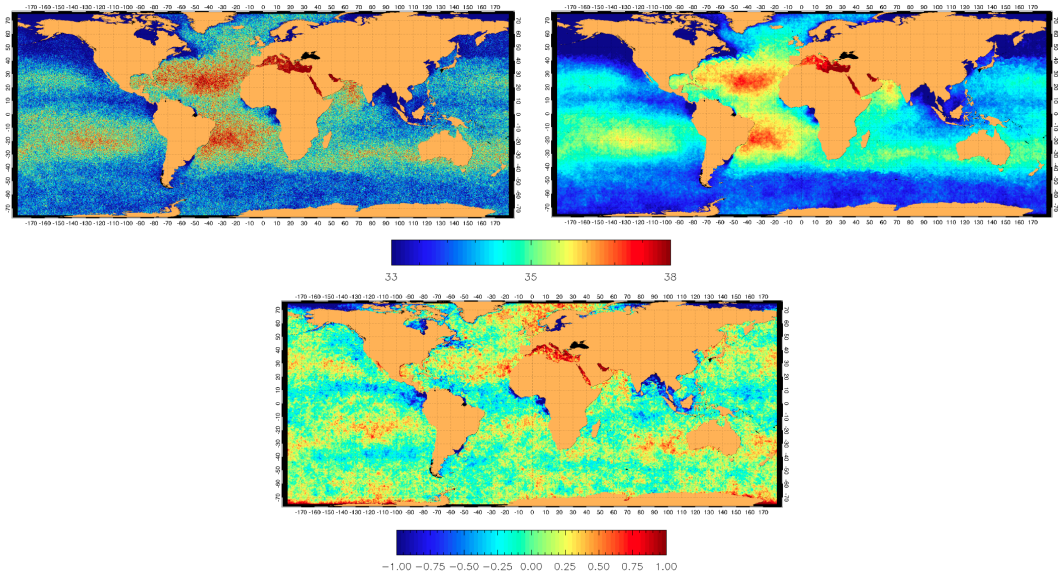

Figure 4.15: Top left: SSS after the introduction of correlated noise with input noise of standard deviation $\sigma_i = 1$ pss. Top right: SSS map after filtering the map on top using SST map as a template. Bottom: Differences between the original (no noise) SSS map and the fused SSS map.

Correlated noise is also appropriately filtered away by our fusion algorithm. The error map has a spatial average of 0.02 and a standard deviation of 0.36 for input noise of standard deviation equal to 1.0, a considerable error reduction slightly worse than in the previous case. The error map is still associated with significant geophysical structures. The restoration of singularity exponents, Figure 4.16, is worse than in the previous case and centered on the main currents.

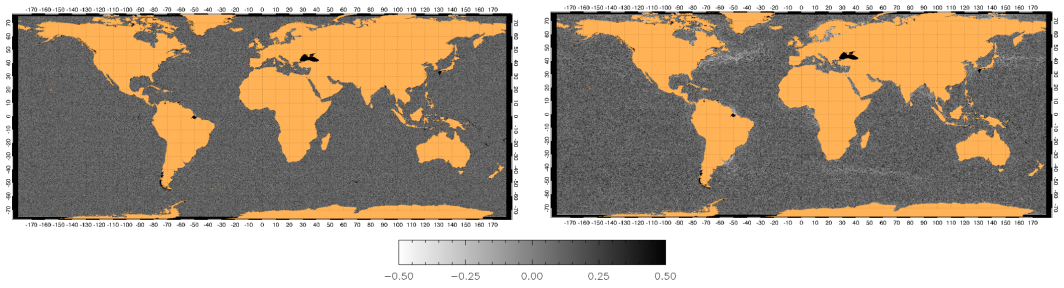

Figure 4.16: Left: Singularity exponents associated with SSS after applying noise of unity amplitude and $\beta = 1$. Right: Singularity exponents derived from the fused SSS map.

4.5.4 Strongly correlated noise ($\beta = 2$)

The correction of strongly correlated noise is deeply challenging for our fusion algorithm, with an important deformation of large scale oceanic features in the original signal. In Figure 4.17 we show an example of noise added to the original SSS map with the spatial correlation of the noise proportional to k^{-2} and of the result of applying the fusion algorithm to it, as well as the difference map.

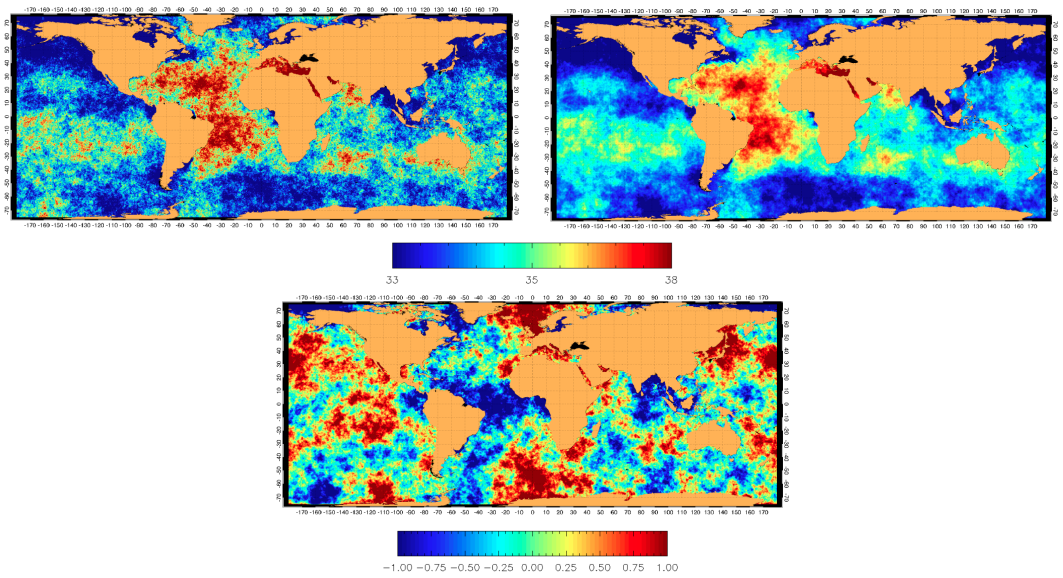

Figure 4.17: Top left: SSS after the introduction of strongly correlated noise with input noise of standard deviation $\sigma_i = 1$ pss. Top right: SSS map after filtering the map on top using SST map as a template. Bottom: Differences between the original (no noise) SSS map and the fused SSS map.

The strongly correlated noise introduces large-scale structures, which are not of geophysical origin, but even so the error map has a negligible spatial average of 0.014. Submitted to such a strong perturbation, the standard deviation of the error is larger in this case, arriving at a value 0.66 for input noise of standard deviation of 1.0; significant but not quite satisfactory. The error map has a fuzzy structure, and the main resulting structures are devoid of geophysical meaning. The restoration of singularity exponents, Figure 4.16, is even worse than in the previous case and even the main currents are hard to recognize.

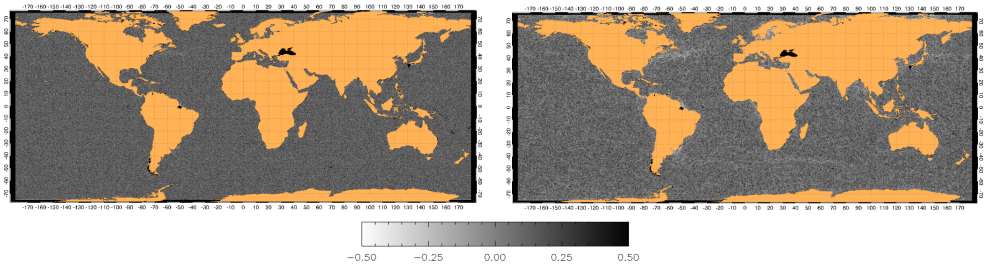

Figure 4.18: Left: Singularity exponents associated with SSS after applying noise of unity amplitude and $\beta = 2$. Right: Singularity exponents derived from the fused SSS map.

4.5.5 Dependence of the reconstruction quality on noise intensity

To quantify the quality of our fusion algorithm, we define the output noise level, σ_o, as the standard deviation of the error field, calculated over the whole domain (in fact the average error is always lower than 0.02 and negligible by comparison, so the standard deviation and the root squared error are almost identical). We define the input noise, σ_i, as the standard deviation of the injected noise.

In Figure 4.19 we show the evolution of the ratios between the output noise by respect the input noise. We observe that there is a crossover value σ_c below which fusion is not useful: for any input noise $\sigma_i < \sigma_c$ the output noise σ_o is equal to σ_c (and then the ratio σ_o/σ_i diverges). On the other hand, when the level of input noise if large enough the capability of our fusion algorithm to remove noise stagnates at a fixed percentage of input noise (the asymptotic maximum percentages of noise removal are 91% ($\beta = 0$), 83% ($\beta = 1$) and 43% ($\beta = 2$). Those ratios are satisfactory, implying the fusion approach is always a favorable strategy even for highly noisy images.

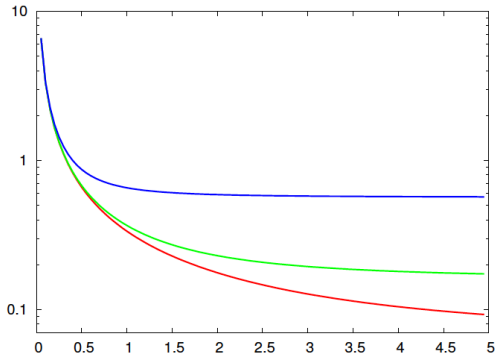

Figure 4.19: Evolution of the ratio output noise/input noise depending on the value of input noise. Red curve: decorrelated noise ($\beta = 0$); Green curve: correlated noise ($\beta = 1$); Blue curve: strongly correlated noise ($\beta = 2$). The estimated asymptotic values for the input/output ratios are 0.09, 0.17 and 0.57, respectively. The crossovers (passing by 1) occur for input noise levels of 0.33, 0.33 and 0.40, respectively.

Chapter 5

Synergy between different variables: Application to SMOS SSS

In this chapter we apply the data fusion methodology presented in Chapter 4 to SMOS L3 (Chapter 3) to produce SMOS L4 maps at 0.25° spatial grid and 9 days and monthly averages for the year 2012. Synergy of SMOS SSS (signal) with sea surface temperature (template) results in SSS L4 products with less noise and higher spatial resolution.

The consequences of combining SMOS SSS data with alternative templates of sea surface temperature (SST) remote sensing maps and other ocean variables as absolute dynamic topography (ADT) obtained from altimetry is also presented and evaluated. The study of auxiliary parameters employed in the method and the use of mean values for these parameters to improve the resulting SSS L4 is also investigated. Finally, an assessment of the quality of the resulting SSS L4 maps as compared to SSS L3 and SSS OI maps is developed by using several indicators: validation against in situ data and climatologies and characterization of their multifractal structure.

5.1 SMOS Level 4 SSS maps

5.1.1 9-day SSS products

The results of the application of data fusion using as an input the L3 SSS data and OSTIA SST as a template for 1st-9th of June 2012 is shown in Figure 5.1. The data fusion is applied both to the original L3 SSS (section 3.2.1) resulting in **L4-1** SSS, and to the L3 SSS coming from an alternative filtering of L2 data (section 3.5.1) resulting in **L4-2** SSS. In both cases, L4 maps have greater spatial coherence and lower level of noise compared to the observations before data fusion is applied (Figures 3.2top and 3.20top). Extrapolation is allowed up to 4 pixels from the input L3 point to avoid unrealistic extrapolations. Due to the data filling characteristic of the algorithm, even if there are no data at a given point we can still estimate $\hat{a}$ and $\hat{b}$ taking into account that they are defined by local averages, which include other points with distance-decreasing weight. As the L3 SSS obtained with a more restrictive filtering of L2 data has more

The multifractal fusion approach was first presented and applied to SMOS data in: ***Umbert, M., Hoareau, N., Turiel, A., and Ballabrera-Poy, J., 2014. New blending algorithm to synergize ocean variables: the case of SMOS sea surface salinity maps. 44th International Liege Colloquium Special Issue, Remote Sensing of Environment, in press.***

Partially developed during the third PhD stage in L'Institut Français de Recherche pour l'Exploitation de la Mer (IFREMER) in Toulon (France), under the supervision of Dr. Nicolas Reul.

gaps, the L4 algorithm performs more extrapolation and regularization on the **L4-2** SSS than on the **L4-1**.

To assess the quality of both 9-day L4 SSS products (**L4-1** and **L4-2**) calculated every three days, an extensive validation using data from Argo profilers has been carried out following the procedure outlined in Chapter 3. Figure 5.2 shows the differences of the L4 maps with respect to Argo in situ data at the buoy matchup (using uppermost valid salinity value) for the full year 2012. The results show larger differences between L4 SSS and in situ close to land, in high latitudes and at areas of higher spatio-temporal variability associated with the main currents as in the Western boundary currents and Antartic circumpolar current. Compared to the L3 product from where they were derived, a uniform global reduction of the difference with Argo SSS can be observed. **L4-2** presents a remarkable reduction of the differences compare to **L4-1**.

Tables 5.1 and 5.2 synthesize results on validation of L4 products. To quantitatively assess the error in L4 SSS maps, buoy collocation are sorted by latitude bands, distance to coastal areas, depth of the Argo uppermost measurement and SST differences between Argo and ECMWF. The matchups are accumulated during the year 2012 and the average and standard deviation of the L4 products minus Argo value are calculated.

Latitude		**Global**	**60S-60N**				**30S-30N**				**Zone 122**			
Maximum depth				**>10 m**				**>10 m**				**>10 m**		
Coast distance					**1000 km**				**1000 km**				**1000 km**	
ECMWF-Argo SST						**<0.3 ºC**				**<0.3 ºC**				**<0.3 ºC**
L4-1	n	238213	233676	225551	131954	87501	126949	124175	75652	57915	7690	7571	6279	5116
	$\langle \Delta S \rangle$	-0.14	-0.12	-0.11	-0.04	-0.05	-0.14	-0.14	-0.11	-0.11	-0.15	-0.15	-0.12	-0.11
	$\sigma_{<\Delta S>}$	0.53	0.50	0.50	0.44	0.33	0.35	0.35	0.27	0.27	0.22	0.21	0.21	0.21

*Table 5.1: Statistics of the differences between 9-day **L4-1** vs Argo SSS measurements for the year 2012.*

Latitude		**Global**	**60S-60N**				**30S-30N**				**Zone 122**			
Maximum depth				**>10 m**				**>10 m**				**>10 m**		
Coast distance					**1000 km**				**1000 km**				**1000 km**	
ECMWF-Argo SST						**<0.3 ºC**				**<0.3 ºC**				**<0.3 ºC**
L4-2	n	229146	225474	217858	130655	86633	121618	119047	74553	57142	7672	7554	6269	5107
	$\langle \Delta S \rangle$	-0.03	-0.02	-0.02	0.01	-0.01	-0.06	-0.06	-0.06	-0.07	-0.13	-0.13	-0.10	-0.10
	$\sigma_{<\Delta S>}$	0.49	0.47	0.47	0.44	0.33	0.35	0.35	0.27	0.27	0.22	0.22	0.21	0.21

*Table 5.2: Statistics of the differences between 9-day **L4-2** vs Argo SSS measurements for the year 2012.*

The number of total matchups are of the order of two-hundred thirty thousand. At global scale the standard deviation of SMOS minus Argo differences is higher (0.53) for **L4-1** than for **L4-2** (0.49); the bias is -0.14 for **L4-1**, what is considerably reduced (-0.03) for the case of **L4-2**.

With the aim of analyzing the different contributions to the error, data are selected by latitudinal bands and distance to coast. Results in Zone 122 [0-30S, 120-150S], far from RFI emissions and land contamination, are also analyzed. As soon as the data are restricted to the central latitudinal band, the random error is reduced. In the case of **L4-1**, the global standard deviation of the difference with Argo reduces from 0.53 (global), to 0.50 (bounded by latitude 60), to 0.35 (bounded to latitude 30) and to 0.22 (in Zone 122). The biases are -0.14 (global), -0.12 (bounded by latitude 60), -0.14 (bounded to latitude 30) and -0.15 (in Zone 122); as the

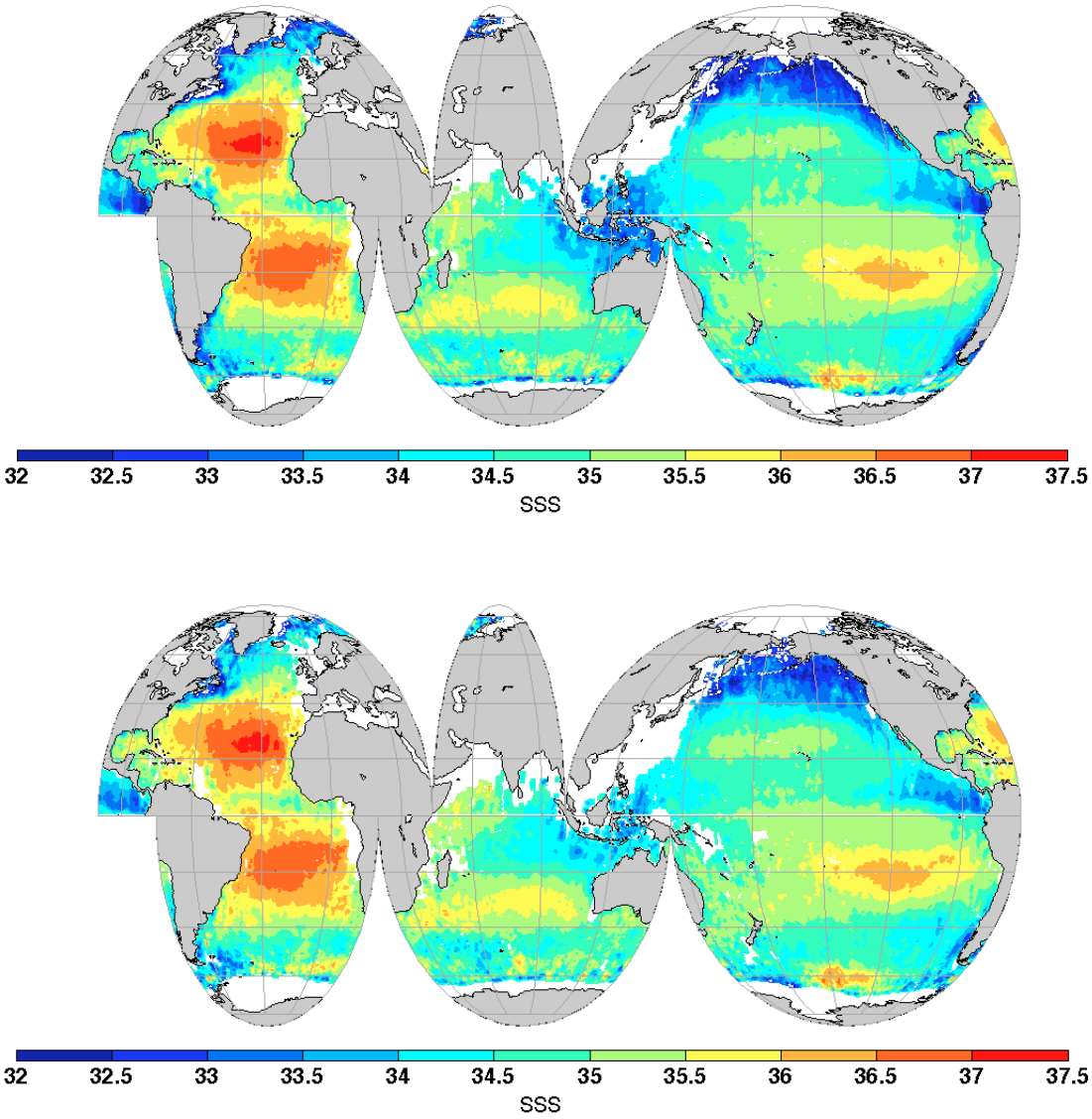

*Figure 5.1: Top: Map of surface salinity obtained after applying data fusion on SMOS L3 (**L4-1**) and on L3 using the same filtering of L2 as in section 3.5.1 (**L4-2**) for the first nine days of June 2012 (bottom).*

results show, the bias is not reduced for this product independently if the validation is restrict in latitude bands. In the case of **L4-2**, the global error reduces from 0.49 (global), to 0.47 (bounded by latitude 60), to 0.35 (bounded to latitude 30) and to 0.22 (in Zone 122). The biases of **L4-2** are greatly reduced compared to **L4-1**: -0.03 (global), -0.02 (bounded by latitude 60), -0.06 (bounded to latitude 30) and -0.13 (in Zone 122); it follows that in this last case the bias is not reduced when restricting the matchups to latitudinal bands.

Statistics also improve when considering only matchups located farther than 1000 km from coastlines. In the case of the differences between **L4-1** and Argo, the standard deviation is reduced from 0.50 (60° latitude band) to 0.44 and the bias is also reduced from -0.12 to -0.04. At the tropical band, the standard deviation is reduced from 0.35 to 0.27 and the bias is also

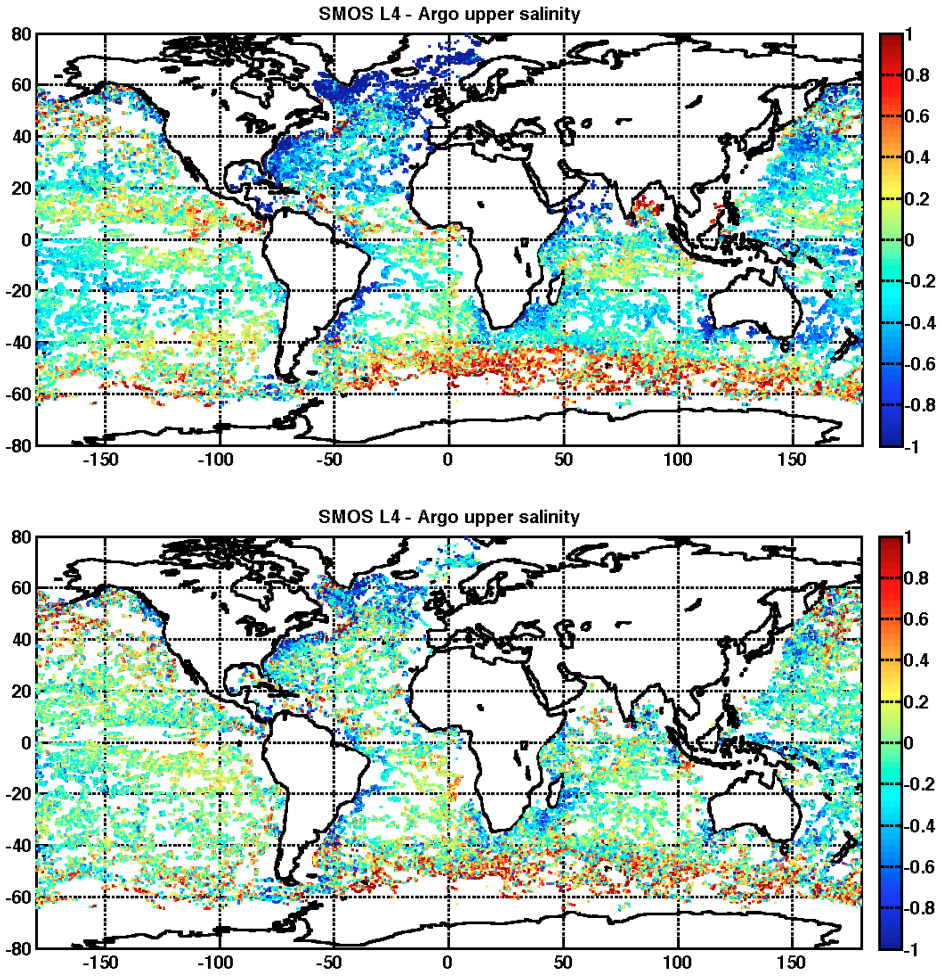

*Figure 5.2: Global maps of SSS differences of **L4-1** SSS (top) and **L4-2** SSS (bottom) with respect to the collocated Argo data for year 2012.*

reduced from -0.14 to -0.11. The larger negative bias in the tropical band could be related to the increase of the frequency of rain events. In the case of **L4-2**, the standard deviation is reduced from 0.47 (60° latitude limit) to 0.44 and the bias is slightly reduced from -0.02 to 0.01. At the tropical band, the standard deviation is reduced from 0.35 to 0.27 and the bias is the same (-0.06).

To sum up, when the data is taken more than 1000 km from the coast, the Argo measurement in the first 10 m below the ocean surface and at points with differences between reference and in situ SST lower than 0.3°C, the differences between **L4-1** and Argo SSS estimates have negative biases of -0.05, -0.11 and -0.11 at the 60°, 30° latitude bands and Zone 122 respectively, and standard deviations of 0.33, 0.27 and 0.21 at the 60°, 30° latitude bands and Zone 122 respectively. For the case of **L4-2** SSS versus Argo SSS, the salinity estimate has slight negative biases of -0.01, -0.07 and -0.10 at the 60°, 30° latitude bands and Zone 122 respectively, and standard deviations of 0.33, 0.27 and 0.21 at the 60°, 30° latitude bands and Zone 122 respectively.

Histograms and scatter plots of the matchup salinity differences are shown in Figure 5.3 for 9-day **L4-1** and in Figure 5.6 for 9-day **L4-2** when the matchup of SMOS SSS is taken at 60°

latitude band against the Argo uppermost valid salinity value if that value has been measured in the first 10 meters of the water column. The matchup has also to be located more than 1000 km from the coast and the differences between the reference SST used for the retrieval of the salinity should differ from the Argo uppermost temperature value by less than 0.3°C.

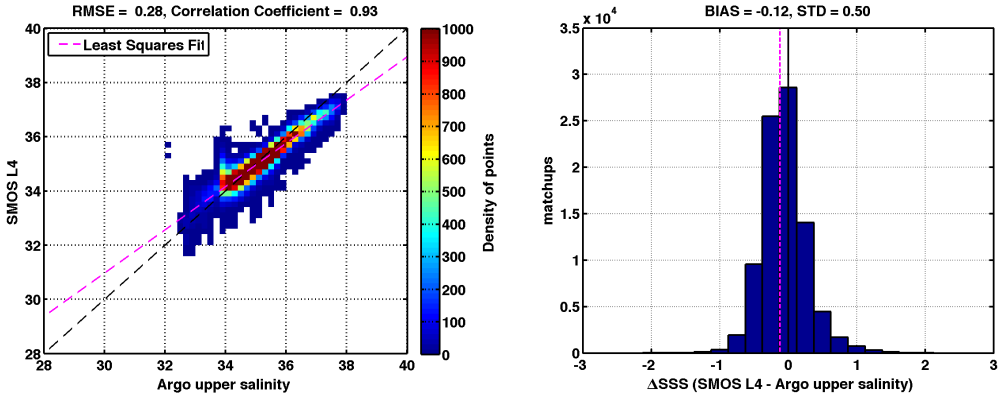

*Figure 5.3: Histograms of the difference of SMOS 9-day **L4-1** with Argo data (top). Scatter plot for SMOS (abscissa) and collocated buoy data (ordinate) for 9-day **L4-1** SSS (bottom) for the entire year 2012.*

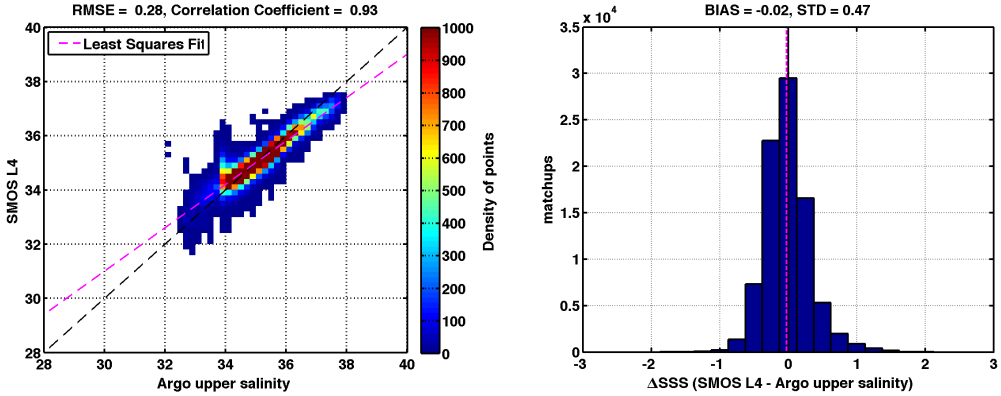

*Figure 5.4: Histograms of the difference of SMOS 9-day **L4-2** with Argo data (top). Scatter plot for SMOS (abscissa) and collocated buoy data (ordinate) for 9-day **L4-2** SSS (bottom) for the entire year 2012.*

The results for **L4-2** estimate is in slight better agreement with buoy data than **L4-1** SSS product, what is evidenced by a histogram of the difference which is more centered (bias equal to -0.12 for **L4-1** and -0.02 for **L4-2**). The scatterplot **L4-1** SSS vs Argo show a similar scatter than the scatterplot **L4-2** vs Argo. Both the RMSE and the correlation coefficient are the same: 28 % and 0.93 for both L4 estimates.

5.1.2 Monthly SSS products

To assess if the SMOS mission requirements (accuracy of 0.1-0.2 over one month) are being achieved a monthly quality assessment for both **L4-1** and **L4-2** SSS monthly products (Figure 5.5) is done with respect to both climatological fields and in situ data using products with a 0.25° spatial grid. In the case of monthly products the coverage is similar for both L4 products, as before, extrapolation it is only allowed 4 pixels beyond an original L3 SSS measurement.

Figure 5.6 shows the monthly **L4-1** and monthly **L4-2** differences with Argo SSS at the buoy matchup for the year 2012. The differences between SMOS products and in situ measurements increase especially close to coast for **L4-1** monthly maps. Tables 5.3 and 5.4 synthesize the results of buoy collocation differences by latitude bands (global, 60S-60N, 30S-30N, and Zone 122), distance to coastal areas, depth of the Argo uppermost measurement and SST differences between Argo and ECMWF to quantitatively assess the SSS maps errors.

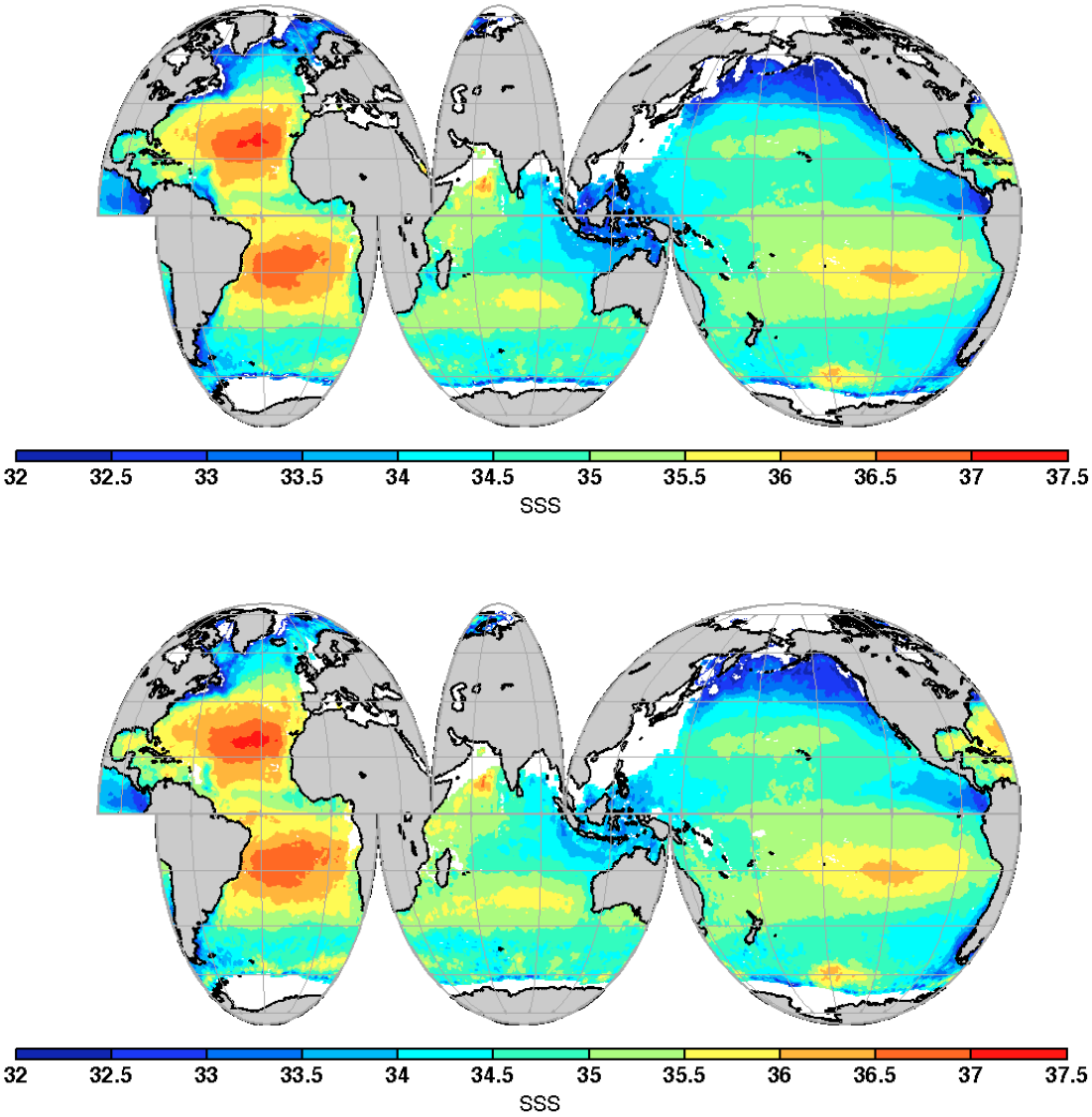

*Figure 5.5: Map of surface salinity **L4-1** (top) and **L4-2** (bottom) for the entire month of June 2012 (bottom).*

In the case of monthly products, the total number of matchups is reduced to the order of seventy-five thousand (two-hundred thousand for 9-day SSS maps). The reason for the higher number of matchups in the 9-day products is that the same Argo measurement will matchup with various 9-day maps. As the 9-day maps are produced every 3 days, consecutive maps have overlapping days. At global scale the standard deviation of SMOS minus Argo differences is

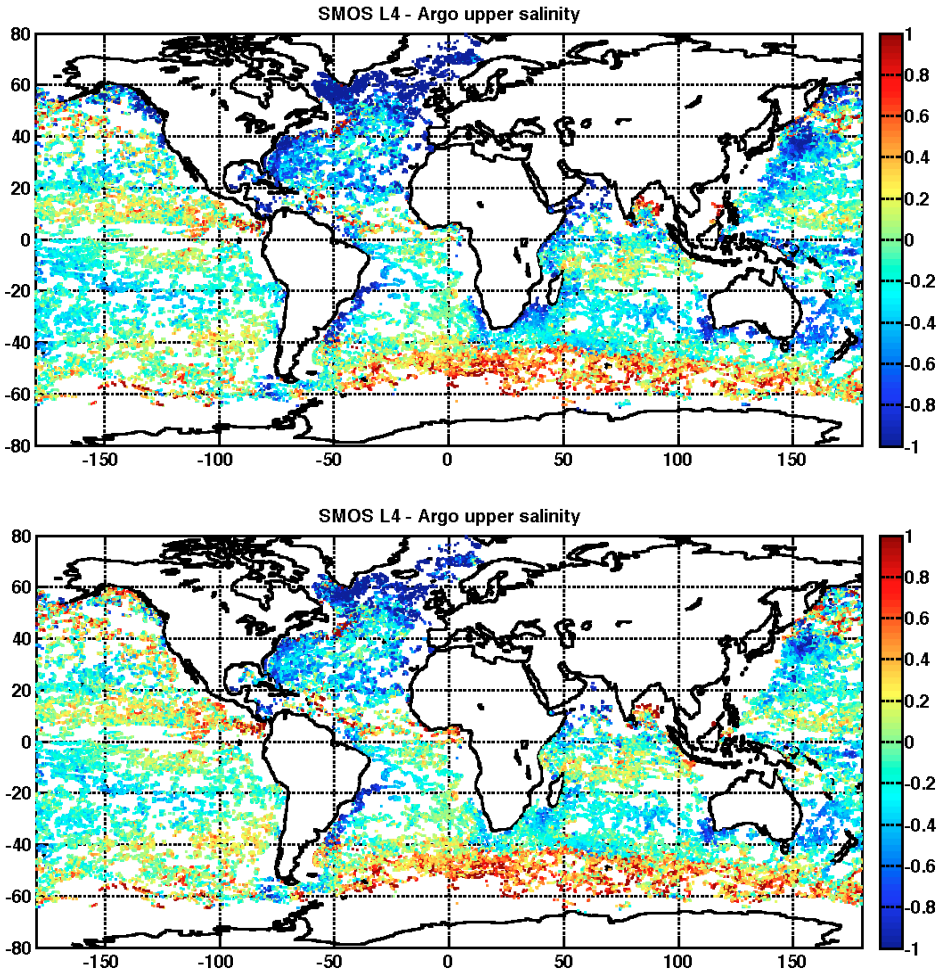

*Figure 5.6: Global maps of SSS differences for **L4-1** SSS (top) and data **L4-2** SSS (bottom) minus the collocated Argo data.*

Latitude		**Global**	**60S-60N**				**30S-30N**				**Zone 122**			
Maximum depth				**>10 m**				**>10 m**				**>10 m**		
Coast distance					**1000 km**				**1000 km**				**1000 km**	
ECMWF-Argo SST						**<0.3 ºC**				**<0.3 ºC**				**<0.3 ºC**
L4-1	n	77267	75595	72833	41829	27640	41088	40161	23990	18295	2421	2383	1973	1609
	$\langle \Delta S \rangle$	-0.20	-0.17	-0.16	-0.07	-0.08	-0.17	-0.17	-0.13	-0.13	-0.16	-0.16	-0.13	-0.12
	$\sigma_{<\Delta S>}$	0.55	0.50	0.50	0.41	0.32	0.35	0.35	0.27	0.26	0.20	0.20	0.20	0.20

*Table 5.3: Statistics of monthly **L4-1** SSS vs Argo SSS measurements for the year 2012.*

not reduced for the case of **L4-1** when monthly averages are used (0.55 when in was 0.53 for the 9-day product validation). On the other hand the standard deviation is reduced from 0.49 to 0.48 for **L4-2** when using monthly products. Compared to 9-day products, the biases are increased for monthly maps, from -0.14 to -0.20 (**L4-1**), and from -0.03 to -0.09 (**L4-2**).

The comparison with matchups restricted in latitude results in reduced standard deviation errors. In the case of **L4-1**, the global error reduces from 0.55 (global), to 0.50 (bounded by latitude 60), to 0.35 (bounded to latitude 30) and to 0.20 (in Zone 122). In the case of **L4-2**, the global error reduces from 0.48 (global), to 0.46 (bounded by latitude 60), to 0.34 (bounded

Latitude		Global	60S-60N				30S-30N				Zone 122			
Maximum depth				>10 m				>10 m				>10 m		
Coast distance					1000 km				1000 km				1000 km	
ECMWF-Argo SST						<0.3 ºC				<0.3 ºC				<0.3 ºC
L4-2	n	75182	73693	71068	41596	27493	39795	38929	23764	18152	2421	2383	1973	1609
	$\langle \Delta S \rangle$	-0.09	-0.08	-0.07	-0.02	-0.04	-0.09	-0.09	-0.09	-0.09	-0.14	-0.13	-0.11	-0.10
	$\sigma_{<\Delta S>}$	0.48	0.46	0.46	0.41	0.31	0.34	0.34	0.26	0.26	0.20	0.20	0.20	0.20

*Table 5.4: Statistics of monthly **L4-2** SSS vs Argo SSS measurements for the year 2012.*

to latitude 30) and to 0.20 (in Zone 122).

matchups located farther than 1000 km from coast lead in the case of **L4-1**, to an standard deviation reduction from 0.50 (60° latitude limit) to 0.41 and the bias is also reduced from -0.17 to -0.07. At the tropical band, the standard deviation is reduced from 0.35 to 0.27 and the bias is also reduced from -0.17 to -0.13. In the case of **L4-2**, the standard deviation is reduced from 0.46 (60° latitude limit) to 0.41. At this latitude band, the bias is also reduced from -0.08 to -0.02. At the tropical band, the standard deviation reduces from 0.34 to 0.26 and the bias is the same: -0.09.

To conclude, if matchups at regions where well known issues exist (land-sea contamination, low surface water temperature, high surface wind) are not used, the monthly **L4-1** SSS produces a salinity estimate with negative biases of -0.08, -0.13 and -0.12 at the 60°, 30° latitude bands and Zone 122 respectively and standard deviations of 0.32, 0.26 and 0.20 at the 60°, 30° latitude bands and Zone 122 respectively. For the case of monthly **L4-2** SSS, the salinity estimate has also negative biases of -0.04, -0.09 and -0.10 at the 60°, 30° latitude bands and Zone 122 respectively, and standard deviations of 0.31, 0.26 and 0.20 at the 60°, 30° latitude bands and Zone 122 respectively.

Histograms and scatter plots of the matchup salinity differences are shown in Figure 5.7 for monthly **L4-1** and in Figure 5.8 for monthly **L4-2** restricting the matchups to 60° latitude band and uppermost valid Argo salinity value in the first 10 meters of the water column. The matchups have also been chosen more than 1000 km from the coast and the differences between the reference SST used for the retrieval of the salinity should differ from the Argo uppermost value by less than 0.3°C.

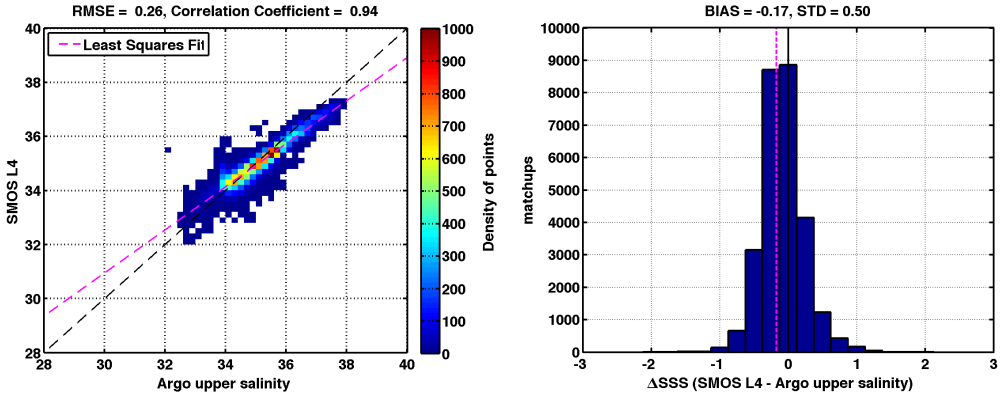

*Figure 5.7: Histograms for SMOS-buoy differences monthly **L4-1** (top). Scatter plot for SMOS (abscissa) and collocated buoy data (ordinate) for monthly **L4-1** SSS (bottom) for the entire year 2012.*

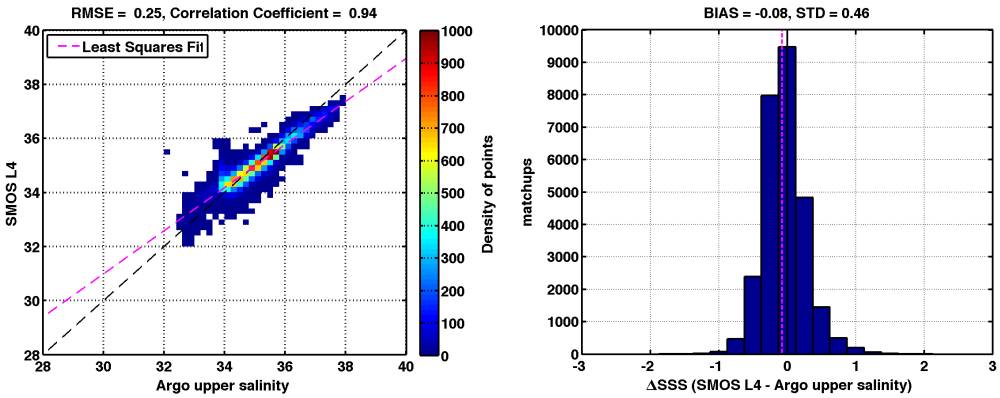

*Figure 5.8: Histograms for SMOS-buoy differences monthly **L4-2** (top). Scatter plot for SMOS (abscissa) and collocated buoy data (ordinate) for monthly **L4-2** SSS (bottom) for the entire year 2012.*

As the graph shows, the **L4-2** estimate is in better agreement with buoy data than the **L4-1** SSS product, as evidenced by a more centered histogram. The RMSE are the same, 28%, and the correlation coefficients are also the same, 0.93 for both the **L4-1** and **L4-2**.

In a second part of the validation of the monthly L4 products, we study the anomaly associated with reference values of SSS. The difference between monthly **L4-1** and **L4-2** with respect to World Ocean Atlas version 2009 (WOA09) climatology for June and ISAS-13 SSS for the month of June 2012 is shown in Figures 5.9 and 5.10 respectively. As we have already seen, observations contains systematic errors, precise parts of the anomalies highlights these deficiencies in lower levels of the SMOS processing chain, as zones affected by RFI, low sensitivity to SSS at high latitudes or coastal areas. The anomalies are reduced when L4 maps are compared to ISAS SSS for the month of June, especially in the tropical Pacific. This could reflect the time agreement between SMOS SSS data and Argo data-based ISAS SSS (in this case the year 2012). WOA climatologies could reflect long term SSS patterns not present today leading to the observed higher discrepancies.

Notice that the retrieval of SMOS SSS uses WOA09 as ancillary data; therefore, it is not an independent source of validation of this product. WOA13 and ISAS monthly SSS product have also been used to test the monthly SSS products accuracy. Tables 5.5 and 5.6 synthesize the validation results of monthly **L4-1** and **L4-2** respectively against the three different reference products used at different latitudinal bands for the entire year 2012. The best statistics are achieved when comparing with ISAS: the global standard deviation are 0.94 for **L4-1** and 0.83 for the **L4-2**, and biases systematically negative again (-0.22 for **L4-1** and considerably reduced to -0.03 for the case of **L4-2**). Globally the satellite estimates are fresher than the climatological SSS values. Although as seen in Figures 3.18 and 3.19, the satellite estimates are saltier depending on the region, near Equatorial regions the saltier estimated could result from the contain higher time resolution of SMOS relative to that of climatologies, in the Southern Ocean it is clearly related to inaccuracies in the retrieval of salinity due to cold waters and high winds.

To remove data points in cold waters and data points under the influence of large winds, also known to reduce the accuracy of the salinity retrievals, a latitudinal restriction for validation with Argo buoys is performed. For the case of monthly comparison against ISAS, restricting the

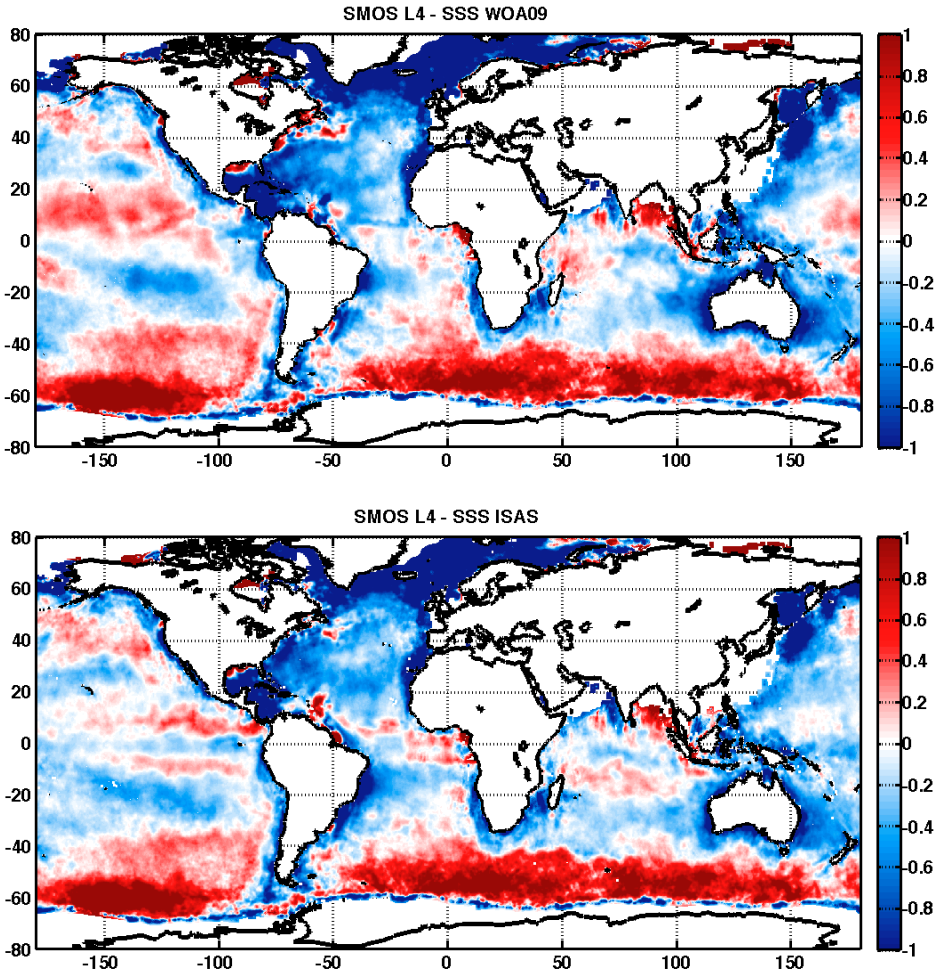

*Figure 5.9: **L4-1** SSS minus WOA09 climatology for June (top) and **L4-1** SSS minus ISAS for June 2012 (bottom).*

Latitude		**Global**			**60S-60N**			**30S-30N**			**Zone 122**		
Climatology		WOA09	WOA13	ISAS	WOA09	WOA13	ISAS	WOA09	WOA13	ISAS	WOA09	WOA13	ISAS
L4-1	$\langle \Delta S \rangle$	-0.23	-0.24	-0.22	-0.13	-0.14	-0.14	-0.18	-0.18	-0.19	-0.16	-0.17	-0.17
	$\sigma_{<\Delta S>}$	0.95	0.95	0.94	0.51	0.54	0.51	0.42	0.44	0.42	0.19	0.20	0.18

*Table 5.5: Statistics of the comparison between monthly **L4-1** vs climatological SSS for the year 2012.*

latitude leads to a reduced standard deviation: from 0.94 (global) to 0.51 (bounded by latitude 60), 0.42 (bounded by latitude 30) and 0.18 (Zone 122) for the case of **L4-1** and from 0.83 (global) to 0.47 (bounded by latitude 60), 0.41 (bounded by latitude 30) and 0.18 (Zone 122) in the case of **L4-2**. The bias is reduced when restricting in latitude for the case of **L4-1**: from -0.22 (global) to -0.14 (bounded by latitude 60), -0.19 (bounded by latitude 30) and -0.17 (Zone 122). However the bias is not reduced for the case of **L4-2**, although is lower than for the case of **L4-1**. It is the same at global and bounded by latitude 60 (-0.03), -0.09 (bounded by latitude 30) and -0.14 (Zone 122). The impact of the two different filtering strategies applied to L2 SSS is less evident in terms of standard deviation, but important in terms of bias for the case of monthly products.

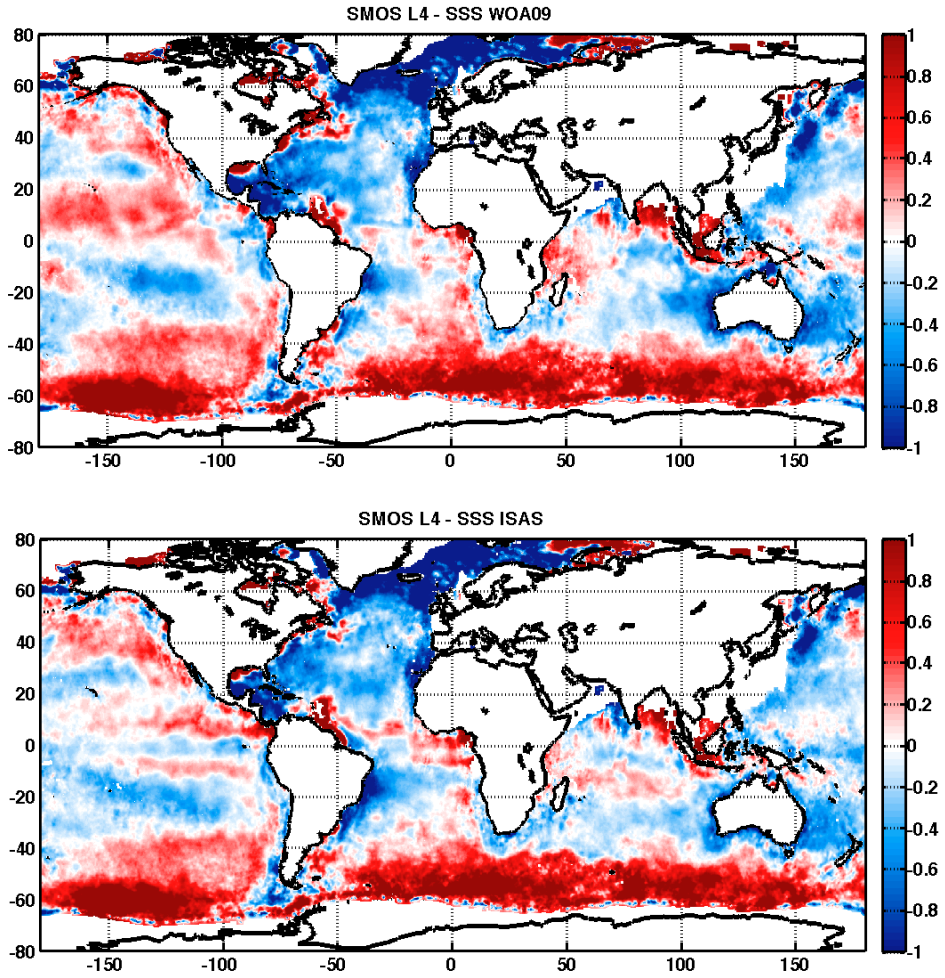

Figure 5.10: ***L4-2*** *SSS minus WOA09 climatology for June (top) and* ***L4-2*** *SSS minus ISAS for June 2012 (bottom).*

Latitude		Global			60S-60N			30S-30N			Zone 122		
Climatology		WOA09	WOA13	ISAS	WOA09	WOA13	ISAS	WOA09	WOA13	ISAS	WOA09	WOA13	ISAS
L4-2	$\langle \Delta S \rangle$	-0.03	-0.04	-0.03	-0.01	-0.01	-0.03	-0.07	-0.07	-0.09	-0.13	-0.14	-0.14
	$\sigma_{<\Delta S>}$	0.83	0.81	0.83	0.47	0.50	0.47	0.40	0.42	0.41	0.20	0.20	0.18

Table 5.6: Statistics of the comparison between monthly ***L4-2*** *vs climatological SSS for the year 2012.*

5.2 Fusion using different templates

In this section we are going to use different templates to produce alternative 9-day SSS L4 maps, first using as a template a different product of sea surface temperature: the Level 4 AVHRR OI Global Blended Sea Surface Temperature Analysis produced daily on a 0.25 degree grid at the NOAA National Climatic Data Center. This product uses optimal interpolation, ingesting data from the 4 km Advanced Very High Resolution Radiometer (AVHRR) Pathfinder Version 5 time series (when available, otherwise operational NOAA AVHRR data are used) and in situ ship and buoy observations.

Secondly, we analyze the L4 salinity product obtained using as a template for data fusion a different variable. To this goal, delayed-time Maps of Absolute Dynamic Topography (MADT)

provided by AVISO are used. This product merges up-to-date data sets using all missions available at a given time. MADT are gridded maps of absolute dynamic topography above the geoid; dynamic topography is the sum of sea level anomaly (SLA) and mean dynamic topography (MDT), both being referenced over a twenty-year period (from 1993 to 2012) of altimeter measurements. A mapping procedure using optimal interpolation with realistic correlation functions is applied to produce SLA and ADT maps (MSLA and MADT or L4 products) at a given date. The procedure generates a combined map merging measurements from all available altimeter missions (Ducet et al., 2000). We use data from year 2012 onwards, when the following missions were available on orbit: Envisat extension phase, Jason-2, Cryosat-2 and SARAL/AltiKa.

5.2.1 AVHRR SST

The difference between OSTIA SST (Donlon et al., 2012) and AVHRR OI SST (Reynolds et al., 2007) products, is evidenced in Figures 5.11 and 5.12, that show examples of both products (linearly interpolated to the 0.25^o degree grid and with a time window of 9-day of SSS maps) with their associated singularity exponents.

The OSTIA system produces an estimate of the foundation SST (i.e. with no diurnal variability signal). SST data are filtered based on surface wind speed data to remove diurnal variability and adjusted to represent the SST at depth of 0.2-1 m. On the other hand, AVHRR OI SST represents the raw surface temperature, leading to a higher SST estimates when compared to OSTIA SST. Singularity analysis reveals oceanic structures at finer resolution in the case of AVHRR OI SST than in the OSTIA SSS product.

We reproduce the results of last section using as a signal and AVHRR SST as template, to produce **L4-1-AVHRR** and **L4-2-AVHRR** SSS maps (a sample map is presented in Figure 5.13). The validation of the resulting 9-day **L4-AVHRR** SSS products calculated every three days is made using close-to-surface data from Argo profilers (table 5.7 for **L4-1-AVHRR** and table 5.8 for **L4-2-AVHRR**).

Latitude		**Global**	**60S-60N**				**30S-30N**				**Zone 122**			
Maximum depth				**>10 m**				**>10 m**				**>10 m**		
Coast distance					**1000 km**				**1000 km**				**1000 km**	
ECMWF-Argo SST						**<0.3 ºC**				**<0.3 ºC**				**<0.3 ºC**
L4-1-AVHRR	n	237999	233464	225342	131841	87420	126813	124041	75582	57854	7682	7564	6276	5114
	$\langle \Delta S \rangle$	-0.14	-0.12	-0.11	-0.04	-0.05	-0.14	-0.14	-0.11	-0.11	-0.15	-0.15	-0.12	-0.11
	$\sigma_{<\Delta S>}$	0.53	0.50	0.49	0.44	0.33	0.35	0.35	0.27	0.27	0.22	0.22	0.21	0.21

*Table 5.7: Statistics between 9-day **L4-1-AVHRR** vs Argo SSS measurements for the year 2012.*

Latitude		**Global**	**60S-60N**				**30S-30N**				**Zone 122**			
Maximum depth				**>10 m**				**>10 m**				**>10 m**		
Coast distance					**1000 km**				**1000 km**				**1000 km**	
ECMWF-Argo SST						**<0.3 ºC**				**<0.3 ºC**				**<0.3 ºC**
L4-2-AVHRR	n	229146	225474	217858	130655	86633	121618	119047	74553	57142	7672	7554	6269	5107
	$\langle \Delta S \rangle$	-0.03	-0.02	-0.02	0.01	-0.01	-0.06	-0.06	-0.06	-0.07	-0.13	-0.13	-0.10	-0.10
	$\sigma_{<\Delta S>}$	0.49	0.47	0.47	0.44	0.33	0.35	0.35	0.27	0.27	0.22	0.22	0.21	0.21

*Table 5.8: Statistics between 9-day **L4-2-AVHRR** vs Argo SSS measurements for the year 2012.*

Both **L4-AVHRR** SSS estimates exhibits the same results as for the case of using OSTIA

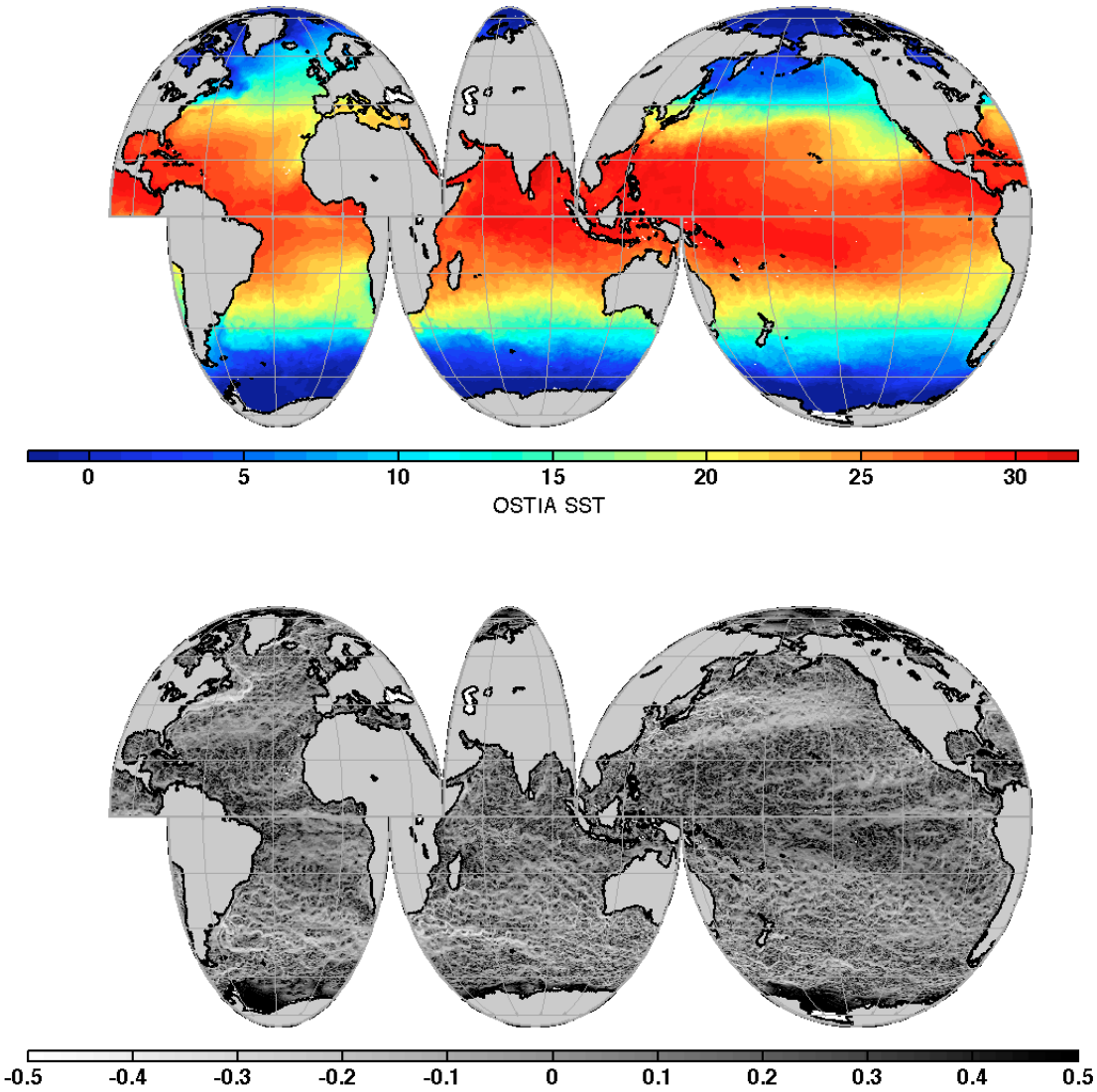

Figure 5.11: **Top:** *OSTIA SST map (°C) corresponding to the average of the days 1 to 9 June, 2012.* **Bottom:** *Associated singularity exponents.*

SST as template of the data fusion when validating against Argo data (see tables 5.1 and 5.2 for comparison). Although the higher resolution revealed by the singular structure of AVHRR SST (Figures 5.11 and 5.12), the global validation against Argo does not reveal any significant difference between using as a template one or the other SST products.

5.2.2 AVISO MADT

As a depth-integrated quantity dependent upon the density structure of the water column, altimeter ADT estimations reveal the presence of mesoscale structures and allow for the retrieval of surface currents using geostrophic balance (Tandeo et al., 2014). Theoretically, the upper ocean turbulence for horizontal scales between 50 km to few hundred kilometers is still consistent

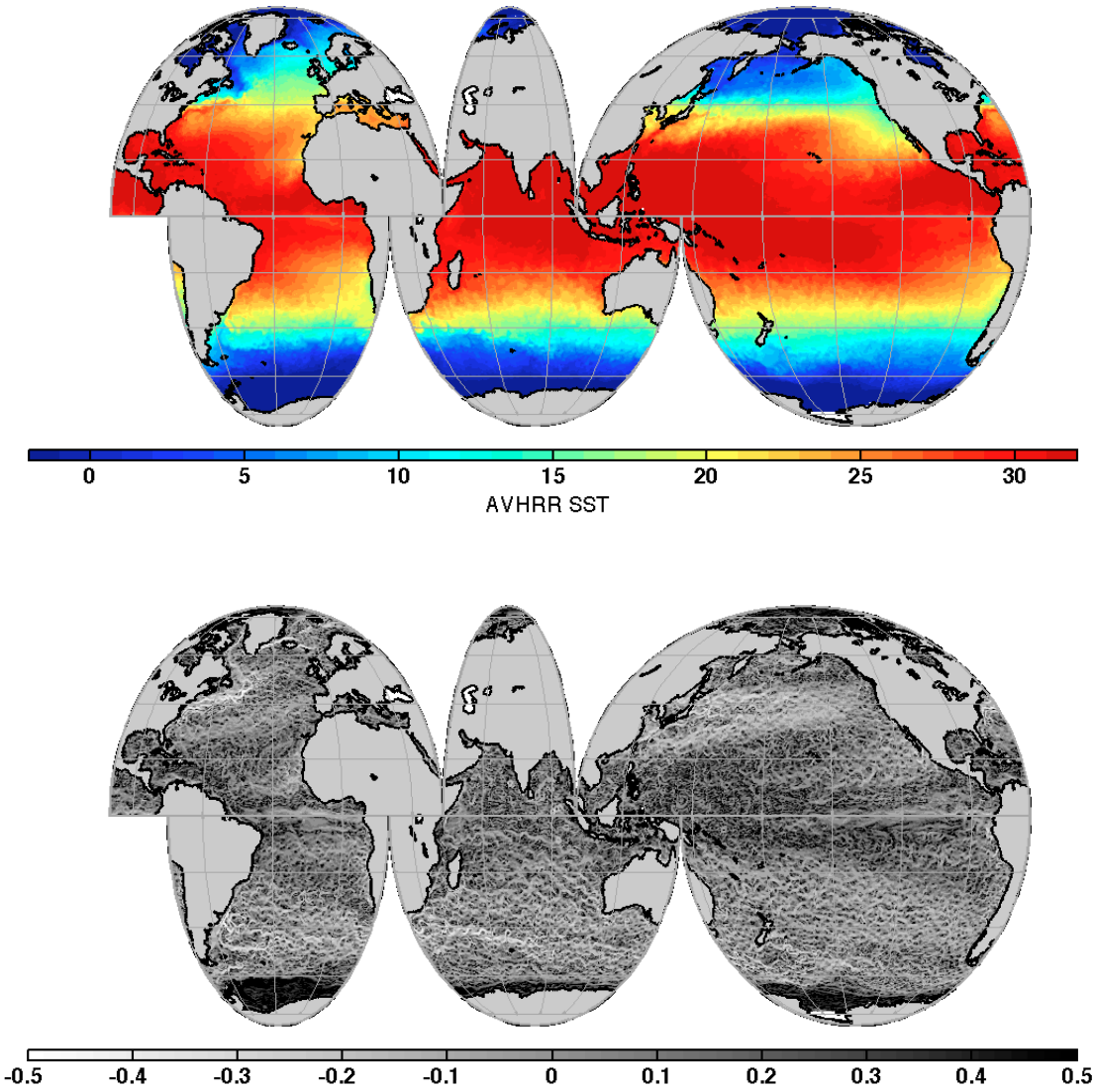

Figure 5.12: Map AVHRR SST (°C) (top) and (bottom) associated singularity exponents for the first nine days of June 2012.

with the geostrophic turbulence theory. Under this assumption, the upper ocean dynamics can be inferred from pressure variations, driven by sea level high and in a second order, surface density horizontal variations which are dominated by SST and SSS variations (Isern-Fontanet et al., 2006; LaCasce and Mahadevan, 2006).

The temporal evolution of ADT is significantly different from that of SST or SSS, as ADT is an active scalar driving the circulation and so it is not simply passively advected by the flow; in particular, its evolution is highly non-linear. For instance, the ADT response to changes in large-scale winds can be described as long first baroclinic mode Rossby waves whose evolution depends on the meridional advection of the background potential vorticity gradient. This term is important at large spatial scales. Nevertheless, horizontal advection is the dominant process

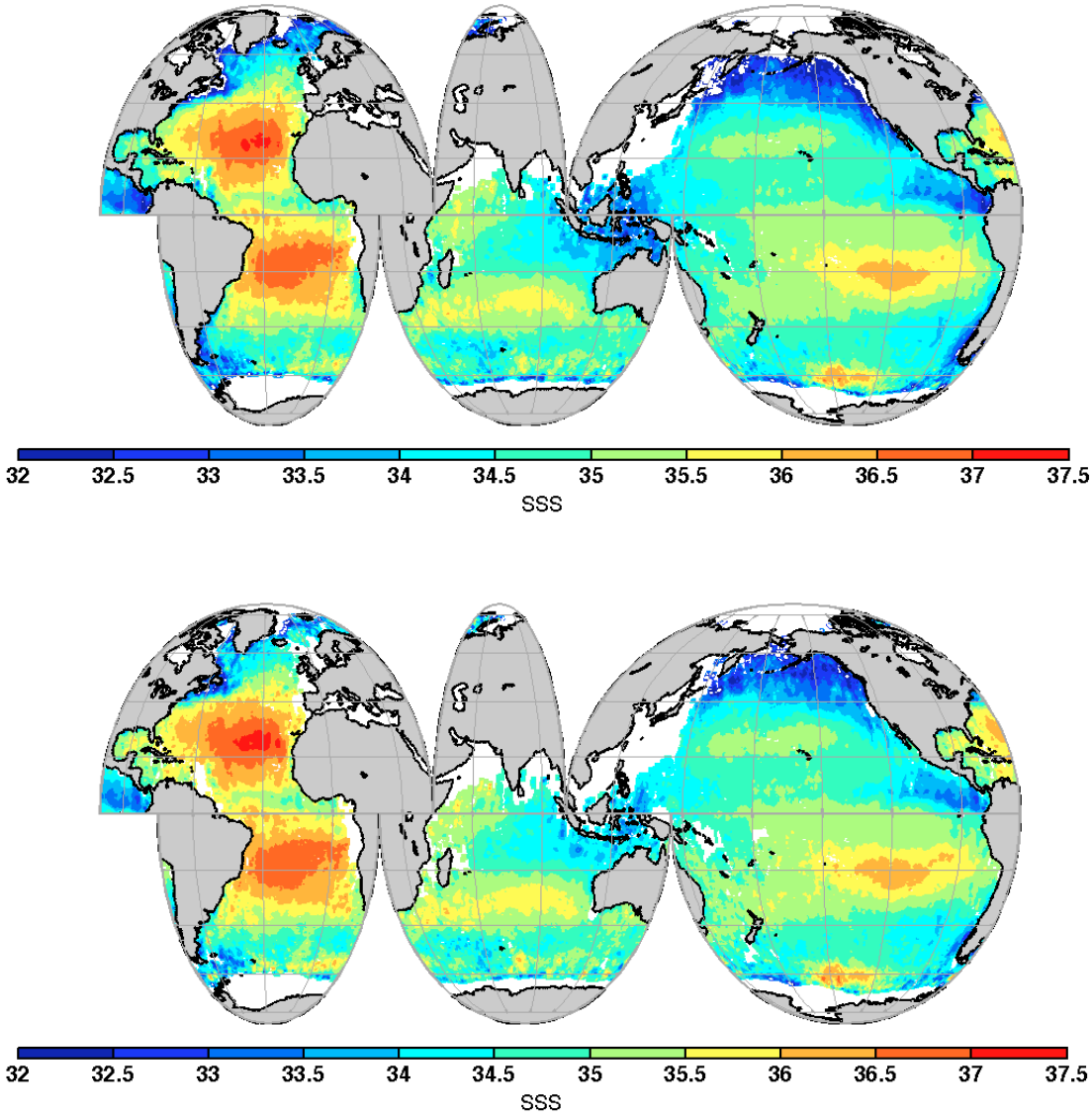

Figure 5.13: ***L4-1-AVHRR*** *SSS (top) and* ***L4-2-AVHRR*** *SSS (bottom) for the first nine days of June 2012.*

in the creation of localized strong gradients in ADT at the mesoscale. On a given passive or non-passive scalar such that horizontal advection is the only term inducing sharp transitions that is, introducing singular structure in the scalar, it follows that the singularity exponents derived from that scalar will be related to streamlines (Isern-Fontanet et al., 2007; Turiel et al., 2009), independent of the particular scalar of choice. The regions of the largest gradients in the ADT are associated with mesoscale fields where the Rossby number is large (we define the Rossby number as U/fL where U is the velocity scale, L is the length scale, and f is the Coriolis parameter). As advection becomes important at large Rossby numbers, we expect that the singularity fields of ADT will be similar to those of other scalar fields.

Using AVISO MADT as template (a sample map with the correspondent singularity exponents is presented in Figure 5.14), the data fusion is applied both to the original L3 SSS (section

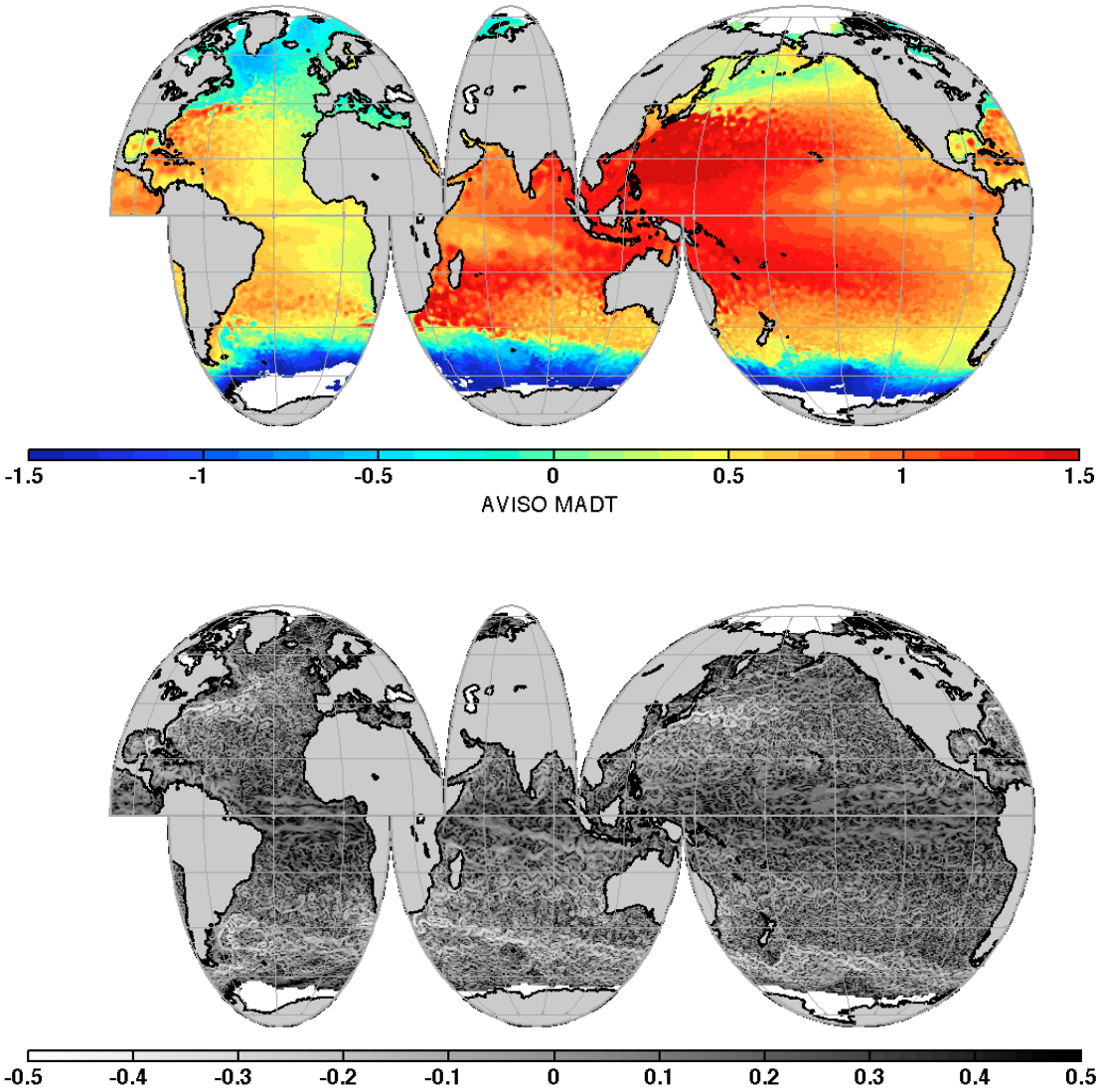

Figure 5.14: Map AVISO MADT (m)(top) and (bottom) associated singularity exponents for the first nine days of June 2012.

3.2.1) resulting in **L4-1-MADT** SSS, and to the L3 SSS coming from an alternative filtering of L2 data (section 3.5.1) resulting in **L4-2-MADT** SSS. A sample map of both **L4-MADT** products is presented in Figure 5.15. The validation of the resulting 9-day **L4-MADT** SSS products calculated every three days is made using close-to-surface data from Argo profilers following the same procedure as in previous sections (see tables 5.9 and 5.10).

The number of total matchups are of the order of two-hundred thirty thousand. Both **L4-1-MADT** and **L4-2-MADT** have similar statistics than **L4-1-AVHRR** and **L4-2-AVHRR** (see tables 5.7 and 5.8 for comparison). At global scale the standard deviation of the SMOS minus Argo differences is slightly increased to 0.50 for **L4-2-MADT** SSS (it was 0.49 when using AVHRR SSS as a template); however the bias is reduced to -0.01 (it was -0.03). When

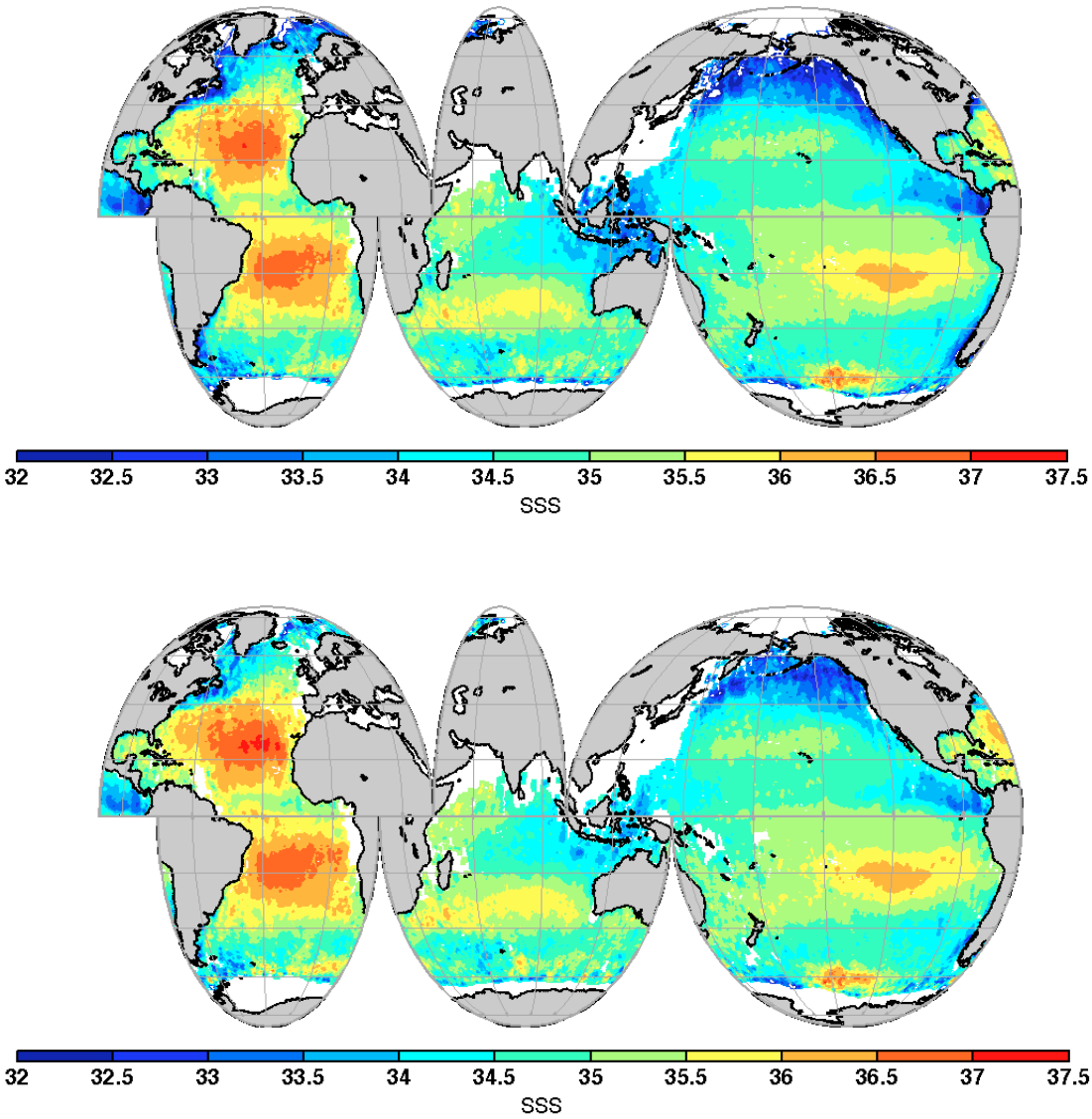

*Figure 5.15: Map **L4-1-MADT** SSS (top) and **L4-2-MADT** SSS (bottom) for the first nine days of June 2012.*

Latitude		**Global**	**60S-60N**				**30S-30N**				**Zone 122**			
Maximum depth				**>10 m**				**>10 m**				**>10 m**		
Coast distance					**1000 km**				**1000 km**				**1000 km**	
ECMWF-Argo SST						**<0.3 ºC**				**<0.3 ºC**				**<0.3 ºC**
L4-1-MADT	n	237999	233464	225342	131841	87420	126813	124041	75582	57854	7682	7564	6276	5114
	$\langle \Delta S \rangle$	-0.11	-0.10	-0.09	-0.02	-0.05	-0.15	-0.15	-0.13	-0.14	-0.18	-0.18	-0.14	-0.14
	$\sigma_{<\Delta S>}$	0.53	0.50	0.50	0.45	0.35	0.36	0.36	0.28	0.28	0.21	0.21	0.20	0.20

*Table 5.9: Statistics of 9-day **L4-1-MADT** vs Argo SSS measurements for the year 2012.*

data are selected by latitudinal bands and distance to coast, the global error reduces from 0.50 (global) (it was 0.49), to 0.49 (bounded by latitude 60; it was 0.47), to 0.37 (bounded to latitude 30; it was 0.35) and to 0.22 (in Zone 122 it was the same 0.22). The biases are -0.01 (global; it was -0.03), 0.00 (bounded by latitude 60; it was -0.02), -0.07 (bounded to latitude 30; it was

Latitude		Global	60S-60N				30S-30N				Zone 122			
Maximum depth				>10 m				>10 m				>10 m		
Coast distance					1000 km				1000 km				1000 km	
ECMWF-Argo SST						<0.3 ºC				<0.3 ºC				<0.3 ºC
L4-2-MADT	n	229146	225474	217858	130655	86633	121618	119047	74553	57142	7672	7554	6269	5107
	$\langle \Delta S \rangle$	-0.01	-0.00	0.00	0.02	-0.00	-0.07	-0.07	-0.08	-0.08	-0.16	-0.15	-0.12	-0.12
	$\sigma_{<\Delta S>}$	0.50	0.49	0.49	0.45	0.35	0.37	0.37	0.28	0.28	0.22	0.22	0.21	0.21

*Table 5.10: Statistics of 9-day **L4-2-MADT** vs Argo SSS measurements for the year 2012.*

-0.06) and to -0.16 (in Zone 122; it was -0.13). The bias is not reduced for this product when the matchups are restricted to narrower latitudinal bands.

When the data is requested to be more than 1000 km from the coast, the upper Argo measurement in the first 10 m below the ocean surface and points with differences between reference and in situ SST lower than 0.3°C, **L4-2-MADT** SSS estimates have biases of 0.00, -0.08 and -0.12 at the 60°, 30° latitude bands and Zone 122 respectively; and standard deviations of 0.35, 0.28 and 0.23 at the 60°, 30° latitude bands and Zone 122 respectively. Compared to the results when OSTIA SST or AVHRR SST were used as a template at the global and 60°, 30° latitude band, standard deviation are slightly worse, but the bias of **L4-MADT** are slightly better. In 30° latitude bands and Zone 122, **L4-MADT** SSS estimates are similar or do not improve the results.

Although resulting maps qualitatively differ, it is not clear which template give better results when validating with Argo measurements at a global scale, although using SST templates give slightly better results than using absolute dynamic topography. In next chapter we will analyze the effect of using different templates in the specific case of Western boundary currents, where the high mesoscale activity will give us more insight in the relation between SSS and the different variables used as template in the data fusion.

5.3 Fusion using mean auxiliary parameters

Our fusion method is based on estimating the local functions $a(\vec{x})$ and $b(\vec{x})$ of the linear approximation, Eq. (4.31), and then applying them to the SST template in order to construct the fused SSS map. As previously discussed, we have not in general access to those functions but to certain estimates, that we have calculated here by means of the expression in Eq. (4.33). The estimates for the local slope and local intercept functions, $\hat{a}(\vec{x})$ and $\hat{b}(\vec{x})$, provide particular useful information about the structure of the ocean, as they convey information on the local functional dependence between SST and SSS. In Figure5.16 we show an example of the monthly mean of both estimates for the month of June 2012.

Positive values of $\widehat{a}(\vec{x})$ are found in areas where SSS increases as SST also increases; this situation, which is typically found in the subtropical gyres, is more intense in the Atlantic Ocean than in the Pacific Ocean. This relation varies during the year largely driven by the seasonal cycle of sea surface temperature. On the other hand, the local slope, $\widehat{a}(\vec{x})$, is negative at those places where SST increases as SSS decreases. This is the situation which happens around the equatorial bands; see for instance the warm pool in Pacific Ocean, the footprint by

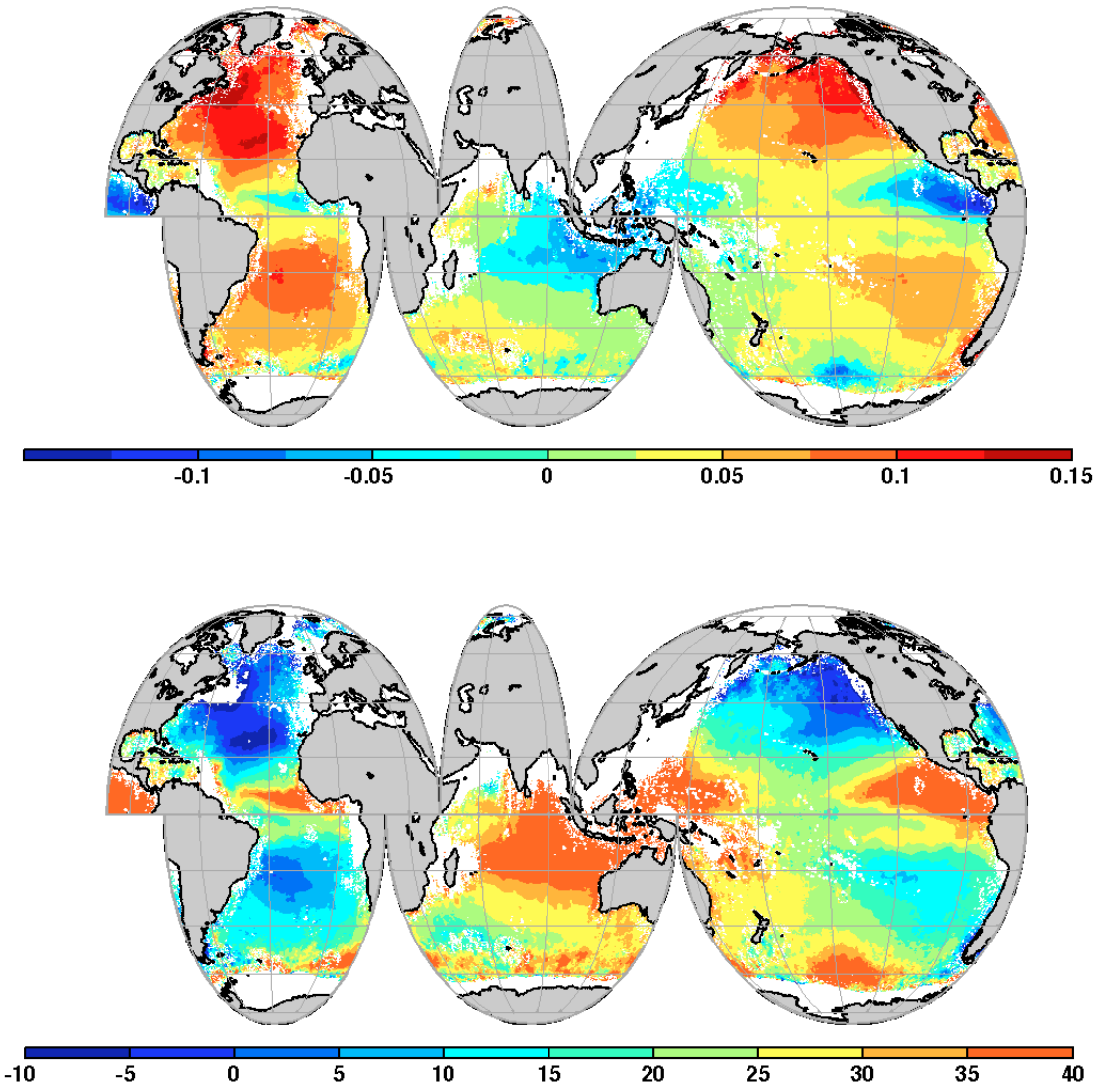

Figure 5.16: **Top:** *Local slope estimation* $\hat{a}(x)$. **Bottom:** *Local intercept estimation* $\hat{b}(x)$. *Monthly mean of the estimations used in the derivation of the 9-day* ***L4-2*** *maps as presented in Figure 5.1 for June 2012.*

the Amazon, Congo and Niger plumes in the Equatorial Atlantic, and a vast area of exchange between the Pacific and the Indian Oceans. In those regions, although the SST is the highest in the globe, salinity is affected by major river discharges and rainfall that decrease salinity. The other observed negative structures, all in the Southern Ocean, should be taken with caution given the present limited capability of the instrument to provide an accurate SSS signal under strong winds and low SST.

The band of cool and fresh waters apparent all along the Equator with the strongest signal in the Pacific and Indian Oceans also corresponds to the highest values of the local intercept $b(\vec{x})$. In this regions, a reverse correlation between SST and SSS confirms that exist a different dynamic adjustment between SST and SSS and are thus dominated by specific processes. The

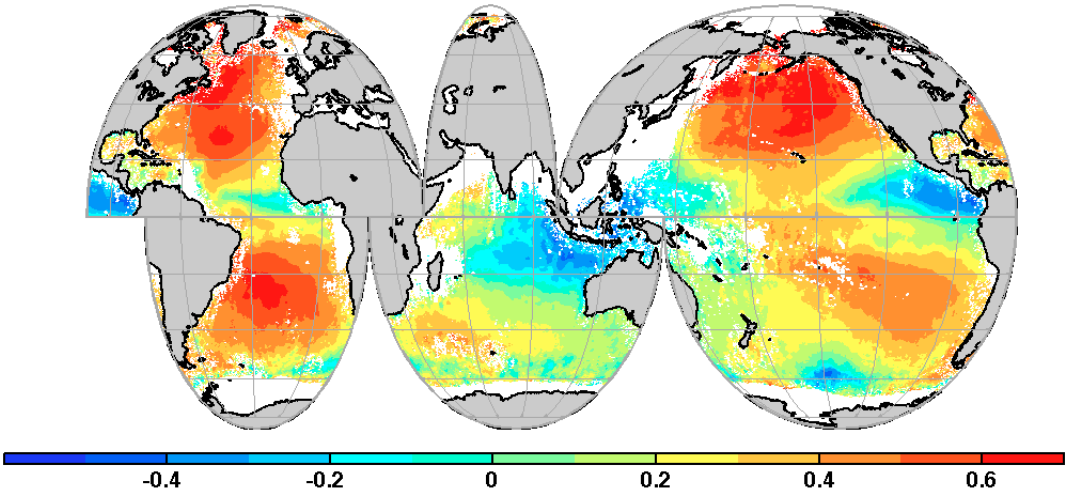

*Figure 5.17: Mean local regression coefficient of the estimation of local parameters used to produce the 9-day **L4-2** maps as presented in Figure 5.1 for June 2012.*

assumption of a local linear relation between SST and SSS is here less reliable, as the region has the lowest regression coefficients (Figure 5.17).

Local regression coefficients above 0.6 (in absolute value) are rare. The regression coefficients are not expected to be large due to present levels of noise in SMOS data. In the Equatorial Atlantic, Pacific and Indian Ocean, either additional variables should be taken in consideration to further improve the adequacy of our algorithm, or a more sophisticated relation between SSS and SST should be used. Interestingly enough, these regions are found around the Equator. This implies first that geostrophic adjustment is not valid on those regions and thus the flow are less barotropic; and secondly, they are affected by higher influxes of fresh water (coming from the river plumes in the case of the Atlantic, and in the Pacific and Indian Oceans given by rain discharges). It is also worth highlighting that although the size of the regions and their position (especially in the Equatorial Atlantic) vary with time, they are almost permanent features along all the year.

A further step is here taken by using the monthly mean values of local regression coefficients as an alternative extrapolation ability of our fusion method. Now the L4 SSS ($\tilde{s}$) is computed by:

$$\tilde{s}(\vec{x}) \;=\; \overline{a}(\vec{x})\,\theta(\vec{x}) \;+\; \overline{b}(\vec{x}) \tag{5.1}$$

where $\overline{a}(\vec{x})$ and $\overline{b}(\vec{x})$ are monthly mean values of the estimates $\hat{a}(\vec{x})$ and $\hat{b}(\vec{x})$ in Eq. (4.33) presented in Chapter 4.

Following Eq. 5.1, we produce 9-day **L4-AB** SSS maps using OSTIA SST as a template, and mean local regression coefficients. The mean values of the local regression coefficients are computed as monthly averages of the 9-day correlation coefficients from the generation of **L4-2** SSS (section 5.1) without any extrapolation. A sample map of the resulting **L4-AB** is presented

in Figure 5.18 for the first 9-day of June 2012 (compare to 5.1 bottom where the **L4-2** is produced by extrapolation).

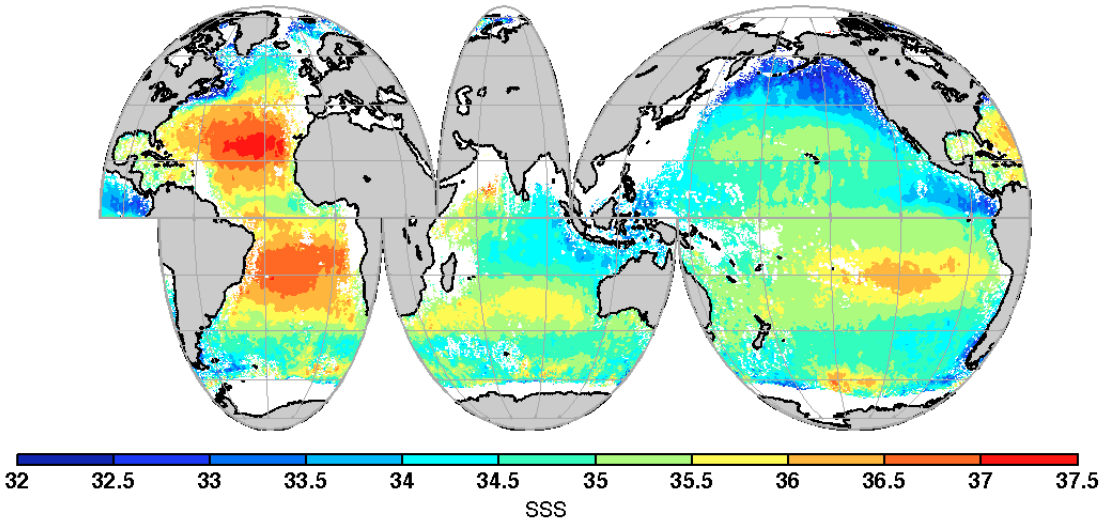

Figure 5.18: Map of surface salinity applying data fusion OSTIA SST using monthly mean linear coefficients for the first nine days of June 2012.

Latitude		**Global**	**60S-60N**				**30S-30N**				**Zone 122**			
Maximum depth				**>10 m**				**>10 m**				**>10 m**		
Coast distance					**1000 km**				**1000 km**				**1000 km**	
ECMWF-Argo SST						**<0.3 ºC**				**<0.3 ºC**				**<0.3 ºC**
L4-AB	n	216188	213257	206580	129817	85970	113856	111463	73361	56254	7567	7448	6274	5129
	$\langle \Delta S \rangle$	-0.03	-0.02	-0.02	0.01	-0.01	-0.07	-0.07	-0.06	-0.07	-0.12	-0.12	-0.09	-0.09
	$\sigma_{<\Delta S>}$	0.47	0.46	0.46	0.43	0.33	0.31	0.31	0.27	0.26	0.21	0.21	0.21	0.21

*Table 5.11: Statistics between **L4-2** SSS using mean $\overline{a}(\vec{x})$ and $\overline{b}(\vec{x})$ parameters vs Argo SSS measurements for the year 2012.*

The results of buoy collocation differences by latitude bands, distance to coastal areas, depth of the Argo uppermost measurement and SST differences between Argo and ECMWF (following procedure used in previous sections) to quantitatively assess the new SSS L4 maps errors are presented in table 5.11.

The number of total matchups are of the order of two-hundred thousand. At global scale the standard deviation of the SMOS minus Argo difference is reduced to 0.47 (it was 0.49 for **L4-2** in section 5.1), and the bias is the same: -0.03. The bias is as before systematically negative probably due to a bias in the processing or to the fact that Argo measures salinity several meters below the surface.

Isolating the different contributions, we have once again taken data selected by latitudinal bands: the standard deviation of L4 SSS is reduced from 0.47 (global) to 0.46 (bounded by latitude 60), to 0.31 (bounded to latitude 30) and to 0.21 (in Zone 122). The biases are -0.03 (global), -0.02 (bounded by latitude 60), -0.07 (bounded to latitude 30) and to -0.12 (in Zone 122); the mean biases are reduced from -0.03 (global), -0.02 (bounded by latitude 60), -0.07

(bounded to latitude 30) and to -0.12 (in Zone 122). This implies an improvement in standard deviation and a slightly worse bias as compared to the validations both for **L4-1** and **L4-2** presented in section 5.1.

When the data is requested to be more than 1000 km from the coast, the upper Argo measurement in the first 10 m below the ocean surface and points with differences between reference and in situ SST less than 0.3°C, **L4-AB** SSS estimates have negative biases of -0.01, -0.07 and -0.09 at the 60°, 30° latitude bands and Zone 122 respectively, and standard deviations of 0.33, 0.26 and 0.21 at the 60°, 30° latitude bands and Zone 122 respectively. When restricting the validation to the regions without known associated issues, the errors are similar to the **L4-2**, and better than in the case of **L4-1** presented in section 5.1. The use of monthly mean values of local regression coefficients allows a better global validation, particularly in most problematic areas as high latitudes and close to lands, but as this approach uses monthly mean local regression coefficient values and not the specific ones for the image produced, the quality degrades in locations where no extrapolation was needed or where the standard approach already provided an accurate SSS estimate.

5.4 Inter-comparison and Validation

This section aims at inter-comparing the best 9-day SSS maps obtained using the presented mapping methodologies. After the sensitivity tests undertaken in Chapter 3 and the validation against Argo data, we can conclude that the best L3 SSS is the one where a more restrictive L2 data filtering has been applied (as in section 3.5.1), the best OI SSS obtained is the one that uses ISAS as a background (as in section 3.5.2), and the best L4 SSS is the **L4-2** as in section 5.1 of this chapter. The inter-comparison and validation of these three 9-day products is done by using not only a validation against in situ data but also using the singularity exponents framework. In general, the singularity exponents reveal geophysical patterns as well as image artifacts that are not directly visible from the original satellite images and give us valuable information on the scales being represented by each product.

In Figure 5.19 we show an example of the application of the fusion algorithm, taking L3 SSS as signal and OSTIA SST as template in a region characterized by a strong salinity gradient: the Amazon plume.

As shown in the Figure, the fused image is considerably less noisy than the original one, although the actual amplitude of SSS gradients seems to be attenuated. When analyzing the structure of singularity exponents, we see that the original SSS is considerably noisy so just few structures can be recognized in the map of singularity exponents. On the contrary, the SST template exhibits a great richness of patterns associated with the circulation in the area. Singularity analysis applied to the fused SSS image reveals that all the structures present in the SST map are re-integrated in this map; additionally, specific SSS structures, such as the strong gradient associated with the Amazon plume, which are virtually absent in SST, appear clearly delineated by the singularity exponents of the fused SSS.

The chosen area is a favorable case, with the presence of a sharp, strong SSS gradient. For

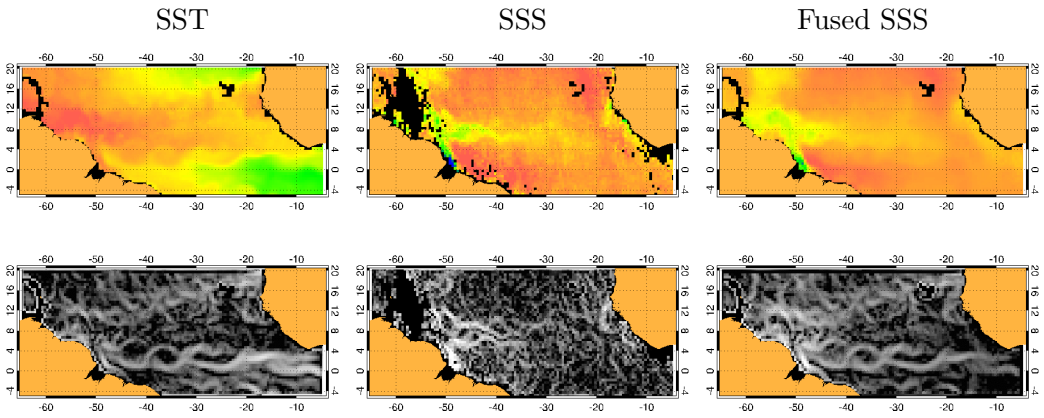

Figure 5.19: Detail on the performance of the fusion algorithm for a 9-day image on the Amazon plume area. First row: original data; Second row: associated singularity exponents.

assessing and inter-compare the quality of our fusion method at global scale, we have used L3 SSS and OI SSS maps as a reference.

In Figures 5.20, 5.21 and 5.22 we present three sample maps for L3 (as in section 3.5.1), OI (as in section 3.5.2) and L4 SSS (**L4-2** as in section 5.1), along with the associated singularity exponent maps. The original L3 data are affected by many noise and bias sources that break up spatial coherency, what is evidenced by the absence of structure in the singularity exponent map. On the contrary, both the OI and L4 SSS maps have a significant amount of the singularity structure restored.

For comparison on the singularity structure, see Figure 5.11 that shows the average OSTIA SST map for the same period and its associated singularity exponents. As the singularity lines align with the streamlines of the flow, we can recognize in the singularity analysis the main oceanic currents, that should be present independent on the scalar analyzed. Our present fusion algorithm falls short in restoring all the singularity structure present in the SST maps, what implies that further efforts should be conducted in that direction in the future. On the other hand, although OI restores the most relevant singularity fronts in SSS, it also introduces various spurious structures (many "eddy-like" circles in open ocean, probably a consequence of having a finite correlation radius).

To assess the amount of noise removed by one or the other technique we have calculated the difference between the original L3 SSS map and the SSS maps coming from our two filtering methods: optimal interpolation and data fusion. We compare the results of L3 (as in section 3.5.1), OI (as in section 3.5.2) and L4 (**L4-2** as in section 5.1). An example for the first 9-day of June 2012 is shown in Figure 5.23.

We observe that OI corrections are rather uniform in space and time, while L4 corrections are related to the intensity of the signal and therefore vary in space and time. The difference between the L3 and OI products lacks of spatial structure because the OI works as a Gaussian low pass filter acting upon the binned map. Given the limitations of the instrument, binned maps lack of small scale structure. On the contrary, the difference between the L4 and the binned

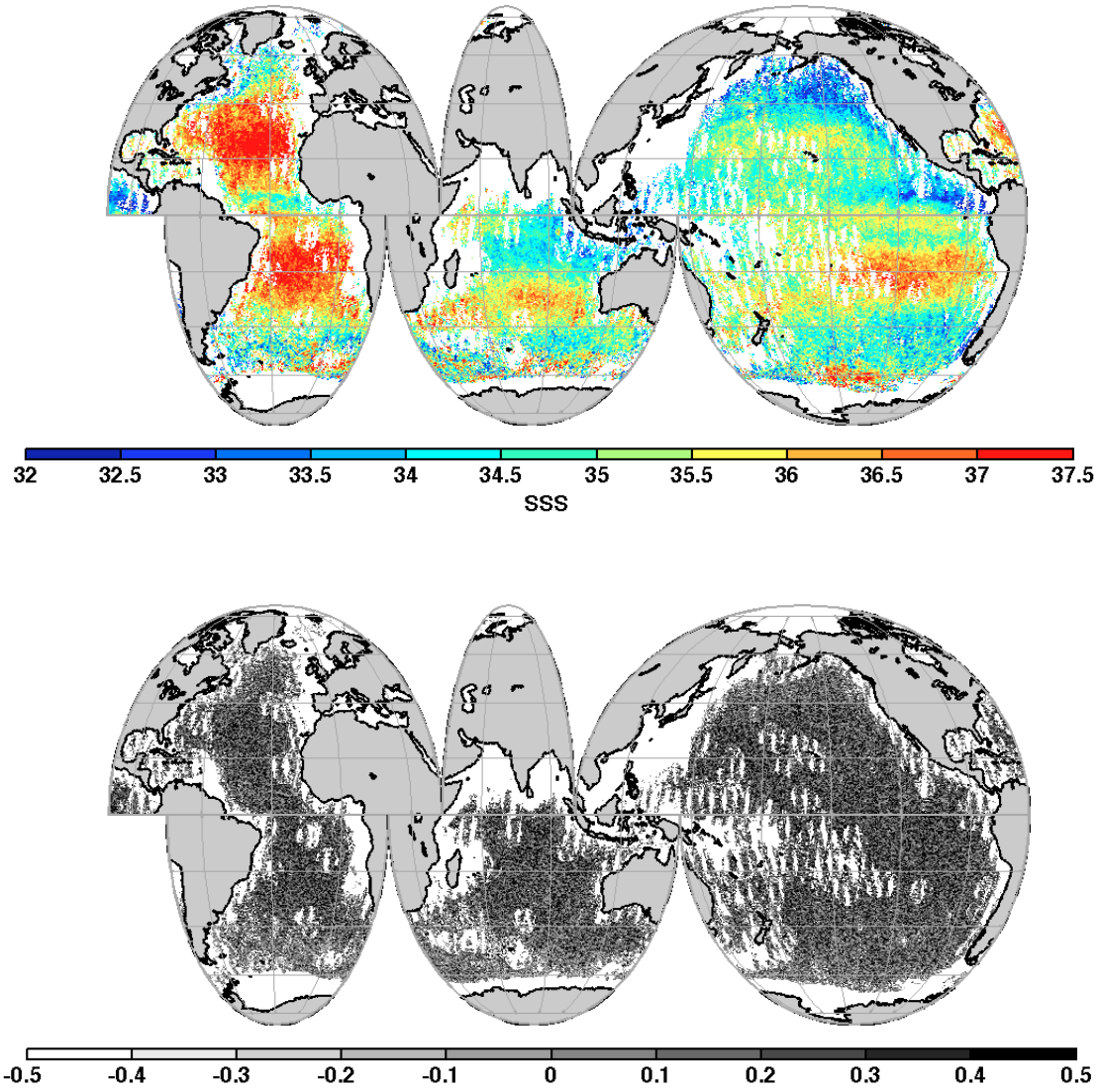

Figure 5.20: **Top:** *L3 SSS map corresponding to the average of the days 1 to 9 June, 2012 (section 3.5.1).* **Bottom:** *Associated singularity exponents.*

product displays large, spatially coherent structures. As shown in Chapter 4, the weights of L4 filter depend on the sign of the spatial correlation between SST and SSS. Thus corrections clearly differ between regions where evaporation is larger than precipitation (where correlations are predominantly positive) and regions where surface is affected by large precipitations or river discharges (where correlations are usually negative). As a result, the L4 filter is partially restoring spatial structure in the SSS maps coming from the SST maps, and this is observed in the difference map.

As the errors are likely to be related to the signal level, L4 corrections seem more physically meaningful than those of OI; notice also that OI only accounts for the second order statistics of SSS, and thus it deals incompletely with higher-order, non-linear effects. The absolute value

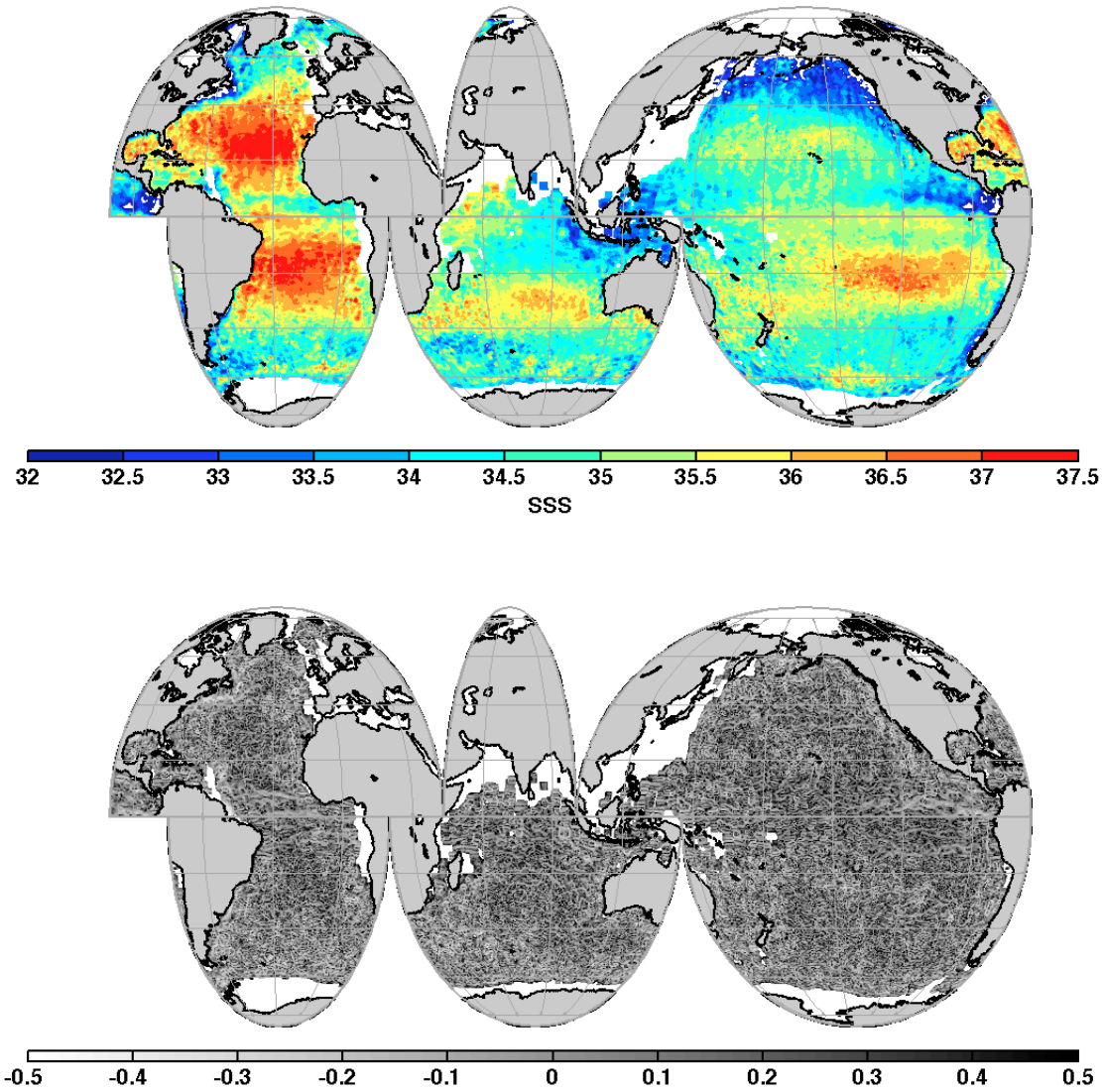

Figure 5.21: **Top:** *OI SSS map corresponding to the average of the days 1 to 9 June, 2012 (section 3.5.2).* **Bottom:** *Associated singularity exponents.*

of the differences, averaged over the entire global ocean and all the year 2012, is -0.00 with a standard deviation of 0.63 in the case of OI SSS and 0.00 with a standard deviation of 0.61 in the case of data fusion.

We compare the three types of SSS maps for the whole year 2012 with the measurements of quasi-surface salinity given by Argo floats following a different strategy as in previous sections. The matchup is done for each uppermost salinity of Argo, and each difference with respect to the SSS map is accumulated at a given grid point, without previous averaging of Argo data in the same spatio-temporal grid of satellite SSS, as in previous validations. Figure 5.24 shows the histogram of the differences between the L3 (section 3.5.1 blue), OI (section 3.5.2 green) and L4 (**L4-2** as in section 5.1 red) SSS and Argo SSS. The histogram refers to those points which are

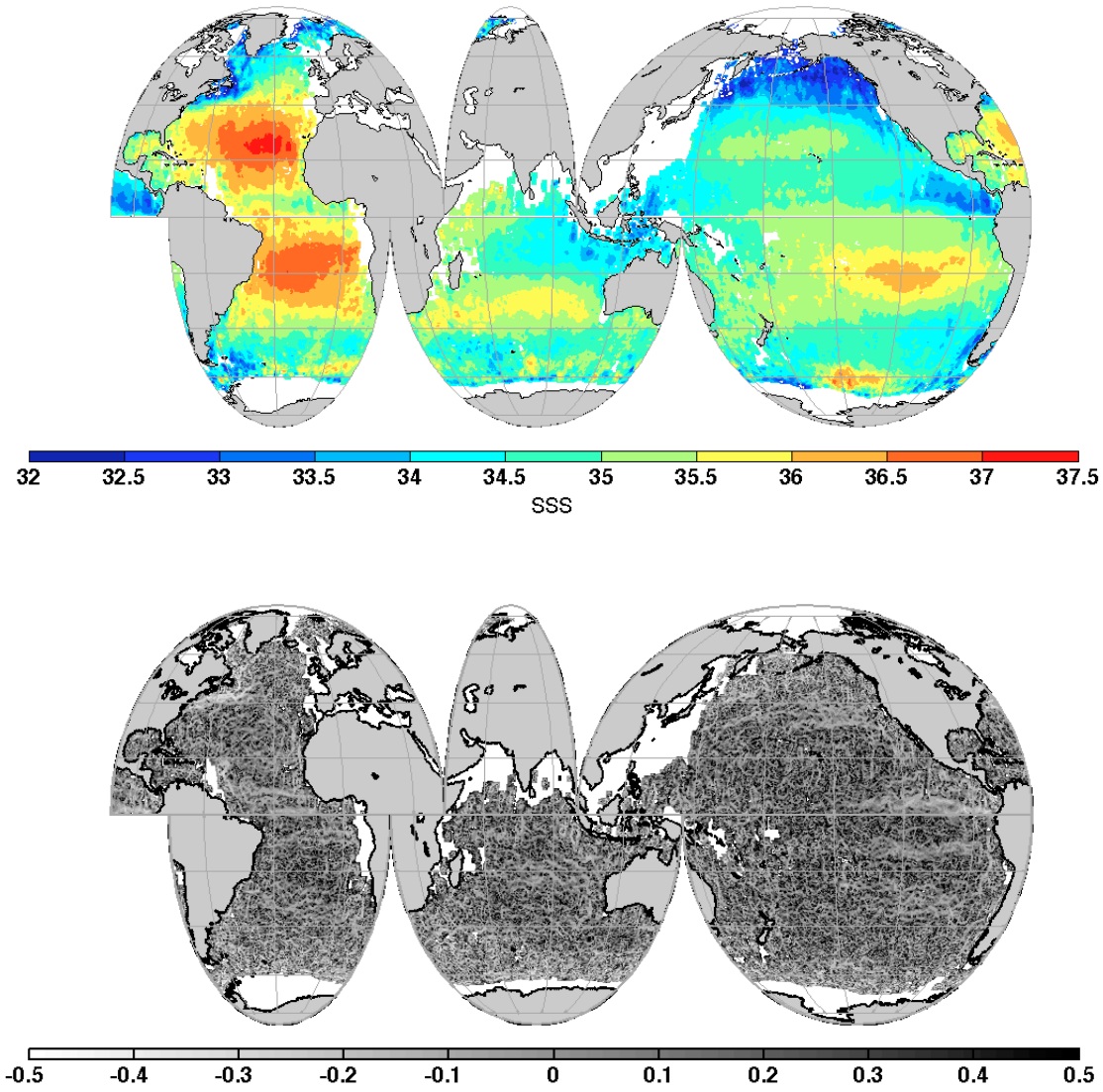

Figure 5.22: **Top:** *L4-2 SSS map corresponding to the average of the days 1 to 9 June, 2012.* **Bottom:** *Associated singularity exponents.*

defined in the L3 maps, since we do not want to analyze here the extrapolation capabilities of the OI or the fusion algorithm. The bias is almost the same ($\pm$ 0.00) for the three SSS products. Fusion leads to a considerable reduction of the standard deviation of the difference against Argo (from 0.75 to 0.49). OI it is also able to reduce the standard deviation (0.49, the same as for fusion). This implies that a homogenization as the one given by OI seems to lead to the same quality products as for the case of data fusion, at least in which regards to the amplitude of the signal.

However, the error is not homogeneously distributed over space. Argo floats tend to concentrate at given areas as on the edges of subtropical gyres. Some of these areas are particularly

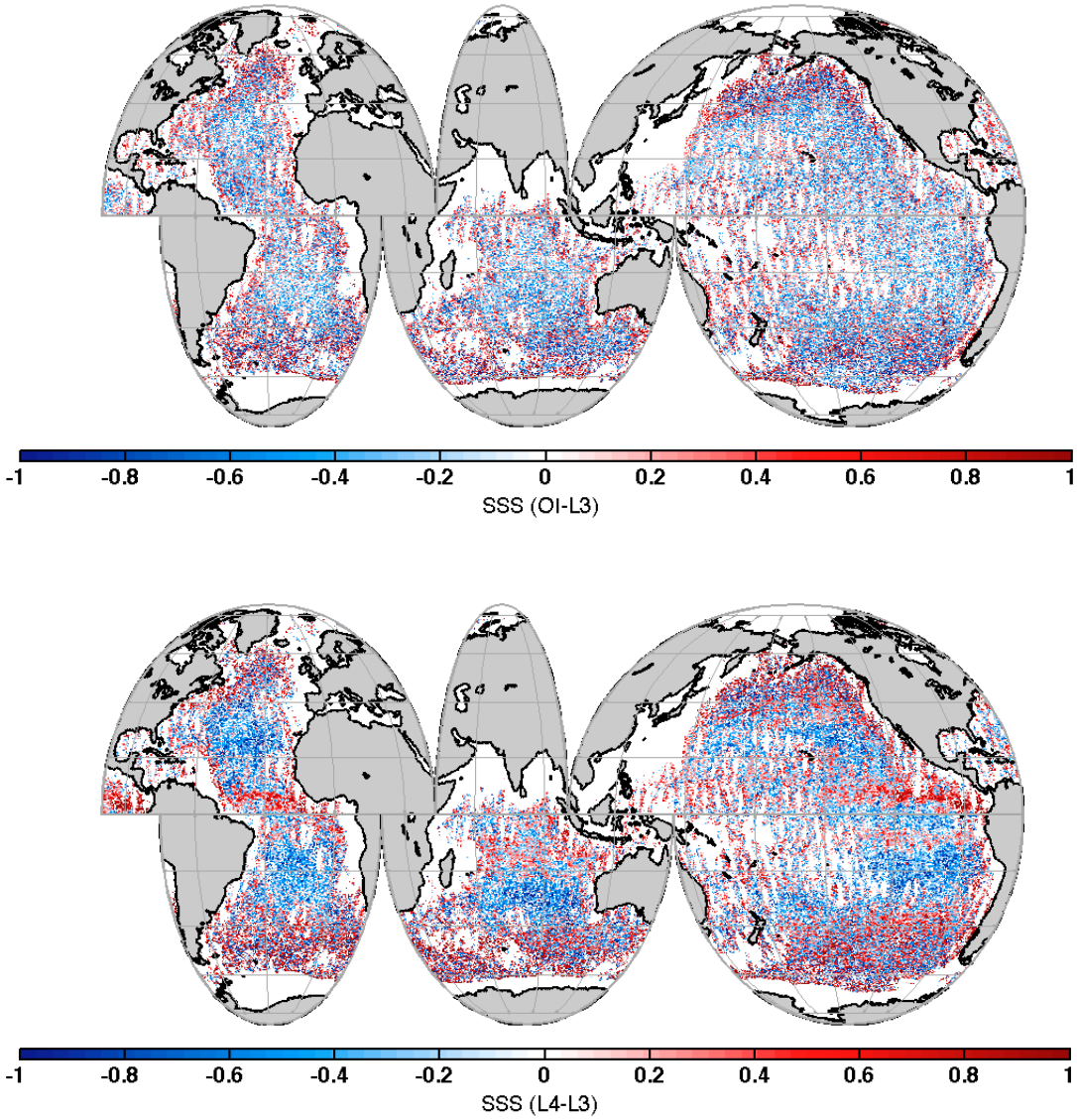

Figure 5.23: Difference of original and filtered salinities. **Top:** *OI SSS (section 3.5.2) minus L3 SSS (section 3.5.1).* **Bottom:** *L4-2 SSS minus L3 SSS (section 3.5.1).*

noisy, as for instance in North Atlantic, due to heavy contamination by RFI. Hence, relatively narrow geographic areas are given an excessive weight, offering an erroneous perception on the instrument performance and on the product quality. To correct this effect and illustrate the methodological improvement of L4 maps, we divide the global ocean by taking a more homogeneous sampling into 1° degree boxes. We define a quality metric associated to this homogeneous sampling by simply computing the mean and standard deviation of the differences SMOS-Argo at each box. We characterize the quality of the SSS maps on the boxes that contain a number of Argo data large enough; here this number has been fixed to 10 (to improve the confidence on this metric, it would be preferably to raise this number to at least 30, by extending the studied

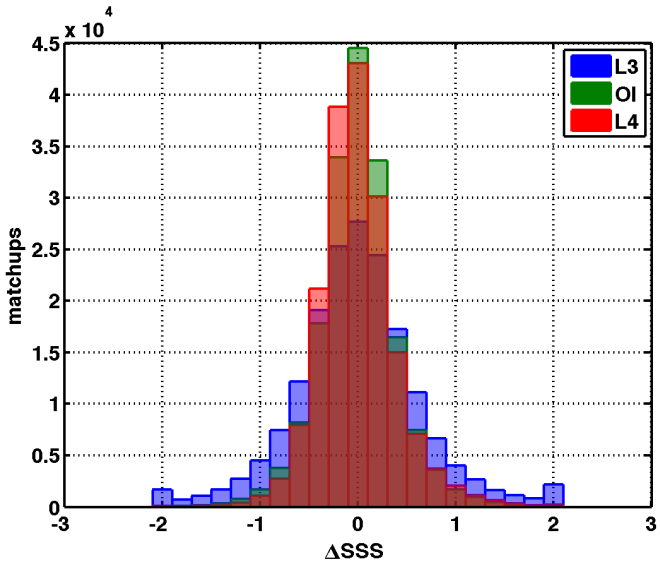

Figure 5.24: Histogram of the differences of SMOS maps minus quasi-surface minus Argo measurements. Blue: L3 SSS. Green: OI SSS data. Red: L4 SSS data. Notice that the bars at ±2 are excess bars (accounting for all the points deviating 2 or more from Argo). The mean and standard deviation for original SMOS SSS maps are -0.00 and 0.75, respectively; for OI SSS they are 0.00 and 0.49; and for L4 SSS they are -0.00 and 0.49.

period -one year- to a minimum of three years). In Figure 5.25) we present the average error with respect to Argo, while Figure 5.26 shows the associated standard deviations, in both cases for the full year 2012.

As shown in Figure 5.25 the biases of OI maps are better than L3 and L4, although the average biases are very similar over the whole ocean: -0.01, for L3 and L4, and -0.00 for OI. The data fusion approach seems to spread the biases already present in L3. Any systematic error in the data (as for example land-sea contamination) will be incorporated and spread in the L4. Land-sea contamination have a slow variation in space (typical scale of variability of 1000 km). Therefore the fusion method will not be able to mitigate this effect.

On the contrary, L4 is reducing the random uncertainty. As it is forcing the singularity exponents of SSS to be similar to the ones of SST, the data fusion approach removes incoherent structures (typical of uncorrelated noise). The standard deviations maps, Figure 5.26, show a clear progression according to the used data set. L3 maps have relatively large standard deviations (average: 0.51), which tend to be larger at regions which are known to be problematic: high latitudes in the North Atlantic and the North West Pacific (due to of the presence of ice and large RFI) and in the Southern Ocean (by reason of the limitations in the Geophysical Model Function for brightness temperatures and the incomplete knowledge of the effect of sea roughness (Guimbard et al., 2012)). OI maps lead to a considerable improvement in the standard deviation of the error relative to Argo (average: 0.29), with higher errors placed at the same difficult regions. Fused maps reduce still further the error in a significant level (average: 0.22), with the greatest error reduction taking place in the open ocean. This additional gain in error correction can possibly be explained by the partial restoration of the spatial coherence by use of the SST template.

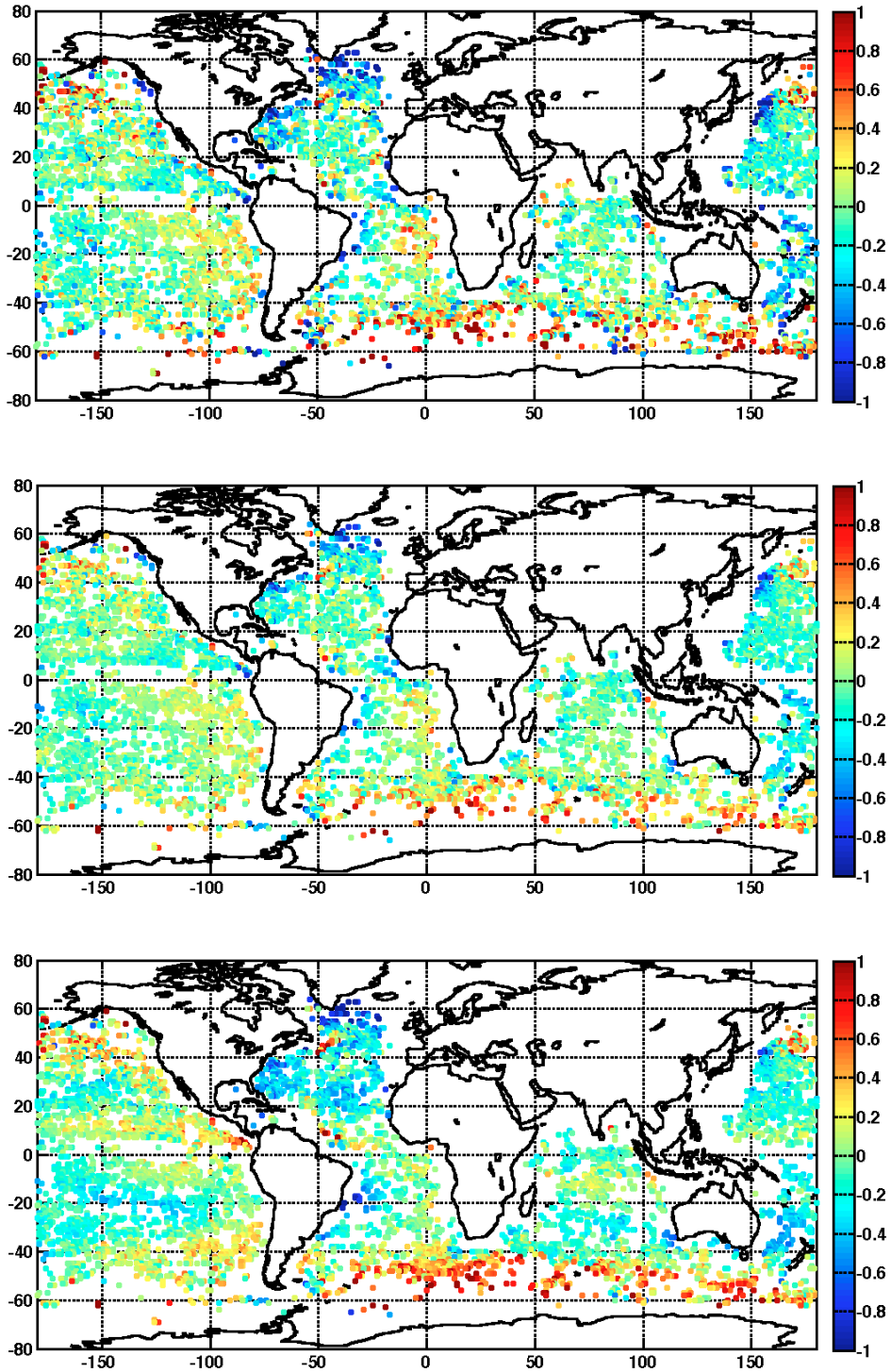

Figure 5.25: Spatial distribution of the differences of SMOS data minus Argo measurement. Each 1° degrees box contains the average of the ΔSSS recorded at that location; a minimum of 10 co-locations of SMOS data minus Argo is required, otherwise the box is left empty. Top: Original L3 SSS data; middle: OI SSS; bottom: L4 SSS. The spatial average errors (giving all the boxes the same weight) are -0.01, -0.00, -0.01 respectively.

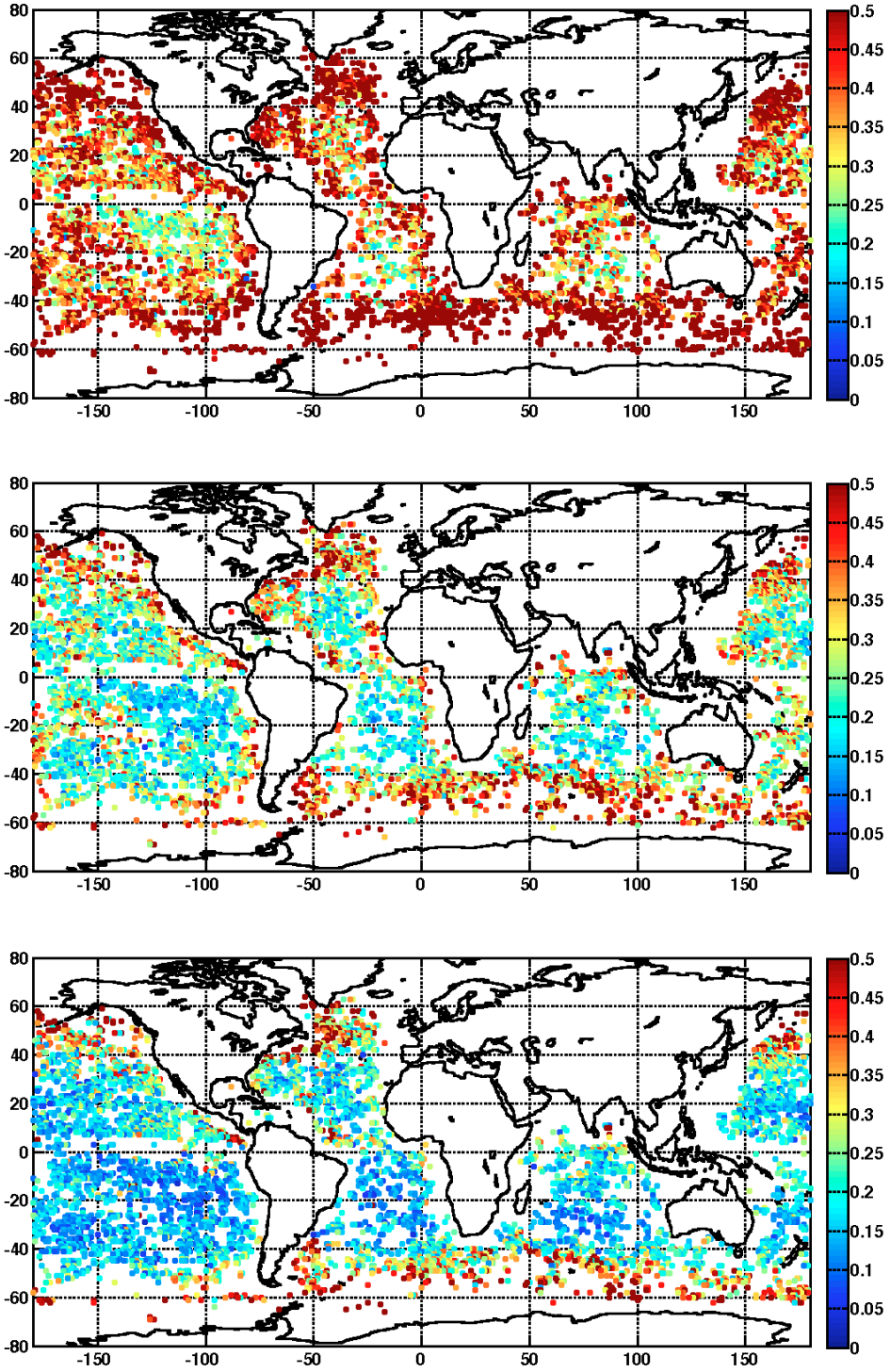

Figure 5.26: Spatial distribution of the standard deviations of SMOS data minus Argo measurement. Each 1° degrees box contains the standard deviation of the ΔSSS at that location; a minimum of 10 co-locations of SMOS data minus Argo is required, otherwise the box is left empty. Top: Original L3 SSS data; middle: OI SSS; bottom: L4 SSS. The spatial averaged standard deviations (obtained from the average variance, giving all the boxes the same weight) are 0.51, 0.29 and 0.22, respectively.

Chapter 6

Oceanographic application: SSS signature of mesoscale rings in western boundary currents

Large-scale winds and Earth rotation create five major subtropical gyres that define ocean circulation at global scale. Due to Earth rotation and the existence of ocean basins water circulation is intensified on the western boundaries of each subtropical gyre creating what is known as western boundary currents (WBC) (Sverdrup et al., 1942). All subtropical ocean basins have one of these western boundary currents: 1) the Gulf Stream in the North Atlantic Ocean, 2) the Brazil Current in the South Atlantic Ocean, 3) the Agulhas Current in the Indian Ocean, 4) the Kuroshio Current in the North Pacific Ocean and 5) the East Australian Current in the South Pacific Ocean. Westen boundary currents are fast-flowing currents releasing heat and moisture to the atmosphere along their paths (Wu et al., 2012). Dynamic instabilities and smaller-scale dynamics lead to a nonlinear generation of eddies and filaments (Figure 6.1). Studying the salinity signatures in the western boundary currents and associated mesoscale eddies will be the focus of this chapter.

We have analyzed in detail two western boundary currents: the Gulf Stream (GS) and Brazil Current (BC). The goal is to characterize SSS dynamics at the mesoscale (from 100 km and 3 days). In a WBC, mesoscale activity appears in the form of meanders and rings spawn by these currents. We will discuss on the fitness of the different SMOS SSS products presented along this thesis, to study the SSS structure of the mesoscale rings both in the Gulf Stream and the Brazil-Malvinas Current System. The work in this chapter extends a previous work (Umbert et al., 2015) on the use of the data fusion method (Chapter 4) on Aquarius SSS measurements, which lead to a product on which the mesoscale structures can be properly tracked and characterized, in contrast with the Aquarius L2 data, which due to its lower resolution cannot resolve eddy structures.

We have focused our study on the year 2012. Over the full year we have studied SMOS L3 SSS 9-day maps and L4 SSS maps obtained by fusing SMOS with two different geophysical templates: absolute dynamic topography (ADT) from AVISO and sea surface temperature (SST) from AVHRR. To provide quality metrics, we have first validated the different products against

A similar study to the one in this chapter using Aquarius SSS was presented in: ***Umbert, M., Guimbard, S., Lagerloef, G., Thompson, L., Portabella, M., Ballabrera-Poy, J. and Turiel, A., 2015. Detecting the surface salinity signature of Gulf Stream cold-core rings in Aquarius synergistic products. Early Scientific Results from the Salinity Measuring Satellites Aquarius/SAC-D and SMOS, Journal of Geophysical Research: Oceans, in press.***

Partially developed during second PhD stage in Washington University and Earth and Space Research (ESR) in Seattle (USA), under the supervision of Prof. LuAnne Thompson and Prof. Gary Lagerloef.

available in situ data in the mentioned WBC regions, and secondly, a verification of the expected SSS signature of the eddies is carried out by using and automatic eddy detection and tracking method presented in Mason et al. (2011).

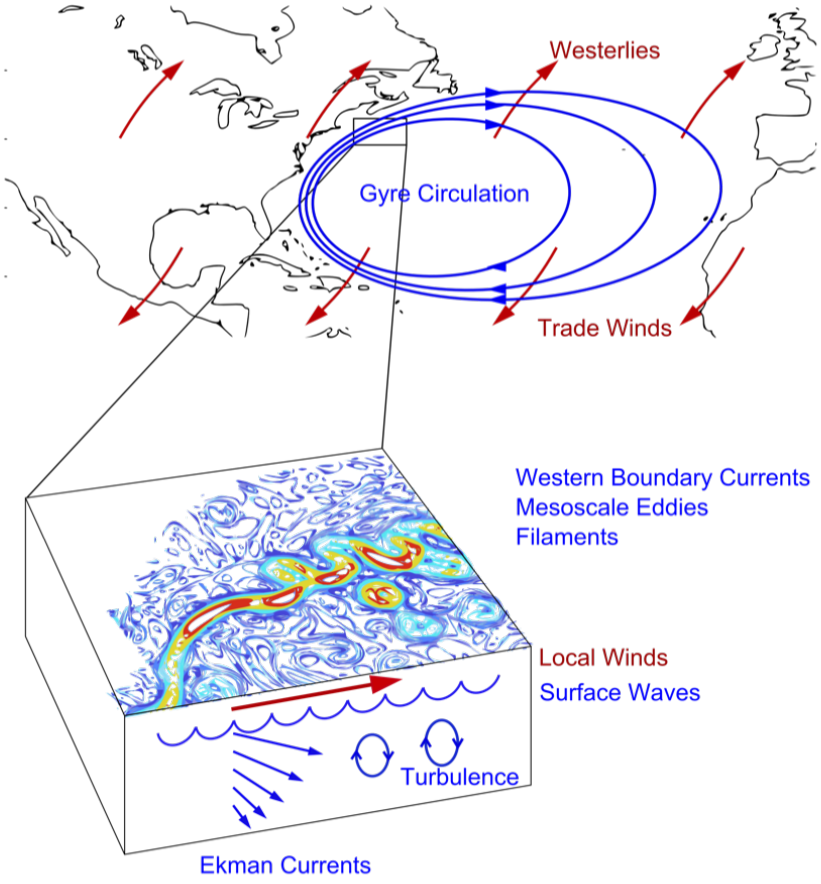

Figure 6.1: Schematic of near-surface currents focused on the western boundary current of the Gulf Stream (Image source: Kathleen Dohan (Earth and Space Research, Seattle))

6.1 Case studies: Gulf Stream and Brazil current

The difference in land mass distribution between the Northern and Southern Hemispheres leads to fundamental differences among WBCs. The Southern Hemisphere WBCs interact strongly with the Antarctic Circumpolar Current, especially in the Indian and Atlantic sectors, where heat is transported toward the pole via eddies associated with the WBC extensions. Heat loss over WBC extensions of the Northern Hemisphere tends to be stronger than over those of the Southern Hemisphere, provided that adjacent larger continental land masses on the west provide colder, dryer air masses over them (Siedler et al., 2013).

The **Gulf Stream** (GS) is a large-scale, WBC which transports warm (26-29°C) water

northward along the East Coast of North America. It leaves the coast near Cape Hatteras and heads into the North Atlantic Ocean. Between Cape Hatteras (75°W and 35°N) and the New England Seamounts (i.e. roughly east of 65°W and north of 37°N, Figure 6.2) strong horizontal density gradients extend throughout the water column. The GS plays a major role in the meridional transport of heat and salt across the North Atlantic Ocean acting as a barrier between the cold (10-18°C during Summer) and relatively fresh (salinities around 30-32 in the practical salinity scale, (Lewis, 1980)) waters from the Labrador Current and the warm (23°C), salty (36), clear, and unproductive waters of the Sargasso Sea.

After leaving Cape Hatteras, the Gulf Stream forms large-amplitude meanders (180-380 km) (Savidge, 2004) fed by a combination of baroclinic and barotropic instabilities. The size of the meanders may become large enough to break off the stream and loop back onto themselves to form detached rings (Saunders, 1971; Evans et al., 1985). Meanders that separate north of the stream axis become anti-cyclonic rings of Sargasso Sea warm water surrounded by the cold waters of the continental margin. Conversely, the meanders separating south of the stream axis become cyclonic rings of tropical water around a cold, nutrient-rich center (Richardson, 1983; Tomczak and Godfrey, 2003). The diameter of the rings typically range from 100 to 400 km (Parker, 1971). They may have a signature in temperature and velocity down to the ocean floor, at depths of more than 4000 m, and usually move westward when they detach from the Gulf Stream and eastward when attached (Fuglister, 1977; Csanady, 1979). Thus, warm-core rings can bring significant amounts of warm tropical water to the continental slope and near-shelf seas north of the Gulf Stream. Similarly, cold-core rings bring cold, nutrient-rich shelf water, to the biologically barren Sargasso Sea waters (Pingree et al., 1979; Chelton et al., 2011).

The **Brazil Current** is the WBC of the South Atlantic subtropical gyre (Figure 6.2), it originates in the South Equatorial Current (SEC), which is the northern part of the South Atlantic subtropical gyre (Stramma et al., 1990; Peterson and Stramma, 1991). The Brazil Current flows southward confined to the continental shelf varying in size between 15-100 kilometers wide and 200-400 meters depth (Garzoli, 1993). The Brazil Current brings relatively warm, saline subtropical waters and separates from the western boundary where it meets the northward-flowing Malvinas Current. The combined flow of the two currents causes a strong thermohaline frontal region, called the Brazil–Malvinas Confluence (BMC). The Malvinas Current, which originates as a branch of the Antarctic Circumpolar Current, transports relatively cold, fresh subantarctic water northward along the 1000–1500 m isobaths of the Patagonian slope to the BMC near 39.5°S (Saraceno et al., 2004). After colliding over the continental slope, both currents turn offshore and develop large-amplitude meanders (wavelenghts of 400-500 km and amplitudes of 200 km) (Gordon, 1989).

Warm-core eddies are formed as a detachment of the southward extension of the Brazil Current. Cold-core eddies are also observed, though they are reported to form less frequently (Garzoli and Garraffo, 1989). The most energetic expression of the Brazil-Malvinas Current System occurs during summer in the Southern Hemisphere. The most challenging difference when studying both the Northern and Southern Hemispheres, is that there are far fewer observations of WBCs in the Southern Hemisphere. This is particularly acute for the Brazil and Agulhas

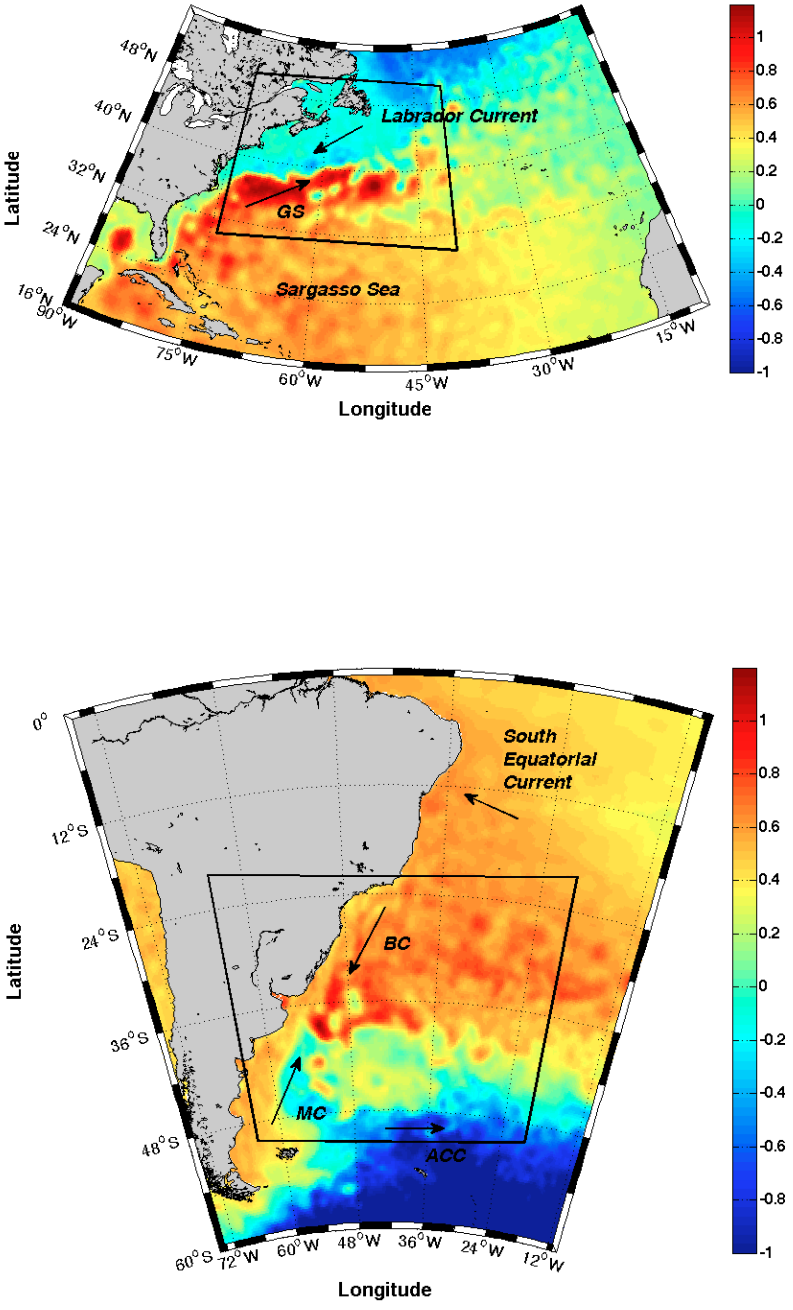

Figure 6.2: Absolute dynamic topography map (meters) for the 1st of June of 2012 in the Gulf Stream area (top) and in the Brazil Current area (bottom).

Currents, where long-term observations are largely needed (Siedler et al., 2013).

6.2 Conceptual model of Eddy Properties

The conceptual model (Chelton et al., 2011; Everett et al., 2012) used in the following sections describe the eddy surface properties expected in the different ocean variables used in this chapter. The conceptual model states that cyclonic eddies (also called cold-core rings (CCRs), as they trap colder waters inside the rings compared to the surrounding water) have anomalies that are negative ADT, SST, SSS and positive chlorophyll concentration as a result of cold nutrient rich waters trapped in the center of cyclonic eddies. Anticyclonic eddies (also called warm-core rings (WCRs), as they trap warmer waters inside the rings compared to the surrounding water) have positive anomalies for ADT, SST and SSS, with a deeper surface mixed layer and therefore lower chlorophyll concentrations.

Figures 6.3 and 6.4 show an example of satellite images of absolute dynamic topography, sea level anomaly, surface temperature and chlorophyll in the Gulf Stream for the 11th of September and in the Brazil Current for the 7th of November 2012. Superimposed to each image, the surface velocities from OSCAR current product are indicated by vectors allowing to distinguish cyclonic and anticyclonic structures. Accordingly with the conceptual model, CCR (closed structures turning anticlockwise in the Northern Hemisphere and clockwise in the Southern Hemisphere) have negative sea level and temperature anomalies, and higher chlorophyll concentration. On the other hand, WCR (closed structures turning clockwise in the Northern Hemisphere and anticlockwise in the Southern Hemisphere) present positive sea level anomalies, warm waters and low chlorophyll concentrations.

Satellite detection of WCRs on the continental slope and near-shelf seas has frequently been reported and is well documented (Lentini et al., 2006). As the surface temperature inside the ring is higher than the surrounding water, warm rings can be easily identified using infrared imagery and radar altimeters (Saraceno and Provost, 2012), and their monitoring is only limited by data missing due to clouds, aerosols, or orbital gaps. Absolute dynamic topography (ADT) has the advantage of offering all season/all weather satellite tracking. But as ADT maps are constructed from altimetry tracks, they have limited temporal and spatial resolution as compared with satellite imagery. Infrared sea surface temperature (SST) imagery (excluding cloud areas) can be used to identify fronts, meanders and/or eddies with good spatial resolution, although seasonal forcing of the mixed layer may mask the surface signatures. On the other hand, as warm rings are islands of nutrient-poor water in a nutrient-rich environment, they are also easily distinguished in ocean color images (Cornillon et al., 1994; Leterme and Pingree, 2008; Lee and Brink, 2010).

The presence of CCRs has been found more challenging to track by thermal imagery as their originally cold surface water is rapidly warmed by solar radiation. The enhanced surface stratification leads to a progressive warming of the surface and a CCR gradually becomes less distinguishable through surface temperature (Kelly et al., 2010; Hausmann and Czaja, 2012). As cold water persists below the warm surface lid, CCRs can be detected by vertical profiles of temperature and salinity (Dewar, 1986). In contrast, CCRs maintain its low SSS signature longer than the SST one (The Ring Group, 1981). As such, satellite SSS imagery is expected

to help longer term tracking CCRs. SSS would have shorter horizontal scales of variability compared to SST considering that SSS has no direct exchange with the atmosphere unlike SST, where the atmosphere tend to smooth lateral variations of SST (Kolodziejczyk et al., 2015).

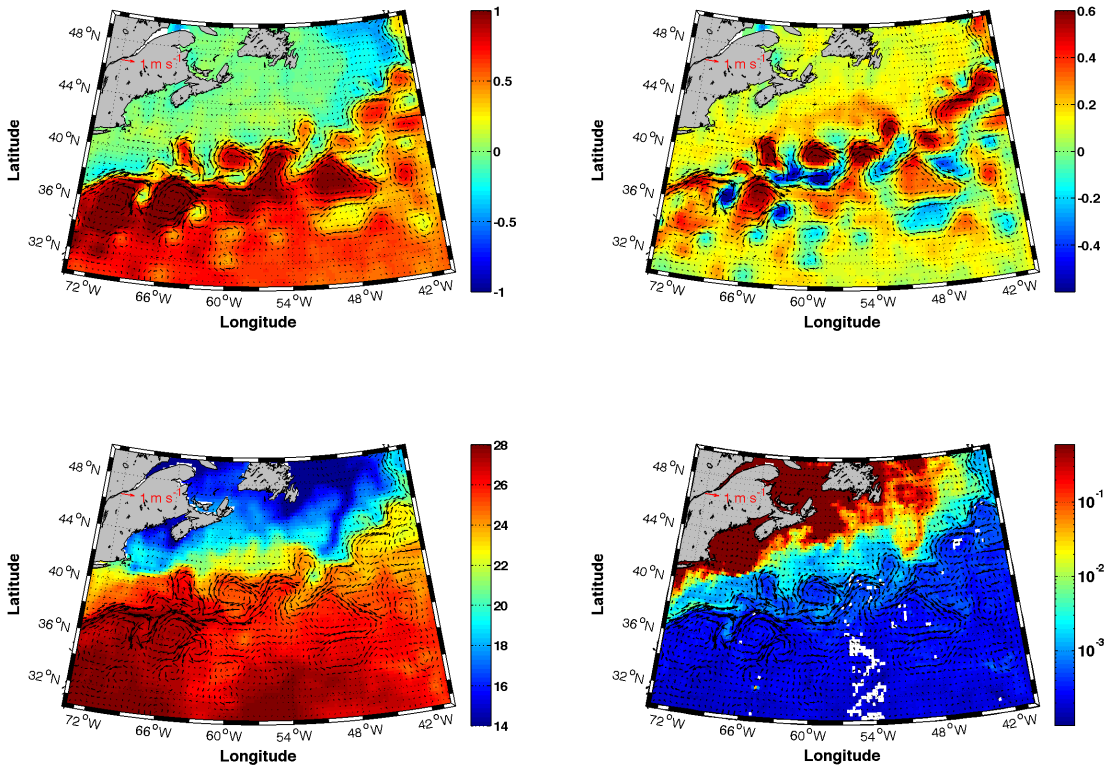

Figure 6.3: Top left: MADT (m); Top right: MSLA (m); Bottom left: SST (°C), and Chl-a (mg m^{-}3) (bottom right) for the 11th of September 2012 (0.25° resolution) in the Gulf Stream region. Surface velocity from OSCAR currents are indicated by vectors.

.

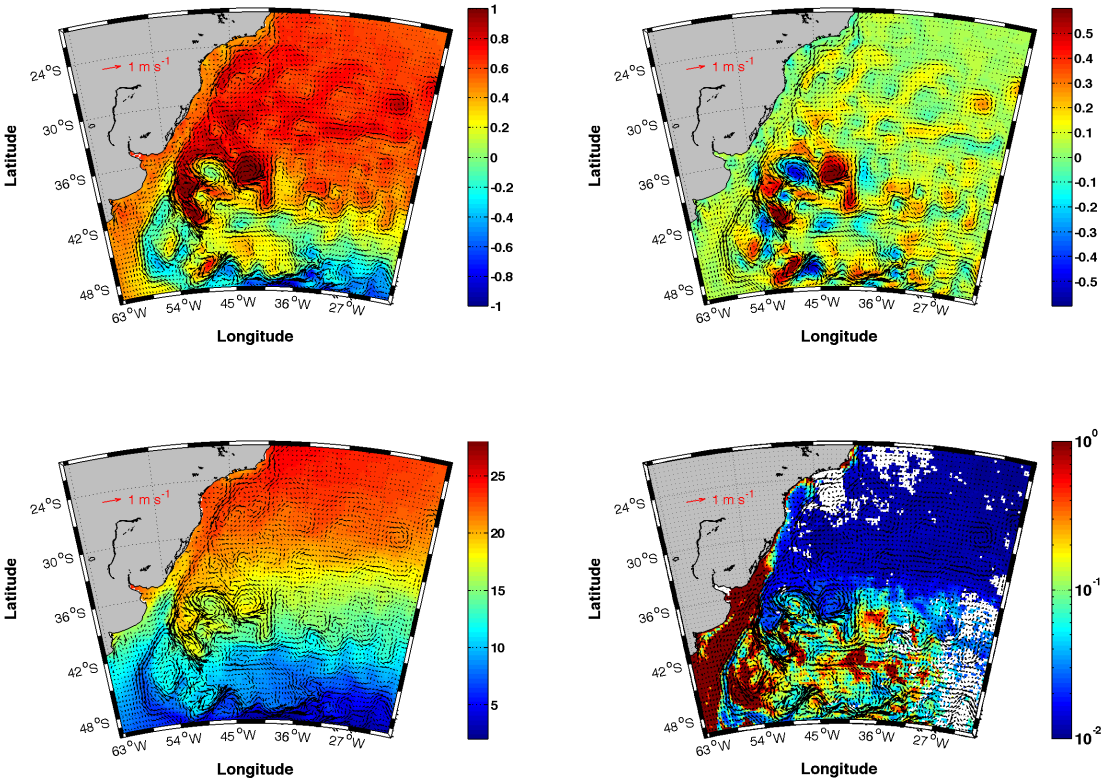

Figure 6.4: Top left: MADT (m); Top right: MSLA (m); Bottom left: SST (° C) and Chl-a (mg m−3) (bottom right) for the 7th of November 2012 (0.25° resolution) in the Brazil Current region. Surface velocity from OSCAR currents are indicated by vectors.

.

6.3 Signature of rings in SSS maps

Measurements acquired by SMOS during 2012 in the western North Atlantic was already used to reveal the evolution of the SSS structures meandering Gulf Stream in a previous study by Reul et al. (2014a) using CATDS-IFREMER SMOS SSS products. The resolution (45-km spatial resolution and three-day repeat subcycle) of SMOS observations allow the detection of meanders and ring structures of the Gulf Stream from SSS maps.

The superimposition of OSCAR velocity on L3 SSS maps for both studied areas (Figure 6.5) confirms the salinity signature stated by the conceptual model proposed in previous section 6.2. The cyclonic eddies correspond with fresh anomalies while anticyclonic rings correspond to salty anomalies. The data gaps of the image are related to the filtering strategy of the L2 SMOS SSS data, land-sea contamination and RFI. Note that the L3 is the product as described in Chapter 3 section 3.5.1, where a restrictive swath of 300 km is used to get rid of lower quality retrievals far from the center of the track of the satellite swath, and a swath of 100 km is used when we

are closer than 500 km of the coast to diminish the impact of land-sea contamination. Although it has better global scores against Argo in situ measurements, the amount of data gaps in the zone of the Gulf Stream WBC is rather considerable.

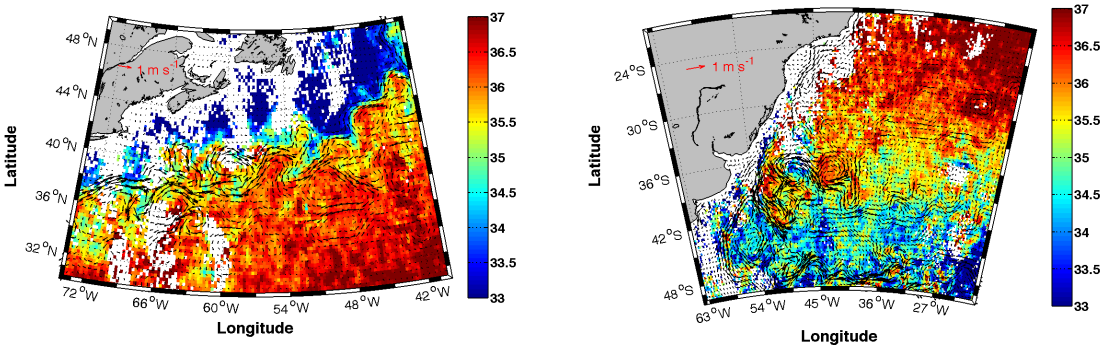

Figure 6.5: SMOS 9-day L3 SSS starting on September 11, 2012 in the Gulf Stream (left) and November 7, 2012 in the Brazil Current (right). Superimposed the OSCAR currents indicated by the vectors.

Figure 6.5 reveals that SMOS L3 can be used to detect the location of the haline front associated with the WBCs. The SSS signatures of the rings are also visible although noise and data gaps are quite pervading in the L3 SSS maps.

The data fusion algorithm (Chapter 4) is applied to 9-day SMOS L3 SSS maps for the year 2012 using two different templates, ADT and SST, as described in Chapter 5 section 5.2. The resulting L4 SSS maps will be called hereafter L4-ADT and L4-SST respectively. Figure 6.6 shows an example of both L4-ADT and L4-SST in the Gulf Stream (left) from September 11th and in the Brazil Current (right) from November 7th. The data fusion algorithm reduces the amplitude of the haline front associated with both WBCs and smooths the SMOS L3 map reducing the level of noise due to retrieval issues of SMOS salinity data.

Cyclonic and anticyclonic rings (as delineated by the OSCAR velocity field) exhibit the expected salinity signature also in Level 4 maps (see section 6.2). However, not all L4 products show the same amount of salty/fresh anomalies associated with anticyclonic/cyclonic rings. In particular, the L4-ADT (Figure 6.6 top) shows a larger amplitude in salinity anomalies as compared with the L4-SST (Figure 6.6 bottom). Indeed, the L4-ADT product exhibits a salinity signature, which coincides with most of the Gulf Stream meanders and rings depicted by OSCAR velocities (Figure 6.6 top). The L4-SST product does not reproduce a clear fresh anomaly for most of cyclonic rings in the Gulf Stream (Figure 6.6 bottom). The main drawback of using SST as a template in this region is linked to the fact that remote sensing SST have not enough accuracy to describe small changes in amplitude associated with the thermal degraded cold rings as the SST response in the shallow mixed layer results in heat fluxes veiling this mesoscale signals and so leading to over-smoothed fused images. This effect is particularly evident in summer.

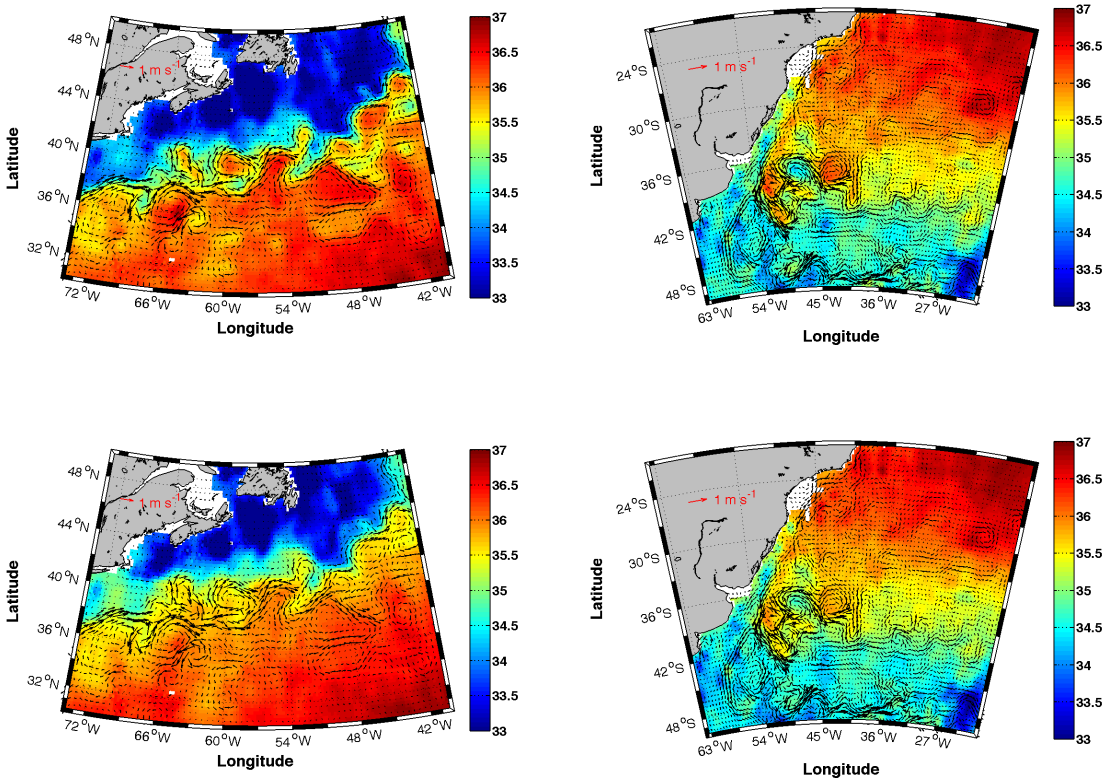

Figure 6.6: 9-day L4-ADT (top row) and L4-SST (bottom row) starting in September 11th in the Gulf Stream (left) and in November 7th in the Brazil Current (right). OSCAR currents, indicated by the vectors, superimposed.

6.4 In situ validation

A validation of the resulting SSS products is performed using in situ TSG salinity data from four different cruise campaigns carried out during 2012. We used 4 Thermosalinograph (TSG) data sets available during the period of the study by the following ships: Explorer (C6TN4), TARA (FVNM), Ronald H. Brown (WTEC) and the TMM Sinaloa (ZCDJ6). The TSG data are smoothed with a running Hanning filter of half width of ∼12.5 km (approximately half width of the quarter degree grid resolution) to have a spatial resolution to those of L3 and L4 SSS products. Due to the poor quality of SMOS SSS data near to the coast (the land-sea contamination is intense in this area), TSG data with distance from the coast smaller than 350 km were not considered.

Figure 6.7a shows the salinity values measured by TSG during the year 2012. The histograms of the differences between the different satellite products and TSG salinity data are shown in Figure 6.7, panels b-d. SMOS L3 (Figure 6.7b) presents the largest discrepancies from in situ observations, both in terms of the standard deviation and the inter-quartile range (iqr). In contrast, L4 data fusion products (Figure 6.7c-d) present a reduction of both the central value of the difference (mean or median) and the error when compared to the L3 product (Figure

6.7b). Of all the fused products, the L4-ADT (Figure 6.7c) is the closest to the in situ data (bias of -0.19 and error of 0.35), while the L4-SST (Figure 6.7d) presents worse scores (bias of -0.21 and error of 0.40).

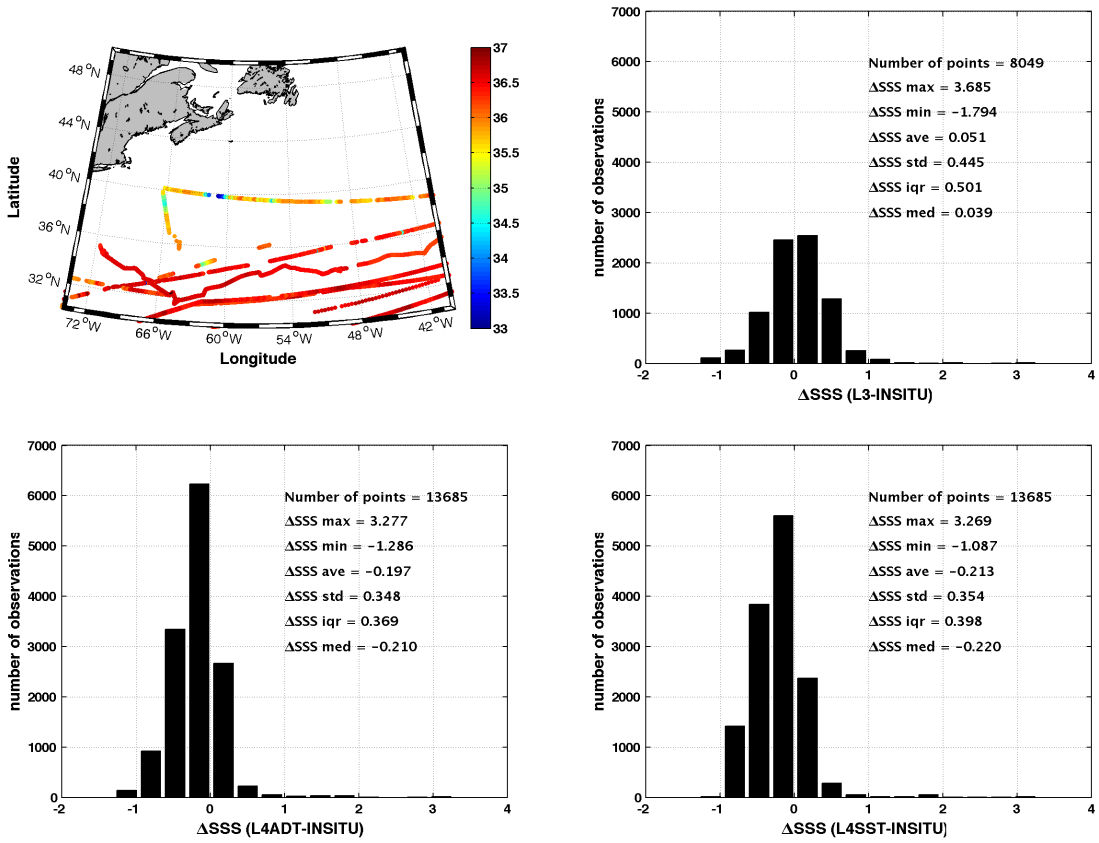

Figure 6.7: TSG in situ salinity (top left). SSS difference histogram with in situ data L3 SSS (top right), L4-ADT (bottom left) and L4-SST (bottom right).

Figure 6.8 shows a TSG transect from the Explorer vessel in the period August 13-17. In Figure 6.8a, the transect (thick solid line) is drawn on top of the L4-ADT map from August 15. The SSS map suggests that the Explorer TSG transect crosses the GS as well as two structures with apparent CCR signature (those around 56°W and around 50°W). Notice that west of the GS (65°W,40°N), the in situ SSS is higher than 35.5 indicating the presence of a WCR. The various salinity products show this salty anomaly and the location of the saline front associated with the GS (61-62°W,40°N).

In Figure 6.8b, the SSS data along the transect is shown for all the salinity products. The local salinity minimum around 56°W, as indicated by the TSG data, is completely missing in the L3 SSS product. The L4-SST product displays a slightly shifted (at 55°W) and a secondary minimum, while the L4-ADT displays a well-defined salinity minimum at the location of the CCR, i.e., in line with the TSG data. Although the amplitude of the minimum salinity is

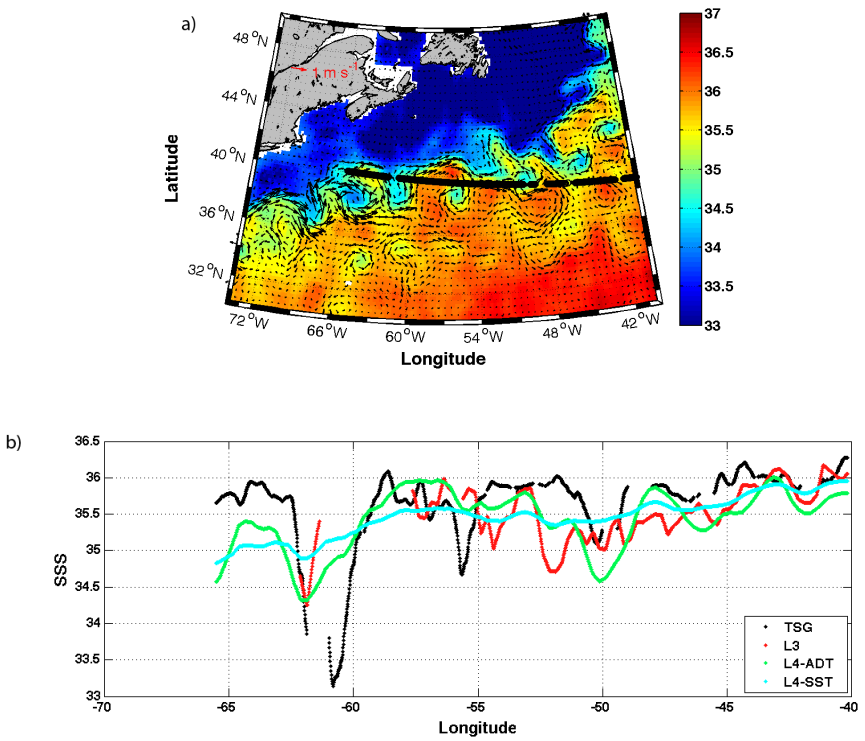

Figure 6.8: L4-ADT for the 15th of August with TSG positions of Explorer from 13-17 August 2012 in black dots (a). Comparison of in situ data along the transect in (a) with L3 SSS and L4 SSS maps of 15th of August (b).

weaker than that observed by in situ data (almost 1.5), the salinity difference between the inner-core and its western limit is as large as 1. On the other hand, the TSG salinity minimum located at 50°W is completely missing in L4-SST. Both SMOS L3 and the L4-ADT detect a negative salinity anomaly, although slightly displaced towards the west. Again, the L4-ADT product recovers the low salinity anomaly, showing a salinity difference between the CCR outer and inner parts (∼1) similar to the difference of the in situ data, although the absolute value is fresher.

In the Brazil Current area there not available TSG data for the year 2012, therefore Argo profiles are used as an independent source of validation for the SSS maps. Figure 6.9a shows the upper-most salinity value and positions of Argo for the year 2012. The histograms of the differences between the different satellite products and the upper-most salinity measured by Argo floats data are shown in Figure 6.9b-d. The L3 (Figure 6.9b) present the largest discrepancies from in situ observations, both in terms of the standard deviation and of the inter-quartile range (iqr). In contrast, L4 data fusion products (Figure 6.9c-d) present a reduction of both the central value of the difference (mean or median) and the error when compared with the L3 products (Figure 6.9b-c). The L4-SST (Figure 6.9d) is the closest to in situ data (bias of 0.10 and error of 0.43), while the L4-ADT (Figure 6.9c) presents slightly worse scores (bias of 0.13 and error

of 0.43).

An example 9-day SSS map of L4-ADT starting the 21st of January with the available Argo measurements (black dots) in the area the same days are shown in Figure 6.10a. An Argo value was found inside a WCR the 23st of January at (46.9W,40.2S) (red dot). The salinity and temperature measured along this Argo profile with depth is shown in Figure 6.10c. The upper-most salinity for the Argo profiler was 35.6 at 6 meters depth. The matchup of satellite products closer to the Argo measurement is the L4-ADT (35.18), while L4-SST and L3 SSS give an estimate of 34.99 and 34.98 respectively. Regarding the temperature of this WCR, the Argo upper-most value is 22.42°C, while the AVHRR SST estimate is 21.53°C. The difference between satellite and in situ temperature value (-0.89°C), corresponds to differences in salinity of -0.62, -0.61 and -0.42 for L3, L4-SST and L4-ADT respectively. In this case L4-ADT product achieves the best score against Argo measurement. Notice that the effect of stratification is not negligible in this case, although the observed differences, especially in temperature, are more likely due to representativity errors (as the time and space scales of SSS products are quite different from those of an Argo measurement).

Another Argo float is found inside a CCR ring the 25th of February; the corresponding 9-day map of L4-ADT starting the 23rd of February with the position of the Argo (red dot) is shown in Figure 6.10b. The temperature and salinity profile for this Argo in the first 1000 meters is shown Figure 6.10d. The upper-most salinity for the Argo profiler was 34.3 at 4.7 meters depth. The matchup of satellite products closer to the Argo measurement is in this case the L4-SST (34.09), followed by L4-ADT (33.86) and finally L3 SSS (33.49) give the worse estimate. Regarding the temperature inside the CCR, the Argo upper-most value is 19.98°C, while the AVHRR SST estimate is 18.84°C. The difference between satellite and in situ temperature value (-1.14°C), corresponds to differences in salinity of -0.81, -0.21 and -0.44 for L3, L4-SST and L4-ADT respectively. In this case L4-SST product achieves the best score as compared to Argo measurement. Again, stratification and scale representativity are probable causes explaining the observed differences.

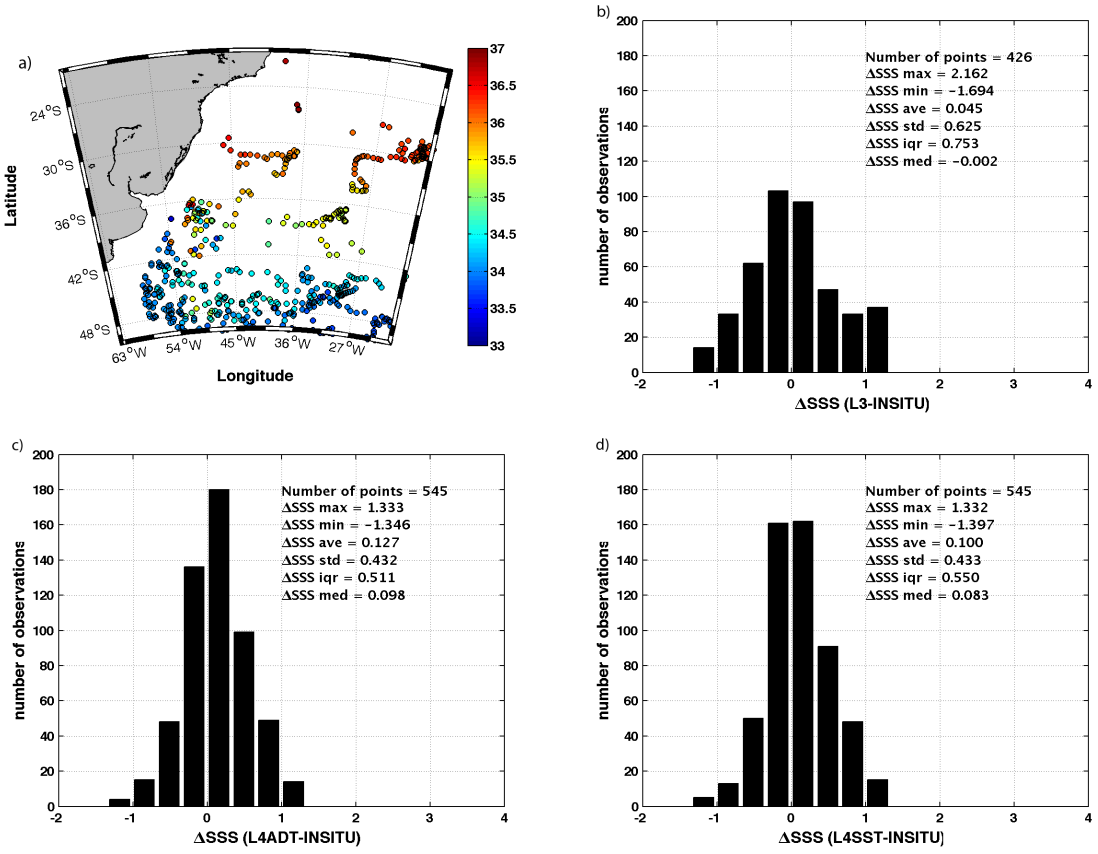

Figure 6.9: Available Argo positions and upper-most salinity value for the year 2012 (a). SSS difference histogram with Argo data for L3 SSS (b), L4-ADT (c) and L4-SST (d).

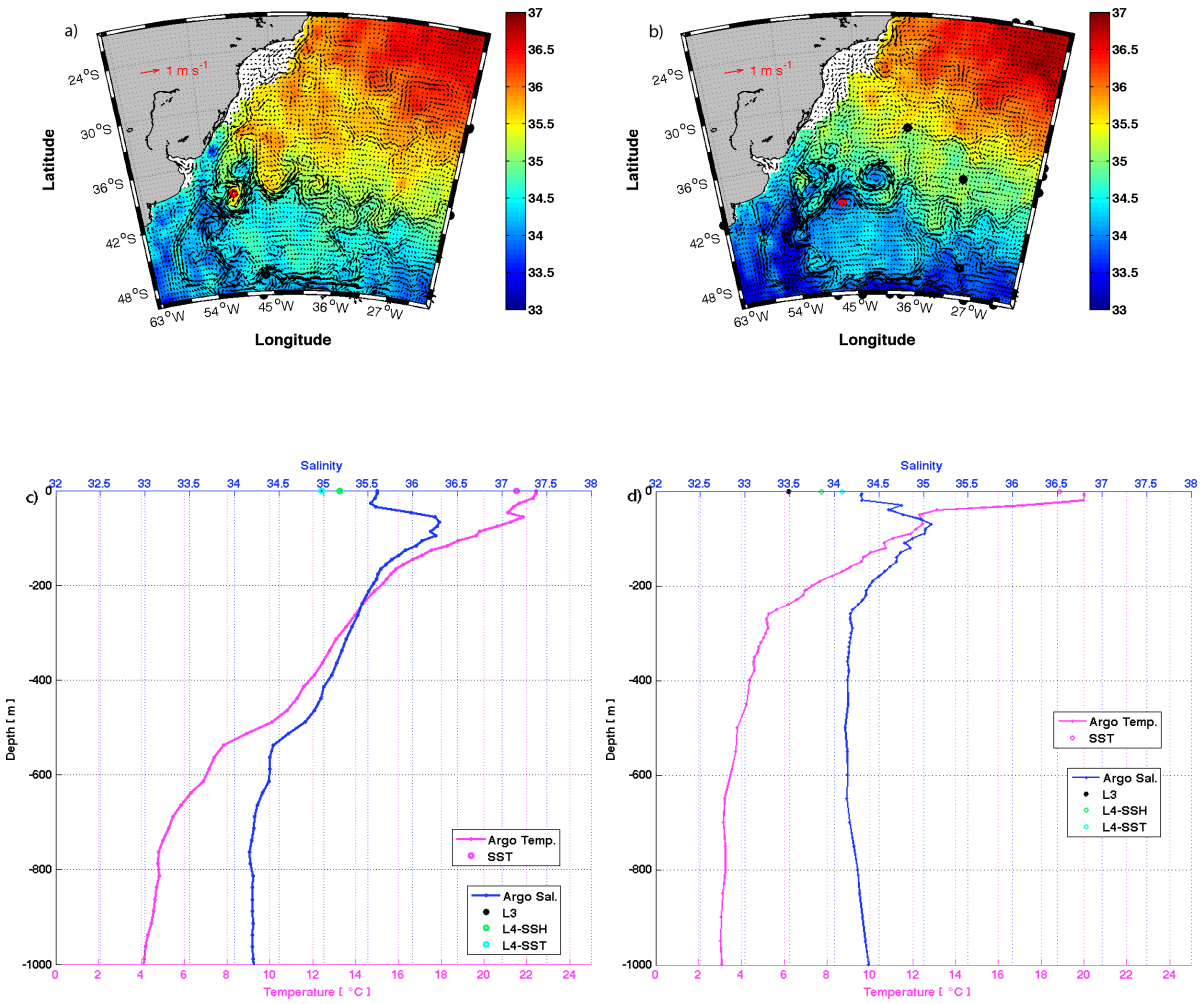

Figure 6.10: L4-ADT with available Argo positions overimposed for 9-day periods starting on 21st of January (a) and starting on 23rd of February (b) of 2012. Argo profile values for salinity and temperature for the first 1000 meters with collocated surface values of AVHRR SST, L3 SSS, L4-ADT and L4-SST at (50.3W,39.1S) for the 23rd of January (c) and at (46.9W,40.2S) for the 25th of February (d) of 2012.

6.5 Vortex identification and tracking

Due to scarcity of in situ data, the presence, size and center of the eddies was obtained from sea level anomalies by using the version 2.0.2 *py-eddy-tracker* free software described in Mason et al. (2014). The daily SLA maps provided by AVISO are used to locate cyclonic (and anticyclonic) eddies. The *py-eddy-tracker* software performs a spatially high-pass filter of AVISO SLA fields. The high-pass filter is achieved removing a smoothed field obtain from a Gaussian filter with a zonal radius of 10° and a meridional radius of 5°. Contours of SLA are computed for levels ranging from -100 to 100 cm at every 0.25 cm intervals. For a given SLA level, eddies are identified as closed contours which verify a set of geometric criteria (further details on the algorithm can be found in Mason et al. (2014)). As input, the code requires sequential maps of SLA. Output files contain eddy properties, including position, radius, amplitude, and azimuthal (geostrophic) speed. Additionally, a tracking record of each eddy through time is produced.

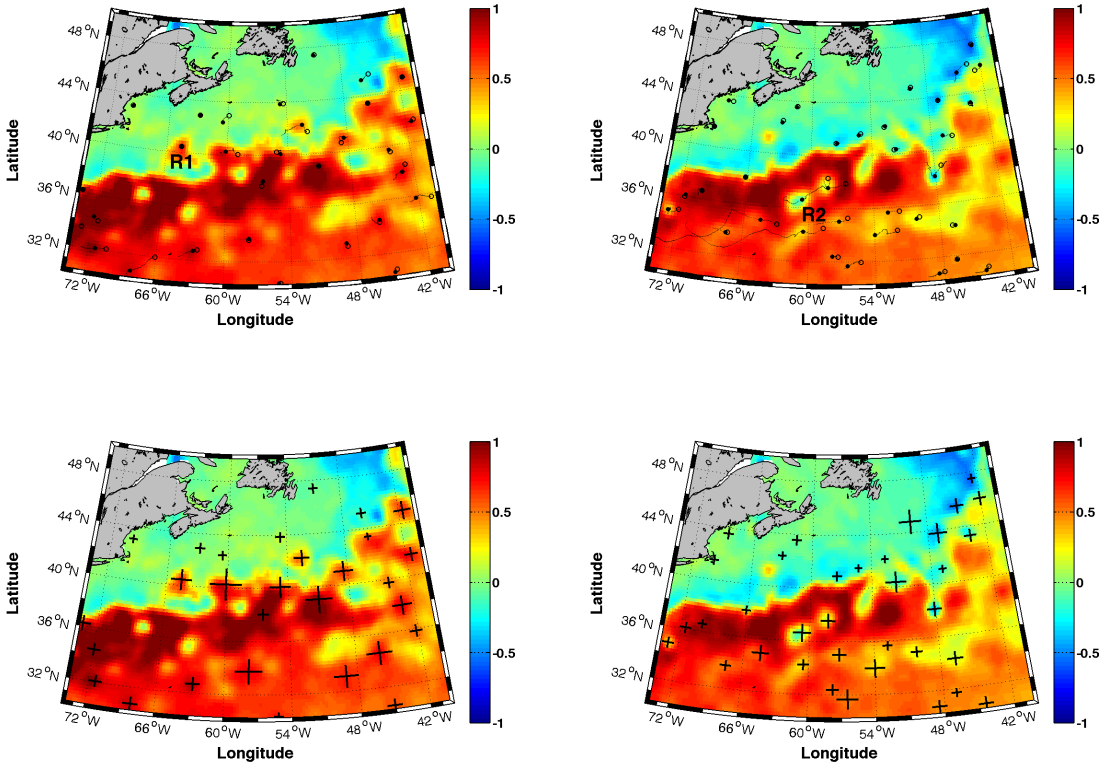

Figure 6.11: ***Top row:*** *AVISO ADT (meters) background with black dots representing anticyclonic/cyclonic (left/right) eddy centers found by py-eddy-tracker for September 20th (left) and June 1st (right), the initial eddy location (open black circle) and the path followed by each eddy (black line).* ***Bottom row:*** *ADT field for the same days with the position and amplitude of the detected anticyclonic/cyclonic (left/right) eddies; with the size of the crosses indicate the size of the ADT anomaly associated with the eddy.*

Py-eddy-tracker is used to study the spatial and temporal coherence of the retrieved SSS field

patterns/structures in all the locations where cyclonic eddies are identified from altimetry maps accordingly to the conceptual model in section 6.2. Figure 6.11 shows the ADT corresponding to September 20th (left) and June 1st (right), in the Gulf Stream region. The black dots correspond to the center of the anticyclonic/cyclonic eddies identified by *py-eddy-tracker* for that date (Figure 6.11 left/right panels respectively). The maps also show the initial eddy location (open black circle) and the path followed by each eddy (black line). The effective radius of each of the eddies identified by *py-eddy-tracker* is shown with black crosses in Figure 6.11 bottom.

The expected SSS structure of anticyclonic/cyclonic eddies has a positive/negative salinity gradient between the center and its surroundings. The salinity gradient along all detected anticyclonic/cyclonic eddies (the difference between the center and the outer part of the ring) is calculated for the diverse salinity products (L3 and the two Level 4 products). The center of the rings is located by the *py-eddy-tracker*. The salinity outside the ring is estimated by considering the median of the four grid points located at twice the radius distance from the eddy center (note that eddies have different radius values and these can also vary with time).

In 2012, there were a total of 13939 anticyclonic and 15530 cyclonic detected eddies in the daily SLA snapshots in the GS region. Note that not all ring structures detected by *py-eddy-tracker* correspond to a closed structure in ADT; occasionally they correspond to Gulf Stream meanders. The average radius of the anticyclonic/cyclonic eddies automatically detected by py-eddy-tracker in the Gulf Stream is about 68/71 km, with half of the eddies having a radius between 46/47 km and 81/89 km (the minimum radius is 26/27 km and the maximum 274/260 km). In L3 maps, 55% of detected anticyclonic rings have an associated salty core, while in the Level 4 products the percentage of salty cores is 82% and 62% for L4-ADT and L4-SST respectively. Regarding the cyclonic eddies, in L3 maps, 60% of the cyclonic rings have an associated fresh core. In the Level 4 products the percentage of fresh cores are 86% and 65% for L4-ADT and L4-SST respectively.

Figure 6.12 shows two example maps of the AVISO MADT in the Brazil Current corresponding to January 21st with the detected anticyclonic eddies (left), and corresponding to February 23rd with the detected cyclonic eddies (right). As for the previous image 6.11, the black dots correspond to the center of the eddy identified by *py-eddy-tracker* for such a date. The map also shows the initial eddy location (open black circle) and the path followed by each eddy (black line). The effective radius of each of the eddies identified by the *py-eddy-tracker* is shown with black crosses in Figure 6.12 bottom.

The total number of eddies detected in SLA daily images by *py-eddy-tracker* in the Brazil Current area for the year 2012 is 21155 anticyclonic and 23324 cyclonic eddies. The average radius of the anticyclonic/cyclonic eddies automatically detected by py-eddy-tracker in the Brazil Current area is about 75/73 km, with half of the eddies having a radius between 49/49 km and 92/88 km (the minimum radius is 27/25 km and the maximum 295/291 km).

In the Level 4 products the percentage of salty cores is 59% and 60% for L4-ADT and L4-SST respectively, and in L3 maps, the percentatge of salty cores is only 51% of the total. Regarding the cyclonic eddies, the total number of eddies detected in SLA daily images by *py-eddy-tracker*

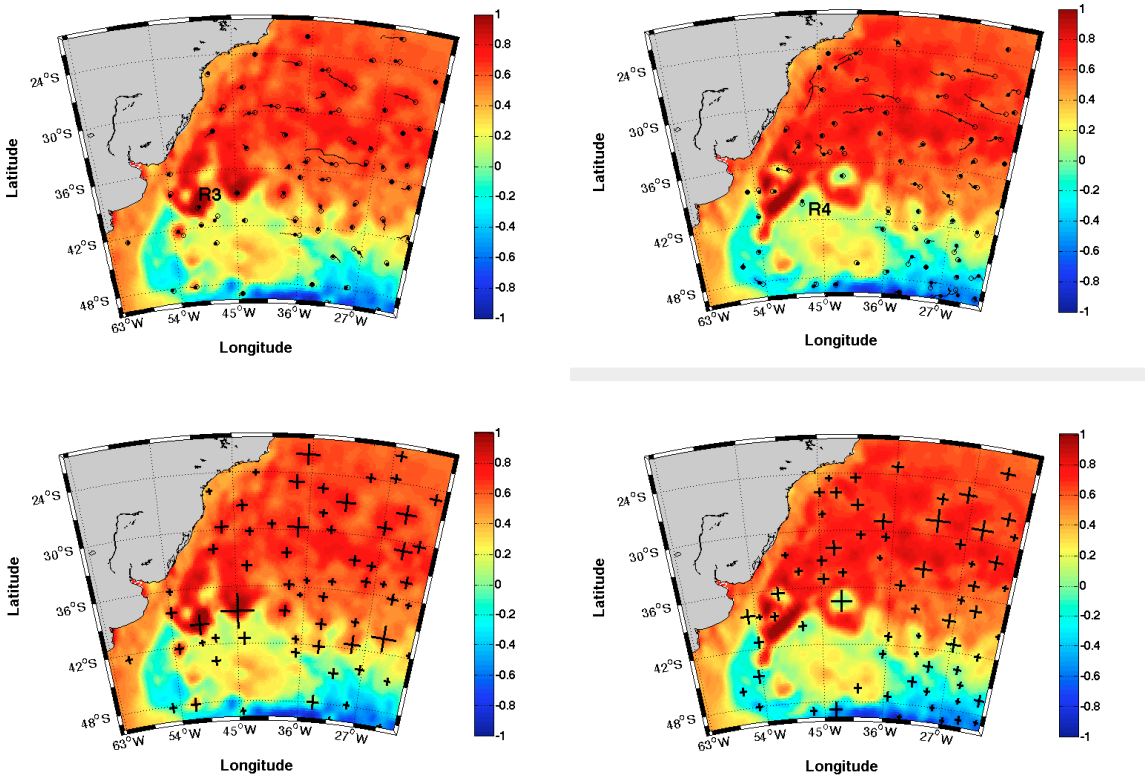

Figure 6.12: ***Top row:*** *AVISO ADT (meters) background with black dots representing anticyclonic/cyclonic (left/right) eddy centers found by py-eddy-tracker for January 21st (left) and February 23th (right), the initial eddy location (open black circle) and the path followed by each eddy (black line).* ***Bottom row:*** *ADT field for the same days with the position and amplitude of the detected anticyclonic/cyclonic (left/right) eddies with the size of the crosses indicating the size of the ADT anomaly associated with the eddy.*

in the Brazil current area for the year 2012 is 23324. In L3 maps, 10259 eddies (51% of the total) have an associated fresh core. In the Level 4 products the number of fresh cores are 12225 (62%) and 12805 (64%) for L4-ADT and L4-SST respectively.

The expected salinity gradient of an anticyclonic eddy is positive between the center and its surroundings. Figure 6.13 (left column) displays sections of ADT and SSS fields (L3 top, L4-ADT middle, L4-SST bottom) across the vortex called R1 (Figure 6.11). The vertical lines indicate the position of the center and twice the radius of the cyclonic eddies found by the *py-eddy-tracker*. The graph reveals a correspondence between the L3 salinity field and the ADT maximum across the R1 ring (Figure 6.13a), although marked data gaps are present and the L3 SSS is nosier compared to the ADT section. The SSS transects of both L4 reveal a salinity maximum well aligned with the ADT maximum, with a higher gradient for L4-ADT.

The salinity gradient along all detected anticyclonic eddies in the Gulf Stream (the difference between the center and the outer part of the ring) is calculated for the three salinity products (L3 and both Level 4 products) for the entire year 2012. The histograms of the salinity gradients

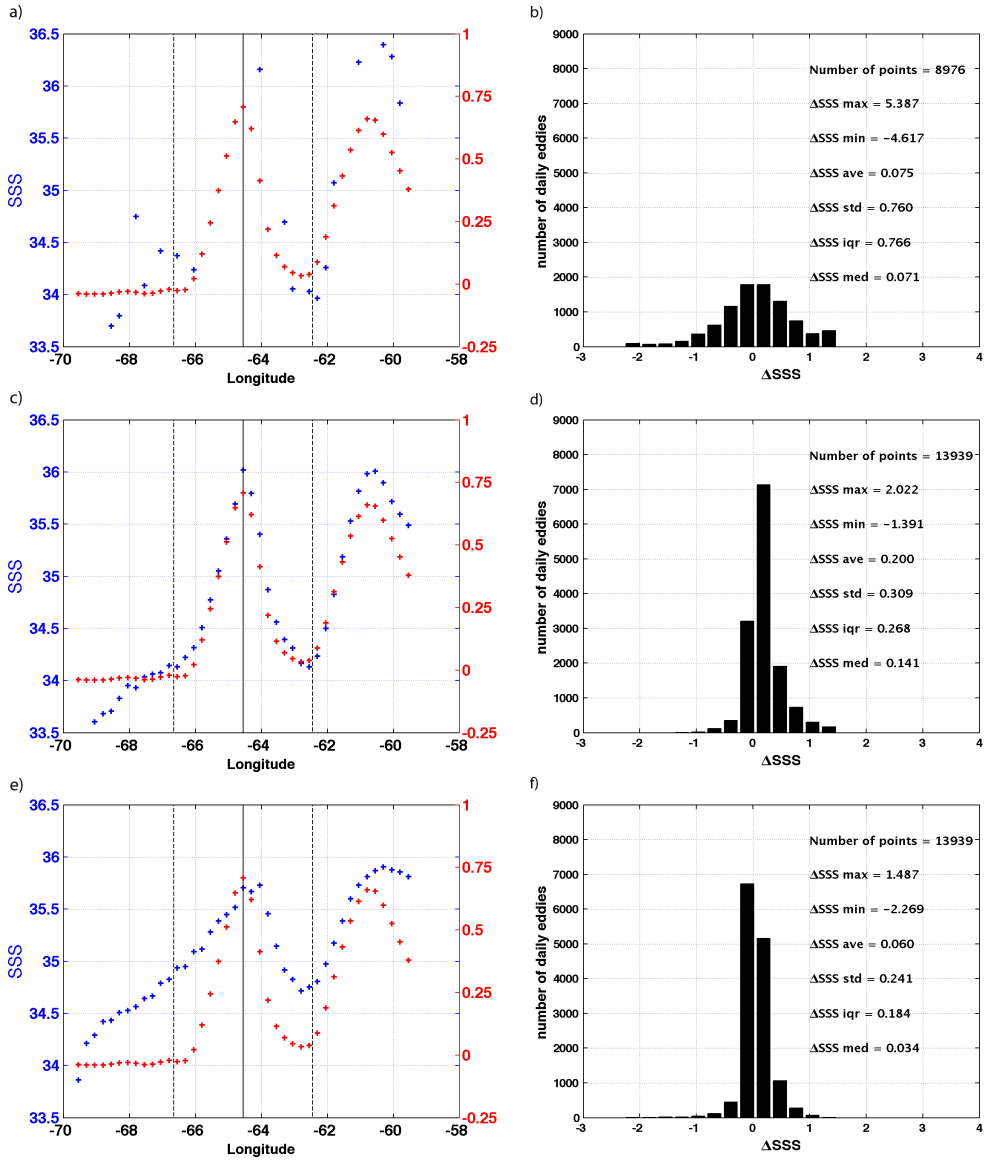

Figure 6.13: Section along the vortex R1 shown in Figure 6.11 for absolute dynamic topography (meters) and Sea Surface Salinity (L3 (a), L4-ADT (c) and L4-SST (e)) January 21st. Vertical lines indicate the center (solid black line) and the edge of the eddy (i.e, a distance of 1 radius of the eddy center, dashed lines). SSS difference histogram between inside and outside the anticyclonic vortex found for the entire year 2012 of the analysis for SMOS L3 (b), L4-ADT (d) and L4-SST (f).

for the different products (Figure 6.13 right column) show that the mean salinity gradient inside the anticyclonic eddies is positive for all products and has an average value of 0.07 for L3, 0.2 for L4-ADT and 0.06 for L4-SST. Note that the total anticyclonic rings detected in the SSS L3 maps is lower (8976, it was 13939 in both Level 4 products) due to the data gaps in the L3 images.

When analyzing the SSS structure of cyclonic eddies in the Gulf Stream area (Figure 6.14), a negative salinity gradient between the center and its surroundings is expected. Transects of

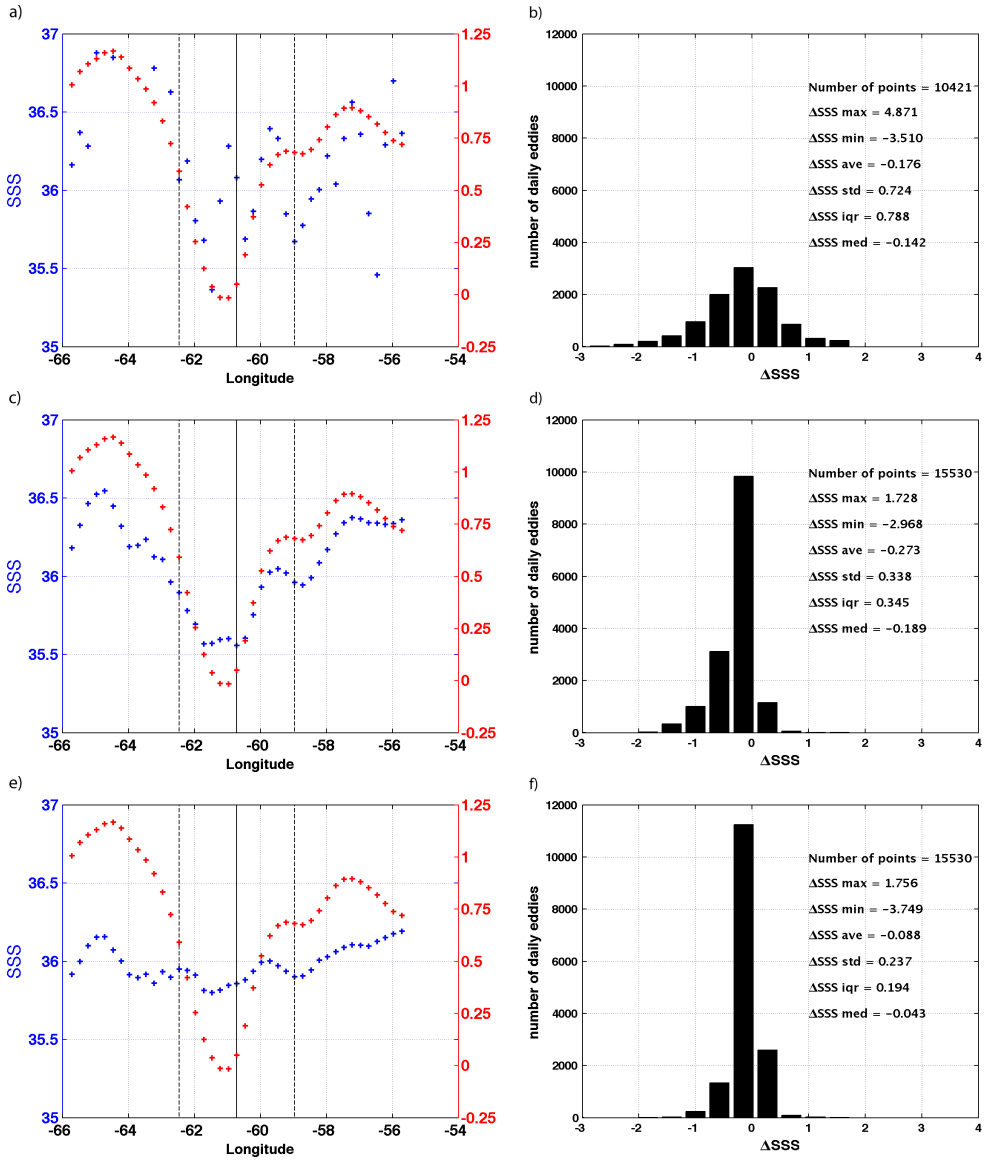

Figure 6.14: Section along the vortex R2 shown in Figure 6.11 for absolute dynamic topography (meters) and Sea Surface Salinity (L3 (a), L4-ADT (c) and L4-SST (e)) February 23rd. Vertical lines indicate the center (solid black line) and the edge of the eddy (i.e, a distance of 1 radius of the eddy center, dashed lines). SSS difference histogram between inside and outside the cyclonic vortex found for the entire year 2012 of the analysis for SMOS L3 (b), L4-ADT (d) and L4-SST (f).

ADT and SSS fields across the vortex called R2 (Figure 6.11) reveal a minimum of salinity aligned with the one in ADT for the case of L4-ADT, and also for the case of L4-SST, although with a smaller gradient. In this case the graph reveals only a small correspondence between the L3 salinity field and the ADT minimum across the R2 ring. Histograms of the salinity gradients (Figure 6.14 right column) reveal an average value of -0.02 for L3, -0.27 for L4-ADT and -0.08 for L4-SST.

When analyzing the anticyclonic eddies in the Brazil Current area, also a positive salinity

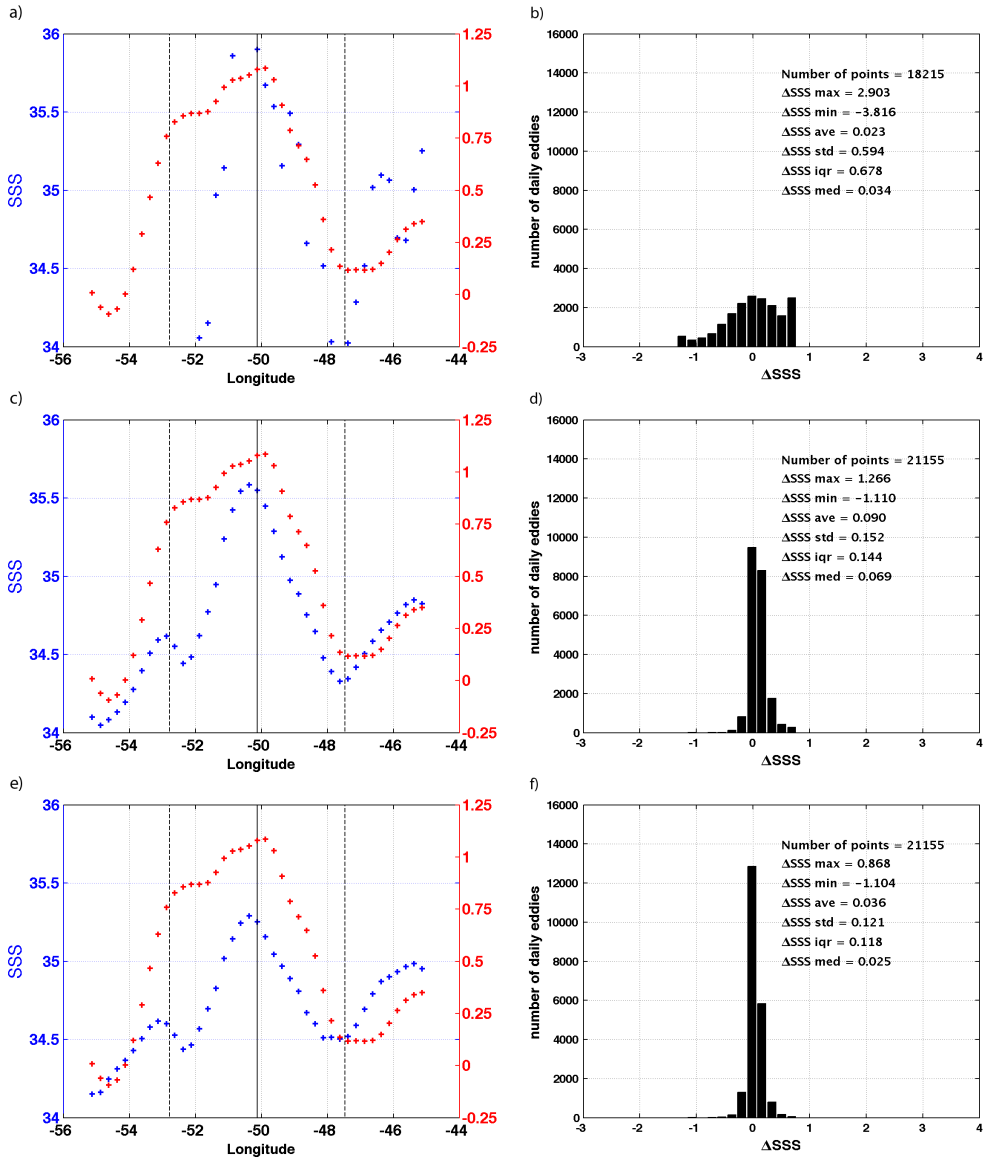

Figure 6.15: Section along the vortex R3 shown in Figure 6.12 for absolute dynamic topography (meters) and Sea Surface Salinity (L3 (a), L4-ADT (c) and L4-SST (e)) January 21st. Vertical lines indicate the center (solid black line) and the edge of the eddy (i.e, a distance of 1 radius of the eddy center, dashed lines). SSS difference histogram between inside and outside the anticyclonic vortex found for the entire year 2012 of the analysis for SMOS L3 (b), L4-ADT (d) and L4-SST (f).

gradient between the center and its surroundings is expected. Figure 6.15 displays the sections of ADT and SSS fields across the vortex called R3 (Figure 6.12). As for the case of the anticyclonic ring analyzed in the Gulf Stream region (R1 in Figure 6.11), the L3 SSS section presents a maximum of salinity aligned with the ADT section, although it is nosy and in worse correspondence with the structure of the ADT section. In contrast, the salinity transects of L4-ADT and L4-SST reveal a salinity maximum well aligned with the ADT maximum, with a higher gradient in the case of L4-ADT.

The salinity gradients along all detected anticyclonic eddies in the Brazil Current area are computed for the three salinity products for the entire year 2012 (Figure 6.15 right column). The histograms present a mean positive salinity gradient inside the anticyclonic eddies for all products and has an average value of 0.02 for L3, 0.09 for L4-ADT and 0.03 for L4-SST. Note that the total anticyclonic rings detected in SSS L3 maps is lower (18215, it was 21155 in both Level 4 products) due to the data gaps in L3 images.

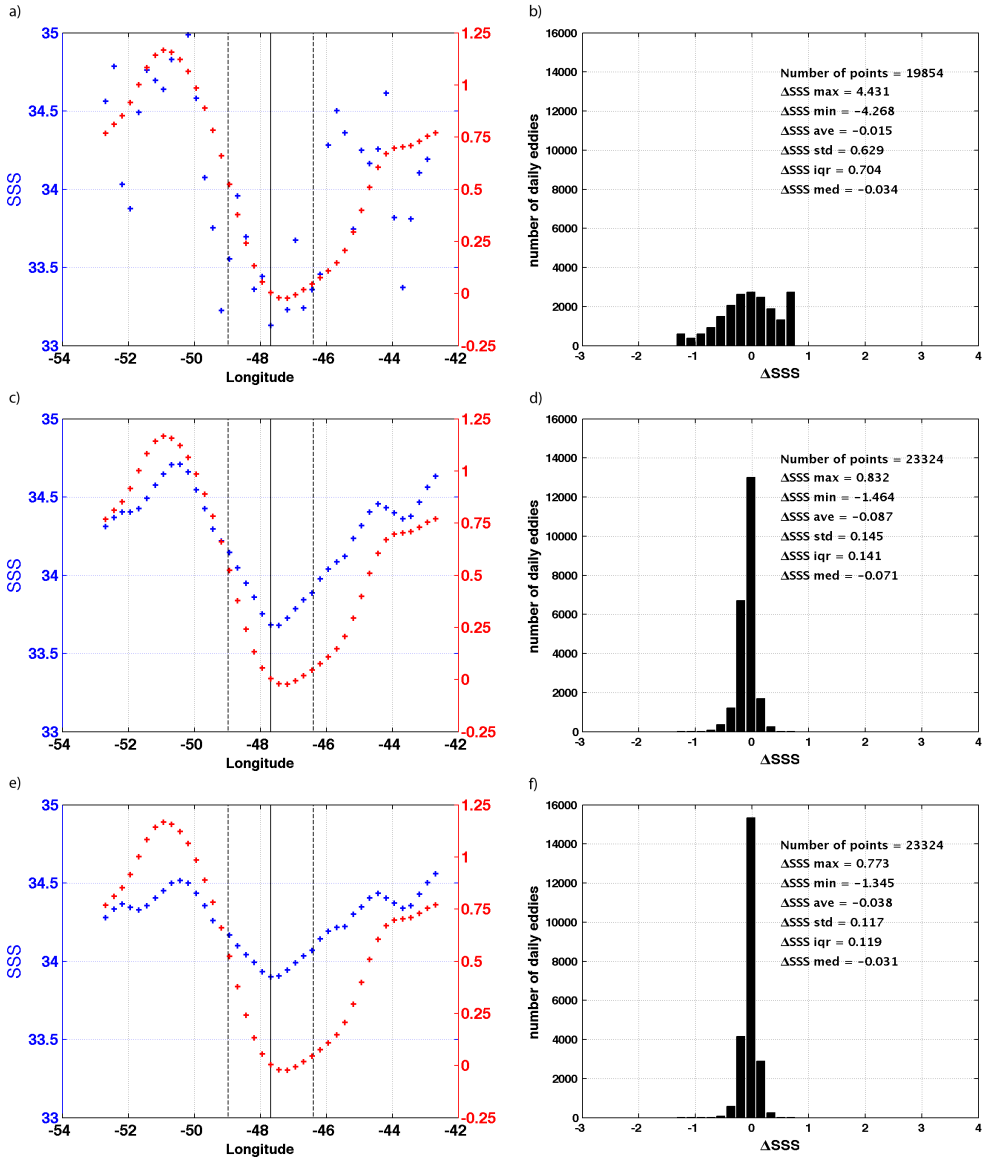

Figure 6.16: Section along the vortex R4 shown in Figure 6.12 for absolute dynamic topography (meters) and Sea Surface Salinity (L3 (a), L4-ADT (c) and L4-SST (e)) February 23rd. Vertical lines indicate the center (solid black line) and the edge of the eddy (i.e, a distance of 1 radius of the eddy center, dashed lines). SSS difference histogram between inside and outside the cyclonic vortex found for the entire year 2012 of the analysis for SMOS L3 (b), L4-ADT (d) and L4-SST (f).

Finally, we analyze the SSS structure of cyclonic eddies detected by the *py-eddy-tracker* in

the Brazil current (Figure 6.16). The three SSS fields across the vortex called R4 (Figure 6.12 left column) have a negative salinity gradient between the center and its surroundings. The graph reveals a noisy correspondence between the L3 salinity field and the ADT minimum across the R4 ring. In contrast, the salinity transects of L4-ADT and L4-SST reveal a salinity minimum well aligned with the ADT minimum, with a smaller gradient in the case of L4-SST. Histograms (Figure 6.12 right column) of the salinity gradient along cyclonic eddies in the Brazil Current region for the entire year 2012 reveal an average value salinity gradient of -0.01 for L3, -0.08 for L4-ADT and -0.04 for L4-SST.

The Level 4 estimates are systematically less noisy than the L3 SSS. Regarding the mean gradient amplitude inside the anticyclonic eddies in the Gulf Stream (where a positive gradient is expected), L4-ADT estimates are greater (+0.13) than the value estimated from L3, while L4-SST gives a slightly lower mean gradient amplitude than the L3 (-0.02) estimate. In the Brazil Current, L4-ADT estimates are also greater (+0.07) than the value estimated from L3, and L4-SST gives a greater (+0.01) mean gradient amplitude than L3.

Inside the cyclonic eddies a negative salinity gradient is expected. In the Gulf Stream L4-ADT estimates yield greater gradients (+0.10) than the value estimated from L3, while L4-SST gives a lower mean gradient amplitude than L3 (-0.09). Regarding the mean gradient amplitude inside the cyclonic eddies in the Brazil Current, L4-ADT estimates are greater (+0.07) than the value estimated from L3, and also L4-SST gives a greater (+0.02) mean gradient amplitude than L3. Using SST as a template gives systematically lower SSS gradients inside the eddies than when using the ADT as a template.

The general conclusion is that L4-ADT represents better the geometric structure of WCR and CCR, with a greater estimation of the salinity gradient amplitude associated with the mesoscale rings. L4-SST products estimate correctly the geometric structure in the majority of the cases, but tend to produce a considerably over smoothed product and for that reason its mesoscale gradients are significantly lower than those of L4-ADT. Finally, L3 products are quite noisy and thus the geometry of WCR and CCR is not always well described except for particularly sharp, well-defined rings. The mesoscale salinity gradients tend to be slightly greater than those of L4-SST but this could be an effect of noise.

6.6 Singularity structure of SSS maps

As discussed in section 4.2, the singularity exponents provide information about the geometry of the underlying flow and thus should be independent of the particular scalar from which they are derived, i.e., they are basically related to a component of the signal which is common to all ocean scalars (the advection term). In practice, due to errors, noise and limitations of the algorithm used to estimate the singularity exponents, certain singularity exponents associated with the streamlines of the flow are lost and the correspondence is not perfect (Turiel et al., 2009). Previous studies show that the singularity fronts (bright white lines) of high-quality ocean surface remote sensing maps are highly aligned with altimeter-derived surface currents. An example of the comparison of singularity lines from ADT(left) and SST(right) with OSCAR

velocity product (Figure 6.17), shows an accurate qualitatively correspondence with the flow streamlines: OSCAR velocities align well with the lines of singularity exponents, especially for the case of ADT derived singularity exponents, as OSCAR product is mainly nourished of altimeter information. The singularity maps shown in Turiel et al. (2009) and in Figure 6.17 right are certainly similar to those in Figure 6.17 left, indicating that AVISO ADT is indeed a geophysically consistent product.

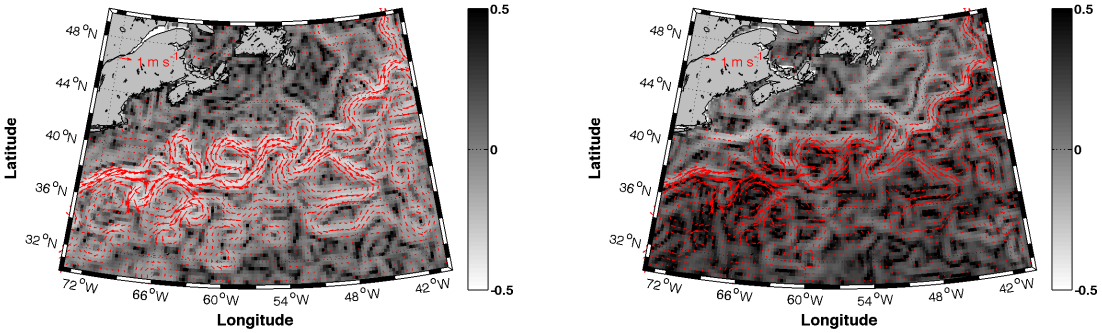

Figure 6.17: Singularity maps derived from AVISO ADT (left) and AVHRR SST (right) for September 11th 2012, both compared with OSCAR velocities for the same date (red arrows).

Maps of singularity exponents (calculated as in Turiel et al. (2008b)) generated from SMOS L3, AVISO ADT, AVHRR SST, L4-ADT and L4-SST maps are shown in Figure 6.18 for the Gulf Stream region in September 11 and in Figure 6.19 for the Brazil Current in November 7, 2012.

As revealed by its singularity map, the SMOS L3 product (Figures 6.18 and 6.19b) is quite noisy and leads to unstructured singularity maps, where only few parts of the large-scale structures (such as the salinity front associated with the Gulf Stream) can be recognized and many sampling artifacts are noticeable.

The singularity maps of the L4-ADT product (Figure 6.18c and 6.19c) show that the fusion algorithm is able to restore much of the singularity structure present in the ADT map (Figures 6.18e and 6.19e). Similarly, the L4-SST singularity maps (Figures 6.18d and 6.19d) incorporates much of the singularity structure of the SST singularity maps (Figure 6.18f and 6.19f). The singularity exponents of L4-ADT and L4-SST are thus better defined than in the L3 map but are not as rich as in the original ADT or SST maps, due to the known limitations of the present fusion algorithm. Both in the Gulf Stream and more notably in the Brazil current area, the singularity exponents of both L4 products are really close, able to resolve the large-scale western boundary currents structures with their meandering and associated ring structures. The analysis of singularity exponents also demonstrates that the extrapolated areas in the Level 4 products are geophysically consistent.

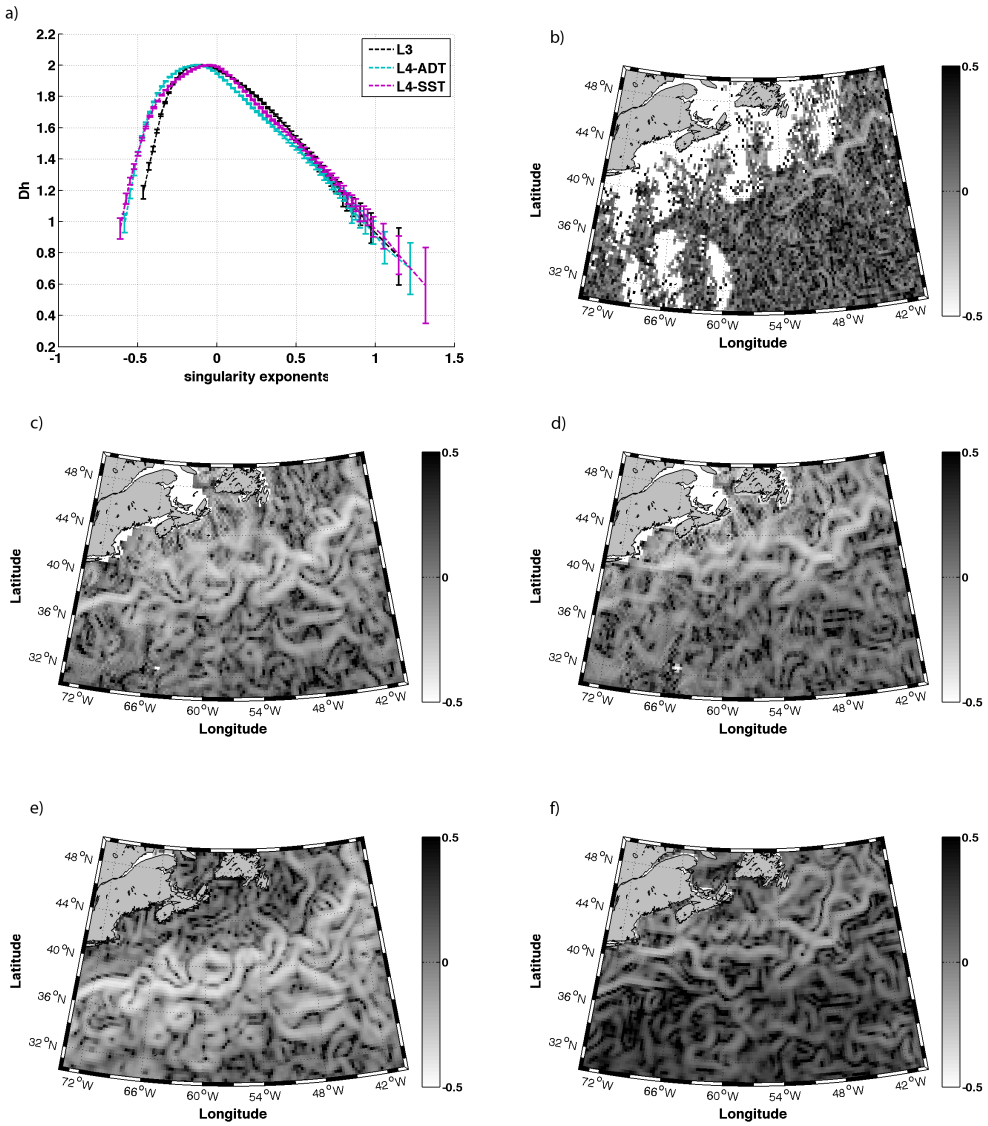

Figure 6.18: Singularity spectra for L3 and L4 products corresponding to the Gulf Stream area days during the year 2012 (a). Maps of singularity exponents derived from L3 (b), L4-ADT (c), L4-SST (d), AVISO ADT (e) and AVHRR SST (f) in September 11 2012.

Going further in the characterization of the signals through the analysis of their singularity exponents, we can fully characterize the statistical behavior of changes of scale in multifractal systems by means of the so-called singularity spectrum (Parisi and Frisch (1985); Frisch (1995); Pont et al. (2009)). The singularity spectrum of a multifractal system, $D(h)$, is a scale-invariant function that for each singularity exponent informs us about the fractal dimension of the associated fractal component in the multifractal hierarchy. The fractal components are sets of points at which the variable under study presents different scaling properties.The multifractal spectrum can be calculated from the distribution of the singularity exponents at a given scale

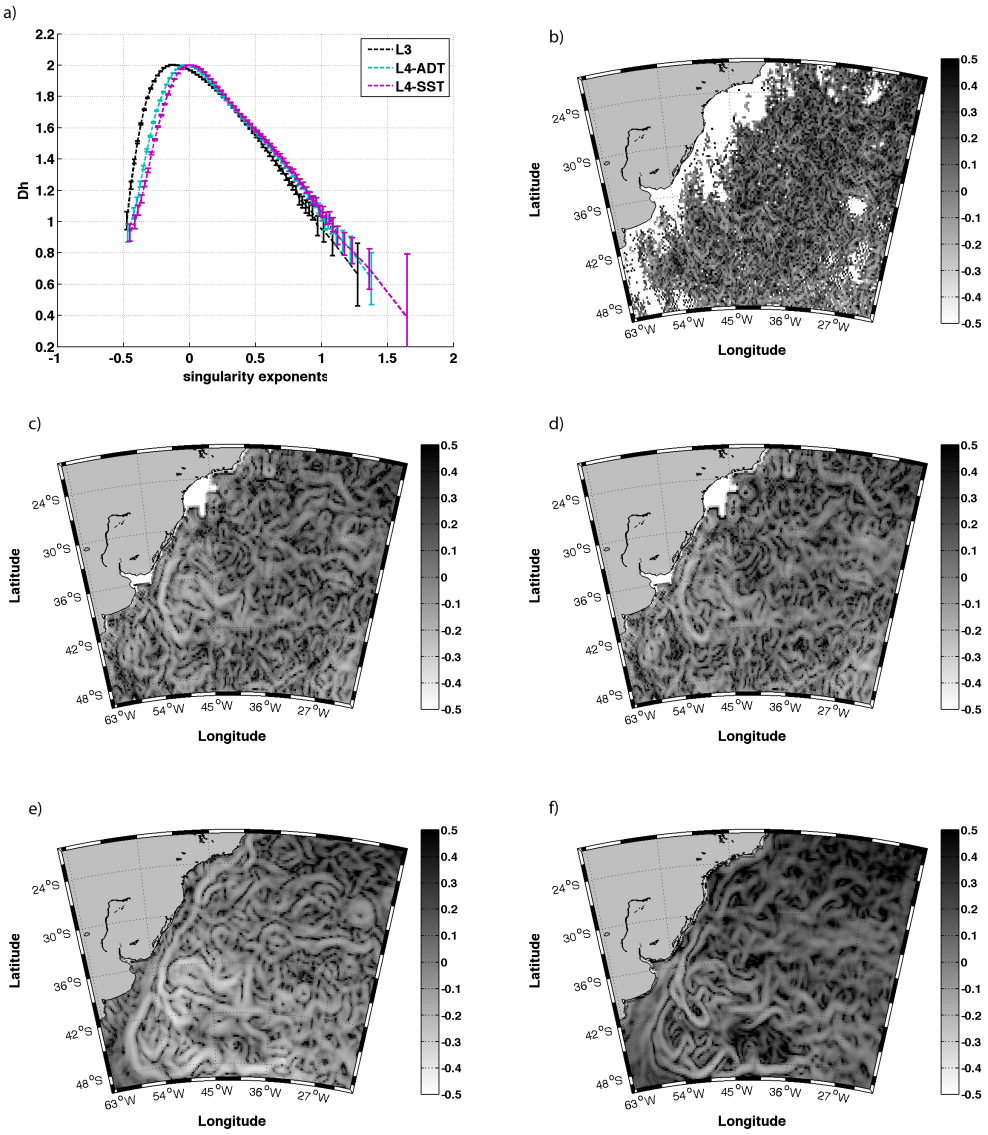

Figure 6.19: Singularity spectra for L3 and L4 products corresponding to the Brazil Current area during the year 2012 (a). Maps of singularity analysis exponents derived from L3 (b), L4-ADT (c), L4-SST (d), AVISO ADT (e) and AVHRR SST (f) in the November 7 2012.

(Pont et al., 2009). Its shape is linked to the energy cascade dissipation (Turiel et al., 2008b) and it should be the same for all parameters advected by the same flow considering it is assumed that all of them have the same underlying multifractal hierarchy. The computation of the singularity spectra is done as in Turiel et al. (2006): the empirical histogram of the values of singularity exponents $h(\vec{x})$ is log-transformed and normalized to compute $D(h)$. The singularity spectra associated with the products used in this chapter can be found in Figures 6.18a and 6.19a. The method also allows evaluating the errorbars associated with sampling size (note that errorbars are shown in Figures 6.18a and 6.19a). These errorbars do not account though for the

uncertainty associated with the method itself, which is estimated to be about 0.1 (Turiel et al., 2006, 2008b).

The right part of the spectrum (positive singularity exponents) corresponds to the less singular values, which are represented using dark colors in the maps of Figures 6.18b-f and 6.19b-f. Large differences exist among the SSS products in this part of the spectrum as a result of the less singular (i.e., positive) values are associated with the more regular and smooth parts of the function, and are therefore more sensitive to noise and artifacts. The left part of the spectrum corresponds to the most singular (negative) values, corresponding to the brightest (whitest) areas in the maps of singularity exponents of Figures 6.18b-f and 6.19b-f. Negative values identify regions of abrupt changes in the flow, such as fronts or filaments, but also, as mentioned earlier, potential sampling artifacts. In this part of the spectrum, the spectra can present an excess bump just above -0.5 which is the typical signature of sharp edges, e.g. coastlines and, in specific products, artifacts like orbital gaps. To remove this statistical excess of sharp transitions, all points side by side of a boundary are discarded from the statistics.

The spectra of L4-ADT and L4-SST are close on the full range of values of the spectrum, but the difference with L3 is larger than the error bar associated with both the sampling size and the uncertainty in the method used to calculated singularity exponents (which accounts for a horizontal displacement of the full spectra by ± 0.1). This means that the singularity exponents of L3 do not follow the same distribution as the fused products. A close inspection of the spectra shows that the spectra associated with L3 products are a bit narrower than those associated with L4-ADT and L4-SST. Notice that the spectrum of L3 in Figure 6.19a is slightly shifted to the left: we know this because of the constraint imposed by translational invariance on the singularity exponent at which the tangent line has a slope exactly equal to 1, see Turiel and Parga (2000) for a deeper discussion. Corrected by this shift, the spectra in Figures 6.18 and 6.19 evidence a relative lack of singularity exponents on the negative part of the singularity spectrum of L3 with respect to the spectra of L4-ADT and L4-SST. This means that the many singularity fronts associated with current lines have been destroyed as a result of the noise and only those associated with the most evident features are still present in L3 maps, as is confirmed by the visual inspection of singularity maps.

6.7 Discussion

In this chapter, the ability of SMOS SSS maps to characterize mesoscale processes has been investigated. The evaluated data are Level 3 maps as presented in Chapter 3 and Level 4 maps obtained using data fusion as described in Chapter 5. We have also discussed the convenience of using one template or another in the generation of L4 products; in particular, we have used AVHRR SST and AVISO ADT as templates and SMOS L3 SSS as signal. The regions under study were the Gulf Stream area and the Brazil Current area, two examples of western boundary currents where mesoscale activity in form of meanders, filaments and eddies has been well documented.

SMOS L3 maps can be used for such purpose since, despite certain processing artifacts, they

reveal the SSS signature of such mesoscale phenomena (Reul et al., 2014b). Here we have focused on the ability of L3 and L4 remotely sensed SSS products to reproduce anticyclonic/cyclonic rings detached or close the mean flow of both western boundary currents. Anticyclonic/cyclonic rings are known for having a warm/cold, salty/fresh water core as a result of the exchange between water masses separated from this frontal area.

It has been shown that the examined L3 data only poorly resolve the rings and their evolution due to the high level of noise and artifacts still present in the data. To enhance the SSS signature of such mesoscale features, the fusion algorithm as presented in Chapter 4 based on the multifractal properties of ocean scalars has been applied to L3 data. The method merges the information coming from two different ocean scalars to generate a new product of improved quality and resolution. The templates (AVISO ADT and AVHRR SST) are used to improve the quality of the signal by restoring the singular structure that ocean variables should share.

A first quantitative validation of the different fused products using in situ SSS data as reference has shown a reduction in systematic (bias) and random errors in the L4 fused SSS products in comparison with the SMOS L3. Also, the expected relatively salty/fresh anomaly inside (w.r.t. outside) the anticyclonic/cyclonic rings, observed by in situ data, is better reconstructed by the L4 fused SSS products. To assess the ability of the fused products to recover the cyclonic/anticyclonic salinity structure, an eddy detection method has been used. This method allows the detection of anticyclonic/cyclonic vortices using SLA maps. A mean decrease in salinity between the ring center and the outside (i.e., negative anomaly) of about 0.1 is found in cyclonic eddies for the different products in the year 2012. In the case of anticyclonic eddies, a mean increase in salinity between the ring center and the outside (i.e., positive anomaly) of about 0.1 is found for the different products in the year 2012.

The L3 product fused with ADT data (L4-ADT) is clearly superior to the rest of the products, i.e., L3 and L3 fused with SST (L4-SST) in resolving the cyclonic/anticyclonic salinity signature. Moreover, the L4-ADT CCR negative anomalies are significantly better aligned with those observed by several in situ cruise campaigns than those from the other L3 and L4 products. Although the L4-ADT product shows the best results in terms of resolving eddies and validation against TSG data, poor altimetry sampling can lead to spurious eddies and therefore spurious SSS anomalies in the L4-ADT product.

Singularity analysis of the different SSS maps has been carried out to validate the fusion method applied to L3 SSS data. The fusion method is correctly padding the singularity structure of the template on the fused images. Thus, L3 SSS benefits from the geophysical consistency brought by ADT and SST data.

A similar study presented in this chapter was published in Umbert et al. (2015) fusing Aquarius SSS data with three different geophysical templates: sea surface height (SSH) from AVISO, SSS from SMOS (CATDS-IFREMER), and sea surface temperature (SST) from AVHRR. The study focused in the negative salinity anomalies of the cyclonic eddies identified from sea level anomaly maps in the area of the Gulf Stream. It was shown that Aquarius L3 data poorly resolve the cold core rings and their evolution due to the relatively poor spatial and temporal

resolution (in comparison with SMOS). The fusion algorithm as presented in Chapter 4 was applied to improve the characterization of the SSS signature of such mesoscale features. In that study Level 2 Aquarius SSS (version 3.0) data (http://oceandata.sci.gsfc.nasa.gov/Aquarius/) were used to produce L3 daily quarter-degree SSS maps with a temporal window of ± 3 days for the year 2012.

The results of Umbert et al. (2015) also found a reduction in bias and random errors in the L4 fused SSS products in comparison with the Aquarius and SMOS L3 products using in situ SSS data, and the expected relatively fresh anomaly inside the CCRs observed by in situ data was also better reconstructed by the L4 fused SSS products. The ability of the fused products to recover the CCRs salinity structure was assessed with the same eddy detection method as used in this chapter (although previous version *py-eddy-tracker* 1.3.0 was used), exhibiting a mean decrease in salinity between the ring center and the outside (i.e., negative anomaly) of about 0.3-0.4 for the different products using Aquarius SSS as an input. The Aquarius L3 product fused with ADT data was also found superior to the rest of the products, (i.e., Aquarius L3, SMOS L3, Aquarius fused with SMOS SSS and Aquarius fused with SST) in resolving the CCRs salinity signature and in monitoring the CCRs evolution, by showing both larger negative SSS anomalies and larger temporal persistence of such anomalies.

This type of oceanographic processes studies allows, not only to provide a comprehensive view of salt exchanges across western boundary currents, but also to evaluate the realism of remote sensing products. The data fusion technique has proved to be able to take advantage of low quality products by improving the mesoscale information of Level 4 maps using information from different remote sensing variables.

Chapter 7

Application to different remote sensing variables

As an outlook of this thesis, preliminary results on applying the data fusion approach to improve the spatial coverage of a different signal is presented. The algorithm is applied to daily Aqua MODIS Level-3 chlorophyll maps by using MODIS SST maps as a template. Spatial variability studies of pigment images found not difference between the spectra of SST and ocean color maps, leading to the conclusion that phytoplankton cells in dynamic areas behave as passive scalars (Denman and Abbott, 1994; Doney et al., 2003). In Nieves et al. (2007) it was shown that sea surface temperature and chlorophyll maps have the same multifractal structure, interpreted as a consequence of the turbulent advection at the scales of observation.

Global maps of Chl-a concentration at the sea surface, similarly to what happens with other remote sensing variables, suffer of many data gaps. This is especially true for high-spatial resolution (few kilometers) daily maps, where orbital voids add to the data loss due to clouds, aerosols or sun glint. For this kind of products, gap-filling in addition to noise-reduction are crucial tasks to provide uniform products suitable for applications such as real-time, or near real-time, environmental monitoring, initialization of ecosystem models and data assimilation.

The local correspondence of SST and Chl-a singularities -(a fact that can be explained in terms of the theory of turbulence (Frisch, 1995) as the existence of a common cascade process) makes possible to use SST data to infer Chl-a concentration where data are lacking; the inference method to be used is a simple extension of the fusion algorithm used across this thesis. The quality of inference in L4 Chl-a maps is assessed by simulating artificial clouds and comparing the reconstructed and original data. Moreover, the analysis of the auxiliary parameters of the fusion algorithm allows to distinguish seasonal correlation behaviors between Chl-a and SST variables.

7.1 Satellite data

Two Aqua-MODIS ocean color products from the NASA Aqua spacecraft are used in this study: Chl-a concentration Level-3 daily product, and standard MODIS Aqua Level 3 SST (4 μm nighttime), both at $4km^2$ pixel grid (Brown and Minnett, 1999). MODIS (Moderate Resolution Imaging Spectroradiometer) is a key instrument on board the Terra and Aqua satellites from NASA. Our dataset period goes from January to December 2006. The data were downloaded from the Ocean Color web portal. According to many studies it is assumed that Chl-a follows a

The results presented in this chapter are summarized in the following paper (used revision): ***Umbert, M., Guimbard, S., Ballabrera-Poy, J. and Turiel, A., 2015. Synergy between of ocean variables: multifractal fusion of remotely sensed temperature and chlorophyll. Geophysical Research Letters.***

log-normal distribution (Campbell, 1995). Due to limitations with the coded dynamic range, the raw data from Ocean Color are in fact log-Chl-a concentrations, so we work with the logarithm of chlorophyll concentrations for ease of use (in addition, theoretically the singularity exponents should not change if a monotonic function is applied to the data, but numerically it is more comfortable to work with a dynamic range comprising fewer orders of magnitude).

7.2 Results

Figure 7.1 shows examples of daily maps of MODIS Chl-a concentration and SST in January 1st, 2006. The values of Chl-a are derived from measurements in the visible part of the spectrum that are affected by artifacts like aerosols, sun glint, sun angle and high turbidity in the water. As so, a high number of quality flags have been introduced to characterize Chl-a data. As a result, maps of Chl-a usually suffer from a larger incompleteness than in the case of SST, which is derived from infrared measurements in the 4 μm range.

An example of the application of the fusion algorithm in the global ocean for January 1st, 2006 is shown in Figure 7.1bottom. We can infer a value of Chl-a at any location, even within gaps, provided that the point is assigned a valid SST to which the estimated local regression coefficients $\widehat{a}(\vec{x})$ and $\widehat{b}(\vec{x})$ can be applied. As stated in Chapter 4, the algorithm allows estimating the local regression by taking into account all possible data pairs in the neighborhood of the target point. Fused Chl-a maps integrate the relation between structures present in the SST map and Chl-a specific structures; as we will next show, in fused daily products we recognize the expected Chl-a global patterns. In short, Chl-a maps provide information about phytoplankton concentration, as it is a light-harvesting pigment requited to carry out photosynthesis. Near the ocean surface, where availability of sunlight is not limiting, phytoplankton growth depends on temperature and nutrient levels. Then, high chlorophyll concentrations are found in nutrient-rich, cold polar waters and in the places where ocean currents cause upwelling, which brings nutrient-rich deep-cold water to the surface.

We concentrate in the specific region of the Gulf of California, a narrow sea between the mainland of Mexico and the Baja California peninsula where high primary productivity levels are found, as a result of an efficient nutrient transport of waters from under a shallow pycnocline into the euphotic zone (Valdéz-Holguín and Lara-Lara, 1987). Figure 7.2 shows both the input variables (top panel: Chl-a, middle panel: SST) of our algorithm and the output fused Chl-a (bottom panel). The corresponding singularity exponents are shown in the right column. Rich singularity structures can be recognized in the original chlorophyll concentration map associated with the fronts mainly caused by the advection of high primary production waters of the region into less productive areas, although the image is affected by data gaps in the Pacific region. The SST field exhibits also the richness of patterns associated with the circulation in that area, spatially similar to chlorophyll singularity structure (although not in the magnitude of the exponents), when both images are not affected by data gaps. Places where the correspondence of both singularity images fails may identify places at which the intrinsic dynamics of the variable is in competition with flow advection.

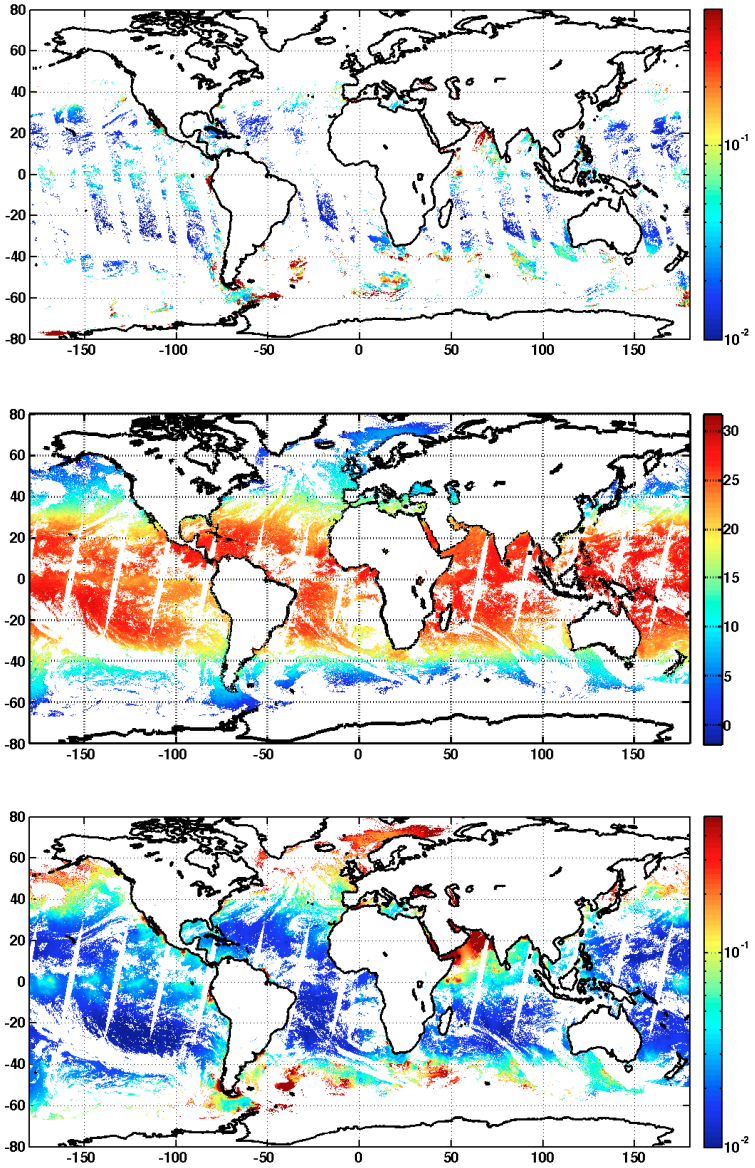

Figure 7.1: MODIS Aqua Level 3 Global daily 4km Chl-a (top) and MODIS Aqua Level 3 SST (4 µm nighttime) daily 4km (middle), L4 Chl-a concentration extended to the areas where MODIS SST was available for January 1st of 2006.

Once the data fusion is applied in the standard way, the L4 Chl-a is extrapolated to all the pixels where SST was available (the parameters $\widehat{a}$ and $\widehat{b}$ can be estimated everywhere as they are defined by weighted averages defined on the full domain). The structure of Chl-a is well represented (compared with the original image), although as usual when the fusion approach is applied a smoothing of the input variable degrades the image resolution. The singularity exponents of the fused Chl-a data reveal that most of the structures present in the SST map are re-integrated in the chlorophyll map at the same time that Chl-a specific magnitude and structures are maintained; for instance, the strong gradient associated with the biological activity present in the Gulf of California, appear clearly delineated in the fused Chl-a. This implies that

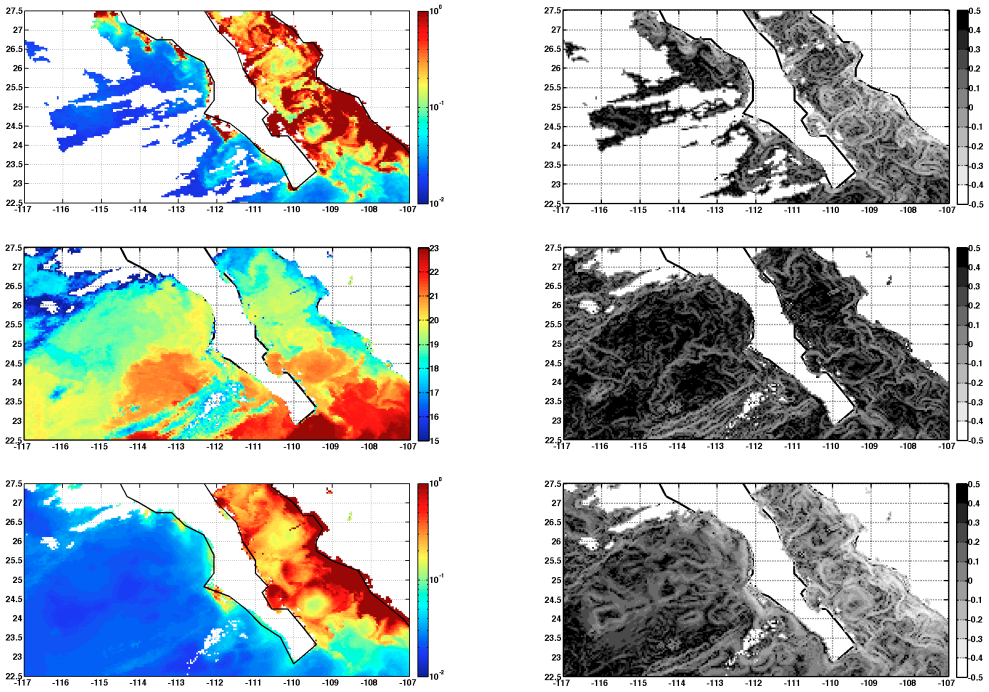

Figure 7.2: MODIS Chl-a, MODIS SST and fused Chl-a for January 1st 2006 and 4 km resolution (left column) and associated singularity exponents (right column).

the fusion algorithm is able to partially integrate SST structures without destroying Chl-a ones.

7.3 Validation of reconstruction

To assess the quality of the extrapolation resulting from our data fusion method, we validate it by analyzing 5 different regions (as shown in Figure 7.3); each region has at least an area of $6 \times 10^5 km^2$ (200×200 pixels). For each of these areas a mask representing typical cloud structure is defined; those masks have a surface of around 30% of the region on which they will be applied. To assess the quality of the fusion algorithm, we proceed in three steps. In the first step, points lying in the masked area of a daily CHL-a map are removed (notice that there will be additional missing points in the CHL-a map, as it is a real map affected by the usual gaps; for instance, in the EP area (see below) the average percentage of missing points is 85%). In the second step, the fusion algorithm is applied to the masked CHL-a map using the corresponding daily SST map as a template, extrapolating to the missing values. Finally, in the third step, the extrapolated values are compared to the available original ones on the masked area for each image during the entire year 2006 (365 daily images). This strategy allows comparing the original Chl-a and the retrieved one at the available masked points, and therefore the extrapolation ability of the fusion method.

The performance of the algorithm is studied in different Chl-a regimes: oligotrophic regions (Central Atlantic, CA and Pacific in front of California, CL) and eutrophic regions in higher latitudes (North Atlantic, NA), coastal upwelling areas (Benguela upwelling, BG) and the Equator (Equatorial Pacific, EP).

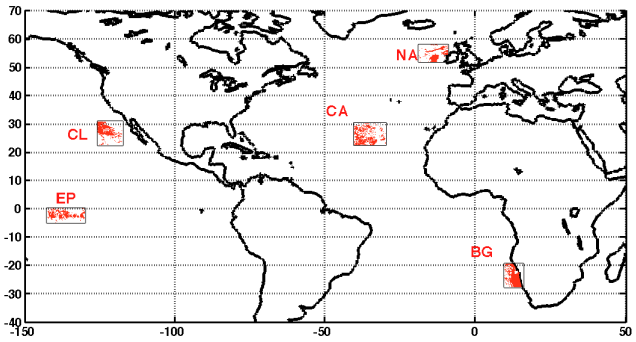

Figure 7.3: False clouds generated for validation purposes in the Central Atlantic (CA), Bengal upwelling (BG), California Pacific (CL), Equatorial Pacific (EP) and North Atlantic (NA).

Examples of one daily image validation for each region are shown in Figure 7.4. The quality of the reconstruction of the chlorophyll is given in terms of four parameters: the root mean square (rms) of the reconstruction error, its bias (mean), its standard deviation error (std) and the correlation coefficient (r) between original mask and reconstructed data in each area. For the case of the central Atlantic and California regions, the concentration of chlorophyll is smaller, followed by the values found in the North Atlantic, the Equatorial Pacific and the Bengal upwelling where the highest values of Chl-a concentration are found. Correlations coefficients between L4 and original Chl-a decrease for the regions where lower pigment concentrations are found. Better statics are associated with areas of high primary production.

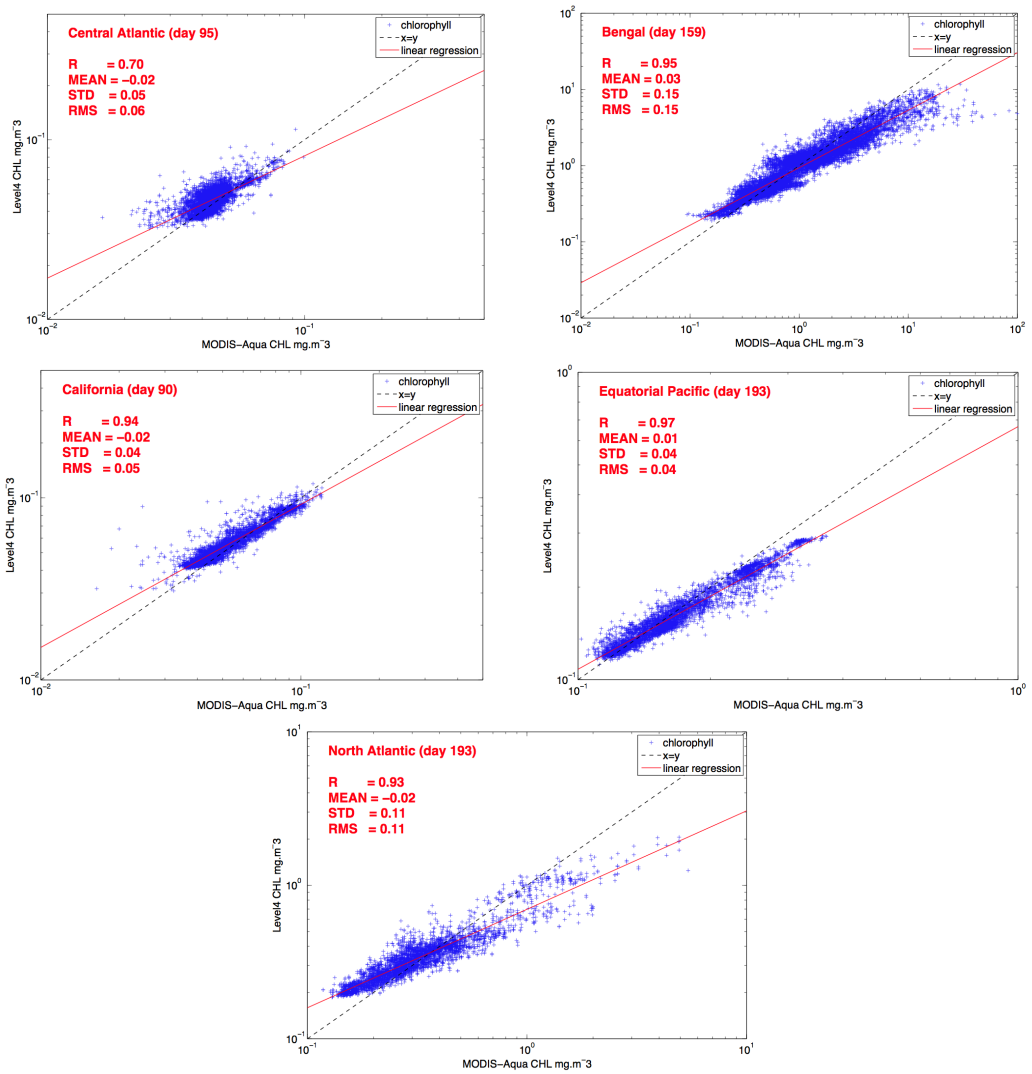

Figure 7.4: Validation of reconstruction under artificial clouds for MODIS Chl-a 2006. For CA region day 95, BG region day 159, CL day 90, EP day 193, and NA day 193.

The validation for the entire year 2006 is summarized in table 7.1, the minimum, maximum and mean values for each one of the statistical parameters and clouds are included. Our data fusion method succeeds in filling gaps with maximum correlation coefficients ranging from 0.92 to 0.99 for the studied period and artificial clouds. Oligotrophic regions have mean correlation coefficients of 0.62 and 0.80 (North Atlantic and California respectively), which are significantly lower that the mean correlation coefficients values of 0.92, 0.92 and 0.95 for the equatorial Pacific, the North Atlantic and the Bengal upwelling regions respectively. A slightly mean negative bias is systematically found, meaning that the L4 estimates are smaller than the original Chl-*a* values, probably due to the smoothing generated by the weighting functions used in the fusion algorithm (Eq. 4.34 in Section 4.4.3).

	R			R^2			$BIAS$			RMS		
	Min	Max	Mean	Min	Max	Mean	Min	Max	Mean	Min	Max	Mean
cloud CA	0.01	0.92	0.62	0	0.84	0.50	-0.25	-0.01	-0.06	0.03	0.31	0.11
cloud BG	0.86	0.97	0.95	0.74	0.95	0.91	-0.18	0.01	-0.01	0.08	0.28	0.14
cloud CL	0.27	0.97	0.80	0.07	0.95	0.69	-0.23	-0.01	-0.07	0.03	0.30	0.11
cloud EP	0.53	0.99	0.92	0.28	0.97	0.85	-0.11	0.03	-0.01	0.02	0.15	0.06
cloud NA	0.87	0.96	0.92	0.76	0.91	0.85	-0.07	0.03	0.00	0.08	0.17	0.11

Table 7.1: Results of daily reconstruction validation under artificial clouds for year 2006.

7.4 Interpretation of auxiliary parameters

The local regression coefficient $r(\vec{x})$ (Section 4.4.3) has small values along the Equatorial Pacific, and in the Southern and Indian Ocean (Figure 7.5). This indicates that the horizontal distribution of Chl-a cannot be locally explained by SST variability in these regions only. Therefore, either additional variables should be taken into account, or a more sophisticated relation between Chl-a and SST should be used. For example, in ocean regions known as High Nutrient Low Chlorophyll (HNLC) as the Equatorial Pacific and the Southern Ocean, low Chl-a concentrations are due to a stoichiometric imbalance of iron which have clearly no link to SST. Another possible cause for the low values of $r(\vec{x})$ in some regions is the lack of enough points to provide a quality reconstruction. For instance, 85 % of the data points are missing in the Equatorial Pacific due to the large cloudiness. This could be verified by segregating the regressions in function of the coverage of Chl-a.

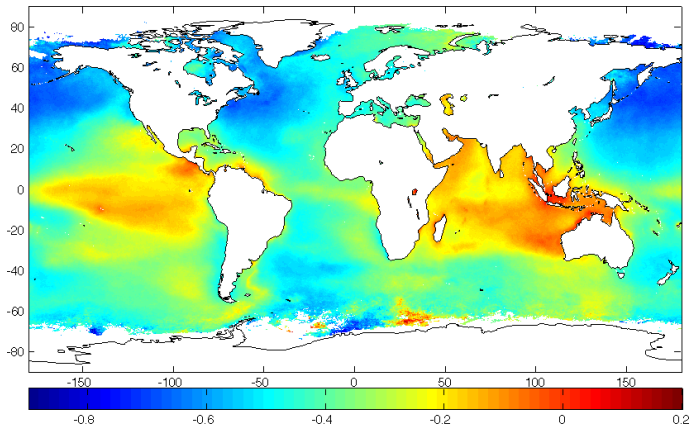

Figure 7.5: Mean local regression coefficient $r(\vec{x})$ for year 2006.

The functions $\widehat{a}(\vec{x})$ and $\widehat{b}(\vec{x})$ (Section 4.4.3) provide information about the local functional dependence between SST and Chl-a. The local slope, $\widehat{a}(\vec{x})$, will be negative at those places where SST decreases as Chl-a increases. Considering cold waters tend to have more nutrients than warm waters, phytoplankton is more abundant where surface waters are cold. So, as we move from one given point to another with colder water, Chl-a would usually increase and the slope $\widehat{a}(\vec{x})$ will be negative. However, the statistical relationship changes from point to point and

it should be expected to change from one image to the next one. Figure 7.6 shows the seasonal average of the slope and intercept (considering winter as Jan-Feb-Mar, spring as Apr-May-Jun, summer as Jul-Aug-Set and fall as Oct-Nov-Dec).

The coherent patterns of the auxiliary parameters of the method delineate areas with different relation between Chl-a and SST. In the same spirit, Longhurst (1998) introduced the concept of ocean biogeochemical provinces, characterized by their particular physical and biological behavior. Longhurst definition is based on the mixing layer depth (upper layer of the sea that is homogenized by turbulence induced by wind stress) lying close to the ocean-atmosphere interface. Specific provinces have common characteristics and can generally be classified as four general biomes: the coastal, polar, westerly and trade winds biomes. A visual comparison between local functions of the fusion method and the Longhurst definition is shown in Figure 7.6.

As expected, negative slopes are present in the upwelling areas associated with the eastern-most currents of the great anticyclonic gyres corresponding to the Bengal and Canary currents in the Atlantic Ocean and the Peru and California currents in the Pacific Ocean. Notice that this negative slope is present through the whole year. These ocean areas, as well as the upwelling zones and continental margins, are rich in Chl-a as a result of the proximity to areas where the resurgence of nutrients take place and the local circulation is favorable to nutrient accumulation. A band of cool, chlorophyll-rich water is also apparent all along the Equator; the strongest signal at the Atlantic Ocean and the open waters of the Pacific Ocean also leads to negative values of the local intercept $b(\vec{x})$.

Negative values of $\widehat{a}(\vec{x})$ are also found in areas where Chl-a concentration decreases as SST increases; this situation, which is typically found in the (oligotrophic) subtropical gyres, intensifies in the Atlantic Ocean during the northern hemisphere winter and spring. The Pacific Ocean exhibits an intensified negative pattern in the Northern subtropical gyre during boreal spring and a negative pattern in the southern hemisphere during austral spring. In both cases, such intensification in the oligotrophic subtropical gyres is driven by the seasonal cycle of sea surface temperature.

Subpolar gyres are also characterized by high Chl-a concentrations linked to nutrient accumulation during winter, when the mixing layer reaches the deep ocean followed by the stratification of the water column during spring. When nutrients accumulate near the ocean surface during the dark winter months, the local slope between SST and Chl-a is positive. However, when sunlight returns during spring and summer, the phytoplankton flourishes in high concentration, identified as negative values of $\widehat{a}(\vec{x})$.

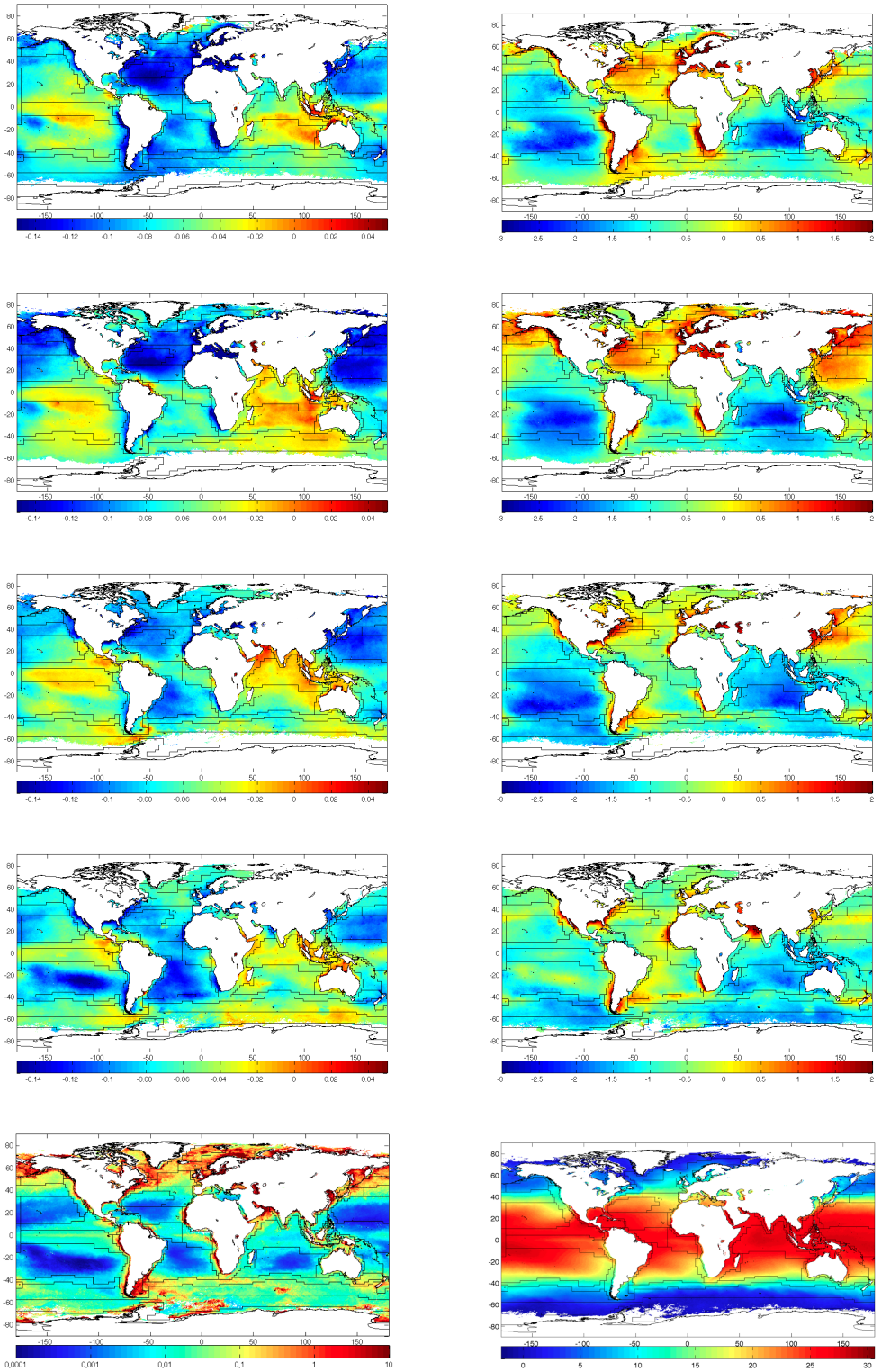

Figure 7.6: (First 4 rows only) : Left column: Seasonal mean local slope estimation $\hat{a}(x)$ for spring, summer, fall and winter. Right column: Local intercept estimation $\hat{b}(x)$ for spring, summer, fall and winter. These are the mean estimations used in the derivation of the fused map presented in Figure 6.6. Bottom row: Chl-a mean concentration for year 2006 and SST mean for the same year. Overlying all maps: Boundaries of Longhurst biogeochemical provinces.

Conclusions and Perspectives

Systematic measurements of Sea surface salinity (SSS) had never been acquired from satellite until November 2009 when the European Space Agency launched the Soil Moisture and Ocean Salinity (SMOS) satellite. SSS is an oceanic variable of recognized importance in the climate system and it has been identified by GCOS (Global Climate Observing System) as an Essential Climatic Variable. Accurate knowledge of SSS is essential as it is a key variable in various climate phenomena such as the thermohaline circulation, the balance between evaporation and precipitation in the ocean-atmosphere interphase and the hydrological cycle.

The experimental and novel features of the SMOS mission makes that, after almost 6 years in orbit, the SSS retrievals still have specific unsolved issues. The interferometric concept of the instrument requires a complex image reconstruction technique using the correlations between the measurements of its individual 69 antennas, and the quality of the reconstruction is strongly subsidiary of many parameters that are not always well-known and that may even drift with time. Thus, image reconstruction of brightness temperature is yet a considerable source of inaccuracies at Level 1. Another two critical issues affecting the quality of the data are anthropogenic radio frequency interference (RFI) sources and the transitions between land and ocean (i.e., the so-called land-sea contamination). Therefore, data mapping methodologies to improve the final SSS maps are required at this stage of the mission, and will still be useful even when L1 issues are mitigated.

This work has focused on studying, developing, and implementing methodologies for spatial interpolation and noise removal that have been applied to create maps of SSS from remote sensing data. The methodologies discussed across this thesis allow the generation of spatio-temporal averaged gridded maps from remote sensing measurements improving their quality in terms of coverage, noise reduction and geophysical consistency. These methodologies have been applied in the generation of global Level 3 and Level 4 SSS maps in regular cylindrical grids of 0.25^o spatial resolution for 9-day and monthly time windows. We have started by applying two classical objective analysis methods: weighted average and optimal interpolation (Chapter 3). The weighted average method has allowed us to generate Level 3 global maps by simply average in space and time the salinity values retrieved along the satellite tracks (i,e., the L2 SSS values), weighting each SSS value by its theoretical uncertainty and its spatial footprint. Such weighting has lead to the reduction of the noise level in the averaged SSS retrievals. The second classical method, i.e., the optimal interpolation (OI), has been studied and applied to generate OI SSS maps. In OI, the analysis field is a linear combination of a reference field and the difference between observations and such reference field. The coefficients of the linear combination are a function of the error of the observations and the error of the reference field. Assuming that these errors are Gaussian distributed and unbiased, the statistical properties of the errors are completely determined by their covariance matrices. In our implementation, we have also assumed that the observation errors are uncorrelated, and that these can be estimated

as the standard deviation of the L2 SSS measurements used in the weighted averaging at each grid point. As a test, we have assessed the quality of the OI maps when these errors are set to 10% of the variance, as done in Melnichenko et al. (2014). Two different reference fields, i.e., the World Ocean Atlas SSS climatology and the ISAS product (the latter is an optimally interpolated analysis of Argo data, (Gaillard et al., 2009)) have also been used for validation purposes. When focusing to the classical approaches, the best validation results are obtained using optimal interpolation with ISAS as a reference and with a diagonal observation covariance matrix whose numerical values are equal to the standard deviation of the L2 SSS measurements used in the weighted average at each grid point.

The optimal interpolation method presented in this thesis may be further improved in several ways. First, the excessive influence of the reference field (either ISAS or climatology) may be avoided by using a reference field coming from previous analysis of satellite SSS. By taking the output of a previous analysis step, the reference field would include recent information not present in the climatology and resolving spatio-temporal scales not seen by any analysis relying only on Argo data. On the other hand, using a reference field that includes satellite information from the previous 9-day analysis should be expected to already reveal mesoscale features that will reinforce if seen by observations and weaken them otherwise. A second possible improvement is to use a non-diagonal observation error covariance matrix, in order to introduce the spatial correlations of the observation errors in the algorithm. Although the diagonal assumption is valid for in situ observations, it might not be so for observations derived from satellite due to the actual physical and working characteristics of the instrument. Couplings between errors in the satellite retrievals have small incidence on the signal because geophysical correlations are usually large and longer ranged. However these correlations may have a significant impact on the statistical properties of the observational errors and, in turn, on the errors of the interpolated field. After almost six years of SMOS operations, those error covariances could be empirically estimated using iterative schemes applied to the data for each geophysical location. Additionally, it would be interesting to explore multivariate optimal interpolation approaches (Buongiorno, 2012) by evaluating the impact of using covariance functions that take into account synergistic information coming from other ocean variables or their singularity exponents (see below).

In this thesis we have also presented a novel data fusion approach to produce Level 4 remote sensing maps (Chapter 4). We have used an image processing technique called singularity analysis that allows characterizing the local regularity of any ocean variable by means of the so-called singularity exponents. The singularity exponents of different ocean variables neatly show the patterns of global circulation, and consequently can be used to detect ocean structures, such as currents, fronts, and eddies, from the analysis of individual snapshots of one ocean variable. We have analyzed the output of numerical simulations to confirm that SST and SSS have the same singularity exponents. This property has been exploited, since the theoretical correspondence in singularities associated with different ocean variables implies that there exists a functional relation between their gradients by means of a smooth matrix. After exploring general relations between the gradients of SSS and SST, we have made various simplifying hypothesis and

expressed the SSS as a function of the SST. The function is a local linear transformation with the smooth functions $\hat{a}$ (local slope) and $\hat{b}$ (local intercept). These parameters are estimated by weighted local regressions with a scale-invariant weight kernel. With these estimates the SST template is used to improve the quality of SSS measurements, and even to improve its sampling. The approach presented in this thesis is the first capable of producing high-quality Level 4 products without involving a numerical model or knowledge of a priori statistical parameters. The underlying hypothesis is the existence of turbulence, and the method only requires having another ocean variable observation simultaneously acquired. By avoiding using of statistics based on past observations, this method is well suited in a period characterized by a changing climate as the one we live in, because it adapts to the current situation.

We have investigated the sensitivity of the data fusion method to the presence of noise for different observation types and signal amplitudes by perturbing the output of the numerical model OFES with known sources of noise. Our tests show that the fusion method succeeds in reducing the output noise: the greater the signal amplitude, the greater the absolute and relative reduction. We have analyzed in detail the functional relation between the gradients of the signal and the template, justifying the several simplifying assumptions that lead to the final scalar formula. The particular formulation of the data fusion approach presented in this thesis acts as a low pass filter. This is a consequence of how the parameters $\hat{a}$ and $\hat{b}$ are determined. These parameters are currently determined in a very regularized way by doing a local lineal regression. This represents the principal weakness of our present approach. These parameters could also be estimated by using an alternative scale invariant weighting function. The weighting function currently used is equal to the inverse of the square of the distance to the point of application, but a faster decaying scale-invariant weight could be used instead to better keep the signal structure. Another interesting future research line to be explored is the use of the data fusion presented in this manuscript to carry out reconstructions of fields of SSS from historical observations of SST, using average reconstruction functions $\hat{a}$ and $\hat{b}$. This would allow producing long, systematic records of SSS maps, and using them to assess specific processes during the next decades, as far as SST maps are available.

Following the sensitivity tests and application of the explored methodologies to SMOS SSS data (Chapters 3 and 5), we have performed a thorough validation of the L3, OI, and L4 SSS products. We have used close-to-surface data from Argo profilers during the year 2012 at global scale. The resulting global scores for 9-day products are: biases of 0.0, -0.03 and -0.03 for L3, OI, and L4, respectively, and standard deviations of 0.71, 0.47, and 0.49, respectively. Then the statistics are calculated excluding possible systematic errors or potential contributions to error (i.e., only data farther than 1000 km from the coast, upper Argo measurement in the first 10 m below the ocean surface, and points with differences between reference and insitu SST lower than 0.3°C are used). The validation leads to bias scores of 0.01, 0.01 and -0.10 for L3, OI, and L4, respectively, and standard deviations of 0.36, 0.23 and 0.21, respectively. For the generation of the L3 maps (Chapter 3), we have taken into account the inaccuracies of L2 observations by

testing a strict filtering procedure. This filtering procedure achieves superior scores against in situ data (the global bias for the year 2012 is reduced from -0.10 to -0.01, and the standard deviation reduces from 0.75 to 0.71) as compared to unfiltered data. However, the data coverage decreases (ocean coverage decreases from 64% to 53% for a 9-day map). This is not a major constraint in fact. Since both methodologies (optimal interpolation and data fusion), when applied to L3 maps, can be used to extrapolate data, we are able to fill the gaps generated by the more stringent filtering, achieving an ocean coverage of 74% for the case of OI and 76% in the case of Level 4. In this thesis we have taken into account the extrapolated values produced by both the optimal interpolation and the data fusion techniques, but a detailed validation on the extrapolation capabilities of the data fusion method requires further investigation.

A different strategy is followed to compare the three types of SSS maps for the whole year 2012 using also Argo floats: the matchup is done using the uppermost salinity data from each Argo float, and every difference with respect to the SSS map is accumulated at a given grid point, without previous averaging of Argo data in the same spatio-temporal grid of satellite SSS, as in the previous validations. Then, we study the quality of SSS maps on 1° degree boxes that contain a minimum number of Argo data, i.e., fixed to 10. This strategy allows to generate regular 1° degree maps of bias and standard deviation. The results of this analysis show unbiased scores for OI while for L3 and L4, the bias is -0.01. In terms of standard deviations, L3 maps present relatively large values (average of 0.51), which tend to be larger at regions which are known to be problematic, i.e., high latitudes, RFI-contaminated areas, and in the Southern Ocean. The OI maps lead to a considerable improvement in the standard deviation (average of 0.29), while Level 4 maps reduce even further the error (average of 0.22).

Our results show that by using the proposed methodologies (optimal interpolation and the data fusion approach), the quality of SMOS derived maps is significantly reduced, approaching the initial SMOS mission requirements. The analysis of the singularity exponents derived from L3, OI and L4 maps shows that the original L3 data is affected by many systematic and random error sources that lead to poor SSS spatial consistency, as evidenced by the absence of structure in the corresponding singularity exponent map. On the contrary, the OI and L4 SSS products are able to restore a significant amount of the singularity structure, in agreement with to that obtained with SST maps. In that sense, the thesis shows that appropriate higher level processing is absolutely required in order to use SMOS data in oceanographic applications.

After the thorough discussion on the different methods and their general validation, we have introduced in Chapter 6 an oceanographic application in which we use two different Level 4 maps produced by merging SSS with two different templates (i.e., Reynolds SST and AVISO ADT), to study the salinity signature of mesoscale cyclonic and anticyclonic vortices linked to Western boundary currents of the Gulf Stream and the Brazil Current. With this regional study, the ability of SMOS SSS maps (Level 3 and Level 4) to characterize mesoscale processes has been investigated. This has been done following three steps. In the first step, we have assessed quantitatively the different SSS products using in situ SSS data as reference (termosalinographs

and Argo measurements depending on the availability at the specific area in the year 2012). This comparison has shown a reduction in systematic (bias) and random errors in the L4 fused SSS products in comparison to the SMOS L3 product. In the second step, an eddy detection method has been used (Mason et al., 2014) to detect the center and radius of anticyclonic/cyclonic vortices using sea level anomaly maps. It has allowed to evaluate the salinity anomaly inside the vortices and to assess if the evolution of the anomaly is geophysically consistent. In the third step, singularity analysis has been applied to the different SSS maps, showing that the quality of the signal is improved after fusion.

An average decrease in salinity between the ring center and the outside (i.e., negative anomaly) of about 0.1 has been found in cyclonic eddies for the different products in the year 2012. On the other hand, for anticyclonic eddies, a mean increase in salinity between the ring center and the outside (i.e., positive anomaly) of about 0.1 is found for the different products in the year 2012. The expected relatively salty/fresh anomaly inside (w.r.t. outside) the anticyclonic/cyclonic rings is better reconstructed by the L4 fused SSS products. The L3 product fused with ADT data (L4-ADT) outperforms the rest of the products, i.e., L3 and L3 fused with SST (L4-SST), in resolving the cyclonic/anticyclonic salinity signature. Although the L4-ADT product shows the best results in terms of resolving eddies and validation against TSG data, poor altimetry sampling can lead to spurious eddies and therefore spurious SSS anomalies in the L4-ADT product. The validation used in the second step is not fully independent as we use altimetry information both in the input of the eddy-tracking and in one of the templates. An alternative validation strategy should be explored.

It would be really interesting to deepen this study by computing a probabilistic census of the detected mesoscale eddies, their persistence, they mean travel distance and research the effect that they have changing the physicochemical properties in the ocean basins they occur. Another interesting outlook of this work would be to estimate the mean transport of properties associated to these mesoscale eddies, assuming a characteristic depth, probably complemented by the use of a numerical model.

At the end of this thesis (Chapter 7), we have also explored the capabilities of our data fusion approach for the extrapolation of Aqua-Modis Chl-a maps by using Aqua-Modis SST as template. The information of the regression coefficients of the data fusion method has allowed to study the relation between these two ocean scalars. We have shown that it is possible to increase the daily spatial coverage of MODIS Chl-a without any prior knowledge about the dynamics of the flow. The extrapolated fields have proved to be consistent with the observed ocean structures. The cross validation, which consists of imposing artificial gaps and then comparing the original with the reconstructed data, results in daily quality reconstructions of mean correlation coefficients ranging from 0.62 to 0.95.

As a summary, during this thesis, three data mapping approaches have been developed, tested, and applied to SMOS SSS data. The resulting algorithms show a clear improvement of the SMOS data quality. As such, they have been implemented in the operational production

chain of SMOS SSS L3, OI, and L4 products, which are served by the Barcelona Expert Center. In particular, the OI and L4 SSS products currently approach the SMOS mission requirements. Moreover, our novel data fusion approach has also been applied to daily Aqua MODIS Level-3 chlorophyll maps using MODIS SST maps as template, and to Aquarius SSS (Umbert et al., 2015), using OSTIA and Reynolds SST, and ADT from AVISO as templates. The resulting Chl-a and SSS Level 4 products contain the mesoscale structures seen in SST and SSH maps, exhibit a significant reduction of the uncertainty, and allow extrapolation to cloud-affected areas or to data gaps.

Bibliography

Alvera-Azcarate, A., Barth, J., and Weisberg, R. (2007). Multivariate reconstruction of missing data in sea surface temperature, chlorophyll and wind satellite fields. *Journal of Geophysical Reserch*. 13

Antonov, J., Seidov, D., Boyer, T. P., Locarnini, R. A., Mishonov, A. V., Garcia, H. E., Baranova, O. K., Zweng, M. M., and Johnson, D. R. (2010). *World Ocean Atlas 2009 Volume 2: Salinity*, volume 2. NOAA Atlas NESDIS 69, S. Levitus. 25, 39

Banks, C. J., Gommenginger, C. P., Srokosz, M. A., and Snaith, H. M. (2012). Validating smos ocean surface salinity in the atlantic with argo and operational ocean model data. *Geoscience and Remote Sensing, IEEE Transactions on*, 50(5):1688–1702. 17

Barth, A., Joassin, P., Beckers, J.-M., and Troupin, C. (2008). Introduction to optimal interpolation and variational analysis. In *Varna Summer School 2008 for "Statistical Analysis of Biological data and Times-Series"*. 39

BEC, B. E. C. (2014). Products description, bec. issue 1.3. Technical report, SMOS-BEC, ICM-CSIC. 29

Berger, M., Camps, A., Font, J., Kerr, Y., Miller, J., Johannessen, J., Boutin, J., Drinkwater, M., Skou, N., Floury, N., et al. (2002). Measuring ocean salinity with esa's smos mission. *ESA bulletin*, 111(113f). 16

Bingham, F. M., Busecke, J., Gordon, A. L., Giulivi, C. F., and Li, Z. (2014). The north atlantic subtropical surface salinity maximum as observed by aquarius. *Journal of Geophysical Research: Oceans*, 119(11):7741–7755. 64

Bonjean, F. and Lagerloef, G. S. E. (2002). Diagnostic model and analysis of the surface currents in the tropical pacific ocean. *J. Phys. Oceanogr.*, 32(10):2938–2954. 24

Boutin, J., Martin, N., Reverdin, G., Morisset, S., Yin, X., Centurioni, L., and Reul, N. (2014). Sea surface salinity under rain cells: Smos satellite and in situ drifters observations. *Journal of Geophysical Research: Oceans*, 119(8):5533–5545. 16

Boutin, J., Martin, N., Reverdin, G., Yin, X., and Gaillard, F. (2012a). Sea surface freshening inferred from SMOS and ARGO salinity: impact of rain. *Ocean Science Discussions*, 9(5):3331–3357. 18, 43

Boutin, J., Martin, N., Reverdin, G., Yin, X., and Gaillard, F. (2013). Sea surface freshening inferred from smos and argo salinity: Impact of rain. *Ocean Sci*, 9(1):183–192. 17, 18

Boutin, J., Waldteufel, P., Martin, N., Caudal, G., and Dinnat, E. (2012b). First assessment of smos data over open ocean: Part II - sea surface salinity. *Journal of Atmospheric and Oceanic Technology*, 21(9):1432 –1447. 21, 28

Bretherton, F., Davis, R., and Fandry, C. (1976). A technique for objective analysis and design of oceanographic experiments applied to MODE-73. *Deep Sea Research*, 23:559–582. 1, 35

Brown, O. and Minnett, P. J. (1999). Modis infrared sea surface temperature algorithm algorithm theoretical basis document. version 2.0. Technical report, University of Miami. 153

Bryden, H. L., Candela, J., and Kinder, T. H. (1994). Exchange through the strait of gibraltar. *Progress in Oceanography*, 33(3):201–248. 11

Buongiorno, B. (2012). A novel approach for the high-resolution interpolation of in situ sea surface salinity. *Journal of Atmospheric and Oceanic Technology*, 29:867–879. 13, 164

Busecke, J., Gordon, A. L., Li, Z., Bingham, F. M., and Font, J. (2014). Subtropical surface layer salinity budget and the role of mesoscale turbulence. *Journal of Geophysical Research: Oceans*, 119(7):4124–4140. 65

Campbell, J. W. (1995). The lognormal distribution as a model for bio-optical variability in the sea. *Journal of Geophysical Research*, 100(C7):13237,13254. 154

Chelton, D., Schlax, M., Samelson, R., and de Szoeke, R. (2007). Global observations of large oceanic eddies. *Geophysical Research Letters*, 34:L15606. 7, 72

Chelton, D. B., Gaube, P., Schlax, M. G., Early, J. J., and Samelson, R. M. (2011). The influence of nonlinear mesoscale eddies on near-surface oceanic chlorophyll. *Science*, 334(6054):328–332. 127, 129

Chelton, D. B. and Xie, S.-P. (2010). Coupled ocean-atmosphere interaction at oceanic mesoscales. *Oceanography*, 23(4):52–69. 7

Clayson, C. A. and Bogdanoff, A. S. (2013). The effect of diurnal sea surface temperature warming on climatological air–sea fluxes. *Journal of Climate*, 26(8):2546–2556. 1

Coachman, L. and Aagaard, K. (1988). Transports through bering strait: Annual and interannual variability. *Journal of Geophysical Research: Oceans (1978–2012)*, 93(C12):15535–15539. 11

Cornillon, P., Lee, T., and Fall, G. (1994). On the probability that a gulf stream meander crest detaches to form a warm core ring. *J. Phys. Oceanogr.*, 24(1):159–171. 129

Crocker, R., Matthews, D., Emery, W., and Baldwin, D. (2007). Computing coastal ocean surface currents from infrared and ocean color satellite imagery. *IEEE Trans. Geosci. Remote Sens.*, 45(2):435–447. 2

Csanady, G. T. (1979). The birth and death of a warm core ring. *J. Geophys. Res.*, 84(C2):777–780. 127

Daganzo-Eusebio, E., Oliva, R., Kerr, Y., Nieto, S., Richaume, P., and Mecklenburg, S. (2013). SMOS Radiometer in the 1400–1427-MHz Passive Band: Impact of the RFI Environment and Approach to Its Mitigation and Cancellation. *IEEE Trans. Geosci. Remote Sens.*, 51(10):4999–5007. 17

Delcroix, T., Hénin, C., Porte, V., and Arkin, P. (1996). Precipitation and sea-surface salinity in the tropical pacific ocean. *Deep Sea Research Part I: Oceanographic Research Papers*, 43(7):1123–1141. 11

Denman, K. L. and Abbott, M. A. (1994). Time scales of pattern evolution from cross-spectrum analysis of advanced very high resolution radiometer and coastal zone color scanner imagery. *J. Geophys. Res.*, 99(C4):7433–7442. 153

Dewar, W. K. (1986). Mixed layers in gulf stream rings. *Dynamics of Atmospheres and Oceans*, 10(1):1–29. 129

Dittmar, W. (1884). Report on the scientific results of the exploring voyage of h.m.s. challenger 1873-76. *Phys. and Chem., Vol. 1H.M. Stationery Office, London.* 10

Doney, S., Glover, D. M., McCue, S. J., and Fuentes, M. (2003). Mesoscale variability of seawifs satellite ocean color: Global patterns and spatial scales. *J. Geophys. Res.*, 108:6.1–6.15. 153

Donlon, C. J., Martin, M., Stark, J., Roberts-Jones, J., Fiedler, E., and Wimmer, W. (2012). The operational sea surface temperature and sea ice analysis (ostia) system. *Remote Sensing of Environment*, 116(0):140 – 158. ¡ce:title¿Advanced Along Track Scanning Radiometer(AATSR) Special Issue¡/ce:title¿. 106

Drucker, R. and Riser, S. C. (2014). Validation of aquarius sea surface salinity with argo: Analysis of error due to depth of measurement and vertical salinity stratification. *Journal of Geophysical Research: Oceans*, 119(7):4626–4637. 21

Ducet, N., Le Traon, P. Y., and Reverdin, G. (2000). Global high-resolution mapping of ocean circulation from TOPEX/Poseidon and ERS-1 and -2. *J. Geophys. Res.*, 105(C8):19477–19498. 35, 106

Evans, R. H., Baker, K. S., Brown, O. B., and Smith, R. C. (1985). Chronology of warm-core ring 82B. *J. Geophys. Res.*, 90(C5):8803–8811. 127

Everett, J., Baird, M., Oke, P., and Suthers, I. (2012). An avenue of eddies: Quantifying the biophysical properties of mesoscale eddies in the tasman sea. *Geophysical Research Letters*, 39(16). 129

Ferrari, R. and Paparella, F. (2003). Compensation and alignement of thermohaline gradients in the ocean mixed layer. *Journal of Physical Oceanography*, 33:2214–2223. 87

Ferrari, R. and Rudnick, D. L. (2000). Thermohaline variability in the upper ocean. *Journal of Geophysical Research: Oceans (1978–2012)*, 105(C7):16857–16883. 76

Ferrari, R. and Young, W. (1997). On the development of thermohaline correlations as a result of nonlinear diffusive parameterizations. *Journal of marine research*, 55(6):1069–1101. 77

Font, J., Camps, A., Borges, A., Martin-Neira, M., Boutin, J., Reul, N., Kerr, Y. H., Hahne, A., and Mecklenburg, S. (2010). Smos: The challenging sea surface salinity measurement from space. *Proceedings of the IEEE*, 98(5):649–665. 2, 17

Frisch, U. (1995). *Turbulence: The Legacy of A. N. Kolmogorov*. Cambridge University Press. 73, 148, 153

Fu, L.-L. and Cazenave, A. (2000). *Satellite altimetry and earth sciences: a handbook of techniques and applications*, volume 69. Academic Press. 8

Fuglister, F. (1977). *A Cyclonic Ring Formed by the Gulf Stream, 1967. In: A Voyage of Discovery: George Deacon 70th Anniversary Volume, Supp. to Deep-Sea Research*. Contribution ... from the Woods Hole Oceanographic Institution. Pergamon Press, Oxford. 127

Gaillard, F. (2012). Isas-tool version 6: Method and configuration. Technical report, Ifremer. 25

Gaillard, F., Autret, E., Thierry, V., Galaup, P., Coatanoan, C., and Loubrieu, T. (2009). Quality control of large argo datasets. *Journal of Atmospheric and Oceanic Technology*, 26(2):337–351. 25, 59, 164

Gandin, L. S. and Hardin, R. (1965). *Objective analysis of meteorological fields*, volume 242. Israel program for scientific translations Jerusalem. 35

Garzoli, S. L. (1993). Geostrophic velocity and transport variability in the brazil-malvinas confluence. *Deep Sea Research Part I: Oceanographic Research Papers*, 40(7):1379–1403. 127

Garzoli, S. L. and Garraffo, Z. (1989). Transports, frontal motions and eddies at the brazil-malvinas currents confluence. *Deep Sea Research Part A. Oceanographic Research Papers*, 36(5):681–703. 127

Gierach, M. M., Vazquez-Cuervo, J., Lee, T., and Tsontos, V. M. (2013). Aquarius and SMOS detect effects of an extreme Mississippi River flooding event in the Gulf of Mexico. *Geophys. Res. Lett.*, 40(19):5188–5193. 18

Gordon, A. L. (1989). Brazil-malvinas confluence–1984. *Deep Sea Research Part A. Oceanographic Research Papers*, 36(3):359–384. 127

Gordon, A. L. and Giulivi, C. F. (2014). Ocean eddy freshwater flux convergence into the north atlantic subtropics. *Journal of Geophysical Research: Oceans*, 119(6):3327–3335. 65

Gourrion, J., Guimbard, S., Portabella, M., and Sabia, R. (2013). Toward an optimal estimation of the smos antenna-frame systematic errors. *Geoscience and Remote Sensing, IEEE Transactions on*, 51(9):4752–4760. 17

Grodsky, S. A., Reul, N., Lagerloef, G., Reverdin, G., Carton, J. A., Chapron, B., Quilfen, Y., Kudryavtsev, V. N., and Kao, H.-Y. (2012). Haline hurricane wake in the Amazon/Orinoco plume: AQUARIUS/SACD and SMOS observations. *Geophys. Res. Lett.*, 39(20):L20603. 18

Guimbard, S., Gourrion, J., Portabella, M., Turiel, A., Gabarró, C., and Font, J. (2012). SMOS semi-empirical ocean forward model adjustment. *IEEE Trans. Geosci. Remote Sens.*, 50(5):1676–1687. 17, 18, 19, 122

Hackert, E., Busalacchi, A. J., and Ballabrera-Poy, J. (2014). Impact of aquarius sea surface salinity observations on coupled forecasts for the tropical indo-pacific ocean. *Journal of Geophysical Research: Oceans*, 119(7):4045–4067. 12

Hallberg, R. and Gnanadesikan, A. (2006). The role of eddies in determining the structure and response of the wind-driven southern hemisphere overturning: Results from the modeling eddies in the southern ocean (MESO) project. *J. Phys. Oceanogr.*, 36:2232–2252. 72

Han, W. and McCreary, J. P. (2001). Modeling salinity distributions in the indian ocean. *Journal of Geophysical Research: Oceans (1978–2012)*, 106(C1):859–877. 11

Hausmann, U. and Czaja, A. (2012). The observed signature of mesoscale eddies in sea surface temperature and the associated heat transport. *Deep Sea Res. Part I*, 70(0):60 – 72. 13, 129

Hernandez, O., Boutin, J., Kolodziejczyk, N., Reverdin, G., Martin, N., Gaillard, F., Reul, N., and Vergely, J. (2014). Smos salinity in the subtropical north atlantic salinity maximum: 1. comparison with aquarius and in situ salinity. *Journal of Geophysical Research: Oceans*. 18, 64

Hoareau, N., Umbert, M., Martínez, J., Turiel, A., and Ballabrera-Poy, J. (2014). On the potential of data assimilation to generate smos-level 4 maps of sea surface salinity. *Remote Sensing of Environment*, 146(0):188 – 200. Liege Colloquium Special Issue: Remote sensing of ocean colour, temperature and salinity. 13

Isern-Fontanet, J., Chapron, B., Lapeyre, G., and Klein, P. (2006). Potential use of microwave sea surface temperatures for the estimation of ocean currents. *Geophysical Research Letters*, 22:L24608. 108

Isern-Fontanet, J., García-Ladona, E., and Font, J. (2003). Identification of marine eddies from altimetric maps. *J. Atmos. Oceanic Tech.*, 20:772–778. 72

Isern-Fontanet, J., Lapeyre, G., Klein, P., Chapron, B., and Hecht, M. W. (2008). Three-dimensional reconstruction of oceanic mesoscale currents from surface information. *Journal of Geophysical Research: Oceans (1978–2012)*, 113(C9). 13

Isern-Fontanet, J., Turiel, A., Garcia-Ladona, E., and Font, J. (2007). Microcanonical multifractal formalism: Application to the estimation of ocean surface velocities. *J. Geophys. Res.*, 112:C05024. v, vii, 2, 74, 109

Johannessen, O. M., Sandven, S., Jenkins, A. D., Durand, D., Pettersson, L. H., Espedal, H., Evensen, G., and Hamre, T. (2000). Satellite earth observation in operational oceanography. *Coastal Engineering*, 41(1):155–176. 6, 13

Johns, W., Yao, F., Olson, D., Josey, S., Grist, J., and Smeed, D. (2003). Observations of seasonal exchange through the straits of hormuz and the inferred heat and freshwater budgets of the persian gulf. *Journal of Geophysical Research: Oceans (1978–2012)*, 108(C12). 11

Johnson, G. C. (2006). Generation and initial evolution of a mode water θ-s anomaly*. *Journal of physical oceanography*, 36(4):739–751. 76

Johnson, G. C., Schmidtko, S., and Lyman, J. M. (2012). Relative contributions of temperature and salinity to seasonal mixed layer density changes and horizontal density gradients. *Journal of Geophysical Research: Oceans (1978–2012)*, 117(C4). 11

Jorda, G., Gomis, D., and Talone, M. (2011). The smos l3 mapping algorithm for sea surface salinity. *Geoscience and Remote Sensing, IEEE Transactions on*, 49(3):1032 –1051. 37, 62

Jouini, M., Lévy, M., Crépon, M., and Thiria, S. (2013). Reconstruction of satellite chlorophyll images under heavy cloud coverage using a neural classification method. *Remote Sensing of Environment*, 131:232. 13

Kelly, K. A., Small, R. J., Samelson, R. M., Bo, Q., Joyce, T. M., Young-Oh, K., and Cronin, M. F. (2010). Western Boundary Currents and Frontal Air-Sea Interaction: Gulf Stream and Kuroshio Extension. *J. Climate*, 23(21):5644 – 5667. 129

Kerr, Y., Waldteufel, P., Wigneron, J., Martinuzzi, J., Font, J., and Berguer, M. (2001). Soil moisture retrieval from space: The soil moisture and ocean salinity mission (smos). *IEEE Trans. Geosci. Remote Sens.*, 39:1729–1735. 2, 15

Klein, L. and Swift, C. T. (1977). An improved model for the dielectric constant of sea water at microwave frequencies. *Antennas and Propagation, IEEE Transactions on*, 25(1):104–111. 16

Klein, P., Isern-Fontanet, J., Lapeyre, G., Roullet, G., an B. Chapron, E. D., Gentil, S. L., and Sasaki, H. (2009). Diagnosis of vertical velocities in the upper ocean from high resolution sea surface height. *Geophysical Research Letters*, 36:L12603. 13

Kolmogorov, A. N. (1941a). Dissipation of energy in a locally isotropic turbulence. *Dokl. Akad. Nauk. SSSR*, 32:16–18. 73

Kolmogorov, A. N. (1941b). The local structure of turbulence in an incompressible fluid with very large reynolds number. *Dokl. Akad. Nauk. SSSR*, 309:301–305. 73

Kolodziejczyk, N., Hernandez, O., Boutin, J., and Reverdin, G. (2015). Smos salinity in the subtropical north atlantic salinity maximum: 2. two-dimensional horizontal thermohaline variability. *Journal of Geophysical Research: Oceans*. 130

LaCasce, J. and Mahadevan, A. (2006). Estimating subsurface horizontal and vertical velocities from sea-surface temperature. *Journal of Marine Research*, 64:695–721. 13, 108

Lagerloef, G. (2012). Satellite mission monitors ocean surface salinity. *EOS, Trans. Am. Geophys. Union*, 93(25):233–234. 15

Lagerloef, G. and Coauthors (2013). Aquarius salinity validation analysis. *JPL Aquarius Project Doc. AQ-014-PS-0016.*, Data version 2.0:36 pp. 19, 39

Lagerloef, G., Colomb, F., Le Vine, D., Wentz, F., Yueh, S., Ruf, C., Lilly, J., Gunn, J., and Chao, Y. (2008). The aquarius/sac-d mission: Designed to meet the salinity remote-sensing challenge. *Oceanography*, 21(1):68–81. 18

Lapeyre, G. and Klein, P. (2006). Dynamics of the upper oceanic layers in terms of surface quasigeostrophy theory. *J. Phys. Oceanogr.*, 36:165–176. 13

Le Traon, P.-Y. (2002). Satellite oceanography for ocean forecasting. In *Ocean Forecasting*, pages 19–36. Springer. 5

Le Traon Pierre-Yves, M. R. (1999). Ocean currents and eddies (chapter 3). *A Handbook of Techniques and Applications (L.-L. Fu and A. Cazenave, Eds). http://archimer. ifremer. fr/doc/00090/20102*. 8

Le Vine, D. M., Lagerloef, G. S., Colomb, F. R., Yueh, S. H., and Pellerano, F. A. (2007). Aquarius: An instrument to monitor sea surface salinity from space. *Geoscience and Remote Sensing, IEEE Transactions on*, 45(7):2040–2050. 18

Lee, C. M. and Brink, K. H. (2010). Observations of storm-induced mixing and Gulf Stream Ring incursion over the southern flank of Georges Bank: Winter and summer 1997. *J. Geophys. Res.*, 115(C8):C08008. 129

Lentini, C. A., Goni, G. J., and Olson, D. B. (2006). Investigation of brazil current rings in the confluence region. *Journal of Geophysical Research: Oceans (1978–2012)*, 111(C6). 129

Leterme, S. C. and Pingree, R. D. (2008). The Gulf Stream, rings and North Atlantic eddy structures from remote sensing (Altimeter and SeaWiFS). *J. Mar. Sys.*, 69(3–4):177–190. 129

LeTraon, P., Nadal, F., and Ducet, N. (1998). An improved mapping method of multisatellite altimeter data. *J. Atmos. Oceanic Technol.*, 15(2):522–534. 35

Lewis, E. (1980). The practical salinity scale 1978 and its antecedents. *Oceanic Engineering, IEEE Journal of*, 5(1):3–8. 10, 127

Liebe, H. J., Hufford, G. A., and Cotton, M. G. (1993). Propagation modeling of moist air and suspended water/ice particles at frequencies below 1000 GHz. In *AGARD 52nd Specialists' Meeting of the Electromagnetic Wave Propagation Panel*, pages 3:1–10. 17

Longhurst, A. R. (1998). *Ecological geography of the sea*. Academic Press. 160

Lovejoy, S., Curri, W., Tessier, Y., Claereboudt, M., Bourget, E., Roff, J., and Schertzer, D. (2001a). Universal multifractals and ocean patchiness: phytoplankton, physical fields and coastal heterogeneity. *J. Plankton Res.*, 23(2):117–141. 9

Lovejoy, S., Schertzer, D., Tessier, Y., and Gaonac'h, H. (2001b). Multifractals and resolution-independent remote sensing algorithms: The example of ocean colour. *Int. J. Remote Sens.*, 22(7):1191–1234. v, vii, 74

Mallat, S. (1999). *A Wavelet Tour of Signal Processing*. Academic Press, 2nd Edition. 80

Martin-Neira, M., Corbella, I., Torres, F., Kainulainen, J., Oliva, R., Closa, J., Cabot, F., Castro, R., Barbosa, J., Gutierrez, A., et al. (2013). Smos instrument performance and calibration after 3 years in orbit. In *EGU General Assembly Conference Abstracts*, volume 15, page 9556. 17

Mason, E., Colas, F., Molemaker, J., Shchepetkin, A. F., Troupin, C., McWilliams, J. C., and Sangrà, P. (2011). Seasonal variability of the canary current: a numerical study. *Journal of Geophysical Research: Oceans (1978–2012)*, 116(C6). 72, 126

Mason, E., Pascual, A., and McWilliams, J. C. (2014). A new sea surface height–based code for oceanic mesoscale eddy tracking. *Journal of Atmospheric and Oceanic Technology*, 31(5):1181–1188. 139, 167

Masumoto, Y. (2010). Sharing the results of a high-resolution ocean general circulation model under a multi-discipline framework: a review of OFES activities. *Ocean Dyn.*, 60(3):633–652. 24

Masumoto, Y., Sasaki, H., Kagimoto, T., Komori, N., Ishida, A., Sasai, Y., Miyama, T., Motoi, T., Mitsudera, H., Takahashi, K., Sakuma, H., and Yamagata, T. (2004). A fifty-year eddy-resolving simulation of the world ocean: Preliminary outcomes of OFES (OGCM for the earth simulator). *J. Earth Simulator*, 1:35–56. 24, 77

McIntosh, P. C. (1990). Oceanographic data interpolation: Objective analysis and splines. *Journal of Geophysical Research: Oceans (1978–2012)*, 95(C8):13529–13541. 35

Mecklenburg, S., Drusch, M., Kerr, Y. H., Font, J., Martin-Neira, M., Delwart, S., Buenadicha, G., Reul, N., Daganzo-Eusebio, E., Oliva, R., et al. (2012). Esa's soil moisture and ocean salinity mission: Mission performance and operations. *Geoscience and Remote Sensing, IEEE Transactions on*, 50(5):1354–1366. 16

Meissner, T., Wentz, F., Ricciardulli, L., Hilburn, K., and Scott, J. (2014). The aquarius salinity retrieval algorithm recent progress and remaining challenges. In *Microwave Radiometry and Remote Sensing of the Environment (MicroRad), 2014 13th Specialist Meeting on*, pages 49–54. IEEE. 19

Melnichenko, O., Hacker, P., Maximenko, N., Lagerloef, G., and Potemra, J. (2014). Spatial optimal interpolation of aquarius sea surface salinity: Algorithms and implementation in the north atlantic. *Journal of Atmospheric and Oceanic Technology*, 31(2014):1583–1600. 17, 19, 35, 38, 39, 61, 62, 66, 67, 164

Montera, L. d., Jouini, M., Verrier, S., Thiria, S., and Crépon, M. (2011). Multifractal analysis of oceanic chlorophyll maps remotely sensed from space. *Ocean Science*, 7(2):219–229. 74

Morrow, R. and Le Traon, P.-Y. (2012). Recent advances in observing mesoscale ocean dynamics with satellite altimetry. *Advances in Space Research*, 50(8):1062–1076. 6

Nieves, V., Llebot, C., Turiel, A., Solé, J., García-Ladona, E., Estrada, M., and Blasco, D. (2007). Common turbulent signature in sea surface temperature and chlorophyll maps. *Geophys. Res. Lett.*, 34:L23602. v, vii, 74, 87, 153

Nieves, V. and Turiel, A. (2009). Analysis of ocean turbulence using adaptive cve on altimetry maps. *Journal of Marine Systems*, 77:482–494. v, vii

Niller, P. P. and Reynolds, R. W. (1984). The three-dimensional circulation near the eastern north pacific subtropical front. *Journal of physical oceanography*, 14(2):217–230. 76

Oliva, R., Daganzo, E., Kerr, Y. H., Mecklenburg, S., Nieto, S., Richaume, P., and Gruhier, C. (2012). Smos radio frequency interference scenario: Status and actions taken to improve the rfi environment in the 1400–1427-mhz passive band. *Geoscience and Remote Sensing, IEEE Transactions on*, 50(5):1427–1439. 17

Parisi, G. and Frisch, U. (1985). On the singularity structure of fully developedturbulence. In Ghil, M., Benzi, R., and Parisi, G., editors, *Turbulence andPredictability in Geophysical FluidDynamics. Proc. Intl. School of Physics E. Fermi*, pages 84–87, Amsterdam. North Holland. 74, 148

Parker, C. E. (1971). Gulf stream rings in the sargasso sea. *Deep Sea Research and Oceanographic Abstracts*, 18(10):981 – 993. 127

Pedlosky, J. (1998). *Ocean Circulation Theory*. Springer. 8

Peterson, R. G. and Stramma, L. (1991). Upper-level circulation in the south atlantic ocean. *Progress in oceanography*, 26(1):1–73. 127

Pingree, R. D., Holligan, P. M., and Mardell, G. T. (1979). Phytoplankton growth and cyclonic eddies. *Nature*, 278(5701):245–247. 127

Pont, O., Turiel, A., and Pérez-Vicente, C. (2009). Empirical evidences of a common multifractal signature in economic, biological and physical systems. *Physica A*, 388:2025–2035. 9, 72, 148, 149

Pont, O., Turiel, A., and Yahia, H. (2013a). Singularity analysis of digital signals through the evaluation of their unpredictable point manifold. *International Journal of Computer Mathematics*, 90(8):1693–1707. 74

Pont, O., Turiel, A., Yahia, H., and Badri, H. (2013b). Global measure of predictability, singularity exponents, and associated sparse image representation. Submitted to *IEEE Transactions on Image Processing*.

Qu, T., Gao, S., and Fukumori, I. (2011). What governs the north atlantic salinity maximum in a global gcm? *Geophysical Research Letters*, 38(7). 64

Qu, T., Gao, S., and Fukumori, I. (2013). Formation of salinity maximum water and its contribution to the overturning circulation in the north atlantic as revealed by a global general circulation model. *Journal of Geophysical Research: Oceans*, 118(4):1982–1994. 64

Reul, N. and CATDS -CECOS Team (2012). SMOS Level 3 SSS Research products - Product User Manual - Reprocessed Years 2010-2012. Technical report, IFREMER-CATDS-CECOS-L3-PUDOC, Issue 2 – Rev 0. 18

Reul, N., Chapron, B., Lee, T., Donlon, C., Boutin, J., and Alory, G. (2014a). Sea Surface Salinity structure of the meandering Gulf Stream revealed by SMOS sensor. *Geophys. Res. Lett.*, 41(9):3141–3148. 131

Reul, N., Fournier, S., Boutin, J., Hernandez, O., Maes, C., Chapron, B., Alory, G., Quilfen, Y., Tenerelli, J., Morisset, S., et al. (2014b). Sea surface salinity observations from space with the smos satellite: a new means to monitor the marine branch of the water cycle. *Surveys in Geophysics*, 35(3):681–722. 11, 151

Reul, N., Fournier, S., Boutin, J., Hernandez, O., Maes, C., Chapron, B., Alory, G., Quilfen, Y., Tenerelli, J., Morisset, S., Kerr, Y., Mecklenburg, S., and Delwart, S. (2014c). Sea surface salinity observations from space with the smos satellite: A new means to monitor the marine branch of the water cycle. *Surveys in Geophysics*, 35(3):681–722. 11

Reul, N., Tenerelli, J., Boutin, J., Chapron, B., Paul, F., Brion, E., Gaillard, F., and Archer, O. (2012a). Overview of the first smos sea surface salinity products. part i: Quality assessment for the second half of 2010. *Geoscience and Remote Sensing, IEEE Transactions on*, 50(5):1636–1647. 17

Reul, N., Tenerelli, J., Chapron, B., Vandemark, D., Quilfen, Y., and Kerr, Y. (2012b). SMOS satellite L-band radiometer: A new capability for ocean surface remote sensing in hurricanes. *J. Geophys. Res.*, 117(C2):C02006. 18

Reul, N., Tenerelli, J. E., Floury, N., and Chapron, B. (2008). Earth-viewing L-band radiometer sensing of sea surface scattered celestial sky radiation. Part II: application to SMOS. *IEEE Transactions on Geosciences and Remote Sensing*, 46(3):675–688. 17

Reynolds, R. and Smith, T. (1994). Improved global sea surface temperature analyses using optimal interpolation. *Journal of Climate*, 7:929–948. 35

Reynolds, R. W., Smith, T. M., Liu, C., Chelton, D. B., Casey, K. S., and Schlax, M. G. (2007). Daily high-resolution-blended analyses for sea surface temperature. *J. Climate*, 20(22):5473–5496. 23, 24, 35, 106

Richardson, P. (1983). Gulf stream rings. In Robinson, A., editor, *Eddies in Marine Science*. Springer Berlin Heidelberg. 127

Rodex, G. I. (1975). On north pacific temperature, salinity, sound velocity and density frontsand their relation to the wind and energy flux fields. *Journal of Physical Oceanography*, 5(4):557–571. 76

Rudin, W. (1987). *Real and Complex Analysis*. Mc Graw Hill, New York, USA. 81

Rudnick, D. L. and Ferrari, R. (1999). Compensation of horizontal temperature and salinity gradients in the ocean mixed layer. *Science*, 283(5401):526–529. 76, 77

Rudnick, D. L. and Martin, J. P. (2002). On the horizontal density ratio in the upper ocean. *Dynamics of atmospheres and oceans*, 36(1):3–21. 76

Sabia, R., Cristo, A., Talone, M., Fernández-Prieto, D., and Portabella, M. (2014). Impact of sea surface temperature and measurement sampling on the smos level 3 salinity products. *Geoscience and Remote Sensing Letters, IEEE*, 11(7):1245–1249. 17

Saraceno, M. and Provost, C. (2012). On eddy polarity distribution in the southwestern atlantic. *Deep Sea Research Part I: Oceanographic Research Papers*, 69:62–69. 129

Saraceno, M., Provost, C., Piola, A. R., Bava, J., and Gagliardini, A. (2004). Brazil malvinas frontal system as seen from 9 years of advanced very high resolution radiometer data. *Journal of Geophysical Research: Oceans (1978–2012)*, 109(C5). 127

Saunders, P. (1971). Anticyclonic eddies formed from shoreward meanders of the Gulf Stream. *Deep-Sea Res. Oceanogr. Abstr.*, 18(12):1207 – 1219. 127

Savidge, D. K. (2004). Gulf stream meander propagation past cape hatteras. *Journal of physical oceanography*, 34(9):2073–2085. 127

Schanze, J. J., Schmitt, R. W., and Yu, L. (2010). The global oceanic freshwater cycle: A state-of-the-art quantification. *Journal of Marine Research*, 68(3-4):569–595. 11

Schmitt, R. W. (1994). Double diffusion in oceanography. *Annual Review of Fluid Mechanics*, 26(1):255–285. 75

Schmitt, R. W. (1995). The ocean component of the global water cycle. *Reviews of Geophysics*, 33(S2):1395–1409. 10

Schmitt, R. W. (1999). Spice and the demon. *Science*, 283(5401):498–499. 76

Schmitt, R. W. (2008). Salinityand the global water cycle. *Oceanography*, 21(1):12. 8, 10

Seuront, L. and Schmitt, F. (2005). Multiscaling statistical procedures for the exploration of biophysical couplings in intermittent turbulence. part i: Theory. *Deep-Sea Research II*, 52:1308–1324. v, vii

Seuront, L., Schmitt, F., Lagadeuc, Y., Schertzer, D., Lovejoy, S., and Frontier, S. (1996a). Multifractal analysis of phytoplankton biomass and temperature in the ocean. *Geophysical Research Letters*, 23(24):3591–3594. 74

Seuront, L., Schmitt, F., Lagadeux, Y., Schertzer, D., and Lovejoy, S. (1999). Universal multifractal analysis as a tool to characterize multiscale intermittent patterns: examples of phytoplankton distribution in turbulent coastal water. *Journal of Plankton Research*, 21:877–922. 74

Seuront, L., Schmitt, F., Schertzer, D., Lagadeuc, Y., Lovejoy, S., et al. (1996b). Multifractal intermittency of eulerian and lagrangian turbulence of ocean temperature and plankton fields. *Nonlinear processes in Geophysics*, 3(4):236–246. 74

Shankaranarayanan, K. and Donelan, M. A. (2001). A probabilistic approach to scatterometer model function verification. *Journal of Geophysical Research: Oceans (1978–2012)*, 106(C9):19969–19990. 66

She, Z. S. and Leveque, E. (1994). Universal scaling laws in fully developed turbulence. *Physical Review Letters*, 72:336–339. 73

She, Z. S. and Waymire, E. C. (1995). Quantized energy cascade and log-poisson statistics in fully developed turbulence. *Physical Review Letters*, 74:262–265. 73

Siedler, G., Griffies, S. M., Gould, J., and Church, J. A. (2013). *Ocean Circulation and Climate: A 21st century perspective*, volume 103. Academic Press. 126, 128

Sirjacobs, D., Alvera-Azcarate, A., Barth, A., Lacroix, G., Park, Y., Nechad, B., Ruddick, K., and Beckers, J.-M. (2011). Cloud filling of ocean colour and sea surface temperature remote sensing products over the southern north sea by the data interpolating empirical orthogonal functions methodology. *Journal of Sea Research*. 13

Smith, N. (2000). The global ocean data assimilation experiment. *Advances in Space Research*, 25(5):1089–1098. 48

Smith, T. M. and Reynolds, R. W. (2004). Improved extended reconstruction of sst (1854 - 1997). *Journal of Climate*, 17(12):2466 – 2477. 13

Stommel, H. (1961). Thermohaline convection with two stable regimes of flow. *Tellus*, 13(2):224–230. 75

Stommel, H. (1993). A conjectural regulating mechanism for determining the thermohaline structure of the oceanic mixed layer. *Journal of physical oceanography*, 23(1):142–148. 77

Stramma, L., Ikeda, Y., and Peterson, R. G. (1990). Geostrophic transport in the brazil current region north of 20 s. *Deep Sea Research Part A. Oceanographic Research Papers*, 37(12):1875–1886. 127

Sverdrup, H. U., Johnson, M. W., Fleming, R. H., et al. (1942). *The Oceans: Their physics, chemistry, and general biology*, volume 1087. Prentice-Hall New York. 9, 125

Tandeo, P., Chapron, B., Ba, S., Autret, E., and Fablet, R. (2014). Segmentation of mesoscale ocean surface dynamics using satellite sst and ssh observations. *Geoscience and Remote Sensing, IEEE Transactions on*, 52(7):4227–4235. 13, 107

Tenerelli, J., Reul, N., Mouche, A., and Chapron, B. (2008). Earth viewing L-band radiometer sensing of sea surface scattered celestial sky radiation. Part I: general characteristics. *IEEE Transactions on Geoscience and Remote Sensing*, 46(3):659–674. 17

The Ring Group (1981). Gulf stream cold-core rings: Their physics, chemistry, and biology. *Science*, 212(4499):1091–1100. 129

Thiébaux, J., Rogers, E., Wang, W., and Katz, B. (2003). A new high-resolution blended real-time global sea surface temperature analysis. *Bulletin of the American Meteorological Society*, 84(5):645–656. 35

Tomczak, M. and Godfrey, J. S. (2003). *Regional oceanography: an introduction*. Daya Books. 127

Turiel, A., Grazzini, J., and Yahia, H. (2005a). Multiscale techniques for the detection of precipitation using thermal IR satellite images. *IEEE Geosci. Remote Sens. Lett.*, 2(4):447–450. v, vii

Turiel, A., Isern-Fontanet, J., García-Ladona, E., and Font, J. (2005b). Multifractal method for the instantaneous evaluation of the stream function in geophysical flows. *Physical Review Letters*, 95(10):104502. doi:10.1103/PhysRevLett.95.104502. 74

Turiel, A., Isern-Fontanet, J., Umbert, M., et al. (2014). Sensibility to noise of new multifractal fusion methods for ocean variables. *Nonlinear Processes in Geophysics*, 21:291–301. 13

Turiel, A., Nieves, V., García-Ladona, E., Font, J., Rio, M.-H., and Larnicol, G. (2009). The multifractal structure of satellite temperature images can be used to obtain global maps of ocean currents. *Ocean Science*, 5:447–460. 74, 109, 146, 147

Turiel, A. and Parga, N. (2000). Multifractal wavelet filter of natural images. *Physical Review Letters*, 85:3325–3328. 73, 150

Turiel, A. and Pérez-Vicente, C. (2005). Role of multifractal sources in the analysis of stock market time series. *Physica A*, 355:475–496. 73

Turiel, A., Pérez-Vicente, C., and Grazzini, J. (2006). Numerical methods for the estimation of multifractal singularity spectra on sampled data: a comparative study. *Journal of Computational Physics*, 216(1):362–390. 73, 79, 80, 149, 150

Turiel, A., Solé, J., Nieves, V., Ballabrera-Poy, J., and García-Ladona, E. (2008a). Tracking oceanic currents by singularity analysis of Microwave Sea Surface Temperature images. *Remote Sens. Environm.*, 112:2246–2260. 74, 77

Turiel, A., Yahia, H., and Pérez-Vicente, C. (2008b). Microcanonical multifractal formalism: a geometrical approach to multifractal systems. Part I: Singularity analysis. *Journal of Physics A*, 41:015501. 2, 9, 73, 74, 81, 147, 149, 150

Umbert, M., Guimbard, S., Lagerloef, G., Thompson, L., Portabella, M., Ballabrera-Poy, J., and Turiel, A. (2015). Detecting the surface salinity signature of gulf stream cold-core rings in aquarius synergistic products. *Journal of Geophysical Research: Oceans*. 14, 125, 151, 152, 168

Umbert, M., Hoareau, N., Turiel, A., and Ballabrera-Poy, J. (2014). New blending algorithm to synergize ocean variables: The case of SMOS sea surface salinity maps. *Remote Sens. Environm.*, 146:172 – 187. 13

UNESCO (1981). The practical salinity scale 1978 and the international equation of the state of seawater 1980. *Tenth Report of the Joint Panel on Oceanographic tables and standards. UNESCO Technical Papers in Marine Science*, 36:25. 10

Valdéz-Holguín, J. E. and Lara-Lara, J. R. (1987). Primary productivity in the gulf of california effects of el niño 1982-1983 event. *Ciencias Marinas*, 13(2):34–50. 154

Verrier, S., Crépon, M., and Thiria, S. (2014). Scaling and stochastic cascade properties of nemo oceanic simulations and their potential value for gcm evaluation and downscaling. *Journal of Geophysical Research: Oceans*, 119(9):6444–6460. 9

Vinogradova, N. T. and Ponte, R. M. (2013). Clarifying the link between surface salinity and freshwater fluxes on monthly to interannual time scales. *Journal of Geophysical Research: Oceans*, 118(6):3190–3201. 10, 21

Weissman, D., Stiles, B., Hristova-Veleva, S., Long, D., Smith, D., Hilburn, K., and Jones, W. (2012). Challenges to satellite sensors of ocean winds: Addressing precipitation effects. *Journal of Atmospheric and Oceanic Technology*, 29(3):356–374. 5

Wong, A., Keeley, R., Carval, T., et al. (2014). Argo quality control manual. Technical report, Ifremer. 21

Wu, L., Cai, W., Zhang, L., Nakamura, H., Timmermann, A., Joyce, T., McPhaden, M. J., Alexander, M., Qiu, B., Visbeck, M., et al. (2012). Enhanced warming over the global subtropical western boundary currents. *Nature Climate Change*, 2(3):161–166. 125

Yin, X., Boutin, J., and Spurgeon, P. (2012). First assessment of smos data over open ocean: Part i—pacific ocean. *Geoscience and Remote Sensing, IEEE Transactions on*, 50(5):1648–1661. 17, 18, 19, 28

Yin, X., Boutin, J., and Spurgeon, P. (2013). Biases between measured and simulated smos brightness temperatures over ocean: Influence of sun. *Selected Topics in Applied Earth Observations and Remote Sensing, IEEE Journal of*, 6(3):1341–1350. 17

Young, W. (1994). The subinertial mixed layer approximation. *Journal of physical oceanography*, 24(8):1812–1826. 77

Yu, L. (2007). Global variations in oceanic evaporation (1958-2005): The role of the changing wind speed. *Journal of climate*, 20(21):5376–5390. 11

Yu, L. (2011). A global relationship between the ocean water cycle and near-surface salinity. *Journal of Geophysical Research: Oceans (1978–2012)*, 116(C10). 10

Yueh, S., Tang, W., Fore, A., Hayashi, A., Song, Y. T., and Lagerloef, G. (2014). Aquarius geophysical model function and combined active passive algorithm for ocean surface salinity and wind retrieval. *Journal of Geophysical Research: Oceans*, 119(8):5360–5379. 19

Yueh, S. H., Tang, W., Fore, A. G., Neumann, G., Hayashi, A., Freedman, A., Chaubell, J., and Lagerloef, G. S. (2013). L-band passive and active microwave geophysical model functions of ocean surface winds and applications to aquarius retrieval. *Geoscience and Remote Sensing, IEEE Transactions on*, 51(9):4619–4632. 19

Zhu, J., Huang, B., Zhang, R.-H., Hu, Z.-Z., Kumar, A., Balmaseda, M. A., Marx, L., and Kinter III, J. L. (2014). Salinity anomaly as a trigger for enso events. *Scientific reports*, 4. 12

Zine, S., Boutin, J., Font, J., Reul, N., Waldteufel, P., Gabarró, C., Tenerelli, J., Petitcolin, F., Vergely, J.-L., Talone, M., et al. (2008). Overview of the smos sea surface salinity prototype processor. *Geoscience and Remote Sensing, IEEE Transactions on*, 46(3):621–645. 16

Zine, S., Boutin, J., Waldteufel, P., Vergely, J. L., Pellarin, T., and Lazure, P. (2007). Issues about retrieving sea surface salinity in coastal areas from SMOS data. *IEEE Trans. Geosci. Remote Sens.*, 45(7):2061–2072. 17, 31

Zweng, M., Reagan, J., Antonov, J., Locarnini, R., Mishonov, A., Boyer, T., Garcia, H., Baranova, O., Johnson, D., Seidov, D., et al. (2013). World ocean atlas 2013. vol. 2: Salinity. *NOAA Atlas NESDIS*, 74:39. 25

Agradecimientos

Una mujer sabia me dijo una vez que el miedo es la antítesis del amor. A veces la prudencia asocia la falta de miedo a la locura. Quizás podría parecer una locura andar desde las ciencias del mar a los exponentes de singularidad, pero el día a día, el esfuerzo y las buenas compañías, me han enseñado que ningún camino es fácil, el que hoy me trae hasta aquí me ha aportado un gran aprendizaje científico y mayor evolución personal.

Antes que a nadie, tengo que agradecer a mi director y codirector de tesis, Dr. Antonio Turiel y Dr. Joaquim Ballabrera, por ser unas personas buenas, atentas y comprometidas. Gracias a Quim por ser el primero en creer en mi y ser mi entrañable profesor de programación, y a Antonio por ser capaz de maravillarme, dejarme ser, andar, aprender por mi misma y ayudarme tanto en la fase final, estaré siempre inmensamente agradecida a los dos.

He tenido la suerte de vivir la ciencia en otros lugares, a Anne Briais, Melanie Gernier y Veronique Garçon muchas gracias por ser unas dulces anfitrionas en LEGOS y la ciudad de Toulouse. A LuAnne Thompson, Gary Lagerloef, mis compañeros de la Universidad de Washington y sobre todo a Rachel Pelela, gracias por una fantástica acogida y experiencia personal tan enriquecedora en Seattle. Al final de mi tesis, gracias a Nicolas Reul, por compartir su experiencia, ser gentil y divertido.

Millones de gracias a Sofia Kalaroni, Nina Hoareau, Marta Ramirez y Ana Trindade, que en estos años me han ayudado muy de cerca, más que nadie, con la complicidad y la risa. Igualmente no me puedo olvidar de todas las mujeres salvajes que he elegido tener a mi alrededor: Lorena Font, Johanna Kergroach, Ester Camacho, Laia Beni, Maite Weinhold, Maria Graells, Kathrin Koerting, Katja Böhm, Maria Coma... millones de gracias a vosotras, mis mayores maestras, porque la vida sin vosotras no tendría ningún tipo de sentido.

Recordaré siempre a todos los componentes del Departamento de Oceanografía Física así como a sus bellísimos estudiantes con muchísimo cariño. Gracias al divertidísimo equipo BEC, todos me han enseñado mucho en este proceso, en especial tengo que agradecer al Prof. Jordi Font por hacerme pasar el mes más maravilloso y apasionante de esta tesis a bordo del Sarmiento de Gamboa, y sobre todo por haber hecho partícipe a nuestro centro de investigación y a tantos como yo de la misión SMOS.

Es muy difícil expresar con palabras todo lo que debo agradecer en esta vida a mi madre. Una mujer de la que siempre podré seguir aprendiendo la generosidad, la humildad, la bondad, el amor incondicional a los suyos. Ella ha estado conmigo cada día, en mis mayores triunfos y mis mayores errores, no hay nadie en el mundo que me conozca mejor que ella. Muchas gracias por todo tu esfuerzo y amor desde lo más profundo de mi corazón. Es un regalo y un privilegio tener como referente una mujer como tú.

Agradecer igualmente a mi padre, por haber tenido la capacidad maravillosa de contagiarme

su pasión por la ciencia y por la música. Por starwars, los beatles, las motos, el ala delta y el mar. De niña y no tan niña, aunque sé que siempre me verás vestida de princesa con zapatos de charol, gracias por las apasionadas conversaciones sobre el universo, la física y la vida. Tu ímpetu y fuerza inagotable, me han ayudado mucho a llegar hasta aquí.

El mayor de todos los agradecimientos a Pol, mi compañero de juegos, el rubio guapo que nació siendo mi hermano y que ha crecido siendo un hombre de bien, sensible, eficiente, divertido, músico, el mejor de mis cómplices y compañero de viajes. Nos quedan muchos y mejores paisajes por ver juntos.

Y por último, volviendo al amor, quiero agradecer profundamente a Sébastien Guimbard. La santa paciencia, la generosidad, haber sido mi guía personal y científica, mi cómplice y mi compañero. Agradezco infinitamente todo lo que me queda por vivir y aprender a tu lado. A ti dedico esta tesis, porque sin ti, dificilmente la hubiera acabado.

Publications and Conferences

PUBLICATIONS

New blending algorithm to synergize ocean variables: the case of SMOS sea surface salinity maps.
Umbert, M., Hoareau N., Turiel A., and Ballabrera-Poy, J.
44th International Liege Colloquium Special Issue, Remote Sensing of Environment, 2014, in press.

On the potential of data assimilation to generate SMOS-Level 4 maps of sea surface salinity.
Hoareau N., **Umbert, M.**, Martínez J., Turiel A., Gourrion J., and Ballabrera-Poy,J.
44th International Liege Colloquium Special Issue, Remote Sensing of Environment, 2014, in press.

Sensibility to noise of new multifractal fusion methods for ocean variables.
Turiel A., Isern, J. and **Umbert, M.**
Special Issue: Nonlinear dynamics in oceanic and atmospheric flows: theory and observations, NPG, 2014, in press.

The contribution of the Barcelona World Race to improve the ocean surface information.
Salat, J., **Umbert, M.**, Ballabrera-Poy, J., Fernandez, P., Salvador, J. and Martinez, J.
IEEE Contributions to Science, 2014, in press.

Detecting the surface salinity signature of Gulf Stream cold-core rings in Aquarius synergistic products.
Umbert, M., Guimbard, S., Lagerloef, G., Thompson, L., Portabella, M., Ballabrera-Poy, J. and Turiel, A.
Early Scientific Results from the Salinity Measuring Satellites Aquarius/SAC-D and SMOS, Journal of Geophysical Research: Oceans, 2015, in press.

Synergy between of ocean variables: multifractal fusion of remotely sensed temperature and chlorophyll.
Umbert, M., Guimbard, S., Ballabrera-Poy, J. and Turiel, A.
Geophysical Research Letters, 2015, under revision.

Synergy of SMOS sea surface salinity with other oceanic variables: recent advances in multifractal fusion.
Olmedo, E., Martinez, J., **Umbert, M.**, Hoareau, N., Guimbard, S., Ballabrera-Poy, J., Portabella, M. and Turiel, A.
Special Issue on SMOS in Remote Sensing of Environment, 2015, under revision.

PROCEEDINGS AND TECHNICAL NOTES

SMOS CP34 Soil moisture and ocean salinity maps.
Font J., Gabarró C., Ballabrera J., Turiel A., Martínez J., **Umbert, M.**, Pérez P., Hoareau N., Portabella M., González V., Gourrion J., Guimbard S., Piles M., Camps A., Vall-llossera M.
IEEE Microrad, 2010.

Turbulence and synergy of ocean variables: Extrapolating chlorophyll maps using SST as a template.
Umbert, M., Guimbard, S., Martinez J., Ballabrera-Poy, J. and Turiel A.
Proceedings of the 2013 ESA Living Planet Symposium.

ORAL PRESENTATIONS

Turbulence-inspired fusion methods for ocean remote sensing data
Umbert, M., Ballabrera, J., Hoareau, N., Portabella, M., Turiel, A.
Liège Colloquium on Ocean Dynamics, 7^{th}-11^{th} *May 2012, Liège, Belgium*

Validation of SMOS SSS using Argo and opportunity ships
Umbert, M., Ballabrera, J., Fernandez, P., Salat, J., Salvador, J.
Second Meeting of Spanish physical oceanography, 14^{th}-16^{th} *November 2012, Madrid, Spain*

Synergy between remote sensing variables: Level 4 research products of SSS and Chl-a
Umbert, M., Guimbard, S., Ballabrera, J., Portabella, M., Turiel, A.
Third Meeting of Spanish physical oceanography, 11^{st}-13^{rd} *June 2014, Canary Island, Spain*

Synergy between remote sensing variables: Level 4 research products of Sea Surface Salinity
Umbert, M., Portabella, M., Guimbard, S., Ballabrera-Poy, J., Turiel, A.

Ocean Salinity Science, 24^{th}-28^{th} *November 2014, Exeter, UK*

Surface salinity signature of western boundary current rings in L-band synergistic products
Umbert, M., Guimbard, S., Ballabrera, J., Portabella, M., Turiel, A.
IEEE International Geoscience and Remote Sensing Symposium, 23^{th}-31^{st} *July 2015, Milan, Italy*

POSTERS

Turbulent-inspired fusion methods for ocean remote sensing data
Umbert, M., Hoareau, N., Turiel, A., Ballabrera, J., Portabella, M.
European Geophysical Union EGU 2012, 22^{nd}-27^{th} *April 2012, Viena, Austria*

SMOS validation using SSS data from Barcelona World Race and Argo profilers
Umbert, M., Ballabrera, J., Fernandez, P., Salat, J., Salvador, J.
European Geophysical Union EGU 2012, 22^{nd}-27^{th} *April 2012, Viena, Austria*

SMOS validation using SSS data from Barcelona World Race and Argo profilers
Umbert, M., Ballabrera, J., Fernandez, P., Salat, J., Salvador, J.
Liège Colloquium on Ocean Dynamics, 7^{th}-11^{th} *May 2012, Liège, Belgium*

Turbulence and synergy of ocean variables: application to the extrapolation of chlorophyll maps with SST templates
Umbert, M., Guimbard, S., Martinez, J., Ballabrera, J., Turiel, A.
ESA Living Planet Symposium, 9^{th}-13^{th} *September 2013, Edinburg, UK*

Noise removal on ocean scalars by means of singularity-based fusion
Umbert, M., Turiel, A., Hoareau, N., Ballabrera, J., Martinez, J., Guimbard, S., Font, J.
AGU Fall Meeting, 9^{th}-13^{th} *December 2013, San Francisco, USA*

High resolution maps of satellite surface salinity from a singularity-based data fusion technique
Umbert, M., Guimbard, S., Martinez, J., Ballabrera, J., Turiel, A.
AGU Ocean Sciences Meeting, 23^{rd}-28^{th} *February 2014, Honolulu, USA*

Funding for this work comes from the Spanish Ministerio de Ciencia e Innovación through projects: “Productos SMOS de Salinidad Oceánica y Humedad del Suelo. Mejoras y Demostración de Aplicaciones” (MIDAS-6, reference AYA2010-22062-C05-01), ”Productos y aplicaciones avanzados de SMOS y futuras misiones: parte CSIC” (MIDAS-7, reference AYA2012-39356-C05-03) and ”SMOS Mission Oceanographic Data Explotation (SMOS-MODE)”, (Acción COST ES1001). Marta Umbert Ceresuela would also like to acknowledge the Ministerio de Ciencia e Innovación for funding through a FPI grant (reference BES-2011-047173).